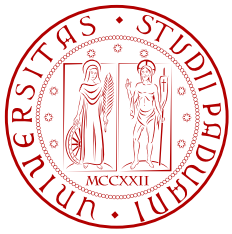

UNIVERSITÀ DEGLI STUDI DI PADOVA
Facoltà di Scienze MM.FF.NN.
Dipartimento di Fisica "G. Galilei"

Scuola di Dottorato di Ricerca in Fisica
Ciclo XXIII

TeV observations of blazars and constraints on their redshifts: a detailed study of PG 1553+113 and PKS 1424+240 with MAGIC

Direttore della Scuola: Prof. Attilio Stella
Supervisore: Prof. Mosè Mariotti
Correlatore: Dott. Fabrizio Tavecchio

Dottoranda: Elisa Prandini

To Andrea,
wings of my life,
and
to my lioness sister,
Marianna

Abstract

This thesis reports the activities performed during three years of Ph.D. at the University of Padova, Department of Physics "G. Galilei" in 2008–10, under the supervision of Prof. M. Mariotti and Dott. F. Tavecchio. The thesis is focused on the characterization of the distances of blazars, starting from the properties of the detected TeV emissions. In particular, the research activity presented may be divided into an *experimental* and a *phenomenological* part, the former carried out as a member of the MAGIC Collaboration.

The purely experimental part of the work is related to the analysis of MAGIC data. MAGIC is a system of two telescopes, located in the Canary island of La Palma, which observes photons from space in the 100 GeV–tens of TeV energy range, also known as Very High Energies (VHE). The origin of VHE γ–ray emitters can be galactic or extragalactic. The large majority of the latter sources are blazars: supermassive black holes accreting material and presenting a narrow jet with a small angle to the observer. The detailed study of VHE γ–ray emission from two uncertain/unknown distance blazars observed by MAGIC, namely PG 1553+113 and PKS 1424+240, will be discussed. In particular, the spectral properties of the emission, also in relation with other frequencies of the electromagnetic spectrum, will be analyzed.

The phenomenological part of the work is aimed to set constraints on the distances of these TeV blazars. We will show how an upper limit on the blazar redshift can be derived from the properties of its observed VHE γ–ray signal. Moreover, a new method to infer the distance of a source will be developed, based on combined high energy (< 100 GeV) and VHE γ–ray observations. These estimates are made possible thanks to the interaction of VHE photons with the optical–infrared light filling the Universe. This radiation is composed of the light emitted by stars and partially reprocessed by dust and redshifted by the expansion of the Universe along the history. In this interaction, where the most powerful shining objects meet their past, two distinct branches of modern astrophysics, VHE γ–rays astrophysics and observational cosmology, overlap each other. The method developed will allow us to estimate, for the first time, the distance of the two TeV blazars with uncertain/unknown distance: PG 1553+113 and PKS 1424+240.

Summary

In this thesis recent results achieved in the young field of extragalactic Very High Energy (VHE) γ–ray astrophysics are presented. This is a promising discipline which is extending the frontier of our knowledge of the emission of distant sources to the upper edge of the electromagnetic spectrum.
Almost all of the 46 sources detected up to now in the energy range between 100 GeV to some tens of TeV (also known as TeV emitters) belong to the class of radio–loud Active Galactic Nuclei (AGNs). They are supermassive black holes accreting material and showing two narrow jets of relativistic particles. In particular, the majority of the sources are blazars, i.e. radio loud AGNs with a jet almost aligned to the line of sight. It is interesting to note that more than a half of these sources have been detected as TeV emitters in the last three years (between 2008 to 2010) thanks to the last generation of Cherenkov telescopes: MAGIC, H.E.S.S. and VERITAS[1]. These discoveries were made possible not only thanks to the improved sensitivity and increased energy range of the instruments, but also thanks to the cooperation between instruments operating at different frequencies, such as optical and γ–rays below 100 GeV.
A peculiar characteristics of the detected AGNs is their relative short distance: the most distant source known so far is 3C 279, located at redshift $z = 0.536$. The reason for this limited distribution of the distances is believed to originate from the interaction of VHE photons with the optical–infrared light filling the Universe (the Extragalactic Background Light, EBL). This radiation is composed of the light emitted by stars and partially reprocessed by dust and redshifted by the expansion of the Universe along the history. Part of the VHE radiation emitted by distant blazars (the intrinsic spectrum) is, in fact, absorbed and the TeV spectrum observed is significantly deformed. The amount of this deformation is an increasing function of the energy of the energetic photon and of the distance of the emitter. Actually, it is possible to define a VHE γ–ray horizon, beyond which the Universe becomes opaque to the TeV radiation.
Another feature of the sample, related to the characteristics of the emitted radiation, is that a number of sources have uncertain or unknown redshift.

This thesis is focused on the characterization of the distances of blazars, starting from the properties of the detected TeV emission. In particular, the research activity presented may be divided into an *experimental* and a *phenomenological* part, the former carried out as a member of the MAGIC Collaboration.
In the first part of the work, a detailed analysis of the VHE γ–ray radiation emitted by the two blazars with uncertain redshift PG 1553+113 and PKS 1424+240 observed with MAGIC is presented. MAGIC is a system of two Imaging Atmospheric Cherenkov Telescopes (IACTs), located in the Canary island of La Palma at ∼2240 m asl. It observes VHE photons coming from space taking advantage

[1] standing for Major Atmospheric Gamma Imaging Cherenkov, High Energy Stereoscopic System, and Very Energetic Radiation Imaging Telescope Array System, respectively.

of the Cherenkov light emitted by particle showers induced by VHE γ–rays.
For each source, the differential energy spectrum and the temporal evolution of the detected integral flux are studied. For the case of PG 1553+113, the new sample presented, composed of the data collected from 2007 to 2009, is combined with previous observations (2005/06). This large sample makes PG 1553+113 one of the longest studied sources at energies above 100 GeV.
Concerning PKS 1424+240, the analysis of 2009 and 2010 datasets is presented. The main feature of 2010 sample is that it is collected in stereoscopic mode, using the upgraded MAGIC stereoscopic system.
Both sources reveal a modest variability in the VHE γ–rays, and a steep spectrum of power law index ~ 4[2]. The results obtained are, in both cases, combined with partially simultaneous observations carried out in other frequencies, from optical to γ–rays. Correlation studies between the optical and the TeV integral flux suggest a connection between these two extreme components, especially for the case of PG 1553+113. Conversely, the small significance of the signal detected from PKS 1424+240 prevents any definitive conclusion about eventual correlation of TeV photons with optical, X–ray and γ–ray data.
Finally, the mean spectra measured at VHE are combined with archival data available for other wavelengths. In both cases a clear two bump structure arises, in agreement with current models of blazar emission. Furthermore, for the case of PG 1553+113, the mean spectral energy distribution is modeled with a one–zone SSC (Synchrotron Self Compton) model, and the main physical parameters governing the emission in the blazar jet are derived.

In the second part of the thesis the results of the phenomenological work are reported, aimed to set constraints on the TeV blazars distances. This work is of particular interest for the current VHE γ–rays astrophysics, since, as mentioned above, many sources have unknown/uncertain redshifts.
First the existing techniques are presented. Such techniques make use of reasonable hypotheses on the VHE γ–rays intrinsic spectrum emitted by blazars to set an upper limit on their distances. The methods are then applied to the PG 1553+113 and PKS 1424+240 observed spectra. In the first case, the requirement that the spectrum corrected for EBL absorption (deabsorbed) does not show a pile up at high energies leads to the most stringent limit on the source distance of $z < 0.67$ at a two sigma level. In the second case, on the contrary, it is the demand of a spectral index softer than 1.5 (also called maximum hardness criterion) to better constrain the source redshift at $z < 0.81$.
Starting from these methods, a new method is developed based on combined GeV and TeV observations. This technique can be seen as a sort of experimental version of the maximum hardness criterion, in which instead of assuming a limiting slope for the deabsorbed spectrum given by theory, the slope measured by *Fermi*/LAT at lower energies, in the High Energy (HE) regime (0.2–100 GeV), is used. Since almost all of these slopes are above the limiting value 1.5, the upper limits that can be set with this method are below the previous limits. Therefore, in principle, this technique is more constraining. In order to check its validity, it is tested on a wide sample of TeV blazars detected also at lower energies by *Fermi*, using different EBL models. The results obtained are satisfactory, and it can be concluded that, for a TeV blazar, the redshift, z^*, at which the deabsorbed slope equals the slope

[2]For the case of blazars, the observed spectra at VHE are often well fitted by laws of the form: $dN/dE = f_0 \cdot E^{-\Gamma}$, with Γ spectral index.

measured by *Fermi*/LAT at lower energies can be considered as an upper limit on the source distance, at least with mean and low density EBL models.
Adopting a mean density EBL model for the blazars PG 1553+113 and PKS 1424+240, the redshift values of $z^* = 0.75 \pm 0.07$ and $z^* = 0.45 \pm 0.15$ are obtained, respectively, which correspond to the $2\,\sigma$ upper limits $z < 0.89$ and $z < 0.75$. As a spin–off, the same procedure is then applied to the two uncertain redshift sources S5 0716+714 and 3C 66A, recently observed at VHE γ–rays. The values $z^* = 0.22 \pm 0.10$ and $z^* = 0.38 \pm 0.05$ are obtained, respectively, in partial contradiction with the (uncertain) redshifts resulting from optical measurements. Following previous works, finally the possibility of a linear relation between the z^* estimates and the real distances of the sources is checked. A linear fit describes quite well the results, independently of the EBL model considered. The relation obtained suggests the use of the z^* estimate not only as an upper limit on a blazar redshift, but also, via the inverse formula, as an evaluation of this distance. This method is demonstrated to be statistically consistent; therefore, it can be used to make a first estimation of the distance of TeV emitting blazars.
The method applied to PG 1553+113 returns the value of 0.43 ± 0.05 for the reconstructed redshift, in agreement with both upper and lower limits estimated with other methods. For PKS 1424+240 the evaluated distance is 0.26 ± 0.05. Regarding the uncertain redshift sources, the value of the redshift of S5 0716+714 that results with this method is 0.12 ± 0.05, where the error quoted is the σ of the Δz distribution. For 3C 66A, the same procedure leads to a redshift estimate of 0.22 ± 0.05.

In conclusion, we have determined, through a detailed study of their TeV emission, new constraints on the distances of the blazars PG 1553+113 and PKS 1424+240. Furthermore we have developed a new technique, based on the comparison among GeV and TeV blazars spectra, which allows to give an estimate, and not only to set a limit, on the distance of TeV emitting blazars. We applied this technique to PG 1553+113 and PKS 1424+240, and obtained for the first time a measure of their redshifts. Moreover, we applied it on other uncertain redshifts blazars. The method developed uses combined information at the highest energies of the electromagnetic spectrum (HE and VHE γ–rays) and takes advantage of the interaction of such photons with the optical–IR light filling the universe.
Hence, in this interaction, where the most powerful shining objects of the Universe meet their past, two distinct branches of modern astrophysics, VHE γ–rays astrophysics and observational cosmology, overlap each other granting us a new tool for the measurement of previously unresolved blazars distances.

Riassunto

Questa tesi si é svolta nell'ambito dell'astrofisica delle altissime energie (VHEs; Very High Energies), giovane e promettente disciplina che sta estendendo all'estremità dello spettro elettromagnetico le nostre conoscenze dello spettro di energia emesso da sorgenti lontane.
La quasi totalità delle 46 sorgenti osservate finora nell'intervallo energetico tra 100 GeV e qualche decina di TeV appartiene alla classe dei nuclei galattici attivi (AGN; Active Galactic Nuclei) detti radio loud (ovvero molto brillanti nelle frequenze radio), galassie contenenti buchi neri supermassivi che accrescono materiale ed emettono getti di particelle relativistiche ben collimati. La maggioranza di queste sorgenti sono blazar, AGN radio loud che presentano un getto praticamente allineato con la linea di vista dell'osservatore. Solo negli ultimi tre anni (tra il 2008 e il 2010), grazie ai telescopi Cherenkov di ultima generazione, MAGIC, H.E.S.S. e VERITAS[3] si é scoperta un'emissione di fotoni ad energie dell'ordine del TeV per più di metà di queste sorgenti. Queste nuove scoperte sono state possibili non solo per merito dell'elevata sensibilità di questi nuovi telescopi e del loro esteso intervallo energetico rispetto ai predecessori, ma anche grazie alla cooperazione con strumenti che osservano a diversi intervalli di energia, tra cui l'ottico e i raggi gamma sotto i 100 GeV.
Una delle principali caratteristiche degli AGN osservati é la loro distanza relativamente contenuta: la sorgente più lontana nota fino ad ora é il blazar 3C 279, avente un redshift $z = 0.536$. La ragione di questa limitata distribuzione delle distanze é dovuta all'interazione dei fotoni TeV con la luce ottica e infrarossa che permea l'Universo (EBL; Extragalactic Background Light). Questo fondo é composto da fotoni emessi dalle stelle e riprocessati dalle polveri, la cui energia si é diluita nel tempo a causa dell'espansione dell'Universo. Una parte della radiazione gamma emessa da blazar distanti viene quindi assorbita e lo spettro TeV osservato può venire significativamente deformato rispetto a quello emesso. Tale deformazione é una funzione (crescente) dell'energia del fotone γ e della distanza della sorgente. Esiste un orizzonte, detto orizzonte gamma, oltre il quale l'Universo diventa opaco alla radiazione TeV, e diventa quindi molto improbabile poter vedere fotoni di tale energia provenienti da distanze maggiori.
Un'altra proprietà legata alle caratteristiche dello spettro emesso dai blazar osservati é che un certo numero di sorgenti ha redshift incerto o addirittura ignoto.

L'obiettivo di questa tesi é la caratterizzazione della distanza di blazar osservati a frequenze VHE a partire dal loro spettro misurato. In particolare, il lavoro é suddiviso in due parti: una parte prettamente sperimentale, svolta in collaborazione con l'esperimento MAGIC, e una parte fenomenologica.

Nella prima parte della tesi vengono presentate le analisi dettagliate dei dati raccolti da MAGIC, riguardanti l'emissione di fotoni γ ad energie superiori ai

[3] rispettivamente Major Atmospheric Gamma Imaging Cherenkov, High Energy Stereoscopic System, e Very Energetic Radiation Imaging Telescope Array System.

100 GeV, di due blazar con distanza ignota: le sorgenti PG 1553+113 e PKS 1424+240. Dal 2009 MAGIC é un sistema di due telescopi Cherekov, MAGIC I e MAGIC II, del tipo IACT (Imaging Atmospheric Cherenkov Telescope), situato a La Palma, nelle isole Canarie, a 2240 metri sul livello del mare. Prima di tale data, e più precisamente tra il 2004 e il 2009, MAGIC consisteva in un unico telescopio, MAGIC I, al tempo il più grande IACT al mondo. Questo strumento misura la radiazione gamma proveniente da oggetti celesti osservando i brevi e deboli lampi Cherenkov emessi da particelle secondarie prodotte dall'interazione dei raggi gamma con i nuclei dell'atmosfera e dalla loro successiva propagazione in aria.
Di entrambe le sorgenti si propone sia l'analisi spettrale dell'emissione che quella temporale: nel caso di PG 1553+113 il campione analizzato viene combinato con precedenti osservazioni di MAGIC, il che rende questo blazar una delle sorgenti più a lungo monitorate al di sopra dei 100 GeV, mentre per quanto riguarda PKS 1424+240, si presentano le analisi dei dati raccolti nel 2009 con MAGIC e nel 2010 con il nuovo sistema stereoscopico.

In entrambe le sorgenti, gli spettri differenziali in energia misurati sono compatibili con una legge di potenza[4] di indice ~ 4, e per quanto riguarda l'analisi temporale si ha una modesta variabilità della componente γ ad altissima energia. I risultati di quest'ultima analisi sono quindi confrontati con quelli ottenuti da osservazioni effettuate da altri strumenti in diverse lunghezze d'onda, dall'ottico ai raggi gamma. Studi di correlazione tra il flusso ottico e quello TeV sembrano suggerire una connessione tra queste due componenti estreme, specialmente nel caso di PG 1553+113. Per la sorgente PKS 1424+240, invece, il ridotto segnale osservato non ha permesso di trarre conclusioni definitive riguardo a eventuali correlazioni. Infine, gli spettri medi osservati ad altissima energia vengono combinati con i dati d'archivio disponibili ad altre lunghezze d'onda ed in entrambi i casi si evince un'evidente struttura a due picchi nella distribuzione spettrale di energia (SED; Spectral Energy Distribution), in accordo con gli attuali modelli di emissione dei blazar. Inoltre, nel caso di PG 1553+113 la SED viene modellizzata in modo da stimare i principali parametri fisici che governano l'emissione del jet del blazar.

Nella seconda parte della tesi, si riportano i risultati ottenuti inerenti al lavoro fenomenologico svolto, finalizzato a definire dei limiti sulla distanza dei blazar osservati al TeV. L'importanza di questo studio risiede nel fatto che, come anticipato in precedenza, molte sorgenti hanno redshift ignoto o incerto: é quindi utile trovare una tecnica che permetta di definirne dei limiti sulla distanza.
Per fare ciò vengono proposte e applicate alle due sorgenti PG 1553+113 e PKS 1424+240 le tecniche esistenti in letteratura: tali tecniche sfruttano ipotesi sulla forma dello spettro intrinseco emesso da questi oggetti ad altissima energia per derivare un vincolo sulla loro distanza. Nel caso di PG 1553+113, la richiesta che lo spettro γ, corretto per l'assorbimento dell'EBL (spettro deassorbito), non mostri la presenza di un terzo picco ad altissime energie porta alla determinazione del limite più stringente sul redshift, pari a $z < 0.67$. Per PKS 1424+240, invece, é la richiesta di un indice spettrale maggiore di 1.5 (chiamato anche criterio di massima pendenza) a porre il vincolo maggiore a $z < 0.81$.
Viene poi sviluppato un nuovo metodo basato sulla combinazione di osservazioni

[4]Nel caso di spettri VHE da blazar, lo spettro osservato segue spesso una legge del tipo: $dN/dE = f_0 \cdot E^{-\Gamma}$, con Γ indice spettrale.

fatte al GeV (da satellite) e al TeV (da telescopi IACT). Questa tecnica, che può essere considerata una sorta di versione sperimentale del criterio di massima pendenza, utilizza come pendenza limite per lo spettro deassorbito l'indice spettrale misurato da *Fermi*/LAT ad energie minori di 100 GeV al posto del valore fissato dalla teoria. Poichè gli indici misurati da LAT sono in pratica tutti al di sopra del valore limite di 1.5, questo approccio fornisce dei vincoli sulla distanza più stringenti di quelli esposti in precedenza e quindi, in linea di principio, la tecnica trovata é più efficace di quella basata sulla teoria. Per valutarne la validità, tale metodo viene testato su un ampio campione di blazar osservati sia al TeV che ad energie minori, usando modelli di EBL differenti per il deassorbimento. I risultati ottenuti sono statisticamente consistenti e permettono di concludere che per un blazar TeV, il redshift z al quale la pendenza dello spettro deassorbito eguaglia quella misurata ad energie più basse può essere considerato un limite superiore alla sua distanza, perlomeno se si utilizza un modello di EBL caratterizzato da una densità di fotoni bassa o media.

Utilizzando un modello standard di EBL si ottengono rispettivamente per PG 1553+113 e PKS 1424+240 i valori $z^* = 0.75 \pm 0.07$ e $z^* = 0.45 \pm 0.15$, corrispondenti a limiti sulle distanze di $z < 0.89$ e $z < 0.75$ entro i $2\,\sigma$ di errore. Come ulteriore applicazione di questo lavoro, la procedura viene utilizzata per stimare un limite sulla distanza di altri due blazar di redshift incerto, S5 0716+714 e 3C 66A, recentemente scoperti come sorgenti di fotoni TeV. Si ottengono rispettivamente i valori $z^* = 0.22 \pm 0.10$ e $z^* = 0.38 \pm 0.05$, in parziale contraddizione con i redshift (incerti) stimati da osservazioni ottiche.

Infine, nella parte conclusiva del lavoro si trova che le stime z^* effettuate con il metodo sopracitato e le distanze vere delle sorgenti sono legati da una relazione lineare. Studi dettagliati evidenziano la solidità di questa funzione a prescindere dal modello di EBL considerato. La relazione ottenuta suggerisce di usare il valore z non solo per porre un vincolo sulla distanza dei blazar, ma anche, tramite la formula inversa, per tentare la stima della distanza. Applicandolo a sorgenti di distanza nota viene dimostrato che il metodo é statisticamente valido e che quindi può essere usato per ottenere una stima della distanza delle sorgenti di fotoni TeV. Il metodo ha permesso di stimarne per la prima volta la distanza di PG 1553+113, pari a a $z = 0.43 \pm 0.05$, in ottimo accordo con i limiti (inferiori e superiori) determinati con altre tecniche. Per PKS 1424+240 si ottiene il valore $z = 0.26 \pm 0.05$, mentre per quanto riguarda le sorgenti di distanza incerta, si ha per S5 0716+714 un redshift di 0.12 ± 0.05, e per 3C 66A un redshift di 0.23 ± 0.05.

In conclusione, lo studio dettagliato svolto in questa tesi dell'emissione alle altissime energie ha portato alla determinazione di nuovi vincoli sulle distanze dei blazar PG 1553+113 e PKS 1424+240. Inoltre e' stata sviluppata una nuova tecnica che permette non solo di porre un limite più vincolante rispetto ai precedenti, ma anche di stimare la distanza di tali oggetti. Grazie a questo metodo per la prima volta si é potuta stimare la distanza di PG 1553+113 e PKS 1424+240 e quella di altri oggetti di distanza incerta.

Questa tecnica, sfruttando l'interazione dei fotoni VHE con i fotoni dell'EBL, e di fatto facendo incontrare i più potenti oggetti dell'Universo con il loro passato, fa intersecare due rami distinti della moderna astrofisica, ovvero quello dell'astrofisica delle altissime energie e quello della cosmologia osservativa, per-

mettendo di effettuare la misura di una quantità precedentemente irrisolta.

Contents

Outline

The observation, study and understanding of the more energetic objects populating our Universe, usually associated with cataclysmic phenomena, is one of the most active and exciting field of modern astrophysics. It is commonly believed that the messengers of such catastrophic events are the cosmic rays, i.e. energetic particles coming from space and entering Earth atmosphere. Cosmic rays are thought to be ejected and accelerated by both galactic and extragalactic objects. In particular, supernova remnants and pulsars belong to the former category. On the other side, classical extragalactic emitters are blazars, i.e. supermassive black holes accreting material and presenting two narrow jets perpendicular to the disk plane and with a small angle to the observer.

Besides protons and other charged particles, which constitute the large majority of cosmic rays, a small fraction is composed of γ–rays. The absence of charge of these particles makes them the ideal messengers of energetic phenomena, since they are not deviated by intergalactic magnetic fields, hence they point directly to their generator. Moreover, they preserve timing information.
In the last decades, a large effort has been done to populate the γ–ray sky: new detectors have been built, both ground based and space borne, and new experimental techniques have been developed. Among these techniques, a successful approach has been the study of very high energy (VHE) γ–rays, i.e. photons with energy between 100 GeV to some tens TeV, from Earth. One of these detector is MAGIC, a system of two telescopes located in the Canary island of La Palma, working since 2004 (the second telescope became operative in 2009).

This work of thesis presents recent results in the field of extragalactic VHE γ–ray astrophysics. In particular, the detailed study of VHE emission from the blazar PG 1553+113 observed by MAGIC will be discussed. Moreover, the analysis of PKS 1424+240, another blazar newly discovered as VHE γ–rays emitter, will be presented. The optical spectral features of both objects make the direct determination of their distance based on spectroscopic methods very difficult, if not impossible. The detection of VHE radiation allows to deduce an upper limit on the sources distance, as will be shown. Moreover, a new method to infer the distance of a source, based on combined High Energy (HE, conventionally set to the interval between 0.1 to 100 GeV) and VHE γ–ray observations will be illustrated. These estimates are made possible thanks to the interaction of VHE photons with the optical–infrared light filling the universe (the so–called EBL, Extragalactic Background Light), composed by the light emitted by stars and reprocessed by dust, redshifted by the expansion of the Universe along the history. In this interaction, where the most powerful shining objects encounter their past, VHE γ–rays astrophysics and observational cosmology overlap each other.

The work can be divided in the following three parts:

Part I: The physics case

In Chapter 1, an introduction on experimental particle astrophysics is given. Recent results about cosmic ray composition and their energy spectrum are discussed. A particular emphasis will be given to new experimental findings and open questions, such as the evidence of a high energy cut–off in the spectrum of cosmic rays, and the cause of the observed positron excess. The physical mechanisms at the basis of cosmic rays acceleration and the possible sites of such acceleration are discussed. Moreover, it will be explained why γ–rays can be considered the ideal messenger of energetic events, and w the main mechanisms responsible for their production and absorption will be presented. A list of γ–ray sources detected by last generations of detectors will follow. At the end, neutrino astronomy is briefly introduced.
Chapter 2 is focused on the description of Active Galactic Nuclei (AGN), which are the main emitters of VHE γ–rays outside our Galaxy. Their physical characteristics and emission mechanisms will be outlined. A particular importance will be given to the description of jets in AGNs and to the properties of their emission, since closely related to VHE γ–ray emission. The two distinct classes of AGNs, namely blazars and radio galaxies will be finally described.
In Chapter 3, that is the last introductory Chapter, an overview of the extragalactic background light is given. This light that fills the Cosmos is of fundamental importance for VHE γ–ray observational astronomy, since it interacts with the energetic radiation emitted by extragalactic objects, such as AGNs, causing a deformation of the observed photon spectrum. This subject will be discussed in depth in other Chapters of the thesis. Here, a report the present status of (direct and indirect) observations is outlined. The models of EBL are then discussed and compared.

Part II:Experimental results

The central part of the thesis is dedicated to the experimental results.
In Chapter 4, the detection technique of VHE γ–rays is presented and compared to other techniques used in the adjacent energy bands. The MAGIC telescopes, operating at the Canary Island of La Palma, are then introduced, and the hardware components described.
Chapter 5 is dedicated to the results of five years of observations of the uncertain redshift blazar PG 1553+113performed by MAGIC from 2005 to 2009. The data analysis chain is presented, and the analysis of three years of data of PG 1553+113, namely from 2007 to 2009, described. Such sample will be then combined with previous data, and a long term study of the properties of the emitted radiation will be performed. In particular, the energy spectrum and light curve will be thoroughly investigated. Correlation studies with other wavelenghts are finally performed, and a broadband spectral energy distribution is built and modeled.
In Chapter 6 the analysis of 2009 and 2010 MAGIC data of PKS 1424+240 will be presented. This is one of the first sources observed with both telescopes, in the so–called stereoscopic mode. Hence, the great improvement given by the use of this technique will be underlined. The results from the temporal and spectral analyses will be finally presented.

Part III: Phenomenological work

In the final part of this thesis, a phenomenological work regarding the TeV blazars and their distance will be presented.
In Chapter 7 a description of the effect of the EBL on blazar VHE γ–ray spectra is given. It will be shown how, based on reasonable hypotheses, this deformation can be used to infer an upper limit on the distance of a blazar. Two different approaches will be discussed and applied to the VHE spectra of PG 1553+113 and PKS 14324+240. Upper limits on the distance of such blazars will be estimated.
In Chapter 8 a new method to infer an upper limit on blazars distance will be developed. Such method, based on the combined spectrum at GeV and TeV energies, is successfully tested on a sample of know distance blazars observed by TeV detectors and the *Fermi*/LAT telescope after 5.5 months of operations. Moreover, an empirical relation between the upper limit and the real redshift is found, which suggests a way to estimate (and not only limit) the redshift of unknown distance sources. An update based on a more recent *Fermi* catalogue will be finally given, in parallel to a discussion on the systematics occurring in the study. Finally, the relation found will be used to give an estimate on the distance of PG 1553+113, PKS 1424+240, and other uncertain redshift sources.

The last Chapter is dedicated to outline the conclusions of this work.

A distant time,
a distant space,
that's where we're living...

Unthought known – Pearl Jam

1 Introduction: Experimental Particle Astrophysics

VERY HIGH ENERGY γ–rays from active galactic nuclei, which are the subject of this work of thesis, can be considered as a drop in the sea of cosmic rays astrophysics.
In this Chapter, a brief introduction to the history and current status of observations of cosmic rays is given. A special emphasis is addressed on recent discoveries and open questions, such as the origin of ultra high energy charged cosmic rays, and that of the electron/positron excess. Moreover, we will explain why photons are the ideal messenger of violent events in the Universe. The main astrophysical emitters of this energetic radiation and the physical mechanisms involved will be also outlined.

1.1 Cosmic rays overview

Cosmic Rays (CRs) are energetic particles coming from space. They were discovered by the Austrian physicist Victor Hess in 1912, with flying balloons. The finding, originally motivated by the study of atmospheric ionization (Schlickeiser, 2002), worth him the Nobel Prize in Physics in 1936.

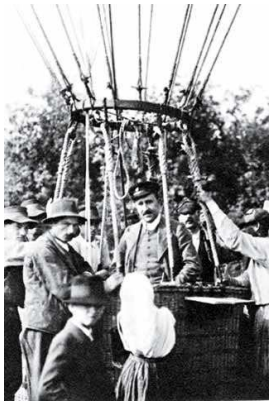

Figure 1.1: Victor Hess, Nobel Prize in 1936.

The extraterrestrial nature of such particles was suggested by Millikan, who first named these particles *cosmic rays*. It was already clear at that time that the particles observed with balloons were not the primary CRs but secondary particles initiated by the interaction of energetic CRs with the atmospheric nuclei.

The composition of these secondary particles has been studied during the decade from 1927 to 1937 by ground based detectors. The study of the so–called *atmospheric showers* is a milestone of particle physics, and led to the discovery of many particles, such as the positron, the muon and the pion. But it was only in the 1960s, when CRs detectors were situated in rockets, that the primary particles could be directly detected.

Since these pioneristic times many detectors were built and contributed to the study of the highest energy particles of the Universe. Never as in this field a multi–frequency and multi–messenger approach is needed. CRs are, in fact, composed of charged particles and anti–particles, as well as photons, neutrinos and neutrons. Hence, different and complementary techniques have been employed to afford this exciting field of research.

CRs detectors can be sorted into:

Ground experiments: this category includes a large variety of instruments. Belong to this category:

- detectors measuring the charged component of the high energy CR flux, like: KASCADE, HiRes Fly's Eye, AGASA and the Pierre Auger Observatory;
- γ–rays detectors like MAGIC, H.E.S.S., Veritas and ARGO-YBJ in the TeV energy range, and Milagro, in the tens of TeV energy range;
- neutrinos detectors, like: IceCube, in the South Pole, and Antares, located in the Mediterranean sea.

Satellite experiments: includes PAMELA and AMS, concentrated on the anti–matter content of the Universe, *Fermi*/LAT and *AGILE*, γ–ray detectors in the MeV-GeV energy range;

Balloon experiments: devoted mainly to the study of the composition of low energy CRs. Belong to this category experiments like Bess, Atic, TRACER and CREAM.

Main characteristics of CRs are:

- they are mainly composed of charged particles, in particular protons;
- low energy CRs are produced within our Galaxy, while at high energies particles have extragalactic origin;
- their spectrum covers more than 16 decades of energy: from some GeV to the ultra–high energy regime ($\geq$energies $\sim 10^{20}$ eV);
- charged CRs are deflected by interstellar and intergalactic magnetic fields: their direction of origin cannot be determined directly.

In the following Sections we present an up to date overview of the main results in the field of charged CRs physics, giving a special emphasis on recent discoveries and open questions.

1.2 Composition

CR particles spectrum covers many energetic decades, from approximately 10^8 to more than 10^{20} eV; within this energy range the particle flux decreases by about 30 orders of magnitude: as a natural consequence, for the CRs study different detection techniques are used. For a detailed review on this subject, the reader can refer to Hörandel (2008).

As far as the composition is concerned, an important feature is that all elements of the periodic table have been found in CRs. The great majority consists of **protons and nuclei** (98%), out of which protons represent the 87% of this fraction, whereas 12% are He^{++}. Figure 1.2 illustrates the relative abundance of protons and nuclei, normalized to $Si = 100$. The abundances measured are in first approximation rather similar to those in the solar system. However, we can notice certain differences, revealing information on the acceleration and propagation of CR, as for example the occurring of spallation processes. It is in particular evident for light elements as well as for element just below iron (Z = 26) and lead (Z = 82). This process brings to light another important aspect of the nature of CRs: only part of them is composed of primaries, i.e. particles produced and accelerated by astrophysical sources. The other part is composed of secondaries, produced from the interaction of particles with interstellar gas[1].

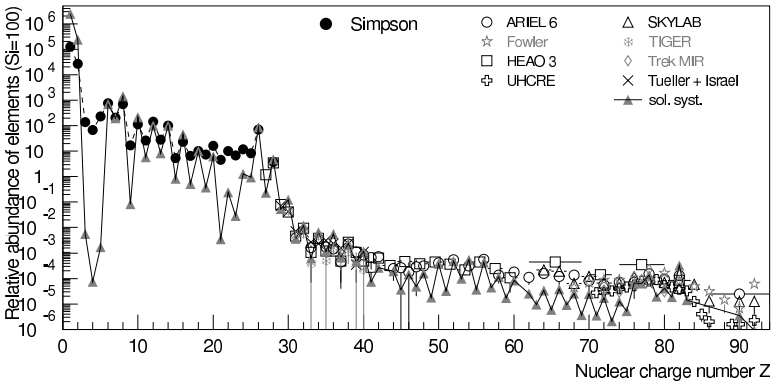

Figure 1.2: Normalized abundance of elements in CRs as a function of their nuclear charge number Z at energies around 1 GeV/n, from Hörandel (2008). The continuous line shows the abundance of elements in the solar system.

A small fraction, ∼2%, of CRs is given by **electrons and positrons** (e^+; e^-). Recent measures of this component are the subject of a hot debate in the CR community, and will be briefly outlined.

Finally, the last component of CRs is constituted by **neutral particles**, such as γ–rays (just a small fraction of the total CR flux), but also neutrons and neutrinos. Neutral messengers are very important because they are not deviated by interstellar magnetic fields, and reveal the origin of the radiation. The second part of this Chapter is devoted to a detailed description of such limited but fundamental component of the CR spectrum.

1.3 Energy spectrum

The overall energy spectrum of the charged component of CRs is shown in Fig. 1.3, where the flux has been multiplied by a factor $E^{2.5}$ to make structures in the steeply falling spectrum visible. In first approximation, it is compatible with a power law of index -3. Two main signatures mark the deviation from the power law: the so called *knee*, at energies around 10^{15} eV, and the *ankle*, at 10^{18}–10^{19} eV.

[1]Belong to the primaries category: electrons, protons and helium, as well as carbon, oxygen, iron and other nuclei synthesized in stars. The secondaries, instead, are nuclei such as lithium, beryllium and boron, as well as a large fraction of anti-protons and positrons. (Nakamura and Particle Data Group, 2010).

Below about 10^{18} eV CRs are usually considered to be of galactic origin; above this energy there is a transition region, up to 10^{19} eV, while above it they are probably of extragalactic origin.

It is interesting to observe that the most powerful particle accelerator, the brand new LHC, reaches energies of $\sim 10^{13}$ eV, seven orders of magnitude less than the most energetic CR ever recorded.

At energies below 300 MeV, the solar wind prevents low energy charged particles to come into the inner solar system (more details in the box about *Geomagnetic effect and solar modulation*). On the other edge of the spectrum, the measure of the spectrum beyond the ankle is difficult, due to the extremely low flux: about 1 particle per square kilometer per century at E = 10^{20} eV. In addition, the interaction of ultra–energetic particles with CMB photons causes a suppression of the flux, known as the GZK cutoff.

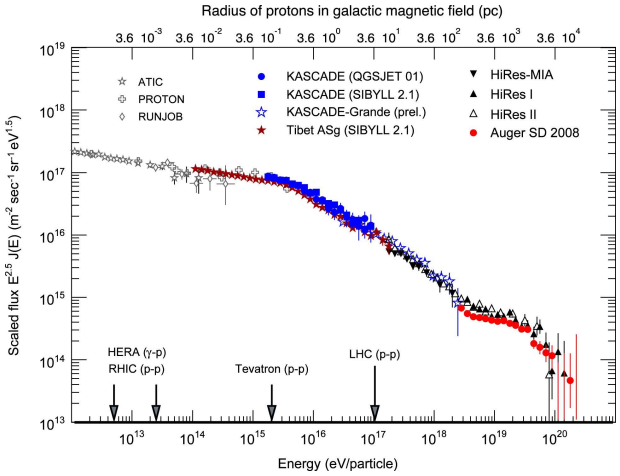

Figure 1.3: All-particle energy spectrum of CRs. To make structures in the steeply falling spectrum visible, the flux has been multiplied by a factor $E^{2.5}$. The radius of protons in the galactic magnetic fields is indicated at the top. From Hörandel (2010).

1.3.1 The GZK cutoff

It was in 1966 when Kenneth Greisen, in *End to the Cosmic-Ray Spectrum?* and Vadimir Kuz'min and Georgiy Zatsepin in *Upper limit of the spectrum of cosmic rays* (Greisen, 1966; Zatsepin and Kuz'min, 1966), independently, suggested a cutoff in the energy spectrum of CRs at Ultra High Energies (UHE).

They predicted that CRs with energies larger than 4×10^{19} eV would interact with cosmic microwave background photons, γ_{CMB}, to produce pions. The cross section of the interaction is dominated by the huge Δ resonance, as sketched in Figure 1.4. The two favourite channels are:

$$\gamma_{CMB} + p \rightarrow \Delta^* \rightarrow p + \pi^0 \tag{1.1}$$

and

$$\gamma_{CMB} + p \rightarrow \Delta^* \rightarrow n + \pi^+ \tag{1.2}$$

The corresponding attenuation length is of the order of some Mpcs, indicating that the effect becomes important only at scales well outside our Galaxy ($\sim$15 kpc). For this reason, if UHE CRs are of extragalactic origin, they are

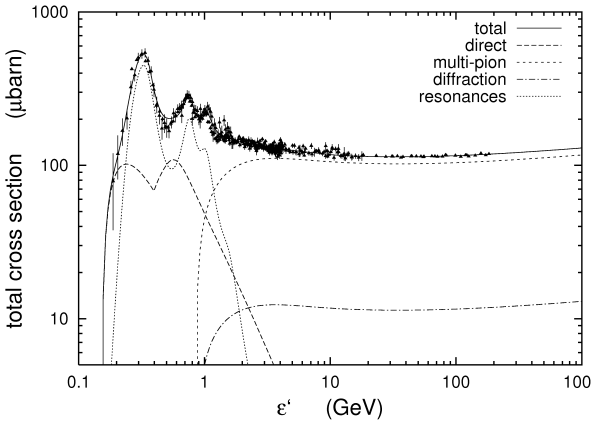

Figure 1.4: The total p-γ cross–section. From Mucke et al. (1999).

strongly suppressed at 10^{20} eV, while in the opposite case, the absorption is negligible. From acceleration models, it seems that CRs of energy larger than 10^{18} eV have to be addressed as extragalactic particles (see Sec. 1.4). Hence, we expect a suppression in the CR flux above $10^{19.5}$ eV.

The theoretical expectation has been challenged by the results of the AGASA (Akeno Giant Air Shower Array) experiment. This pioneering ground array located in Japan presented evidence for a continuation of the spectrum beyond the GZK cutoff, see Figure 1.5, together with a lack of correlation with nearby astrophysical sources (Takeda et al., 1998). The new generation of ground based UHECR detectors has recently published the experimental results, which conversely to AGASA findings, seem in agreement with the existence of a GZK limit, see Figure 1.6. Certainly, more statistics at energies near the GZK cutoff are required in order to achieve a precise flux measurement, and put an end to the debated question.

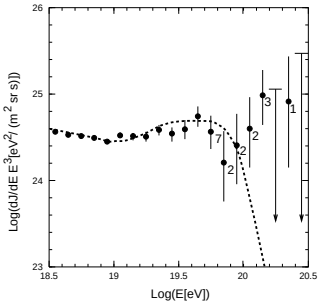

Figure 1.5: AGASA result, from Takeda et al. (1998).

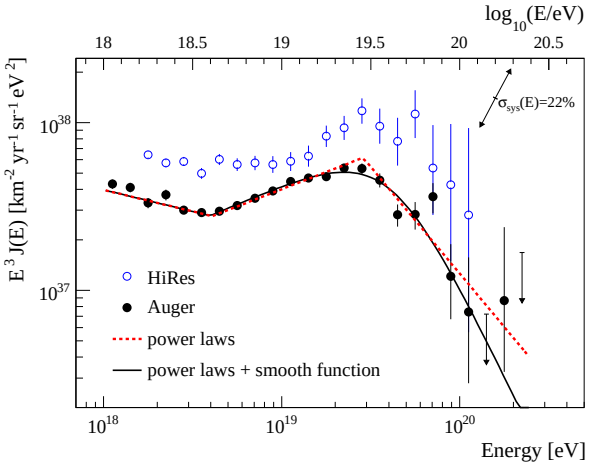

Figure 1.6: The combined energy spectrum from the Pierre AUGER Observatory (filled points) compared to the data from the HiRes instrument (open points). From Pierre AUGER Collaboration et al. (2010).

1.3.2 Antimatter

Another hot topic of the field concerns the spectrum of matter–antimatter ratio of CRs. Recent results include:

- the discovery, by the PAMELA satellite experiment, of a rise in the positron over electron + positron ratio in the energy range 1.5– 100 GeV, Figure 1.7. Data above 10 GeV deviate significantly from predictions of secondary production models. This result is of particular relevance since it could be the first evidence of dark matter particle annihilations. Other explanations include positron production from nearby pulsars.

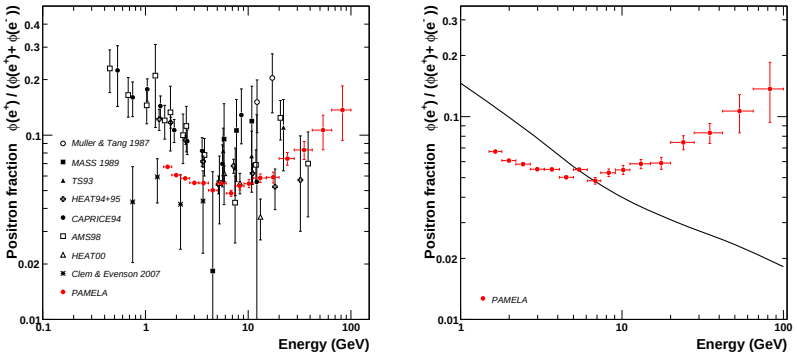

Figure 1.7: PAMELA positron fraction with other experimental data, left panel, and compared with theoretical model, right panel. From Adriani et al. (2009).

- the confirmation, by *Fermi*/LAT, of controversial results in the electrons plus positrons CR flux, suggested by ATIC (Chang et al., 2008) and by H.E.S.S. (Aharonian et al., 2008) data. More precisely, a peak in the e^++e^- flux distribution is seen, Figure 1.8, that is not foreseen by conventional models. This could be an evidence of the presence of one or more local sources of high energy CR electrons and positrons.

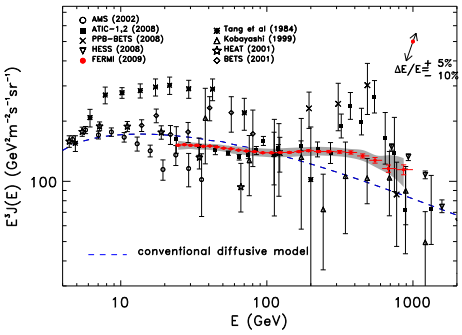

Figure 1.8: The *Fermi*/LAT CR e^++e^- spectrum (filled circles). Systematic errors are shown by a gray band. Other high-energy measurements and the conventional diffusive model are shown. From Abdo et al. (2009).

- the report, by PAMELA experiment, of no evidence of excess in the anti-protons to protons ratio (Adriani et al., 2010). In this case, measurements are consistent with purely secondary production of anti-protons in the galaxy, see Fig 1.9.

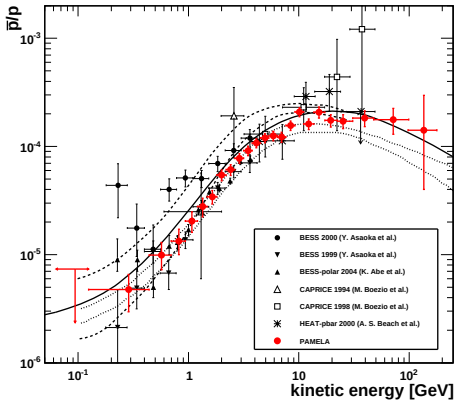

Figure 1.9: The anti-proton-to-proton flux ratio as measured by PAMELA (big marker) compared with contemporary measurements and theoretical calculations for a pure secondary production of anti-protons during the propagation of CRs in the galaxy. From Adriani et al. (2010).

Geomagnetic effect and Solar Modulation

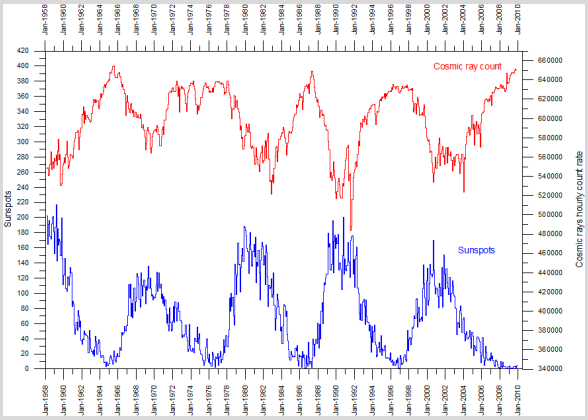

The primary charged cosmic radiation impinging the atmosphere is strongly affected by Earth magnetic field and modulated by the solar wind. The Earth magnetic field deviates charged particles and leads to the **east–west effect**: namely, at all latitudes more (positively charged) particles arrive from the west than from the east.
The effect of the solar wind, which is the expanding magnetized plasma generated by the Sun, is that of decelerating and partially excluding the lower energy galactic CRs from the inner solar system. There is clear evidence for an **anti-correlation between solar activity**, which has an alternating eleven-year cycle, **and the intensity of the CRs with energies below about 10 GeV**, monitored through the counting rate of neutrons at sea–level.
Thus, the intensity of any component of the cosmic radiation in the GeV range depends both on the location and time a adopted for the measure.

References: Nakamura and Particle Data Group (2010); Perkins (2009) The image indicates the variation of CR intensity and monthly sunspot activity since 1958 according to the Germany CR Monitor in Kiel (GCRM) and NOAA's National Geophysical Data Center (NGDC), respectively. From http://www.climate4you.com/

1.4 Origin of CRs

After almost a century from their discovery, the origin of CRs, and in particular UHECRs, remains an open and largely debated question within the astroparticle

community. The main question is related to the energy achieved: which mechanism, in the Universe, can accelerate up to 10^{20} eV energies?

The principal mechanism responsible for particle acceleration was proposed by the Italian physicist Enrico Fermi in 1949, and is based on the fact the energetic particles (v $\sim$ c) can gain energy by elastically scattering off magnetic turbulence structures or irregularities moving with some characteristic velocity **u** (Rieger et al., 2007). Assuming energy conservation in the comoving scattering frame, a particle with momentum **p** and Lorentz factor Γ experiences an energy change:

$$\Delta\epsilon = \epsilon_2 - \epsilon_1 = 2\Gamma^2 \left(\epsilon_1 u^2/c^2 - \mathbf{p_1}\cdot\mathbf{u}\right). \tag{1.3}$$

The energy gain will be positive or negative (loss of energy), depending if the particle collision is head–on or following, respectively. We can differentiate within "second order" and "first order" Fermi acceleration depending on the characteristics of the moving plasma:

Second order Fermi acceleration refers to the case in which the scattering centers have a random velocity. Since, for geometrical reasons, the rate of collisions is proportional to $v_1 u/v_1 \sim (1 v_1 u/v_1^2)$, there is a higher probability for head-on collisions. This gives an average energy gain per collision that is second order in u/c :

$$\frac{\Delta\epsilon}{\epsilon_1} \propto \left(\frac{u}{c}\right)^2. \tag{1.4}$$

First order Fermi acceleration occurs when the energy gain becomes first order in u/c. This happens when a shock wave is present: the acceleration is particularly efficient because the motions are not random. A charged particle ahead of the shock front can pass through the shock and then can be scattered by magnetic inhomogeneities behind the shock. The particle gains always energy from this bounce and flies back across the shock, where it can be scattered by magnetic inhomogeneities ahead of the shock. This enables the particle to bounce back and forth again and again, gaining energy each time. The total energy gain is:

$$\frac{\Delta\epsilon}{\epsilon_1} \propto \frac{u}{c}. \tag{1.5}$$

Hence, astrophysical objects characterized by the presence of shock waves are most probably a preferential site of CR acceleration.

Once we have understood the principal mechanism responsible for the acceleration of CRs, we can depict the characteristic size of an accelerating region (Hillas, 1984). Following the main ideas behind the concept of Fermi's first order acceleration, when the Larmor radius approaches the accelerator size it becomes very difficult to magnetically confine CRs within the acceleration region. Hence, in order to make the acceleration process efficient, the size in pc units L_{pc} of the accelerating region containing the magnetic field must be greater than two Larmor radius:

$$L_{pc} > 2r_L \sim \frac{2E_{15}}{B_{\mu G}\times\beta}, \tag{1.6}$$

where E_{15} is the energy in units of 10^{15} eV, $B_{\mu G}$ is the magnetic field in units of μG, and we have taken into account also the characteristic velocity βc of the

scattering centers. Hence, objects capable to accelerate particles above a certain energy should satisfy the requirement given by Eq. 1.6.

Figure 1.10 represents the famous Hillas diagram, proposed in Hillas (1984), which relates the magnetic field strength with the size of the emitting region. Only extragalactic objects, like active galactic nuclei (Chap. 2), seems to possess the physical conditions for the acceleration of particles up to 10^{20} eV.

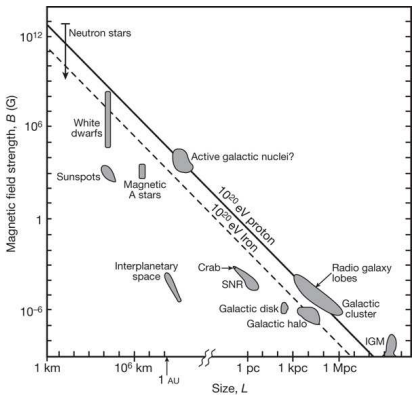

Figure 1.10: Hillas diagram. Objects below the diagonal continuous/dashed line cannot accelerate protons/irons to 10^{20} eV. Crab indicates the Crab nebula; SNR, supernova remnant, IGM, intergalactic magnetic field. From Bauleo and Martino (2009).

1.4.1 Spatial distribution

Charged particles, constituting the large majority of CRs, are deflected by intergalactic magnetic fields and their arrival direction is completely randomized. For this reason, neutral particles, such as photons, are commonly used to study the progenitors of CRs. At energies above tens EeV, however, the interaction is less effective, and UHECRs from nearby sources are supposed to maintain a small angle with the direction of the emitting object. Therefore, the study of the arrival direction of the highest energies particles is a complementary approach to the search for their origin to that of studying neutral particles.

In the last decade, a great effort has been done to search for spatial correlation between the UHECRs recorded and nearby extragalactic objects, such as Active Galactic Nuclei (AGNs; see Sec. 1.5.3). Indications for such correlation have been claimed by the Auger Collaborations in 2008, from a sample of 27 events (The Pierre AUGER Collaboration et al., 2008). Recently, updated results based on a wider sample of 69 events collected up to the end of 2009 have been pub-

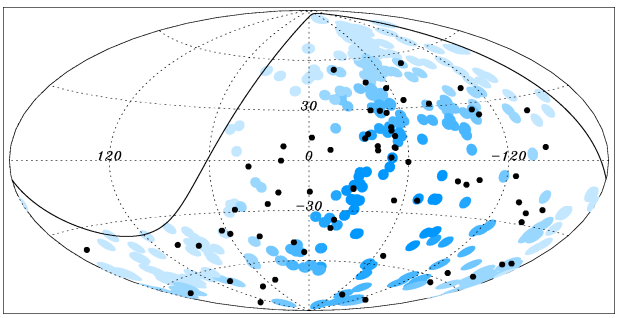

Figure 1.11: The 69 arrival directions of CRs with energy E $\geq$ 55 EeV detected by the Pierre Auger Observatory (black dots), superimposed to the position of 318 nearby AGNs from the VCV catalog (blue circles). From The Pierre AUGER Collaboration et al. (2010).

lished by The Pierre AUGER Collaboration et al. (2010). The new data exhibit a correlation probability less evident than that previously found. Figure 1.11 shows the spatial distribution of these events (black dots), superimposed to 318 nearby AGNs present the VCV catalog (blue circles). A result of particular relevance is the fact that the celestial region around the position of the radiogalaxy Cen A (see Chap.2) has the largest excess of arrival directions with respect to expectations given by an isotropic distribution.

Taking into account the latest results, the question about the UHECRs origin is far from being solved. Further investigations, including correlation studies using more complete catalogs, are foreseen in the next years.

1.5 γ–rays: the ideal neutral messenger

Neutral CRs are the ideal particles to study in order to investigate the ultimate origin of CRs. As mentioned above, such particles do not interact with intergalactic magnetic field, so they:

- point to their generator;
- carry energy information about their generator;
- conserve time information.

There are three known species of neutral particles that could be used as messengers of high energy processes: neutrons, neutrinos and photons. Due to the relatively short lifetime of neutrons, almost all the particles arriving at Earth are secondaries. On the other hand, neutrinos are very difficult to detect. Therefore, γ–rays are the only particles successfully observed from the depth of the Universe, despite the low fluxes involved, as reviewed in the next Sections. Since of particular interest for this thesis, we will present in detail the main absorption and production mechanisms involving energetic photons, together with a list of the principal objects known so far as emitters of very high energy photons.

1.5.1 Production mechanisms

The search for cosmic structures emitting γ–rays is often analogous to the search for regions where high energy leptons or hadrons can be found: energetic gammas in the Universe, in fact, are always produced by *parent particles* of higher energy. The main processes involving high energy γ–ray production are: *synchrotron radiation*, *inverse Compton scattering*, *electron Brehmsstrahlung* and *pion decay*. In what follows, we briefly summarize these mechanisms.

Synchrotron radiation Relativistic electrons in a magnetic field undergo the effect of Lorentz's force. The corresponding motion consists of two components: one is parallel to the lines of force, and the other is rotation around them at the angular frequency of Larmor precession:

$$\omega_L = \frac{eB_\perp}{m_e c} \tag{1.7}$$

Due to the accelerated motion, radiation is emitted. This radiation, called *synchrotron radiation*, is beamed into a cone of angle $\theta \approx m_e c^2/E$ in the

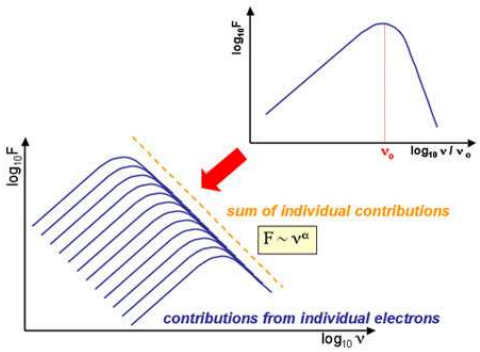

Figure 1.12: Synchrotron spectrum emitted in a typical astrophysical source.

direction of the velocity, and emits a power:

$$\frac{dE}{dt} = \frac{2r_0^2}{3c}(\gamma v)^2 B_\perp^2 \tag{1.8}$$

where

$$r_0 = \frac{e^2}{m_e c^2} = 2.8 \cdot 10^{-15} m \tag{1.9}$$

$$\gamma = (\sqrt{1-\beta^2})^{-1} \tag{1.10}$$

are the electron's classical radius, and the electron's Lorentz factor.

The critical frequency at which the maximum power is emitted is:

$$\nu_c = \frac{3}{4\pi} \frac{\gamma^2 e B_\perp sin\phi}{m_e c} \tag{1.11}$$

where ϕ is the angle between the direction of the magnetic field and that of the electron. A detailed analysis shows that in a gas of relativistic electrons ($\gamma \gg 1$), a continuum spectrum is emitted. The power distribution follows an increasing power law, proportional to $\nu^{1/3}$, until it reaches a maximum, in correspondence to the maximum $\nu_m \approx 0.29\,\nu_c$. Above this maximum, it follows a decreasing exponential law, proportional to $\sqrt{\nu}\, exp(-\nu/\nu_c)$. In astrophysical sources, usually electrons are not monochromatic, but their spectrum follows approximately a power law of index s. In such circumstances, the total power radiation distributes as well as a power law, of index $\alpha = (s-1)/2$, as shown in Figure 1.12.

Generally, *proton synchrotron* radiation is considered an inefficient process (even if not fully ruled out, e.g. Aharonian 2002). The theory can be simply developed by re-scaling the Larmor frequency for electrons ω_L by the factor $m_p/m_e \simeq 1836$. So, for the same energy of electrons and protons, the energy loss rate of protons appears $(m_p/m_e)^4 \simeq 10^{13}$ times lower than the energy loss rate of electrons.

Brehmsstrahlung Charged particles in a gas are deviated by electromagnetic interactions with other particles, such as nuclei or ions, and emit a radiation whose amplitude is proportional to the centripetal acceleration. This process is very efficient only in the electronic case. The radiation emit-

ted is called *Brehmsstrahlung* or *free–free radiation*. Brehmsstrahlung by thermalized electrons, also known as *thermal Brehmsstrahlung*, is the most important emission mechanism in cold ionized plasma, such as the intracluster medium (typical temperature of 10^7 K, emission in the X–ray domain of the spectrum), or the accretion disk in AGNs (see Chap. 2). The electrons, in this case, have a mean velocity related to the temperature of the plasma: $v \simeq (k_B T)/m_e$. The emitted spectrum is flat for frequencies smaller than $(k_B T)/\hbar$, and fall rapidly above this threshold[2] (Padmanabhan, 2000).

The exhaustive quantum mechanical treatment of electron Brehmsstrahlung by an atom is complex because of the screening effects by the atomic electrons and the finite nuclear radius. On average, the spectrum of this radiation is continuum, depends on the gas density ρ_g and on the electron distribution (Nobili, 2002).

Inverse Compton scattering When relativistic electrons scatter on low energy photons, they can transfer part of their energy to them resulting in high energy γ–ray emission. This effect is called *Inverse Compton scattering*.

The Compton scattering is explained by following the rules of conservation of energy and momentum in the frame of the electron at rest. The energy of the scattered photon can be written as:

$$h\,\nu' = \frac{m_e\,c^2}{1 - cos\theta + 1/\alpha} \tag{1.12}$$

where θ is the angle of the scattered photon, and α is the ratio between the rest mass of the electron and the photon energy. In case $\alpha \gg 1$, the energy of the scattered photon is always smaller than the electron rest mass and all the energy goes into the kinetic energy of the scattered electrons.

The cross–sections are calculated in three regimes: in case the $\alpha \gg 1$ the Klein–Nishina cross–section should be considered (Longair, 1992), which at very high energies can be approximated with:

$$\sigma_{KN} \simeq \pi r_e^2 \frac{m_e c^2}{\epsilon}(\ln 2\epsilon + 0.5) \tag{1.13}$$

For $\alpha \leq 1$, i.e. in the Compton regime, the cross–section is:

$$\sigma_C = \frac{8\pi\, r_0^2}{3} \cdot (1 - 3\alpha^2 + 9.4\alpha^2 + \ldots) \tag{1.14}$$

which further reduces to $\sigma_T = 8\pi\, r_0^3/3 = 6.65 \times 10^{-25}\,\mathrm{cm}^2$ in case $\alpha \ll 1$ where the so–called Thompson regime applies.

It can be shown that, in case a population of energetic electrons with a power law distribution of index s interacts with a soft photons distribution of density ρ, the spectrum of γ–rays has the form $\propto E^{-(s+1)/2}$ and a typical characteristic energy of $\gamma_e^n\, h\nu$ where $n = 1, 2$ depending whether the regime is the Klein–Nishina or Thompson one, and γ_e is the electron Lorentz factor. This process could be particularly important for the production of high energy γ–rays in relativistic jets.

[2] An electron with a typical energy $k_B T$ cannot emit photons with energy higher than $k_B T/\hbar$.

High energy protons can also interact with soft photons, but the energy loss rate is suppressed by a factor $(m_e/m_p)^4 \simeq 10^{-13}$ (as in the synchrotron case), and it is significantly lower than the pair production losses (when above threshold).

Pion decay Relativistic protons and nuclei can produce high energy γ–rays in inelastic collisions with ambient gas. Since in this reaction $\pi^{\pm}$ and π^0 are produced with the same probability, one third of the π–mesons produced are neutral. The neutral π^0–mesons provide the main channel of conversion of the kinetic energy of protons into high energy γ–rays. The lifetime of neutral pions is very short ($\tau = \gamma_\pi \cdot 10^{-16}$ s), and their decay produces two gamma rays. For the production of these particles, the kinetic energy of protons should exceed the energy threshold:

$$E_{th} = 2m_\pi c^2(1 + \frac{m_\pi}{4m_p}) \approx 280 MeV \tag{1.15}$$

where $m_\pi = 134.97$ MeV is the mass of the π^0–meson.

The energy of the photons emitted by a π^0 at rest is $E_\gamma = m_\pi c^2 \simeq 67.5$ MeV. If the particle is moving with velocity v= βc, than the energy of the photons in the laboratory frame is:

$$E_\gamma = \frac{1}{2} m_{\pi^0} c^2 \frac{1 + \beta cos\theta_\gamma}{\sqrt{1-\beta^2}} \tag{1.16}$$

with θ_γ the angle between the direction of the photon and the pion.

The decay of charged pions leads to the production of ν_e and ν_μ neutrinos with spectra quite similar to the spectrum of the accompanying π^0–decay γ–rays. However this symmetry can be violated in environments with high gas or radiation densities. In certain conditions, the characteristic time for inelastic interactions of charged pions with nucleons or photons could be shorter than the decay time, so the energy of pions degrades before they decay. At very high energies this would result in significantly smaller fluxes of neutrinos compared to that of γ–rays.

1.5.2 Absorption mechanisms

Once expelled by an astrophysical source, γ–rays traveling long distances to the observer can be absorbed, with the result of a total flux diminution[3]. So, it is very important, in order to estimate the intrinsic spectrum of a source, to know the amount of absorbed photons. There are two processes involving absorption of very high energy gamma-rays: *photon–matter pair production* and *photon–photon pair production*.

Photon–matter pair production Gamma rays can be absorbed by the interaction with matter, as it happens when they penetrate the Earth atmosphere. At high energies, the most important process to consider is pair production in the presence of hadronic or leptonic matter.

Gamma–rays produced by a distant source, both galactic or extragalactic, can be absorbed by particles filling cosmic space. In these circumstances,

[3]Gamma rays can be also absorbed by the source itself.

the radiation length is approximately $38\,\mathrm{g}\times\mathrm{cm}^2$ and the cross–section approximately $10^{-26}\,\mathrm{cm}^2$. The typical density of interstellar space is about 1 atom cm^{-3}, and that of intergalactic space it is more like 10^{-5} atoms cm^{-3}. Typical interstellar distances are 10^4 light–years and intergalactic distances 10^8 light–years. With atoms of mass approximately $10^{-24}\,\mathrm{g}$, the amount of matter encountered in traveling from sources at these distances is much less than a radiation length. In conclusion, we can argue that the the absorption of γ–rays emitted by distant sources by the interstellar and intergalactic matter is negligible.

Photon–photon pair production The main mechanism by which gamma rays are absorbed is pair production:

$$\gamma + \gamma \rightarrow e^+ + e^- \tag{1.17}$$

The reaction can occur if the center-of-mass energy of the photon-photon system exceeds twice the rest energy of the electron squared.

For photons of energy near 100 MeV, the head-on collisions with X-ray photons of $\sim 5\,\mathrm{keV}$ have the highest cross-section. Dense fields of X-ray photons may be encountered in the vicinity of a 100 MeV source and the effect must be taken into account (Dondi and Ghisellini, 1995). However, since this situation rarely occur in the interstellar and intergalactic space, where the X-ray background is small, the effect can be neglected, except for extreme cosmological distances.

At higher energies, i.e. above 100 GeV, photons are mainly absorbed by the interaction with the **Extragalactic Background Light**, hereafter EBL, optical and infra–red light, produced by stars and reprocessed by dust filling the cosmos. Detailed explanation of EBL composition and models will be faced in the next Chapter, while in Chapter 7 the interaction of Very High Energy (VHE) γ–rays (i.e. photons with energy in the range 100 GeV to tens of TeV) from extragalactic sources with photons of EBL will be reported. VHE photons can also be absorbed in the source itself, if dense fields of optical–UV photons are present. This is likely to happen in some AGNs, like the source 3C 279, and the effect must be taken into account for a correct modeling of the final spectrum emitted by the source.

1.5.3 VHE γ–ray sources

We have seen in previous Sections that energetic photons (above tens MeV) are associated with non thermal processes, such as intense magnetic fields and particle acceleration. Figure 1.13 shows the VHE γ–rays sky, compared to the sky seen at lower energies (0.2–300 GeV) by the *Fermi*/LAT instrument. Besides purely energetic considerations, which make VHE emission harder to be produced with respect to the lower energy photons, the large difference in the number of detected objects in the two ranges is also due to other reasons, such as different sensitivities and observation techniques (pointing mode vs survey mode), and the opacity of the Universe to γ–rays emitted by distant sources.

In this Section, we will briefly outline of the main sources responsible for such emission, known so far.

The VHE emitters can be split into two categories: *galactic* and *extragalactic*

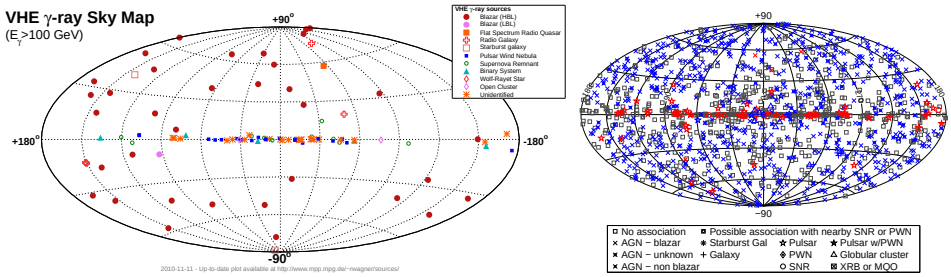

Figure 1.13: Map of all γ–ray sources detected above 100 GeV (left plot, from http://www.mppmu.mpg.de/∼rwagner/sources/), and by the Fermi satellite in the 0.2–300 GeV energy range (right plot, from Abdo et al. 2010b), and

objects. The former, belonging to our Galaxy, are closer and for the most part located on the galactic plane. The updated list counts 61 objects, out of which only three, namely the Crab Nebula, PSR 1706-44 and Vela X, were known at the end of the 1990s. They can be:

- **Supernova remnants (SNR)**: is an extended object, resulting from the gigantic explosion of a star in a supernova. Inside a SNR, expanding shock waves accelerate particles, through the Fermi mechanism. It is widely believed that VHE γ–ray radiation originates from the inverse Compton scattering of energetic electrons with target radiation fields, such as synchrotron or thermal radiation. According to some models, hadronic processes are also likely to play a role.

  Beside being the origin of VHE photons, SNs are also considered the site of CRs production at least at energies below the knee.

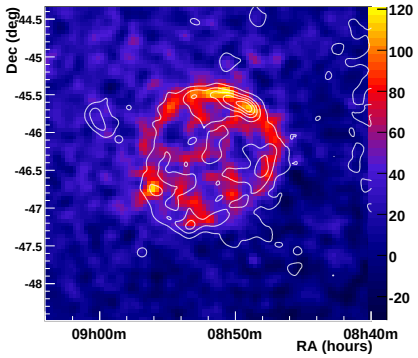

Figure 1.14: VHE emission from the SN RX J0852.0-4622, from Aharonian et al. (2007a), superimposed to the contours of the X-ray data from the ROSAT All Sky Survey for energies higher than 1.3 keV (white lines).

- **Pulsars and associated nebulae**: a pulsar is a fast rotating, magnetized neutron star resulting from the gravitational collapse of a massive star. Since the pulsar formation happens in parallel to a supernova explosion, the final object is composed of a neutron star and a nebula, and is often referred as a plerion. VHE photons have been detected both from the pulsar and from the surrounding material (Albert et al., 2008; Aliu et al., 2008).

  Plerions are among the most abundant sources of VHE γ–rays in the Galaxy. In some cases, the rotational energy of the neutron star is converted by some still not fully understood mechanism, sketched in Fig. 1.15, into a relativistic

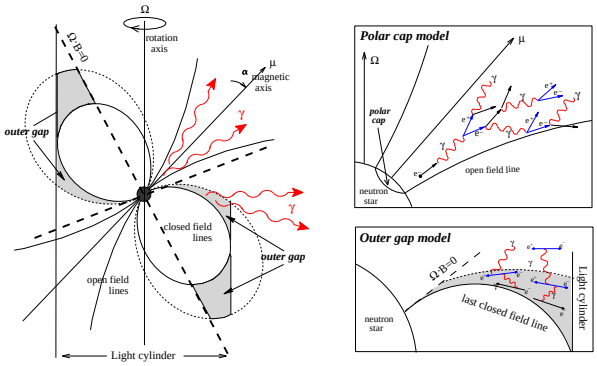

Figure 1.15: Emission models of VHE γ–rays from a pulsar (Lopez et al., 2009).

stream of particles generated near the pulsar, which power up the VHE γ–ray emission, and we have a pulsar wind nebula (PWN) . Indeed, compared to the case of SNRs, the up-scattering process in this case is very efficient, which explains the abundance of PWNs detected at VHEs.

The best studied example of such systems is the Crab Nebula, the remnant of a supernova explosion, located at a distance of 2 kpc, that occurred in the year 1054. The brightness and stability of its emission in the γ–rays regime made this source the standard candle for ground-based and satellite borne γ–ray experiments. Recently, the detection of a variability in region of the Crab Nebula at high energies, reported by the *AGILE* team and soon after confirmed by the *Fermi*/LAT Collaboration (ATel 2855, ATel 2861), has undermined this assumption. It seems, however, that such variability does not affect the VHE regime (ATels 2967 and 2968).

- **Binary systems**: these systems contain a compact object (a neutron star or a black hole) that accretes or interacts with matter outflows from a companion star. Compared to SNRs and PWNs, the Binary Systems (BS) are much more compact. The VHE emission from this kind of objects is still matter of debate; without any doubt, the emission model is not straightforward and it depends on the nature of the central object.

- **Galactic center (GC)**: the center of our galaxy (where the black hole Sgr A* is located) was established in the past years as a steady VHE photons emitter. The GC is a very crowded sky region. There are three compelling candidates for the origin of the VHE emission: a SNR, a PWN and the black hole itself (even if the latter is disfavored due to absence of variability at VHE, despite the strong X-ray activity).

In addition to the listed galactic sources, recently the H.E.S.S. Collaboration has reported the discovery of a **diffuse galactic emission**, at energies above 100 GeV. The emission is thought to come mainly from hadronic collision of CRs with dense molecular clouds and dust in the galactic plane, creating, among others, neutral pions with a subsequent decay into VHE γ–rays. The correlation between the distribution of molecular gas and the emission seems to confirm this scenario.

The extragalactic objects known to date as VHE emitters are 46, divided into:

- **Active Galactic Nuclei (AGNs)**: supermassive black holes accreting matter and, in some cases, emitting ultra–relativistic particles by means of two collimated jets. All but five of the AGNs were discovered in the last

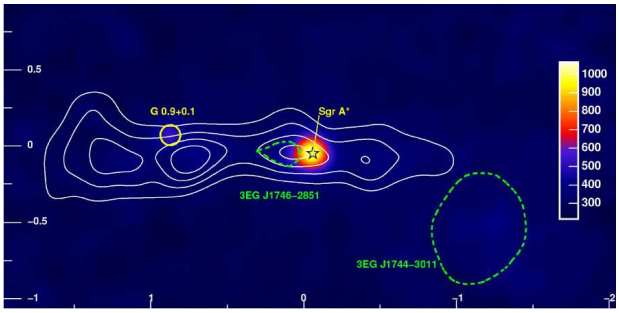

Figure 1.16: The GC region at VHEs. Adapted from The H. E. S. S. Collaboration (2007).

decade. A detailed report on AGN physics and VHE observations will be presented in Chapter 2.

- **Starburst galaxies**: are peculiar galaxies which exhibit in the central region a high rate of supernova explosions, of about 0.03–0.3 yr^{-1} (Lacki et al., 2010). Due to the uncommon SN density, these galaxies are a favourite site of acceleration of charged CRs. The observed VHE γ–rays are most probably the secondary products of decaying pions, created by the collisions of CR protons with interstellar medium nucleons. Of the extragalactic VHE emitters, only two are starburts galaxies: M 82 and NGC 253.

In addition to known categories of sources, VHE γ–ray detectors are also looking for a signal from:

- **Dark Matter (DM) annihilation**: in many dark matter frameworks, the self–annihilation of DM particles can produce γ–rays that extend up to the VHE range. At the moment, the most promising candidates for such emission are the dwarf galaxies, such as Draco or Willman I, characterized by an enhanced mass to luminosity ratio, and clusters of galaxies. No γ–ray emission have been observed yet, maybe due to the very low fluxes involved. Thanks to the high sensitivities foreseen, DM search will be one of the primary target of next generation of VHE γ–ray detectors.

- **Gamma ray bursts (GRBs)**: are highly energetic explosions isotropically distributed in the sky, as shown in Fig. 1.17. GRBs are of extragalactic origin and usually classified by their main burst duration as short and long (the boundary being conventionally set at two seconds). An afterglow emission at lower energies usually follows the burst in γ frequencies. Although the γ–ray emission mechanism is not well understood, yet, these two classes of bursts are likely to originate from distinct types of progenitor systems: while long duration bursts are thought to be produced by the core collapse of massive stars, short duration GRBs have been associated with both early and late type host galaxies, probably in merger events Ackermann et al. (2010). Up to now no GRB has been detected in the VHE band. Nevertheless they are very interesting targets since TeV observations of GRBs could help constraining theoretical models. Many models, in fact, predict the emission of VHE radiation during the prompt and/or afterglow phase.

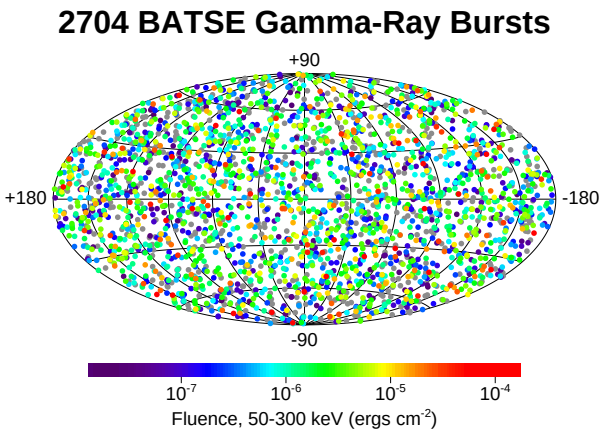

Figure 1.17: Locations of the 2704 Gamma-Ray Bursts recorded with the BATSE detector on-board *CGRO*, during the nine-year mission, from 1991 to 2000.

1.6 Neutrino astronomy

Besides γ–rays, neutrinos are the other neutral particles whose study could be of great advantage for the CRs community. In particular, since associated with hadronic interactions, the detection of a significant neutrino emission correlated with a source would be a unique test for the emission models.

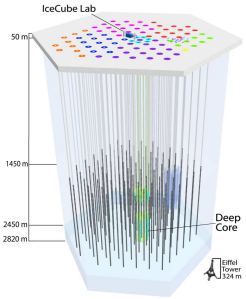

Figure 1.18: Sketch of the IceCube detector.

Due to their nature of very light weakly interacting particles, neutrinos can be detected only using instruments with very large volumes of interacting material. However, the expected neutrino flux from astrophysical sources is so low (and uncertain) that even the largest 'μ-astronomy' projects currently running could not detect, at least up to now, neutrino signal from any astrophysical source, except for the Sun and SN 1987A (box in the next page). Nevertheless, big efforts are currently being done to make neutrino astronomy possible, and a new generation of detectors is under development.

Neutrinos from SN 1987A

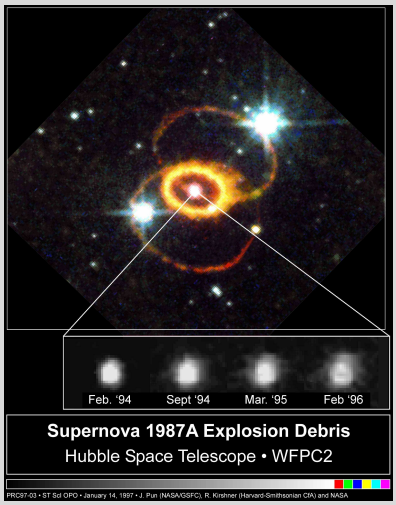

Approximately three hours before the visible light emitted by SN 1987A reached the Earth on February 23, 1987, a burst of 24 neutrinos was observed at three separate neutrino observatories: at 7:35 am Universal time, Kamiokande II detected 11 anti-neutrinos, IMB 8 anti-neutrinos and Baksan 5 anti-neutrinos, in a burst lasting less than 13 seconds. Current models foresee that this was due to the neutrino emission (which occurs simultaneously with core collapse) preceding the emission of visible light (which occurs only after the shock wave reaches the stellar surface). Although the actual neutrino count was only 24, it was a significant rise from the previously-observed background level. This was the first, and up to now only time neutrinos emitted from a supernova were detected directly. The observations are consistent with theoretical supernova models in which 99% of the energy of the collapse is radiated away in neutrinos.

References: Pagliaroli et al. (2009)

The image is a Hubble Space Telescope picture showing Supernova 1987A and its neighborhood. The series of four panels shows the evolution of the SN 1987A debris from February 1994 to February 1996. Material from the stellar interior was ejected into space during the supernova explosion in February 1987. The explosion debris is expanding at nearly 6 million miles per hour.
From http://hubblesite.org/newscenter/archive/releases/1997/03/image/a/

Si capisce che si stava tutti lí, - fece il vecchio Qfwfq, - e dove, altrimenti? Che ci potesse essere lo spazio, nessuno ancora lo sapeva. E il tempo, idem: cosa volete che ce ne facessimo, del tempo, stando lí pigiati come acciughe? Ho detto "pigiati come acciughe" tanto per usare una immagine letteraria: in realtá non c'era spazio nemmeno per pigiarci. Ogni punto d'ognuno di noi coincideva con ogni punto di ognuno degli altri in un punto unico che era quello in cui stavamo tutti.

Tutti in un punto (Le Cosmicomiche) - Italo Calvino

2 Accretion and ejection in AGNs

THE EXTRAGALACTIC sky at energies above 100 GeV counts nowadays 46 objects. Almost all of the sources detected in this energetic regime belong to the class of radio-loud Active Galactic Nuclei (AGNs): supermassive black holes accreting material and showing two narrow jets. The spectral energy distribution of the radiation emitted by these objects is strongly correlated with the viewing angle of the observer.
In this Chapter, we will give an insight into radio loud AGNs physics and spectral characteristics, giving particular emphasis to the sub–class of blazars: AGNs with a jet almost aligned to the line of sight.

2.1 The VHE extragalactic sky

Since 1992, when for the first time TeV photons from an extragalactic source were reported (Punch et al., 1992), the extragalactic sky has been populated by a number of sources. Nowadays, the TeV catalogs count 46 objects, listed in Table 2.1, randomly distributed in the sky, as shown in Figure 2.1. Except for two starburst galaxies, three unidentified sources and other two sources, all the remaining emitters belong to the class of AGNs defined in Chapter 1. These are the sources labeled as HBL, IBL and LBL (corresponding to High, Intermediate and Low–frequency peaked BL Lac), the two Flat Spectrum Radio Quasars (FSRQs), and the two Radio Galaxies (RGs).

The two sources classified as "other" are NGC 1275, which corresponds to the central radio galaxy of the Perseus cluster of galaxies, and VER J0521+211, whose position is consistent, within errors, with the position of the radio–loud active galaxy RGB J0521.8+2112.

One of the aspects characterizing TeV sources is their limited distance: while GeV sources, detected by satellites, distribute over a large range of redshifts (up to z larger than 3), the most distant object observed in the VHE regime has $z = 0.536$ (if we exclude the unknown distance objects). Besides purely energetic reasons, the other cause for this evidence is that energetic photons are absorbed, during their travel, by the interaction with the diffuse light (see Chapter 3, and, more in detail, Chapter 7). Moreover, a significant fraction of the total sample, 9 sources, reveals unknown or uncertain redshift.

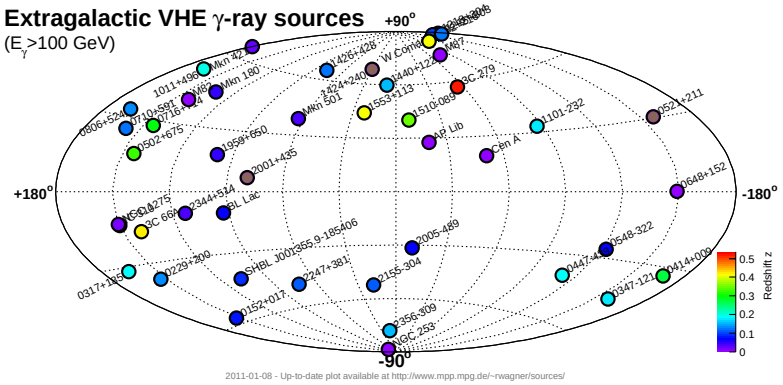

Figure 2.1: Map of the TeV extragalactic sky. From http://www.mppmu.mpg.de/∼rwagner/sources/.

Source	z	Type	Source	z	Type
M82	0.0007	Starb.	1ES 0806+524	0.138	HBL
Centaurus A	0.0007	RG	1ES 0229+200	0.14	HBL
NGC 253	0.0008	Starb.	1ES 1440+122	0.162	HBL
M87	0.0044	RG	H 2356-309	0.165	HBL
NGC 1275	0.0175	Other	1ES 1218+304	0.182	HBL
IC 310	0.019	UNID	1ES 0347-121	0.185	HBL
Mkn 421	0.03	HBL	1ES 1101-232	0.186	HBL
Mkn 501	0.034	HBL	RBS 0413	0.19	HBL
1ES 2344+514	0.044	HBL	PKS 0447-439	0.2	HBL
Mkn 180	0.045	HBL	1ES 1011+496	0.212	HBL
1ES 1959+650	0.047	HBL	1ES 0414+009	0.287	HBL
AP Lib	0.049	LBL	S5 0716+714	0.31^a	LBL
BL Lacertae	0.069	LBL	1ES 0502+675	0.341	HBL
PKS 0548-322	0.069	HBL	PKS 1510-089	0.36	FSRQ
PKS 2005-489	0.071	HBL	PG 1553+113	0.40–0.47^a	HBL
RGB J0152+017	0.08	HBL	4C +21.35	0.432	FSRQ
SHBL J001355.9	0.0948	HBL	3C 66A	0.444^a	IBL
W Comae	0.102	IBL	3C 279	0.536	FSRQ
PKS 2155-304	0.116	HBL	MAGIC J2001+435		HBL
B3 2247+381	0.12	HBL	PKS 1424+240		IBL
RGB J0710+591	0.125	HBL	RGB 0648+152		UNID
1H 1426+428	0.129	HBL	VER J0521+211		Other
1ES 1215+303	0.13^a	LBL	MAGIC J0223+430		UNID

Table 2.1: List of known extragalactic VHE photons emitters. ^{a}: uncertain.

2.2 Radio loud AGNs

The AGNs family is very large, including all those galaxies whose main emission cannot be considered of stellar origin. This means that the bulk of the observed optical radiation is not the sum total of the stellar emission. Such a vague definition renders it almost impossible to draw up a complete AGNs list. For a detailed review, the reader is addressed to Urry and Padovani (1995).

A basic classification, that is also of particular interest for our study, is that

done according to the radio loudness. An AGN is considered *radio loud* if the ratio between the radio flux at 5 GHz and the optical flux in the B band exceeds the value of 10 (e.g. Kellermann et al. 1989). Almost 15–20% of the AGNs are radio loud, while the remaining are classified as radio quiet. Since VHE emission has been found only in radio loud AGNs, we will focus our description on these objects. Hereafter, if not specified, with the term AGNs we will refer to the radio loud subclass of objects.

2.2.1 Unified scheme

One of the most supported and fascinating theory about radio loud AGNs is the so–called *unified model*. According to this model, all the different features of the AGNs are due to a different orientation of the same object with respect to the observer. The situation is well represented in Figures 2.2 and 2.3.

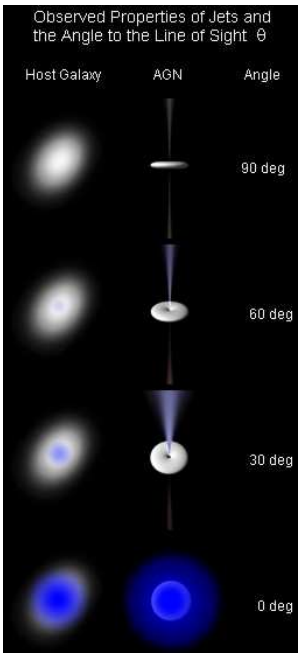

Figure 2.2: Radio loud AGNs seen from different perspectives.

The central engine is a spinning supermassive black hole ($M \sim 10^6 - 10^9 M_\odot$), fed upon accreting matter. It is believed that these objects characterize nearly every galaxy, and play an important role in the galaxy formation. Their mass is closely tied to that of the galaxy bulge, $M_{BH} \approx 10^{-3} M_{bulge}$ (Narayan and Quataert, 2005). In radio loud AGNs, two narrow jets emerge from the hole, and extend for several kilo–parsecs. The typical emission from a jet is non–thermal, mainly synchrotron radiation together with an high energy component probably due to Inverse Compton (IC) scattering, and spans from radio to γ–ray frequencies.

In the majority of AGNs, two regions called Broad emission Line Region (BLR) and Narrow emission Line Region (NLR) surround the hole. The BLR is constituted by relatively dense molecular clouds ($> 10^8$ cm^{-3}) responsible for the broad, mainly optical, emission lines detected in some spectra. Conversely, the NLR, that is responsible for narrow emission lines, is situated far away from the center, and it is filled with molecular clouds, less dense than those present in the BLR ($10^3 - 10^6$ cm^{-3}). Between the last two regions there is a zone of intense electron scattering.

According to the unified model, we can divide the radio loud AGNs into the following categories:

Radio Galaxies: are AGNs whose jets lie at a large (>30 deg) angle w.r.t. the line of sight. The central hole is obscured by the large torus, that reprocesses the light coming from an inner disk and the BLR. The intense radio emission is synchrotron radiation from the jets and the lobes.

Blazars: When the observer line of sight points towards the jet, the spectral features change completely and we have a blazar. Jets in blazars are the favoured site of GeV–TeV photons production. Depending on the characteristic of the emission, blazars are divided into two classes: Flat Spectrum Radio Quasars (FSRQ) and BL Lac objects (BL Lacs).

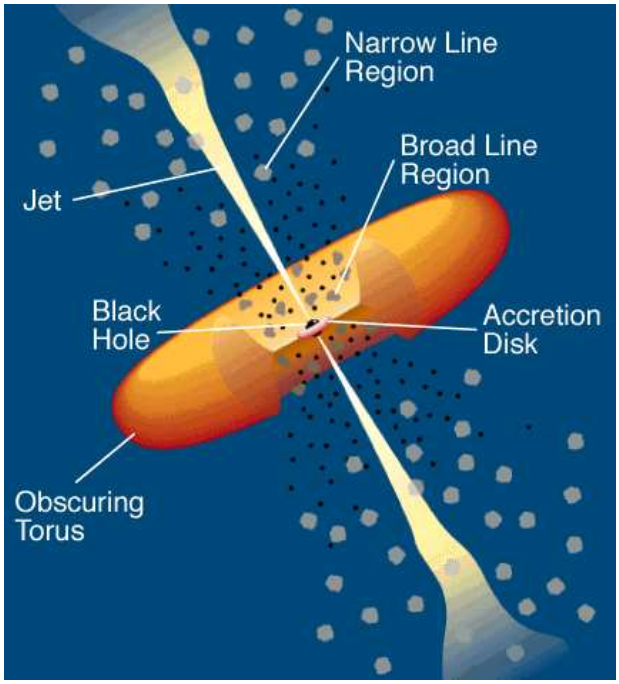

Figure 2.3: Unified scheme for radio loud AGNs. Credit: C.M. Urry and P. Padovani.

FSRQ spectrum has a two bump continuum, shows evidence of BLR and NLR, in addition to a thermal spectrum associated with an accretion disk.

In BL Lacs the observed spectrum shows the typical two bumps continuum, but, conversely to the case of FSRQs, shows no evidence for emission or absorption lines (see Figure 2.4). Their emission is characterized by strong optical polarization and rapid variability. During a *flaring* state[1], their luminosity can reach 40–times its normal value in few hours. Depending on the position of the low energy peak, BL Lacs are classified into LBL, IBL and HBL (peak in the radio, optical and X–ray band). Indeed, since the spectrum is shifted at higher energies, the latter category is the most suited for VHE photons emission.

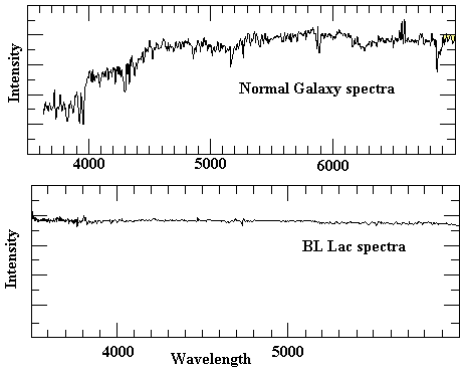

Figure 2.4: Comparison between a spectroscopic image of a normal galaxy and that of a BL Lac.

Quasars: are the intermediate case. A quasar (QUASi–StellAR source) is a galaxy which shows a very luminous, unresolved ($\theta < 1''$) nucleus. The emission from the central object is directly seen, together with the NLR and BLR, which cause typical emission lines in the spectrum. The spectrum

[1] An AGN is considered in a flaring state when its flux exhibit fast variations in a short time period.

is dominated by a non–thermal radio–optical emission, that is recognized as synchrotron emission due to ultra relativistic charged particles in the jet. Hence, weak broad and narrow emission lines are superimposed to this continuum, especially in the optical range.

TeV photons from Starburst Galaxies

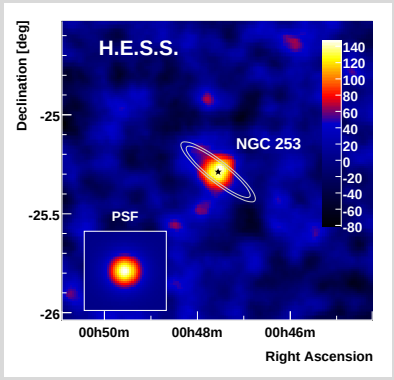

Starburst galaxies are peculiar objects which exhibit in their central region a highly increased rate of supernovae, the suitable sites for cosmic ray acceleration up to energies of $\sim 10^{15}$ eV. A number of models have foreseen a production of VHE γ–rays from these sources, due to the interaction of CRs with interstellar gas and radiation. Two recent detections of VHE gamma rays from starburst galaxies have confirmed such predictions. A significant gamma-ray flux above 100 GeV has been registered in 2009 from NGC 253 and M 82, by the H.E.S.S. and VERITAS arrays of imaging atmospheric Cherenkov telescopes (see Chapter 4). These results strongly support the hypothesis that cosmic-ray acceleration is closely connected to star formation activity, and that supernovae and massive–star winds are the dominant accelerators.

References: Acero et al. (2009); Acciari et al. (2009) and references therein.

Image from Acciari et al. (2009)

2.2.2 Sources of energy in AGN

The total luminosity of AGNs is $\lesssim 10^{47}$ erg s^{-1}. Two are the main mechanisms responsible for such emission, namely:

Accretion of material around the central hole. This mechanism allows the extraction of gravitational energy and its partial conversion into radiation;

Ejection of material from the vicinity of the central object, through two thin jets which accelerate material up to ultra–relativistic energies. The mechanism is deeply coupled with the accretion. The emitted energy, in fact, is thought to be rotational energy of the accretion of matter in addition to that of the black hole.

The accretion mechanism is an efficient process not only for AGNs, but also for compact galactic objects, such as white dwarfs, neutron stars and black holes with masses lower than $100\,M_\odot$. For better understanding this fact we can compare the energy released in a nuclear fusion reaction, to that released by accretion (Frank et al., 1992). A rough estimation of the gravitational potential energy per unity mass that is released by the accretion of a mass m on a neutron star of mass

$M \sim 1 M_{\odot}$ and radius $R \sim 10\,\mathrm{Km}$, is:

$$\frac{\Delta E_{acc}}{m} = GM/R \sim 10^{20}\mathrm{erg/g} \tag{2.1}$$

while the most efficient stellar nuclear fusion, $H \rightarrow He$, releases:

$$\frac{\Delta E_{nuc}}{m} = 0.007c^2 \sim 6 \times 10^{18}\mathrm{erg/g} \tag{2.2}$$

that is less than 10% of the accretion case.

One of the characteristic of accretion is that there is a limit on the total luminosity that can be emitted by an object of a certain mass accreting material, called Eddington limit.

The Eddington limit

The basic idea of the Eddington limit is that AGNs have an upper threshold luminosity above which their accretion is halted. This threshold is reached when the outward force exerted by the pressure radiation exceeds the inward gravitational force driving the accretion. For a simple treatment, it is assumed a steady spherically symmetric accretion and ionized hydrogen as accreting material (Frank et al., 1992). The latter condition means that the photons–matter interactions can be treated as simple Thompson scattering. Moreover, the protons can be neglected because the photon–proton scattering cross–section is a factor $(m_e/m_p)^2 \sim 2 \times 10^{-7}$ smaller than the photon-electron one.

The pressure force exerted on each electron is:

$$F_p = \sigma_T \frac{S}{c} \tag{2.3}$$

where S is the radiant energy flux ($\mathrm{erg \times s^{-1} cm^{-2}}$), and σ_T =$6.7 \times 10^{-25}\mathrm{cm}^2$ the Thompson cross–section. The electrostatic force between electrons and protons acts as a drag force: while they move, electrons carry protons with them.

The gravitational force on each electron–proton pair is:

$$F_g = \frac{GM(m_p + m_e)}{r^2} \approx \frac{GMm_p}{r^2} \tag{2.4}$$

The net force inward on each pair is, then:

$$F \simeq \frac{GMm_p}{r^2} - \sigma_T \frac{S}{c} = (GMm_p - \frac{L\sigma_T}{4\pi c}) \times \frac{1}{r^2} \tag{2.5}$$

where $L = 4\pi r^2 S$ is the total luminosity. The Eddington luminosity is thus defined as:

$$L_{Edd} = \frac{4\pi GMm_p c}{\sigma_T} \simeq 1.3 \times 10^{38} \frac{M}{M_{\odot}} erg \times s^{-1} \tag{2.6}$$

If an object radiates through the accretion mechanism, then its total luminosity cannot overcome the Eddington luminosity. Only in this case accretion can be considered as an efficient mechanism.

Equation (2.6) can also be used for inferring an upper limit on the mass of an accreting object of known luminosity. Historically, this was one of the first evidences of the existence of supermassive objects in the core of AGNs. It must

be noticed, however, that the assumption of spherical symmetric accretion in this case is no longer valid.

In real objects, the dynamics of the accretion flow strongly depends on the efficiency of the radiative process, and, ultimately, on the rate of mass accretion. If L is the luminosity of the object, and $\dot{M}$ the mass accretion rate, then we can define the accretion efficiency, ϵ, as:

$$L = \epsilon \dot{M} c^2, \tag{2.7}$$

which is usually closely tied to $\dot{M}$. In blazars, accretion occurs at sub-Eddington rates[2], and we can distinguish the following cases:

Efficient accretion ($\dot{M} > 0.01\ \dot{M}_{Edd}$): in this condition, usually accretion occurs through (optically thick) thin disks, called accretion disks (see next Section). The efficiency is quite high, at the level of $\epsilon \sim 0.1$, hence also the luminosity is high. It is commonly believed that FSRQs belong to this class of objects.

Inefficient accretion ($\dot{M} < 0.01\ \dot{M}_{Edd}$): typical of objects accreting trough ADAFs (Advection Dominated Accretion Flows), corresponding to optically thin disks (Abramowicz et al., 1998). Is the case of objects such as BL Lacs, characterized by very low efficiency ($\epsilon \ll 0.01$), and low luminosity.

2.2.3 The accretion disk

According to present theories, strongly supported by optical and X–ray observations, when the accretion of matter into a black hole is efficient, such as in FSRQs, it occurs through a thin disk, the so–called *accretion disk*[3].

The dynamics of particles in the disk depends strongly on the nature of the central object: the huge mass of the black hole, in fact, deforms the time–space structure of the surrounding environment, and a general relativistic approach is necessary to describe the system.

A correct analysis should take into account black holes with no charge but with angular momentum, the so–called *Kerr black holes*. Detailed calculations show that accretion from a black hole can be an efficient mechanism only if the particles move in stable orbits around the hole. This is exactly what happens in the accretion disk: particles move on a series of nearly circular orbits gradually loosing their angular momentum until they reach the last stable orbit and fall into the hole without further energy losses. The losses of angular momentum are due to viscose torques acting on the particles. These torques allow the particles to move on circular orbits and to transform their rotational energy into radiative energy.

The emitted spectrum from the disk is a superposition of several thermal spectra, with the warmer part coming from the inner region. Such thermal continuum, observed in optical and X–ray wavelengths for several quasars and referred as the "big blue bump", is an indication that the vertical section of the disk is optically thick.

[2] The Eddington accretion rate is the accretion rate for which the black hole radiates at the Eddington luminosity

[3] Near the black hole, however, as noted by Frank et al. (1992) it is likely that this geometry breaks, and the accretion becomes spherically symmetrical.

Another feature of accretion disks is their strict connection with jets. It is commonly believed, in fact, that the two structures are symbiotically related, despite the precise mechanism of interconnection is not fully understood, yet. The jets are probably generated in the inner region of the disk, near the last stable orbit, where the gas pressure, radiation pressure and gravitational forces becomes comparable. Relativistic jets can drive large amount of energy, extracting energy and angular momentum from the inner part of the disk and the central object, as suggested by the Blandford–Znajek mechanism, discussed in Sec. 2.2.5.

2.2.4 Jets in AGNs

Radio loud AGNs are characterized by two narrow jets pointing opposite directions and nearly perpendicular to the accretion disk plane, if any.

Jets are composed of ionized material, most likely electrons, and probably protons and the products of their interactions, in relativistic motion and immersed in a strong magnetic field. The precise mechanism of jets formation, together with their main characteristics, such as their ultra relativistic nature and their strict collimation, are still largely debated.

It is commonly accepted, however, that the emission from the jets is generated by blobs of electrically charged material accelerated to ultra relativistic velocities by relativistic shock waves. If observed at large angles, in fact, as in the case of radio galaxies, the emission from the jets is dominated by a non–thermal component. This is unanimously attributed to synchrotron radiation emitted by ultra relativistic electrons interacting with the randomly oriented magnetic field presents inside the jet and peaking at radio frequencies. The detection of this emission was the first evidence of the ultra relativistic nature of the emitting particles. A further evidence came from the detection of regions in apparent *superluminal motion* in some quasars.

Superluminal motion

The explanation of these superluminal motion, i.e. motion with apparent velocity greater than the velocity of light c, can be deduced from simple geometrical arguments (see Figure 2.5).

Suppose that a blob of emitting material moves in a direction that forms a small angle θ towards the observer. The observer believes that the blob travels in the direction perpendicular to the line of sight, thus he calculates the apparent velocity (v_{app}) as the ratio between the observed space interval (Δl) and the observed time interval ($\Delta \mathrm{t}_{obs}$) measured as the difference in the arrival time at Earth of two signals emitted by the blobs from the two positions, i.e.:

$$v_{app} = \Delta l / \Delta t_{app} \tag{2.8}$$

The relations between the observed time and space intervals and the real ones are:

$$\Delta l = \Delta t_{real} v_{real} \sin\theta \tag{2.9}$$

$$\Delta t_{app} = \Delta t_{real}(1 - (v_{real}/c)\cos\theta) \tag{2.10}$$

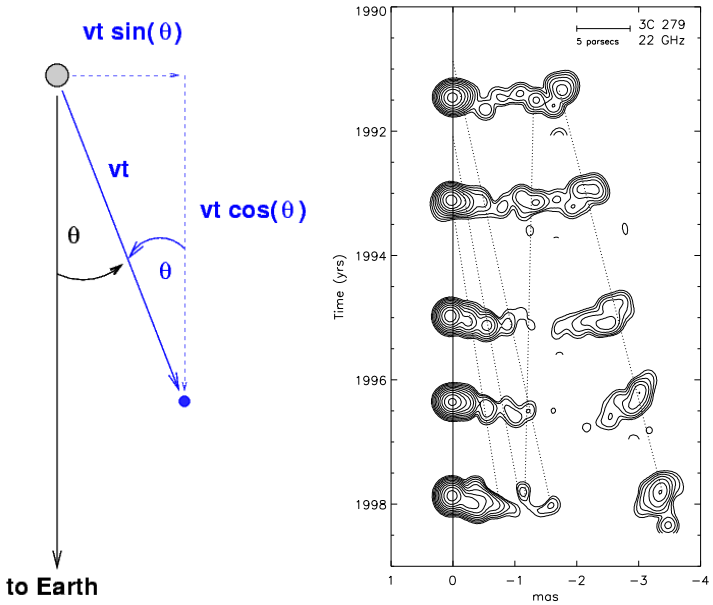

Figure 2.5: Left: schematic view of apparent superluminal motion. A blob of emitting material moves at relativistic speed at a small angle θ to the line of sight. Right: Time-series mosaic of a selection of 22 GHz VLBI images of the FSRQ 3C 279. Courtesy of Wehrle et al. (2001).

So, the observed and the real velocity are related by:

$$v_{app} = \left(\frac{v_{real} \sin\theta}{1 - (v_{real}/c)\cos\theta} \right) \tag{2.11}$$

$$\beta_{app} = \frac{\beta \sin\theta}{1 - \beta\cos\theta} \tag{2.12}$$

For small θ and relativistic velocities, the measured velocity v_{app} exceeds the velocity of light. The maximum apparent velocity is reached if $\cos\theta = \beta$, with $\beta_{app} = \beta\gamma$ and γ is the Lorentz factor of the moving material.

Beaming effects

When the angle between one of the AGN jets and the observer is small, the emitting particles move towards the observer. As a consequence, the radiation undergoes *beaming* effects, furthermore amplified by the relativistic nature of the emitter.

The main features of the observed spectrum are, namely:

1. Due to the relativistic velocities of the emitting particles, the spectrum is collimated into a cone of angle $\sin\theta = 1/\gamma$.

2. The observed time interval doesn't coincide with the time interval of emission:

$$\Delta t_{obs} = \Gamma(1 - \beta\cos\theta)\Delta t_{em} \equiv \frac{\Delta t_{em}}{\delta} \tag{2.13}$$

where δ is the so–called Doppler factor. In the case of blazars the typical Doppler factor is of the order of some tens.

If the jet emission is variable, the timescale is then reduced by this effect. The knowledge of the real variability of a source is very important since it allows to infer an upper limit on the size of the emitting region.

3. The Doppler effect involves also the frequencies of the photons, that are blue-shifted if the motion is toward the observer. The relation between the observed and emitted frequencies is:

$$\nu_{obs} = \delta \nu_{em} \tag{2.14}$$

This means that the flux observed in blazars is shifted at higher energies.

4. Another important feature of this radiation is that its luminosity is highly overestimated. It is demonstrated that the relation between the observed and emitted luminosity is:

$$L_{obs} = \delta^p L_{em} \tag{2.15}$$

where p is a parameter > 1 depending on the jet and emission features (for example, it is 4 for a uniform sphere).

2.2.5 The Blandford–Znajek mechanism

The most accredited theory about the origin of the power channeled into the jets in AGNs is the Blandford–Znajek (BZ) mechanism (Blandford and Znajek, 1977). In their work, the authors suggest that energy and angular momentum can be extracted electromagnetically from a black hole and its surrounding disk. Following the simplified formulation proposed by MacDonald and Thorne (1982), we briefly summarize the idea at the basis of the BZ mechanism.

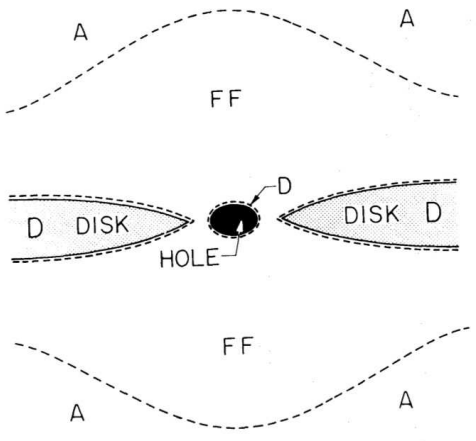

Figure 2.6: The physics case considered in the BZ mechanism: a rotating black hole surrounded by a degenerate accretion disk (region D), dipped in a force free magnetosphere (region FF), which, far out is no longer free nor degenerate (region A) MacDonald and Thorne (1982).

- The system considered is composed of a rotating black hole, of velocity Ω_H, mathematically described by the Kerr metric, surrounded by a thin accretion disk (region D) dipped in a magnetosphere filled with plasma (region FF), which extends far away from the hole (Figure 2.6).

- We assume that:

  1. The system is stationary and axisymmetric;
  2. The disk and the magnetosphere are degenerate ($\mathbf{E} \cdot \mathbf{B} = \mathbf{0}$);
  3. The magnetosphere is forcefree[4];
  4. Far out, the magnetosphere is no longer forcefree nor degenerate (region A);

- From the first assumption, it follows that the flow of electromagnetic angular momentum and redshifted energy in the magnetosphere is described by the poloidal parts of the flux vectors; moreover, the poloidal magnetic field lines are parabolic in the region FF ;

- From the second condition, the magnetic field lines result frozen into the disk plasma, and rotate at the plasma local angular velocity Ω_F;

- From the third condition, follows that there are free charges from the disk and in the region close to the black hole (pairs production from vacuum), and an electric current flows on poloidal magnetic field surfaces. Hence, fluxes of angular momentum and redshifted energy flow without any loss along the poloidal magnetic field lines;

- From the last condition, we have that in the A region (magnetosphere not forcefree, nor degenerate) particles are forced to move at speed lower then the field lines, and a *drag effect* slows down the field lines (in radial motion). This causes a difference between the angular velocity of the disk Ω_D and that of poloidal field lines Ω_F.

In such situation, and taking into account boundary conditions at the horizon, angular momentum extraction from the disk and black hole energy takes place, and a collimated jet forms (BZ effect).

The total power produced in the jet is:

$$P_{BZ} \simeq \frac{1}{128} B_0^2 r_g^2 a^2 c \tag{2.16}$$

where r_g is the gravitational radius and $a = j/jmax$ is the adimensional angular momentum of the black hole (a = 1 for a maximally rotating object). Following Maraschi and Tavecchio (2003), it can be shown that, in the extreme approximation of a spherical free fall accretion, with $P_{acc} = \dot{M}c^2$:

$$P_{BZ} = \frac{1}{64} a^2 P_{acc} = \frac{1}{64} a^2 \dot{M} c^2 \tag{2.17}$$

Therefore, even when the jet is produced at the expense of the black hole rotational energy, the generated power is closely linked to the accretion rate, and consequently to the disk luminosity (see Sec. 2.3.2).

[4]This special case arises when the plasma pressure is so small, relative to the magnetic pressure, that the plasma pressure may be ignored, and so only the magnetic pressure is considered. The name "force-free" comes from being able to neglect the force from the plasma.

2.3 The SED of blazars

Blazars, radio loud AGNs with a relativistic jet pointing towards the observer, are the majority of extragalactic γ–ray sources, both in the High Energy (HE, $E > 100\,GeV$) and VHE regimes. In summary, the main properties of the Spectral Energy Distribution (SED) of blazars are:

- it is dominated by the non-thermal continuum produced within the jet and boosted by relativistic effects (Urry and Padovani, 1995);
- exhibits fast variability at all wavelengths, amplified by beaming effect; from the scale of this variability, the emission region can be constrained:

$$R_S \leq \frac{ct_{var}}{(1+z)} \tag{2.18}$$

- it displays two broad peaks, widely interpreted as due to synchrotron (low frequency peak) and inverse Compton (high frequency peak) mechanisms. However, as proposed in Mannheim (1993), the high energy peak could also be the result of hadronic processes;
- among blazars, BL Lac objects are characterized by extremely weak emission lines in their optical spectra, which often makes a measure of their redshift difficult. The great majority of extragalactic sources detected above 100 GeV belongs to the HBL category (in which the peak of the synchrotron bump is located in the UV-X-ray bands);
- on the other hands, in the SED of quasars the optical lines are more evident. Moreover, in these objects, other extra–components may be visible, such as the "big blue bump", a clear bump in spectrum at optical–UV energies, related to thermal emission from an optically thick accretion disk.

Figure 2.7 shows the SED of the typical HBL Mkn 421 (Abdo et al., 2011), one of the first sources observed simultaneously at almost all the frequencies of the electromagnetic spectrum, including the GeV energy range, which was the missing piece before the launch of the *Fermi* satellite. The SED presented here is the result of a multi–wavelengths campaign carried out in 2009.

Campaigns of this type are becoming the standard approach to the study of well established blazars. Only a complete energy coverage, from radio to TeV photons energy, in fact, may allow a robust study of the emission mechanisms, which, in turn, consents the extrapolation of the basic physical quantities governing the emission region. Moreover, due to the variability of these objects, it is very important that observations done in different energy ranges are carried out at the same time.

2.3.1 Emission models

Two are the different mechanisms proposed for the origin of the photons of the high energy bump observed in the SED of blazars: the hadronic and leptonic mechanism.

According to the **hadronic models**, energetic photons are produced in jets via hadronic interactions, such as synchrotron emission of pair cascades triggered

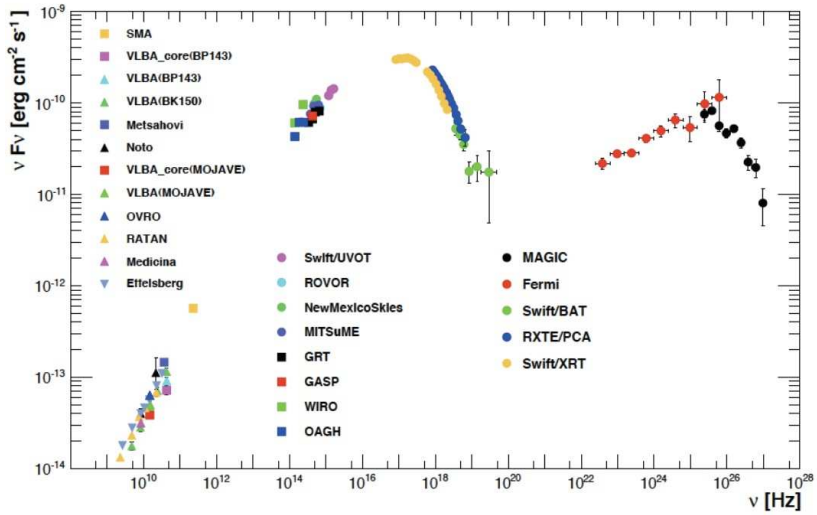

Figure 2.7: SED of the blazar Mkn 421, during the multiwavelength campaign carried out in 2009. Courtesy of Abdo et al. (2011).

by photo–meson process and/or by direct synchrotron emission of protons and mesons (Mannheim and Biermann, 1992; Mannheim, 1993; Rachen and Mészáros, 1998; Aharonian, 2000). From radio observations, relativistic protons are likely present in AGN jets. However, very large proton velocities are necessary to explain the observed AGN luminosities. This fact, together with the very short variability observed in some blazars that is unlikely to happen in relatively slow hadronic processes, render hadronic emission a disfavoured mechanism with respect to the leptonic one.

Leptonic models propose the inverse Compton scattering as leading mechanism for explaining the energetic photons origin. The models differ from the assumed nature of the radiation field. The simplest model is the so–called Synchrotron Self–Compton (SSC) model. According to it, energetic photons observed in blazars are produced by IC scattering of synchrotron photons on the same electronic population emitting them. Moreover, in the single–zone SSC model, the radiation is thought to be produced in a homogeneous emitting region by a single electron population. In νF_ν representation, above and below both peaks the photons distribution can be usually well described with increasing and decreasing power laws. In this case, the primary electron spectrum can be approximated with a broken power law, with indices n_1 and n_2 greater and smaller than 3, respectively below and above the break energy $\gamma_b m_e c^2$, where γ_b is the Lorentz factor of the electrons at the break. Hence, we obtain for the electron spectrum:

$$N(\gamma) = \begin{cases} K\gamma^{-n_1} & \text{if} \gamma < \gamma_b \\ K\gamma_b^{n_2-n_1}\gamma^{-n_2} & \text{if} \gamma > \gamma_b \end{cases} \tag{2.19}$$

With these approximations the system is completely determined by 7 parameters: the magnetic field intensity B, the size of the emitting region R, the Doppler factor δ, the slopes n_1 and n_2, the Lorentz factor of the electrons at the break, γ_b, and the electron density parameter K (Tavecchio et al., 1998). In general this simple model explains quite well a number of observed spectra, except for the radio emission. In the FIR/submm range, the single–zone SSC model foresees

synchrotron self absorption; hence the radio emission observed should be due to other emitting regions along the jet (Maraschi and Tavecchio, 2003). More elaborated models for the observed emission have been proposed in the last years, like SSC models with multiple emission zones (i.e. Graff et al. 2008).

According to other leptonic models, electrons in the jet scatter with external photon fields, such as the accretion disk radiation, reprocessed optical–UV emission from circumnuclear material, infrared emission from a dust torus or synchrotron emission from other regions of the jet itself (see Boettcher 2010 and references therein).

2.3.2 The blazar sequence

As we mentioned in previous Sections, different kinds of objects belong to the class of blazars. A first attempt to find regularities in the various SED was performed by Fossati et al. (1998). From the comparison and classification of the available SED of 126 sources, they suggested the existence of a "blazar sequence", sketched in Figure 2.8.

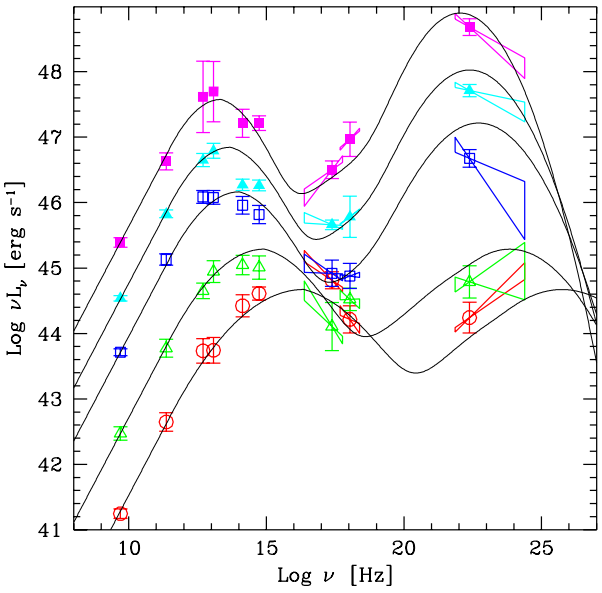

Figure 2.8: The blazar sequence, from Donato et al. (2001) and Fossati et al. (1998).

If we classify blazars according to their radio luminosity, a well defined scheme appears: less powerful objects seem to present the synchrotron peak in the soft-medium X–ray energy range, while their high energy peak is located at highest γ–ray energies. As the total power increases, both peaks shift to lower frequencies, and at the same time the γ–ray luminosity increases its relative importance, arriving to dominate the bolometric output. Starting from this work, Ghisellini et al. (1998) suggested other evidences useful for the classification. One of the most remarkable finding is that different subclasses of blazars occupy different regions of the plot, indicating a well defined sequence. From upper to lower curve (or,

analogously, from left to right) we find FSRQ, LBL, IBL and HBL, respectively.

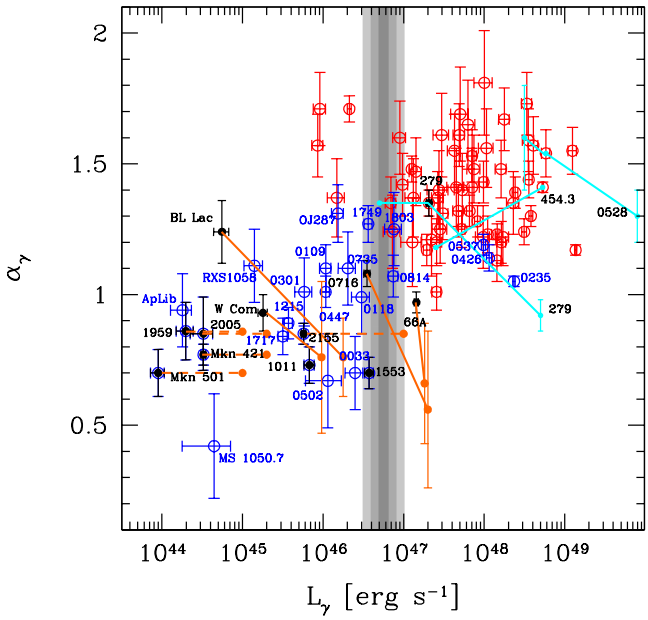

Figure 2.9: The blazar divide obtained with the fist three months *Fermi* catalog. Empty squares and circles are BL Lacs and FSRQs, respectively. Filled symbols correspond to sources already detected in the TeV band. The segments indicate the observed range of γ–ray luminosity and spectral index. From Ghisellini et al. (2009).

The detection of HE radiation from blazars with the *Fermi* satellite (more than 100 objects in the first three months of observations, Abdo et al. 2009) has given the unique opportunity to test this theory in a new energetic range. Observationally, as pointed out by Ghisellini et al. (2009), already after few months the new detections follow and confirm the blazar sequence. Moreover, as shown in Figure 2.9, FSRQs and BL Lacs clearly take place in two different regions of the α_γ– L_γ distribution (separated at $\sim 10^{47}$ erg s^{-1}), which connects the γ spectral index with the γ luminosity. In addition, α_γ and L_γ are clearly correlated. As suggested by the author, this plot represents the γ–ray selected version of the blazar sequence: low power BL Lac objects peak at higher energies, they have smaller γ luminosity and flatter index. FSRQs, instead, peak at lower frequencies, and the peak of their high energy emission (dominating their power output) is below 100 MeV.

The reason for this difference can be related to the accretion regime of the considered source. A possibility is that a source becomes radiatively inefficient below a critical disk luminosity. In this view, FSRQs are objects in which the accretion is efficient, and the region surrounding the disk is full of photons emitted by the disk itself. Moreover, the BLRs are heated up by these photons. In such conditions, the jet propagates in a crowded medium, and its power is strongly reduced by the interactions with the ambient photons. In BL Lac objects, the opposite situation takes place, and the jet particles preserve their energy, propagating in a clean ambient, since the disk accretes inefficiently.

This scheme has been already advanced in Maraschi and Tavecchio (2003).

In that paper, the luminosity emitted by the jet in blazars is compared to that emitted by the disk. Let us define $L_{jet} = \eta P_{jet}$ and $L_{disk} = \epsilon P_{acc}$, with η and ϵ radiative efficiency of the jet and the disk (see Eq. 2.7), respectively, and P_{jet} and P_{acc} power individually associated with the ejection and the accretion. In FSRQs, which as we have seen are high luminosity blazars, we expect a high radiative efficiency for the disk, in order to avoid anomalous accretion rates, and we have $\epsilon_{FSRQ} \sim 0.1$. The radiative efficiency for the jet can be estimated in the range $\eta_{FSRQ} \sim 0.01$–0.1. It turns out that if $L_{jet(FSRQ)} \simeq L_{acc(FSRQ)}$, then $P_{jet(FSRQ)} \simeq P_{acc(FSRQ)}$. If we assume that the latter relation is valid for all blazars, it follows that if, given the low jet luminosity, in BL Lac objects $\eta_{BLLac} \sim 0.01$, then since $L_{jet(BLLac)} > L_{disk(BLLac)}$, the radiative efficiency of the disk is very low, as anticipated in Sec. 2.2.2. In this context, the blazar unification finds a physical basis: BL Lacs and FSRQs could be objects with similar masses, but with different accretion efficiencies, coupled, ultimately, to the radiation efficiency of the accretion disk.

Another important result related to the study of *Fermi* sources is shown in Figure 2.10, where the jet power is plotted as a function of the disk luminosity (directly observed in FSRQ, upper limit in BL Lac objects). A clear correlation is found between the two parameters, which scale linearly. This is in agreement with the expectation of the BZ effect, as reported in Eq. 2.16 and further discussed in Ghisellini et al. (2009).

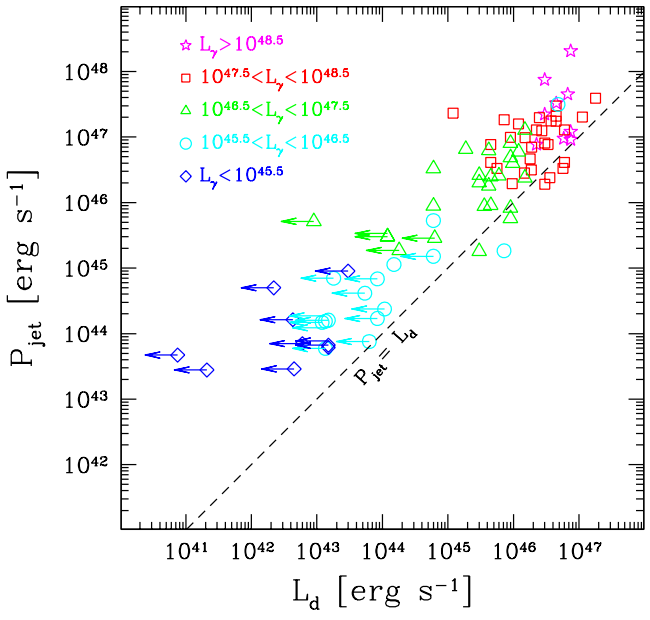

Figure 2.10: The total jet power P_{jet} vs the accretion disk luminosity L_d, from Ghisellini et al. (2009)

2.4 Radio galaxies

Beyond blazars, another class of AGNs shows relativistic mass outflows, even if under large viewing angles: that of giant RadioGalaxies (RG). Thanks to their orientation, in RGs we clearly distinct a central core (usually the obscuring torus which hides the black hole with accretion flow) and two jets which extend to megaparsec scale into the intergalactic medium, as shown in Figure 2.11. The typical emission from the jets, also in this case, is the powerful synchrotron radiation. The host galaxy is usually an elliptical galaxy.

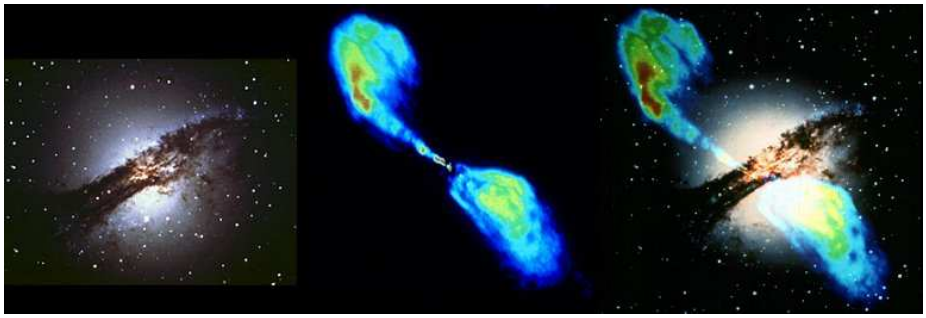

Figure 2.11: Cen A, as seen in visible light (left, NOAO/CTIO), radio telescope view (middle, NRAO/VLA), and a combo of the two views.

Radio galaxies have been speculated to be a powerful accelerator of cosmic rays since the 1960s (Ginzburg and Syrovatskii, 1964), but only recently a VHE γ–ray radiation has been observed from two of these objects: Cen A and M 87. Both these sources are nearby objects, as expected, since the typical radiation emitted by a RG is not amplified by beaming effects. Hence, the γ luminosity is orders of magnitude below that of their relatives blazars, which have been observed up to redshifts larger than 0.5.

2.4.1 The case of M 87

One of the most exciting result of the last years regarding extragalactic γ–ray astrophysics has been the localization of the acceleration site of particles in the radio galaxy M 87. This achievement was made possible thanks to the cooperation, carried out between January and May 2008, of MAGIC, VERITAS and H.E.S.S. telescopes observing in the VHE γ–ray range (see Chapter 4), Chandra X–ray telescope and VLBA radio array of telescopes.

During the campaign, an increased activity in the VHE γ–ray map has been reported. Since the spatial resolution in this energy range is still quite poor, in order to resolve the site of emission, the radio and X–ray map were used. As we have mentioned above, in fact, in case of leptonic scenario we expect a correlation between VHE and lower energy emission, since the electrons responsible for the radio synchrotron emission are thought to be the same which, via IC, generate the VHE emission.

For this reason, in correspondence to the increased VHE γ–ray activity, the region was monitored in radio and X–rays. The resulting lightcurves are shown in Figure 2.12. No evident flare has been observed from the outer region of the jet, neither in X–rays nor in radio. Conversely, an increased radio activity was registered in the proximity of the nucleus, suggesting this as favourite site for

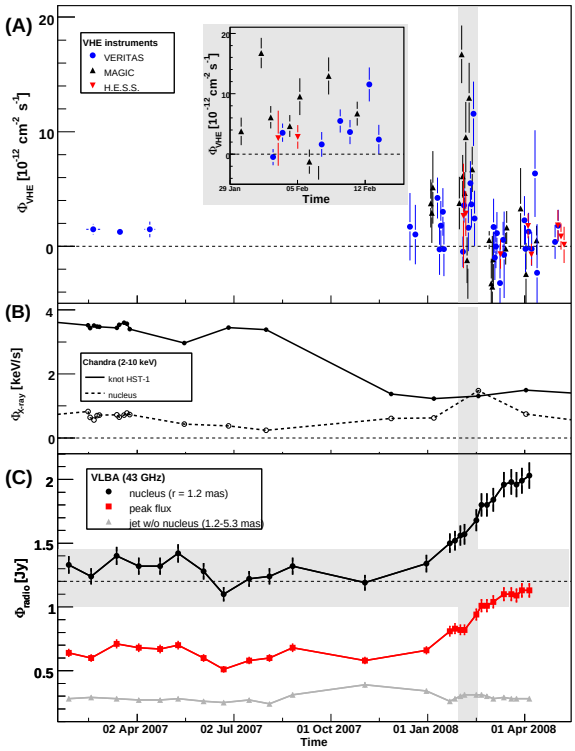

Figure 2.12: Combined M87 lightcurves from 2007 to 2008. (A): VHE γ–ray fluxes ($E > 0.35\,\mathrm{TeV}$). The inlay shows a zoomed version of the flaring activity in February 2008. (B): Chandra X-ray measurements (2–10 keV) of the nucleus and the knot HST–1. (C): Flux densities from the 43 GHz VLBA observations are shown for (i) the nucleus (circular region with radius r = 1.2 milli–arcseconds = $170\,R_s$ centered on the peak flux), (ii) the peak flux (VLBA resolution element), and (iii) the flux integrated along the jet between distances of r = 1.2–5.3 mas. Whereas the flux of the outer regions of the jet does not change substantially, most of the flux increase results from the region around the nucleus. Image from Acciari et al. (2009c).

VHE γ–rays. Thus the coincidence of the VHE and radio flares, separated in photon frequency by 16 orders of magnitude, constrained the VHE emission to occur well within the jet collimation region.

The most incomprehensible thing about the world is that it is comprehensible

Albert Einstein

3

Extragalactic Background Light: theory, observations, and models

In our understanding of the VHE extragalactic sky and its luminosity, a key role is played by the Extragalactic Background Light (EBL). This term refers to the light emitted by stars and partially reprocessed by dust and redshifted by the expansion of the Universe along the history.
In this Chapter, a brief introduction on cosmic photon backgrounds is given, followed by a detailed report on the status of observations and theoretical models regarding the EBL, which includes the UV, optical and IR backgrounds.
As we will see, in the last few years the discrepancy among different models estimated with completely independent methodologies is becoming more and more narrow.

3.1 Photon backgrounds

It is commonly believed that the Universe is a huge empty space, with some clumps of dark matter harbouring galaxies and galaxy clusters, filling this emptiness. In reality, the Universe is permeated by a diffuse electromagnetic radiation, with an energy spanning the entire electromagnetic spectrum shown in Fig. 3.2. In general, these photons may result from a superposition of many unresolved point–like sources or come from a genuine diffuse emission.

In addition to this background, also called *cosmic background*, when we observe from Earth a galactic component contributes to the total observed radiation. Usually this component can be distinguished from the extragalactic one by its anisotropy.

The backgrounds are conventionally subdivided into different categories, from higher to lower energies:

Gamma-ray background (GB) comprises of emission from our Galaxy and the Extragalactic GB (EGB), see Fig. 3.1. The former contribution includes photons emitted by the interaction of CRs with the interstellar medium of the Galaxy. The origin of the EGB is, as yet, unknown; however, it is expected that the intrinsic emission of unresolved, extragalactic point

sources comprises a sizable contribution to the EGB[1] (Venters, 2010).

X-ray background (XB) is constituted, like the GB, by a galactic and an extragalactic component. The galactic X–ray background is thought to be largely produced in nearby hot gas, while the extragalactic, or cosmic part is probably a combination of many resolved (especially below some keV) and unresolved sources (Brandt and Hasinger, 2005). Deep surveys with X-ray telescopes, such as the Chandra X-ray Observatory, have demonstrated that the bulk of the extragalactic X-ray background is resolved in AGNs.

Ultra-violet and optical background (UVOB) the extragalactic part is mainly formed by the stellar light emitted and redshifted by the expansion of the Universe throughout the history. As we will see in detail in the next Sections, the zodiacal light, emitted within our Solar System, is a dominant component of this background.

Infrared background (IB) is formed by the cosmic infrared background (CIB), which arises from stellar light re-emitted by dust to larger wavelengths, accumulated emissions from early galaxy populations spanning a large range of redshifts (Kashlinsky, 2005), and the zodiacal thermal emission and other galactic components[2]. The CIB is thus an integrated summary of the collective star forming events, star-burst activity and other luminous events in cosmic history to the present time.

Cosmic microwave background (CMB) includes the most of the electromagnetic energy of the Universe, and is composed of photons from the last scattering surface which fill the Universe almost uniformly. It has a thermal black body spectrum at a temperature of 2.725 K, thus the spectrum peaks in the microwave range frequency of 160.2 GHz, corresponding to a 1.9 mm wavelength.

[1] Additionally, many of these extragalactic point sources are also sources of VHE γ–rays, which interact with the soft photons of the EBL to create electromagnetic cascades, giving rise to another contribution to the EGB.

[2] Additional component of the galactic IB are: thermal emission of small asteroids in the Solar System, galactic cirrus emission, faint galactic stars, infrared emission of intracluster dust in the Local Group and the tail of the cosmic microwave background.

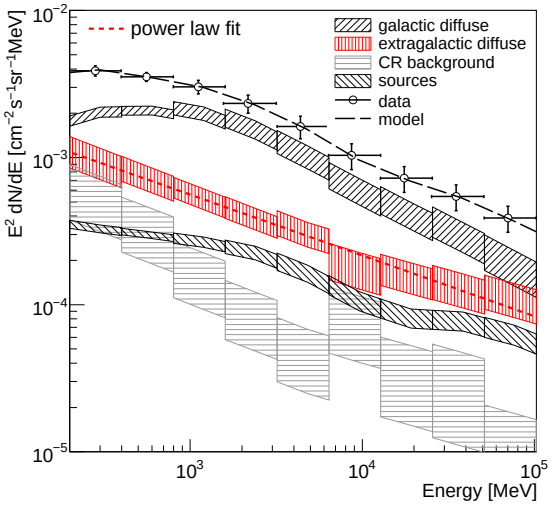

Figure 3.1: GRB reported by the *Fermi*/LAT Collaboration (Abdo et al., 2010).

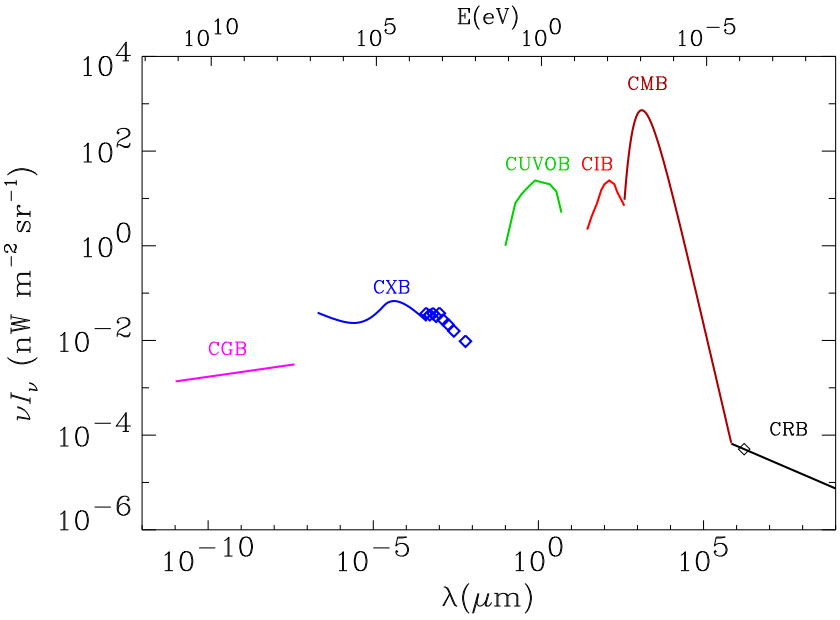

Figure 3.2: The power density spectrum of the backgrounds filling our Universe.

Cosmic Radio background (CRB) is composed of the diffuse extragalactic light at wavelengths above 1 m. In comparison with the other components, is very weak, and is a tracer of non thermal processes in the Universe.

The most energetic component of the overall power density spectrum is indeed the CMB, followed by the CUVOB and CIB components. The merging of the CUVOB and the CIB forms the so-called **Extragalactic Background Light** (EBL). As we will present in Chapter 7, this light may interact by pair production with VHE photons from extragalactic objects, causing a deformation of the spectrum observed from these sources. Hence, a precise modeling of the EBL is of particular interest for the study of the intrinsic spectrum emitted by a blazar (see Chap. 2), and can be used for other studies involving blazars. Part of this work of thesis will be addressed to discuss new methods to constrain the distance of such objects starting from the "deformed" (or absorbed) spectra observed at VHE energies. In this Chapter we present an up-to-date overview regarding the existing EBL theories, observations and models.

3.2 From UV to IR: the EBL

EBL is formed by the diffuse light in the ultraviolet to far-infrared wavelength regime, and carries important information about the star formation history of the Universe. Like any background, except for the CMB, the present EBL consists of the integrated electromagnetic radiation from all epochs.

The electromagnetic radiation experiences, in fact, a cosmological redshifting, due to the expansion of the Universe, that depends on its emission epoch. Light emitted by objects distant in space (or in time), arrives at the observer shifted to lower energy (redshifted). Radiation emitted by nearby sources, instead, arrives at Earth almost unaffected by this expansion. Therefore, the light observed at

a given wavelength is the sum of the light emitted at that wavelength by near objects plus light emitted at higher energy by distant sources, plus light emitted at even higher energy by very far located objects. The formula relating the observed wavelength, λ_{obs}, with the emitted one, λ_{em}, for an observer located at $z = 0$, is:

$$\lambda_{obs} = (1+z) \cdot \lambda_{em} \tag{3.1}$$

with z redshift of the source. For example, optical light emitted by first stars ($\lambda_{em} = 500\,\mathrm{nm}$), supposed to be at redshift $z \sim 20$, is shifted into the IR energy range by the Universe expansion ($\lambda_{obs} = 10.5\,\mu\mathrm{m}$).

The power density distribution of the EBL is sketched in Fig. 3.3. A two peak structure is evident: the first peak in the optical wavelength is produced by starlight, while the second peak, at $\sim$100 μm, which has roughly equal brightness, is due to starlight absorbed and re-emitted by dust. The valley around $\sim$10 μm is created by the decrease of brightness of the stellar component, combined with the rising brightness of the IR component, caused by dust (small grains, large grains, and PAH[3], see Desert et al. 1990 for a review) and AGN non thermal emission Lagache et al. (2005).

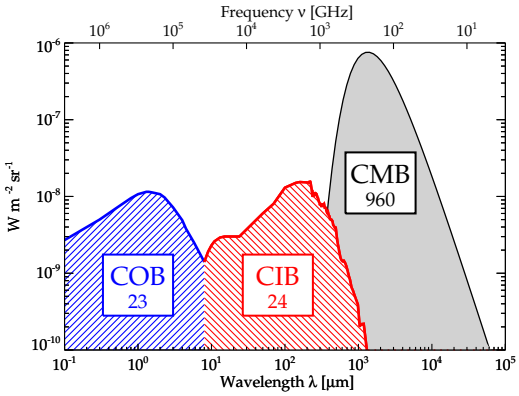

Figure 3.3: Sketch of EBL SED.

3.2.1 Status of the direct measures

Direct measurements of EBL have proved to be a very difficult task since while the background is relatively weak, the various foregrounds are reasonably bright, as illustrated in Figure 3.4. Foreground emission from the solar system (zodiacal light), and secondly from the bright of the Galaxy, are the main problem in unveiling the expected extragalactic light. At wavelengths less than 10 μm, the dominant foreground after removing the zodiacal light model is emission from stars in our Galaxy (Kashlinsky, 2005). At sub-mm wavelengths CMB emission dominates everything else. The latter component, however, is quite easy to subtract, since its (plankian) shape is known with very high precision.

Recent direct EBL determinations include:

- *Hubble* optical measurements (Bernstein, 2007).
- *COBE*/DIRBE data from 1.25 to 2.2 microns (Cambrésy et al., 2001);
- *IRTS* results between 2.2 and 4 microns (Matsumoto et al., 2005);
- *Spitzer* data at 3.6 μm (Levenson and Wright, 2008);
- *COBE*/FIRAS measure at λ >125 microns (Lagache et al., 2000);
- *ISO* estimate of the background at 170 microns (Juvela et al., 2009);

[3]PAH stand for Polycyclic Aromatic Hydrocarbon.

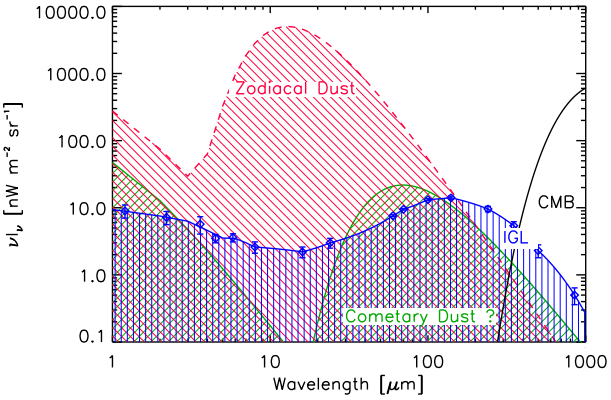

Figure 3.4: Estimates of the relative contributions of the zodiacal dust and integrated galaxy light in a typical extragalactic field. From Chary and Pope (2010).

The reliability of these measurements, however, is often put in doubt. In particular, the background subtraction procedure may easily lead to a faint signal, especially in the near-infrared range where the zodiacal light is huge (Mattila, 2006). A case study is the excess at $\sim 2\,\mu$m, found in *IRTS* data by Matsumoto et al. (2005). In the paper, the detection of a peak in the EBL SED, reported in Figure 3.5, is claimed. This signature could be an evidence of Population III stars (the first stars appeared in the Universe), or a feature due to a non-convenient background subtraction, as pointed out by many authors. A large debate in the community followed this publication, and still today the issue is open. From recent upper limits estimated with TeV data, however, the evidence for Population III stars emission seems to be ruled out.

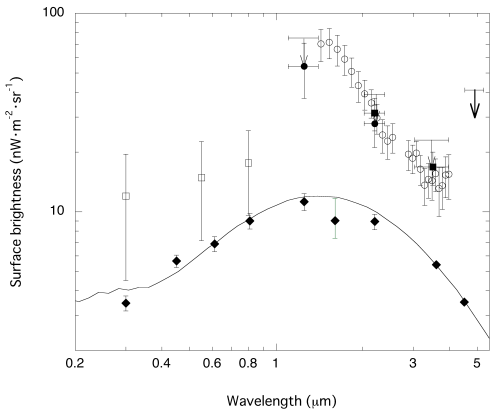

Figure 3.5: The NIR excess, from Matsumoto et al. (2005). Arrows shows upper limits from COBE DIRBE data; open squares presents optical determinations, EBL obtained from the star-subtracted COBE DIRBE data is shown by the filled squares and the filled circles. The filled diamonds represent the integrated light of galaxies.

3.2.2 Indirect measures

Direct determinations of EBL are very difficult, as we have seen in previous Section. Three distinct indirect methods have been proposed in the last decade, in order to set constraints (both lower and upper limits) on the light which constitutes this background. Namely, the methods are:

- Source number counts (lower limits);
- Opacity to TeV photons studies (upper limits).
- Statistical analyses (lower limits);

Since the upper and lower limit determinations resulting from these studies are becoming more and more stringent, we are getting closer to the EBL measure.

Lower limits from source number counts

Deep number counts of emitting sources give very solid lower limits to the overall light filling the Universe. It is plausible to assume, in fact, that the resolved sources are only part of the total emitters. Therefore, the counting approach has been used to infer a lower limit on the EBL by a number of authors, like Béthermin et al. (2010); Madau and Pozzetti (2000); Fazio et al. (2004).

Figure 3.6 shows the differential number counts resulting from a recent analysis of *Spitzer* data at 24 μm. At this wavelength, it is thought that almost 80% of the CIB is resolved. Conversely, at larger wavelengths faint sources are totally blended and impossible to extract since the diffraction increases.

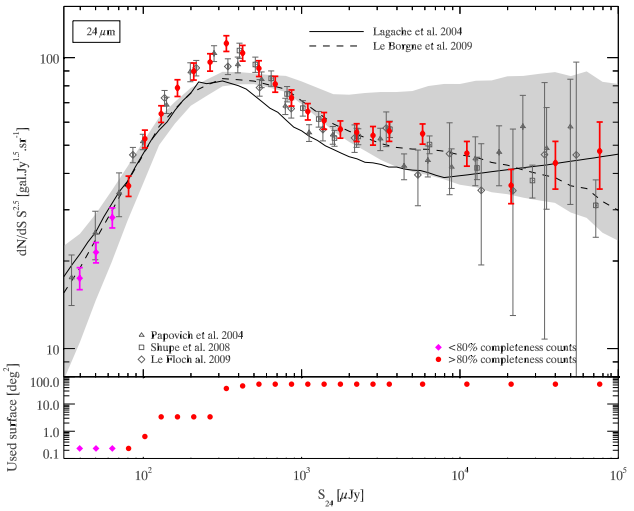

Figure 3.6: Differential number counts of sources at 24 μm. From Béthermin et al. (2010)

Upper limits from studies of TeV photons opacity

As we mentioned before, TeV photons emitted by extragalactic sources interact with EBL photons by pair production. As a result, due to this interaction the VHE spectrum emitted by a distant blazar is deformed. Upper limits on EBL energy density can be estimated by assuming some basic properties in the original spectrum of the TeV photon sources. In particular, the general requirement is a

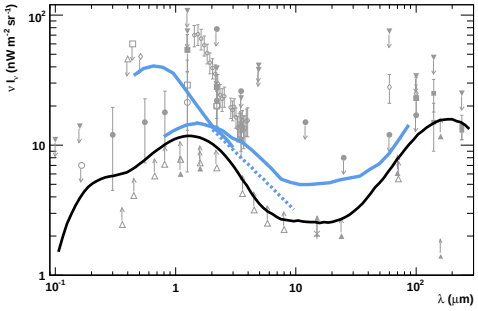

Figure 3.7: EBL limits from the detection of distant VHE γ–rays source (blue curves; Aharonian et al. 2006; Aharonian et al. 2007b; Mazin and Raue 2007), superimposed to some recent EBL measurements (grey markers). The black curve shows the generic EBL model proposed in Raue and Mazin (2008). Image from http://www.desy.de/~mraue/ebl/.

realistic assumption on the shape of the intrinsic spectrum of the blazar. This is

the spectrum that we would observe if there were not an EBL. More details about this approach will be discussed in Chapter 7. A key result is that the present day upper limits obtained with this method are quite close to the lower limits obtained with the others techniques (Figure 3.7).

Limits from statistical analyses

Other methods commonly used to set limit the EBL energy density are based on statistical treatment of the data. A first method, called *stacking technique*, used for example in Dole et al. (2006), consists in piling up the sky maps at 70 μm and 160 μm of very faint far-infrared galaxies, detected at 24 μm but not at smaller frequencies. Even if the single sources are not detected individually, a clear signal comes out at larger wavelength when the maps are summed up together, as shown in Figure 3.8. Lower limits estimated in this way take into account also the contribution from unresolved galaxies, and are closer to the real value with respect to the limits obtained with number counts.

There is a second statistical technique, named *fluctuation technique*, which allows to set upper limits on the EBL. The idea is based on the fact that if at least part of the background is originated from discrete sources, then fluctuations in the number of sources in a determined field of view will produce fluctuations in the measured background brightness. Therefore, measurement of fluctuations in the extragalactic background can reveal information about the number and distribution of contributing sources. Such fluctuations can be characterized by the two dimensional autocorrelation function of the sky brightness (Hauser and Dwek, 2001).

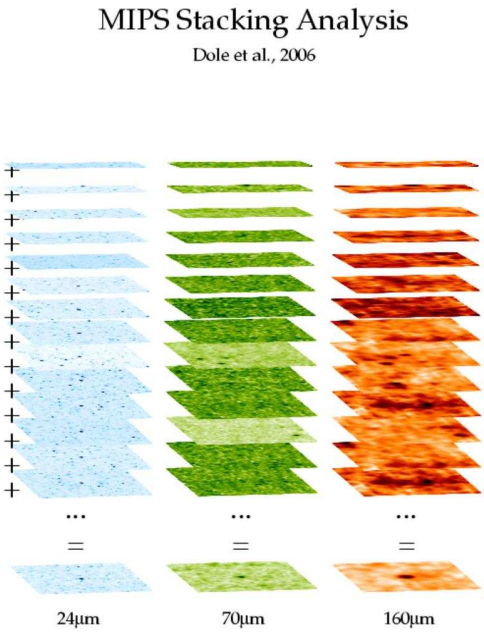

Figure 3.8: Stacking technique, from Dole et al. (2006).

3.2.3 Overall SED

Figure 3.9, from Béthermin et al. (2010), illustrates a collection of current EBL measures, obtained both with direct observations and indirect methods. Arrows indicate upper or lower limits.

3.3 Models

A number of models have been developed in the last decade for calculating the evolving EBL. The issue is analogous to the estimation of the evolving luminosity density as a function of the distance, i.e. the redshift. Figure 3.10 shows the dependence of the radiation field with the redshift.

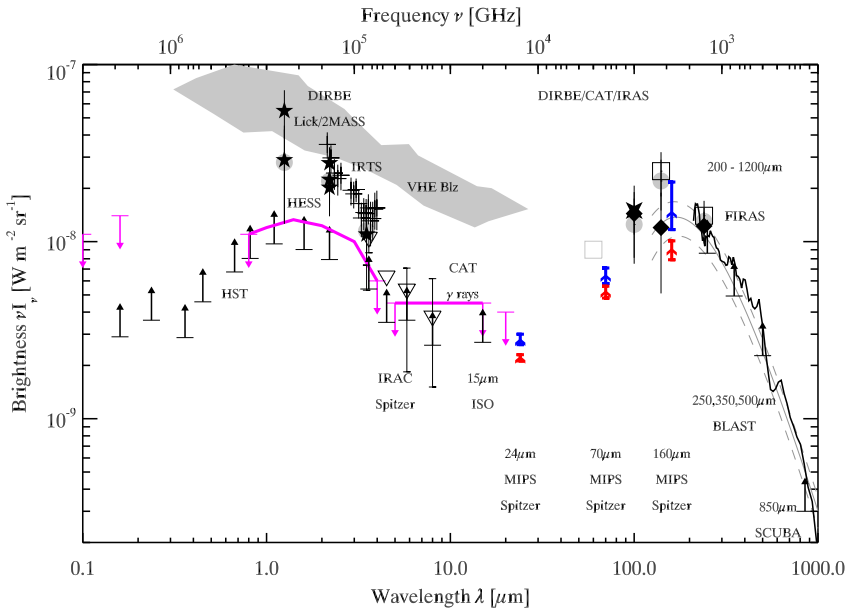

Figure 3.9: Current measurement of the extragalactic background light spectral energy distribution from 100 nm to 1 mm. From Béthermin et al. (2010).

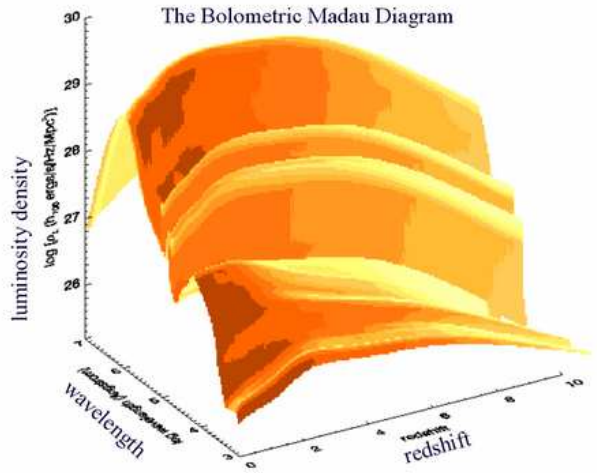

Figure 3.10: The evolving EBL. From Primack et al. (2005).

According to the recent paper of Domínguez et al. (2011), EBL models can be grouped into four categories, that will be briefly introduced in next Sections. The models of galaxy evolution differ in their degree of complexity, physical realism and ability to account for observations.

3.3.1 Forward evolution

Belong to this class those models which assume as a starting point determined cosmological conditions in the past, and make the Universe evolving, taking into account ingredients of galaxy formation by means of Semi–Analytical (SA) models. The most recent model of this kind has been published by Gilmore et al. (2009). In a recent work, Somerville et al. (2008) show how the model is able to predict many observational evidences. However, several potentially serious

discrepancies with data still remain.

The main advantage of SA models is that, in spite of the many adjustable parameters, they provide a physical approach to the formation and evolution of galaxies (Hauser and Dwek, 2001).

3.3.2 Backward evolution

This class of models starts from existing galaxy populations, and make them evolving backward in time. Recent models of this kind are Stecker et al. (2006); Franceschini et al. (2008). The latter is usually referred as one of the most solid EBL model, since it is based on observational constraints. In particular it is founded on the galaxy luminosity function, quantity which can be directly observed and well understood. The background level foreseen by Franceschini model is significantly lower than that predicted by Stecker.

3.3.3 Inferred galaxy evolution

This category includes models that estimate the EBL and its evolution by means of some quantities derived from observations. Recently, two distinct models of this sort have been published, namely Kneiske and Dole (2010) and Finke et al. (2010). In both cases, the evolution of the star formation rate density of the Universe, Figure 3.11, plays a key role.

According to Domínguez et al. (2011), this type of models are vulnerable to

anage.

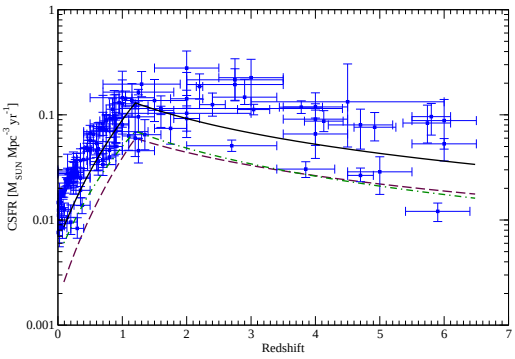

Figure 3.11: Comoving cosmic star formation rate density, used in Kneiske and Dole (2010). The solid line shows the model total star formation rate, while the dashed and dashed-dotted line accounts the contribution from dust-poor and dust-rich galaxies, respectively. From Kneiske and Dole (2010).

3.3.4 Observed galaxy evolution

The last class of EBL models is the most empirical one, and includes those models in which the evolution of the galaxy populations is directly observed. Up to now, only the model published in Domínguez et al. (2011) belongs to this category. The results are in very good agreement with Franceschini model, even at large redshifts.

The main advantage of this approach is that it does not require to extrapolate any luminosity function, conversely to the backward evolution models case. In addition, this approach allows a quantitative study of the uncertainties.

3.4 Conclusions

In conclusion, we show in Figure 3.12 a comparison among some of the models described here, superimposed to some experimental findings. With respect to

some years ago, substantial improvements have been done in the measurements and modelization of the EBL. Upper and lower limits are approaching and the latest models, even though they use very different methodologies, agree quite well.

This is of particular importance for the studies carried out in Chapters 7 and 8, which assume a certain EBL model for the determination of a limit on the redshift of TeV emitting blazars.

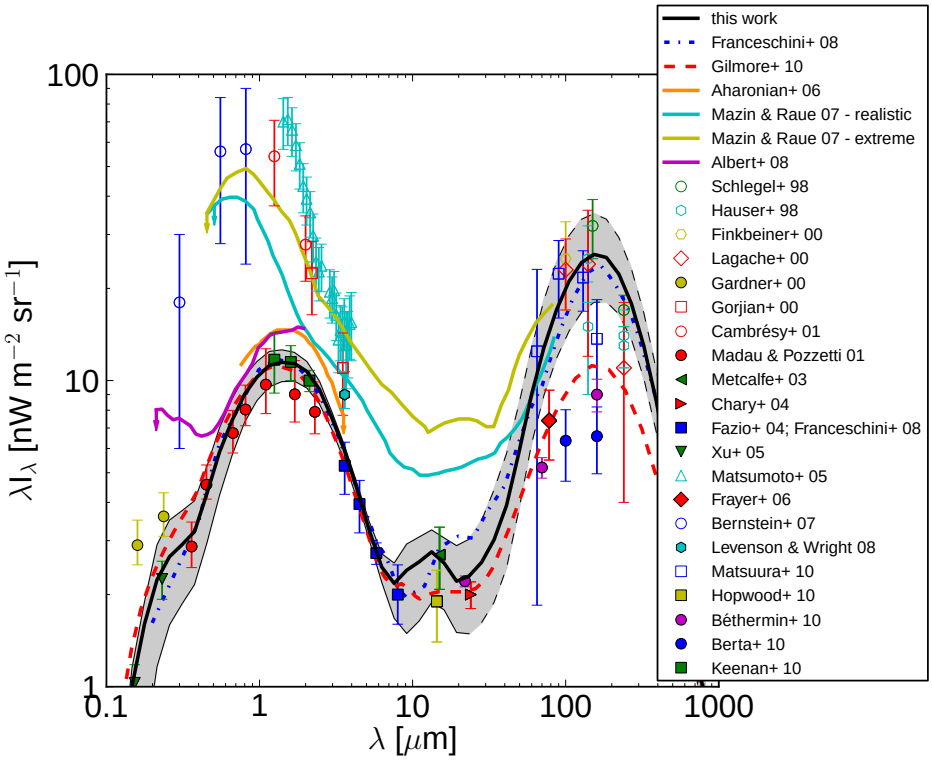

Figure 3.12: Comparison among some EBL models, superimposed to recent experimental findings. From Domínguez et al. (2011).

One dream, one soul, one prize, one goal,
One golden glance of what should be

A Kind of Magic – Queen

4

Detection of very high energy γ–rays: the MAGIC Telescopes

COSMIC RAYS cannot be directly detected by ground–based telescopes: when reaching the Earth atmosphere, in fact, these energetic particles soon interact with other particles, initiating a so–called *atmospheric shower*. The first part of this Chapter is dedicated to the physics of atmospheric showers induced by γ–rays, together with those induced by charged cosmic–rays, which are the main source of background of a γ–ray ground–based telescope. The imaging technique is then outlined, since it is the technique adopted by modern telescopes, among which MAGIC, for the detection and characterization of VHE γ–rays. In the last part of the Chapter, the MAGIC telescopes hardware is described in detail. A special emphasis will be given to the performances of the instrument.

4.1 γ–ray detection from satellites

Except for some radio frequencies and a small window centered in the optical energy range, the electromagnetic radiation coming from space is absorbed and cannot reach the surface of our Planet, see Fig. 4.1. This attenuation, due to the opacity of Earth atmosphere, was a key ingredient for the development of life on Earth. On the other side, it is a great disadvantage for observational astrophysics.

Many telescopes, nowadays, are located on-board of satellites orbitating around Earth or in the space[1]. Regarding γ–rays, they cannot be detected with typical methods, i.e. through lenses or mirrors, like the hard X–rays. Three are the competing processes at the basis of the detection techniques:

- **Photo-electric effect:** it is the dominant process in the energy range between 0.1 and 0.3 MeV. Detectors have characteristics similar to the X-ray telescopes, which use scintillator counters and solid state detectors.
- **Compton scattering:** becomes dominant between 0.5 to 10 MeV, even if in this energetic range the pair production process can not be excluded. Typical Compton instruments consist of two separated detector layers, a *converter* and an *absorber*. An example of this type of detector was the

[1] An exception are the radio telescopes.

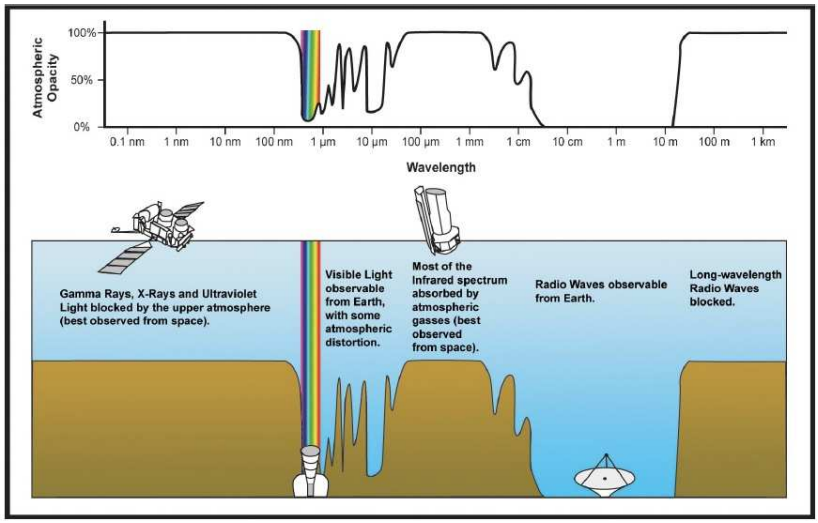

Figure 4.1: Opacity of Earth atmosphere: only radio waves and the photons belonging to the small optical window pass through the atmosphere without being absorbed. As a result, for the *direct* observation of the cosmic radiation, satellite–borne instruments are used.

COMPTEL instrument on board of the *Compton Gamma–Ray Observatory* (*CGRO*).

- **e^+-e^- pair production:** finally, above 30 MeV, this becomes the dominant process. The main elements of a detector in this energy range are a *converter* region where the primary gamma interacts, a *tracker* capable to provide the direction of the e^+ e^- tracks in addition to the dE/dx loss estimation and finally a *calorimeter* region, which brings the electrons and positrons to rest in order to measure their remaining energy. Examples of this kind of instruments were on-board the *OSO-III*, *SAS-II* and *COS-B* satellites or the more recent *CGRO* and *Fermi* satellites.

We know from Chapter 1 that charged nuclei largely dominate the CR flux. Even with instruments with a small field of view pointing at a bright source, the fraction of gammas is very small. Hence, a common requirement for all γ–ray satellite-borne detectors is a good anti-coincidence system, capable to suppress the cosmic-ray background composed of charged particles which isotropically hit the detector.

A very important feature, for our purposes, of satellite-borne γ–ray experiments is that none of them observes enough VHE γ–rays. The reason is that, as described in Chapter 1, the differential spectrum emitted by a cosmic source at hundreds of GeV is a decreasing function of the energy[2]. The small effective area characterizing satellites, renders almost impossible to catch fluxes at the level of the ones emitted by typical galactic or extragalactic sources. Even the most performant instrument, the LAT, has a maximum detecteable energy of about 300 GeV, due to its reduced surface, of $\sim$1 m^2.

[2]Usually, VHE spectra are well approximated by power laws of the form $dN/dE \propto E^{-\Gamma}$, with α larger than 2. For example, the standard candle of γ–ray astronomy, the Crab Nebula, emits $\sim$200 photons above 100 GeV per m^2 per year, out of which only $\sim$7 photons per m^2 per year have energy above 1 TeV.

Hence, if we want to observe VHE γ–rays we need another technique, which involves the Earth atmosphere as a part of the detector. Before passing to explain in detail such technique, we will give a small overview on the LAT instrument, whose results, after the first two years of operations, have played a key role in the VHE source detection methods and source modelization.

4.1.1 The *Fermi*/LAT detector

The *Fermi* telescope is an international γ–ray space telescope operating since mid 2008 nominally in the photon energy range of 8 keV to greater than 300 GeV. In addition to the Large Area Telescope (LAT, the primary instrument), it carries a second instrument, the GLAST Burst Monitor (GBM, the complementary instrument), useful, between other things, for the GRB detection. As mentioned before, the *Fermi*/LAT is an imaging, wide field-of-view, HE γ–ray telescope, covering the energy range from below 20 MeV to more than 300 GeV (Atwood et al., 2009). The LAT is a pair-conversion telescope with a precision *tracker* and *calorimeter*, each consisting of a 4×4 array of 16 modules, a segmented *anticoincidence detector* that covers the tracker array, and a programmable *trigger and data acquisition system*.

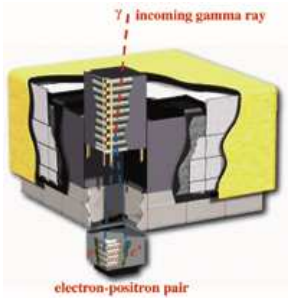

Figure 4.2: *Fermi*/LAT detector scheme.

Each tracker module consists of layers of silicon-strip particle tracking detectors interleaved with thin high-Z converter material (tungsten) foils. The silicon-strip detectors precisely measure the paths of the pair conversion showers. Such measurements are used for the signal detection as well as for the background rejection, mainly composed of charged CRs. The aspect ratio of the tracker (height/width) is 0.4, allowing a large FoV (2.4 sr).

The calorimeter, composed of CsI(Tl) crystals, has a twofold purpouse: it measures the energy of $(e^+;e^-)$ particles, and images the shower profile development. The latter action helps to reject CRs, since their pattern of energy deposition is different from that of γ–rays.

The anticoincidence detector, forms like a hat that fits over the tracker, and is the first line of defense against cosmic rays. It consists of specially formulated plastic tiles producing flashes of light when hit by charged-particle cosmic rays.

Finally, following Atwood et al. (2009), the data acquisition system collects the data from the other subsystems, implements the multi-level event trigger, provides on-board event processing to run filter algorithms to reduce the number of downlinked events, and provides an on-board science analysis platform to rapidly search for transients.

The scientific program of LAT is quite wide. It forsees to:

- notify of GRBs and transients;
- yield an extensive catalog of several thousand high-energy sources obtained from an all-sky survey;
- measure spectra from 20 MeV to more than 50 GeV for several hundred sources;

- localize point-like sources to 0.3–2 arc-minutes;
- map and obtain spectra of extended sources such as SNRs, molecular clouds, and nearby galaxies;
- measure the diffuse isotropic γ–ray background;
- search for dark matter signatures.

The principal characteristics and performance parameters of LAT are listed in Table 4.1.

Table 4.1: Main Characteristics of the *Fermi*/LAT detector, from Atwood et al. (2009).

Energy Range	20 MeV to 300 GeV
Effective Area	9500 cm^2
Energy Resolution	from 18% to below 16%
Angular Resolution	from 3.5° to $< 0.15°$
Field of view	2.4 sr

4.2 Atmospheric showers

We know, from previous Section, that VHE γ–rays cannot be efficiently observed with satellite experiments, due to the small fluxes involved. As often happens in science, man in the last century has successfully tried to solve this problem, finding a way to measure the electromagnetic radiation at such high energies from Earth, where large surface detectors can be employed. The detection technique is based on the experimental evidence that even if we cannot measure directly this radiation from Earth, we can study the products of its interaction with the atoms of the atmosphere.

When a γ–ray, or any charged cosmic ray, interacts with molecules of the Earth atmosphere, a cascade of particles is produced, the so called Extensive Air Showers (EAS). The features of a shower depend principally on the nature of the primary particle (see Figure 4.3).

4.2.1 Electromagnetic showers

The electromagnetic cascade starts when a γ-ray penetrating the Earth atmosphere hits a nucleus and produces an *electron/positron pair*. Each electron/-positron pair generates high energy photons via *Bremsstrahlung*, the secondary photons produce $e^{\pm}$ pairs and so on.

Such a cascade, displayed in Figure 4.4, is called *electromagnetic cascade* due to the physics processes sustaining the shower development.

The average energy of the shower particles lowers during the shower development, till it reaches the critical value E_c. Below such threshold (in air $E_c \sim 83MeV$), the dominant process becomes the ionization of atmospheric atoms produced by electrons. As a result, fewer particles are produced and the shower soon dies out.

Due to their relativistic energies, all particles of a shower are strongly collimated along the incident direction. The main process that broadens the shower transversely is the multiple scattering and, in second order, the deflection of Earth

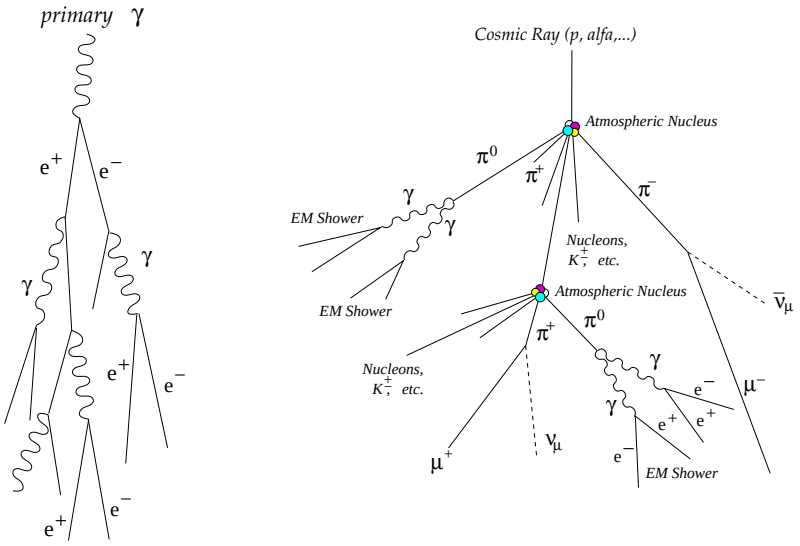

Figure 4.3: Schematic description of EAS. Left: electromagnetic shower. Right: hadronic shower.

magnetic field. Electrons and positrons can also induce electromagnetic showers with identical features than those induced by γ–rays. Thus, electrons and positrons should be considered as an irreducible background for ground–based γ–ray detectors.

For the sake of completeness, one should be aware that also a hadronic and a muon component may be present in the electromagnetic shower. The photoproduction ($\gamma + nucleus \rightarrow hadrons$) and muon production ($\gamma \rightarrow \mu^+\mu^-$) may occur. However, in first approximation, these contributions may be neglected since their cross-section is much smaller than pair-production and Bremsstrahlung[3].

A simple model, proposed by Heitler in 1944 (Longair, 1992), describes with good approximation the main properties of these showers (sketched in Figure 4.4). The *radiation length* ξ_0 of a particle is the mean distance it travels before its energy is reduced by a factor e. For an ultrarelativistic electron in air, the radiation length is $\xi_0 \sim 36.7 g/cm^2$. Let $R = \xi_0 \ln 2$. Then, the electron energy is reduced by a factor $exp(-R/\xi_0) = 1/2$ after traveling a space of thickness R in the atmosphere.

Supposing that the energy of the primary particle is equally distributed into the decaying products, then after a distance nR the number of secondary particles will be 2^n, and their mean energy will be $E_0/2^n$, where E_0 is the energy of the primary γ. The position of the shower maximum is then:

$$X_{max} = R \cdot \ln \frac{E_0}{E_c} / \ln 2 = \ln \frac{E_0}{E_c} \cdot \xi_0 \tag{4.1}$$

where E_c is the critical energy value.

More precise analytical models of the development of these showers have been proposed by Rossi and Greisen in the mid-40's. These theories have been devel-

[3]The photo production cross-section is $100 \mu b/nucleon$ (in air A=14.5 corresponds to 1.5 mb), while the cross-section for the pair-production is $\sim 100 mb$. The muon mass is 200 times the electron mass: thus the muonic cross-section (12 μb, in air) can be neglected respect to that of electrons (500 mb, in air).

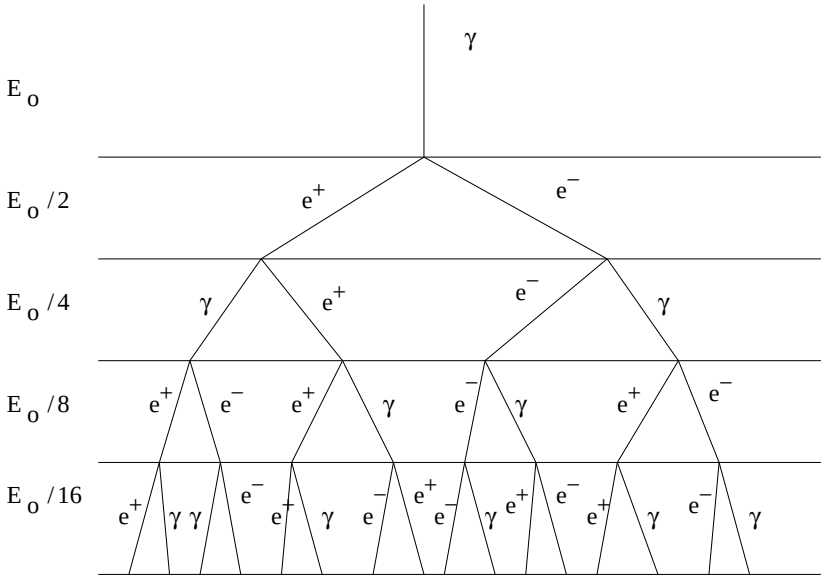

Figure 4.4: Simplified model of an electromagnetic shower.

oped in the so-called "B approximation": every process is neglected except for pair production and energetic loss by Bremsstrahlung. The analytic solution for N_e (i.e. the total number of electrons and positrons above the critical energy) is:

$$N_e(t, E_0) = \frac{0.31}{\sqrt{\ln(E_0/E_c)}} \cdot e^{t \cdot (1 - 1.5 \ln s)} \tag{4.2}$$

where t is the atmospheric depth, s is the *age parameter*, which indicates the development level of the shower and it goes from a value of 0 in the point of first interaction, to 1 at the maximum and 2 at the point where the shower dies.

The variation of N_e with t is often called *longitudinal development* of the shower. Some examples for different values of E_0/E_c are shown in Figure 4.5. The MAGIC telescopes are located at 2245 m of altitude above the sea level, which corresponds to about 22 X_0, as can be seen in Figure 4.5. At energies of 10–100 GeV the maximum development of the shower is at about 10–14 km above the sea level, while at energies around 100 TeV, it is at 6000–7000 m.

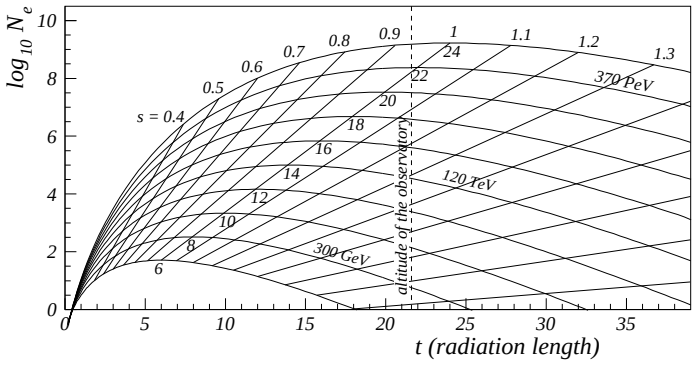

Figure 4.5: Maximum development of an electromagnetic shower in the atmosphere. The position of the MAGIC telescopes is drawn.

The *lateral distribution* of a shower has the main contribution from the particles with low energy, i.e. those produced at lower altitudes.

An analytic description of the lateral distribution is given by the formula of Nishimura-Kamata-Greisen:

$$\rho_e(r,t,E_0) \propto \frac{N_e(t,E_0)}{r_M^2} \cdot (\frac{r}{r_M}) \cdot (1+\frac{r}{r_M})^{s-4.5} \tag{4.3}$$

where r_M is the Moliere radius (about 79 m at sea level).

4.2.2 Hadronic showers

An EAS induced by a proton or any other atomic nucleus is called *hadronic shower*. A hadronic shower has three components: a hadronic, an electromagnetic (also called *soft component*) and a muonic one (referred as *hard component*).

The primary hadronic particle interacts with an atmospheric nucleus, creating pions, kaons and other nucleons. The latter particles constitute the so-called *core* of the shower. The hadronic interactions of the products continue as long as the energy is still sufficient to create pions (~ 1 GeV). Almost 90% of the secondary particles produced in a hadronic shower are pions, 1/3 of which are π^0. These particles suddenly decay into two photons ($\pi^0 \to \gamma\gamma$). Each VHE photon starts an electromagnetic sub-shower, forming the electromagnetic part of the shower, so that about one third of the energy is since the beginning transferred to this component. This process is basically irreversible, therefore one third of the total initial energy is transferred, at the shower end, to the electromagnetic component.

Low energy charged pions feed the muonic component by decaying into muons and neutrinos, according to the reactions:

$$\pi^{\pm} \to \mu^{\pm} + \nu_\mu(\bar{\nu}_\mu) \tag{4.4}$$

Kaons directly contribute to the muon production through the reactions:

$$K^{\pm} \to \mu^{\pm} + \nu_\mu(\bar{\nu}_\mu) \quad 21.1\% \tag{4.5}$$

$$K^{\pm} \to \pi^{\pm} + \pi^0 \quad 63.4\% \tag{4.6}$$

Muons can either decay into $e^{\pm}\nu\bar{\nu}$ or lose energy by ionization. Due to the high initial muon energy, only a few of them decay. Therefore, most of the muons produced in the hadronic cascades arrive at the ground.

From an evolutionary point of view, at the beginning of the shower, strong interactions dominate, while at the end of the shower particles decays dominate.

The lateral spread of the hadronic shower is mainly caused by the transverse momentum of the secondary hadrons after a hadronic interaction. The result is a much wider shower respect to the electromagnetic case. Moreover the hadronic radiation length has almost a double size compared with the electromagnetic one ($\xi_0^{had} \sim 70 g/cm^2$). This causes a larger fluctuations of hadronic showers than electromagnetic ones. These differences are the basis of the discrimination between γ–rays and charged CRs.

The simpler model for describing the hadronic showers is the *Superposition Model*. Assuming that a nucleus with atomic mass A and energy E_0 is equivalent to A independent protons with energy E_0/A, the position of the shower maximum is:

$$X_{max} \propto \ln\left(\frac{E_0}{AE_c}\right) \cdot \xi_N, \tag{4.7}$$

where ξ_N is the nuclear interaction length in the air. From the formula (4.7) it is evident that heavier nuclei are less penetrating than lighter ones. Showers from heavier nuclei have also less fluctuations.

4.2.3 Direct detection of shower particles

The direct detection of air-shower particles offers a method of VHE γ-ray detection with a duty cycle close to 100 % and a very wide field of view.

Figure 4.6: MILAGRO detector.

The water Cherenkov approach, employed by the MILAGRO collaboration, appears to represent the most promising method of achieving complete ground coverage. MILAGRO is composed of 723 photo-multiplier tubes submerged in a 24 million liter water reservoir. It is located at an altitude of 2630 m (Atkins et al., 2003). The best background rejection power and sensitivity of this instrument is in the regime above 10 TeV, which, in a sense, is complementary to the atmospheric Cherenkov detectors, described in next Sections. Due to the high energetic threshold, this kind of telescopes are mainly conceived for galactic objects.

The main challenges of direct detection approach are the rejection of the CR background, based on the muon content of showers and/or the distribution of shower particles on the ground, and directional and energy reconstruction. The large fluctuations present in the particle number at ground level, in fact, make primary energy determination extremely difficult for extended atmospheric showers detectors.

In order to reduce the uncertainties related to the large distance from the detector to the shower maximum, the future generation of this kind of detectors will be built at altitudes above 4000 meters. For example the location of HAWC[4] (High Altitude Water Cherenkov Experiment), the successor of MILAGRO, is Sierra Negra, Mexico, which is a very high altitude (4100 m).

4.3 Cherenkov light in atmospheric showers

Below some TeV, the shower particles are too faint to be detected. Hence, instruments based on direct EAS particles detection have an optimal energy range above this threshold. A different techique, described in Sec. 4.4 is used in the 100 GeV to 30 TeV energy range. It is based on the detection of Cherenkov light emitted by atmospheric showers induced by CRs.

4.3.1 The Cherenkov effect

The Cherenkov effect occurs when a charged particle travels in a dielectric of refractive index n with a speed exceeding the speed of light in the medium (c/n).

[4] http://hawc.umd.edu/index.php

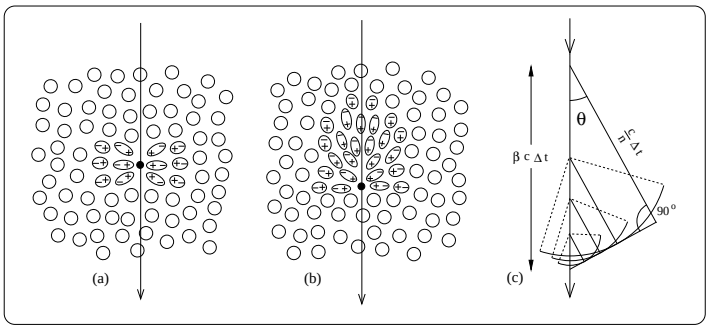

Figure 4.7: In figure (a) is shown the polarization induced by a slow moving charged particle in a dielectric medium. In figure (b) the effect of a fast moving particle. In figure (c) the geometrical description of the Cherenkov angle θ.

When a charged particle moves in a dielectric medium, like the air, polarization occurs (Figure 4.7). When the velocity of the particle v is *superluminal*[5], the particle is moving faster than the electromagnetic wave induced by the polarization; in this case, a coherent wave front appears at an angle θ, and the radiation emitted is called *Cherenkov light*.

The analytical description of the Cherenkov effect can be given using a classical approach (Nobili, 2002). When the particle moves in the medium, it is like just if it emits a succession of spherical waves which propagate with velocity c. If the motion of the particle is superluminal, a coherent front wave appears, separating the external area, having no signal, from the internal one (see Figure 4.7 (c)). In the internal region, the waves are superimposed, meaning that in every point of this region two delayed electron positions coexist and an electric field is formed.

The angle of emission can be derived with simple geometrical arguments yielding:

$$\cos\theta = \frac{1}{\beta n} \tag{4.8}$$

where $\beta = v/c$. The surface delimited by this angle is called *Cherenkov cone*. The limit Cherenkov angle is $\theta_{max} = arccos(n^{-1})$, occurring if $\beta = 1$ (ultrarelativistic particles). As already mentioned, the threshold velocity for Cherenkov light emission is

$$\beta_{min} = 1/n \tag{4.9}$$

which implies a minimum energy threshold for particles of:

$$E_{th} = \frac{m_0 c^2}{\sqrt{1-\beta_{min}^2}} = \frac{m_0 c^2}{\sqrt{1-n^{-2}}} \tag{4.10}$$

where m_0 is the particle rest mass. At sea level, the air refractive index is $\sim$ 1.00029. This correspond to an energy threshold of 21 MeV for electrons, 4.3 GeV for muons and 39 GeV for protons.

The number of emitted photons as a function of the path length and the

[5]In a dielectric medium with refractive index n, the motion of a particle is superluminal when its velocity is higher than the light speed in that medium c/n.

wavelength is:

$$\frac{dN}{dld\lambda} = 2\pi\alpha(1 - \frac{1}{(\beta n)^2}) \cdot \frac{1}{\lambda^2} \tag{4.11}$$

where α is the fine structure constant.

The strength lines of the electric field are radial and point to the actual position of the emitting particle. The electric field diverges on the Cherenkov cone surface, which is a singular surface where the sharp transition of the electric field occur. This front wave propagates at the speed of light c, forming a sort of electromagnetic collision wave, which is at the origin of the impulsive signal registered by the detectors. The Cherenkov radiation can occur only at frequencies for which $n > 1$, i.e. from microwave to UV, but not at higher energies of the electromagnetic spectrum.

4.3.2 Emission of Cherenkov light by showers

The low energy threshold for Cherenkov light emission of electrons (Eq. 4.10), makes them the main emitters of Cherenkov light in atmospheric showers. Electrons in these showers emit Cherenkov radiation at different altitudes, according to the emission model presented in Section 4.2. Thus, the correct model for describing the Cherenkov light emitted by electrons should take into consideration the atmospheric variation with respect to the altitude.

We assume that the atmosphere density ρ scales exponentially with altitude h (the so–called isothermal atmosphere approximation):

$$\rho(h) = \rho_0 \cdot \exp(-h/h_0) \tag{4.12}$$

with $h/0 = 7.1Km$ and $\rho_0 = 0.0013g/cm^3$ (air density at sea level). In this approximation, the refractive index is then:

$$n = 1 + \eta_h = 1 + \eta_0 \exp(-h/h_0) = 1 + 2.9 \cdot 10^{-4} \exp(-h/h_0) \tag{4.13}$$

where $h_0 = 7.1Km$ is the scale–height. The dependence of the refractive index from the wavelength λ can be neglected for our values of λ.

The threshold energy for electrons, according to equation 4.10 is:

$$E_{th}(h) = \frac{0.511MeV}{\sqrt{2\eta_0 \exp(-h/h_0)}} \tag{4.14}$$

The angle θ_{max} can be written as:

$$\cos\theta_{max}(h) = \frac{1}{1+\eta_h} \simeq 1 - \eta_0 \exp(-h/h_0) \tag{4.15}$$

In Figure 4.8 (left), the emission Cherenkov angle at different altitudes for an atmospheric shower is sketched. The radius has a maximum, corresponding to photons emitted between 10 and 20 Km. The light from the shower tail is emitted with a larger Cherenkov angle, but its distance is smaller due to the lower height.

Usually, Cherenkov photons spread over a quite large area, that is a circle with a diameter of $\sim$ 300 m, for altitudes of 2200 m. This huge surface allows the detection of showers with a large **Impact Parameter** (IP: distance between the shower axis and the point of detection). On the other side, this large area decreases the photon density.

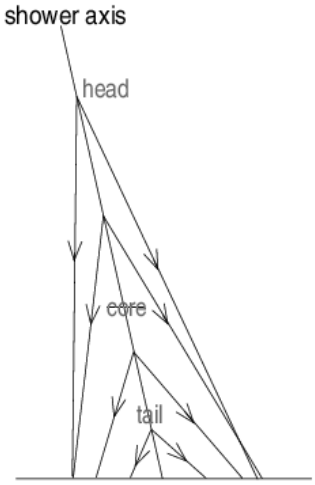

Figure 4.8: Schematic view of the emission Cherenkov angle at different altitudes of an atmospheric shower.

The *zenith angle* of observation is another factor that influences the Cherenkov photons density. At high zenith angles, that is at high angles with respect to the vertical to the ground, the shower passes trough a larger atmosphere layer. Since the distance to the point of the maximum development of the shower increases, the photon density decreases with an increase of fluctuations. This effect is important especially for low energy primary gammas.

4.3.3 The observed Cherenkov light

Cherenkov radiation emitted by shower particles has a typical spectrum ranging from 300 to 600 nm. The emitted spectrum, plotted with the dotted line in Figure 4.9, is attenuated in the atmosphere. The main causes of the attenuation are the absorption and dispersion processes.

When a Cherenkov photon interacts with air molecules, it deviates from its trajectory. This **dispersion** process, also called Rayleigh dispersion, is the main cause of Cherenkov photons flux reduction. The cross section of this process is proportional to $1/\lambda^4$. Thereafter, UV photons are the most influenced.

Another important contribution to dispersion comes from the **Mie scattering**, which is due to the presence in air of aerosols (dust particles). The variability of the aerosol content of the atmosphere makes this scattering difficult to estimate; it is estimated that this contribution is just a few percent with respect to the Reyleigh diffusion.

Absorption processes, mainly due to atmospheric oxygen and nitrogen, become important at wavelength smaller than 200–240 nm. Thus, for Cherenkov photons these processes can be neglected.

A comparison between the emitted spectrum at 10 Km of altitude and the observed spectrum at 2.2 Km is plotted in Figure 4.9. From the Figure, the strong dependence of the absorption with the wavelength is clear. The observed spectrum shows a cut–off at high energies, in the UV range of the electromagnetic spectrum, where the absorption mechanism is more efficient. From this Figure it is also evident that the better range for the Cherenkov light detection is from 300 nm to 400 nm.

The total luminosity observed by a Cherenkov telescope is affected by the contribute of the *Night Sky Background (NSB)*. The NSB is mainly composed of light

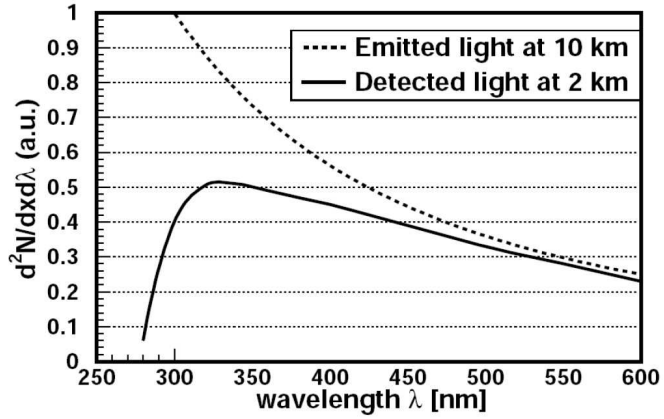

Figure 4.9: Effect of the absorption of Cherenkov light in atmosphere.

emitted by stars, diffuse galactic light, zodiacal light, fluorescence phenomena in high atmosphere and aurorae, together with artificial light (light pollution). Its intensity depends on the sky position: it decreases with increasing galactic latitude and zenith distance. NSB is one of the principal sources of noise in Imaging Cherenkov Telescopes.

Another very important factor that must be considered is the position of the *moon*. The presence of the moon in the sky, especially in its brightest phases, could dramatically deteriorate the Cherenkov light detection. MAGIC is the only IACT (Imaging Atmospheric Cherenkov Telescope) whose electronics have been conceived to take data also in moderate light conditions, i.e. in presence of moon light and during twilight[6].

The *earth magnetic field*, finally, tends to deviate the trajectories of atmospheric showers charged particles, especially the ones with lower energies. A 1 Gauss magnetic field, deviates a 1 GeV particle $\sim$1 mrad every 100 m. The effect is a preferential broadening along the NW direction. Thereafter, the magnetic field breaks the cylindric symmetry around the shower axis. Cherenkov radiation arrives at the detector distributed in an elliptical shape, with the major axis along EW direction. This effect is of particular importance when working in stereoscopic mode and at low energies. For a detailed reference, see Lombardi (2010).

4.4 The imaging technique

The identification of the differences between electromagnetic and hadronic cascades is one of the primary targets of γ–ray ground–based telescopes. The ratio of γ–rays to charged cosmic-rays is, in fact, really small ($\sim 1 \times 10^{-4}$), and a very powerful technique is needed to separate the gamma events from the dominating hadrons. A successful method is the imaging technique. The technique is based on the study of the images produced by Cherenkov photons produced by EAS when focused on a plane.

In this sense, IACTs can be considered as operators transforming arrival direction of photons in points of a *shower image*. The parabolic mirror surface reflects the incoming light and concentrates it into the camera, where parallel photons are focused into the same pixel, as shown in Figure 4.10.

Photons coming parallel to the telescope axes are focused in the central pixel

[6] In presence of moonlight, measurements are taken at 90 degrees distance, where the moon's contribute is minimum

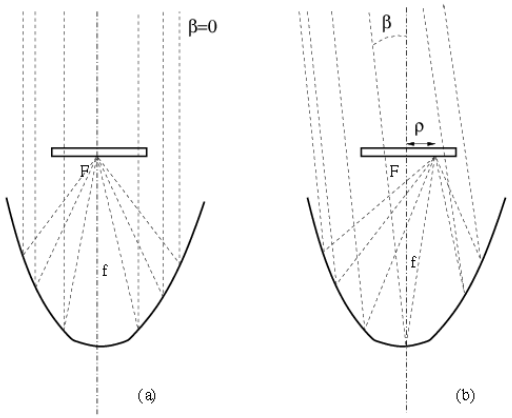

Figure 4.10: Focusing of photons in an IACT: the camera lies in the plane F, that is the focal plane of the mirror surface.

of the camera, image (a), while photons incident with an angle β respect to this plane are focused at a distance ρ respect to the camera center, image (b). In paraxial approximation:

$$\rho \sim \sin \beta f \sim \beta f \tag{4.16}$$

where f is the parabolic mirror surface focal.

Since Cherenkov photons produced in atmospheric showers reach the telescope with different incident directions, as described in Section 4.3.2, they are focused in different pixels, forming an image in the camera plane. The whole process of image formation is shown in Figure 4.11: Cherenkov photons distribute on a surface of *elliptical shape*, whose extremities represent the head and the tail of the shower, see Figure 4.8, while the inner pixels are the core of the shower.

The basic idea of the imaging technique is to use the shape and orientation of the images for extracting physical informations about the primary particle.

The elliptical image can be parametrized by a set of parameters, the *image parameters* indicated in Figure 4.12, which are the indispensable tool of the imaging technique for the characterization of the primary particle.

The main parameters used for our analysis are:

`size` is the total number of photo-electrons collected in the shower image. This parameter, for a fixed zenith angle of observation and impact parameter value, is roughly proportional to the energy of the primary particle.

`width`: Half width of the minor axis of the shower ellipse. This parameter is correlated with the *transversal development* of the shower. From Section 4.2.2 we know that hadronic showers have a larger transversal momentum with respect to the gamma ones, thus the `width` parameter could be important for the background suppression.

`length`: Half length of the major axis of the shower ellipse. This parameter is correlated with the *longitudinal development* of the shower.

`concn` (n=1,...,7): Fraction of photons contained in the n brightest pixels. It provides information about the shower core.

`leakage`: Fraction of the total signal contained in the outer pixels of the camera. This parameter is important because estimating the fraction of signal lost

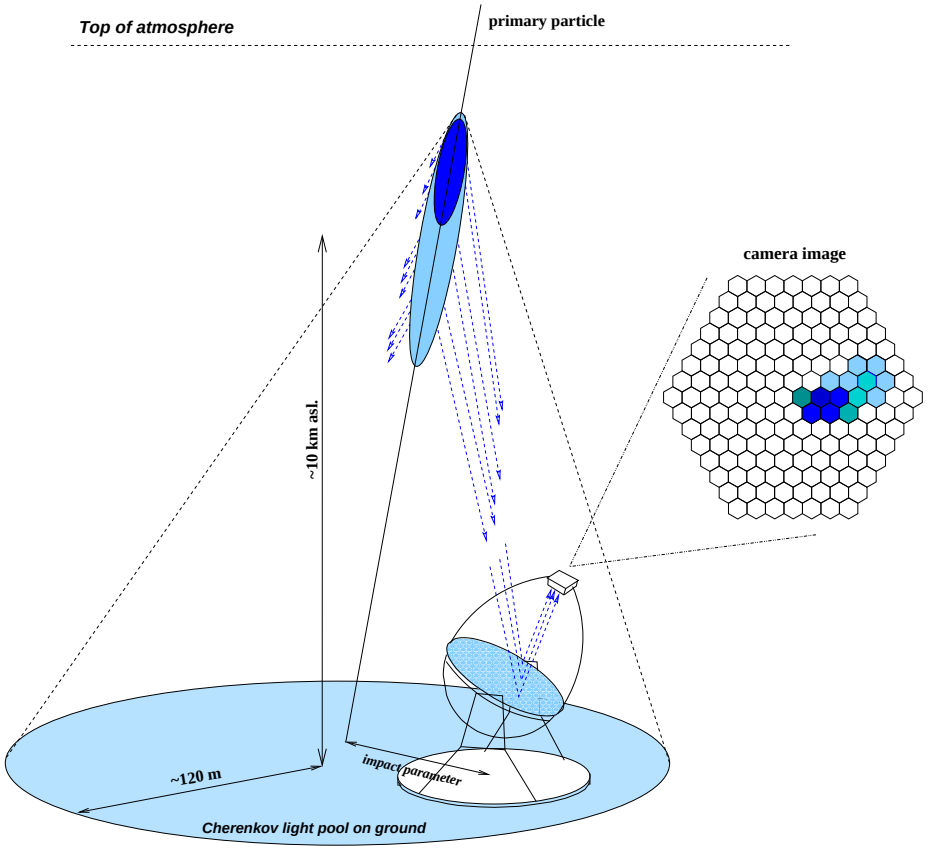

Figure 4.11: Schematics of the IACT detection of atmospheric showers. When the primary particle interacts in the top layers of the atmosphere, an air shower of particles is generated, characterized by a head (dark blue) and a tail (light blue). From the shower, the Cherenkov photons (blue lines) propagate to the ground at increasing angle with increasing shower development and atmospheric depth. The photons are reflected onto the focal plane at a distance from the center of the camera which reflects the shower impact parameter, i.e. the distance from the telescope axis. The camera is pixelized and the image can be reconstructed. Courtesy of Lopez Moya (2007).

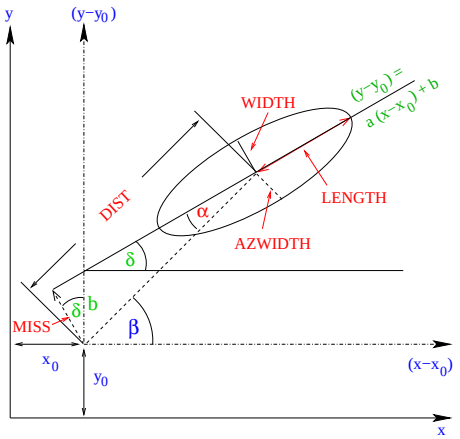

Figure 4.12: Main image parameters.

because of too large impact parameter allows the rejection of those images that cannot be correctly parametrized.

`alpha`: Angle between the major axis of the ellipse and the direction determined by the image center of gravity and the reference point (the nominal position

on the camera of the candidate γ–ray source). Images induced by primary gammas have this parameter close to zero because of their preferential direction, while images due to hadrons have a random distribution of `alpha` (the direction of hadrons is nearly isotropic). For this reason, this is one of the most powerful parameter characterizing γ–like events, in case of point–like sources.

`dist:` Distance of the shower center of gravity with respect to the reference point. It provides information about the distance to the shower maximum and the impact parameter. Thus, it is very important for the energy reconstruction of the primary particle.

`m3long:` It is the third moment of the image along its major axis. It measures the asymmetry of the image, and can be given a sign which depends on the source position, after which it becomes a useful parameter for selecting γ–rays from a point–like source.

In addition to the classical Hillas parameters described above, the MAGIC collaboration has recently developed new parameters based on timing informations (Aliu et al., 2009), which improved significantly the performance of the telescope. The two new parameters are:

`time gradient:` this parameter measures how fast the arrival time changes along the major image axis. The pixel coordinates are projected onto this axis, reducing the problem to one dimension. The sign of this parameter is positive if the arrival time increases as we move away from the location of the source on the camera, negative otherwise. It is therefore a parameter which depends on the position of the candidate γ–ray source.

`time RMS:` the root mean square of the arrival times of all pixels belonging to the image after cleaning. It measures the spread of the arrival times irrespective of the pixel position in the camera.

Once the images are parametrized, they are tagged as background–like (that means with good approximation hadron–like) or γ–like, depending on the values of their parameters.

This procedure, called *gamma–hadron separation*, is based on the fact that gammas and hadrons are characterized by different values of these parameters. For example, when data are collected and the telescope points directly to the source, we expect that images induced by γ–rays have their major axis pointing towards the source position on the camera. Hadrons, instead, have randomly distributed arrival directions. Thus, the `alpha` distribution for hadrons should be flat, while that for gammas should be peaked at low angles.

A complete treatment of the gamma/background separation will be done in the next Chapter. The incoming direction of the primary particle, together with its energy, can be also estimated from these parameters.

In the case of multiple telescopes systems, usually each detector is sinchronized and operated together with the others, in the so–called *stereoscopic mode*. Hence, the showers are seen under different angles by each telescope, and the process of characterization of the primary particle is largely simplified. When two or more telescopes register the same shower, the determination of the incoming direction of the primary particle becomes straightforward, see Fig. 4.13. Moreover, the background suppression at trigger level is much more efficient.

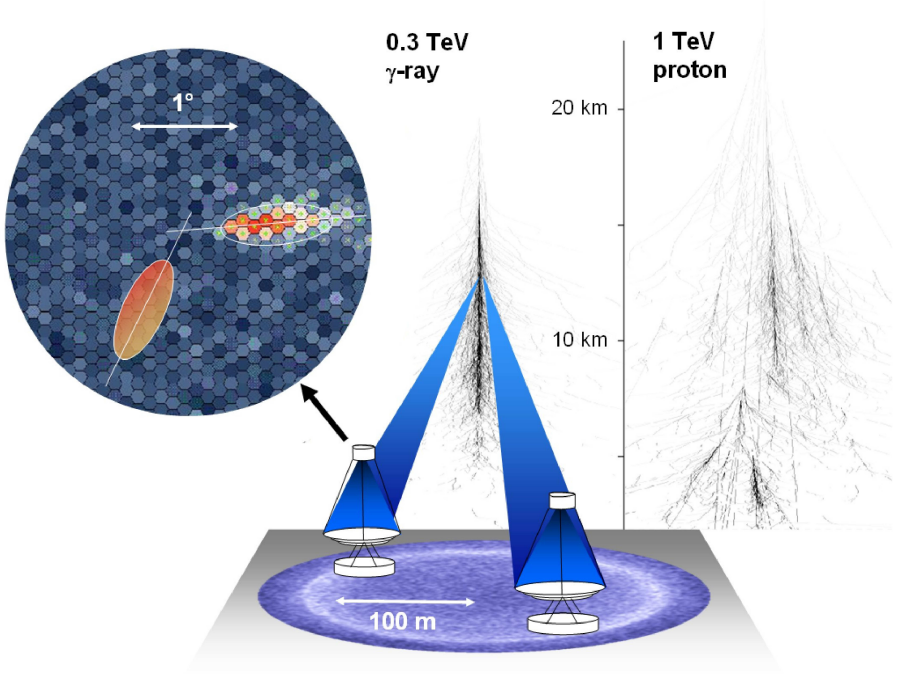

Figure 4.13: Process of image formation for a sterescopic IACT system. Plot adapted from Hinton and Hofmann (2009).

4.5 Design of an IACT

As stated before, the primary scope of an IACT is that of collecting shower images, focusing the Cherenkov light emitted by atmospheric shower particles during their passage through the atmosphere. The necessary hardware elements for this kind of instruments are: a rotating structure, essential for the tracking of γ–rays emitter candidates, a reflective surface, which focuses the light, a camera, where the light forming the image is focused and the signal registered, a trigger, producing a first rough background rejection, and a data acquisition system, which provides the signal storing for the subsequent analysis.

During the design phase of an IACT, different choices can be made, depending on the features that one wants to optimize and the kind of physics at which the instrument is aimed (Tescaro, 2010). Generally speaking, galactic astrophysical sources are characterized by hard spectra of γ–rays, even at high energies, whereas extragalactic AGNs have typically softer spectra which might allow their detection only at relatively low energies (because of the flux attenuation due to the EBL and also due to intrinsic high energy cut-offs foreseen by some of the emission models). Moreover, the galactic center, i.e. the region of the sky where the objects of our Galaxy are more concentrated, is visible at favourable conditions only from the Southern hemisphere.

An IAC telescope is firstly characterized by its *sensitivity*: the minimum detectable γ–ray flux in a given observation time. Two different sensitivities are usually considered: the integral and differential sensitivity, which account for the integral and differential photon energy flux, respectively.[7] The sensitivity is re-

[7]The integral sensitivity is measured in units of $[L]^{-2}[T]^{-1}$, while the differential in $[L]^{-2}[T]^{-1}[E]^{-1}$.

lated, first of all, to the capability of an IACT to discriminate the showers induced by γ–rays from background showers (induced by charged CRs). Hence, the most efficient way to improve it is to operate in stereoscopic mode. The use of two or more instruments which look at the same events increases the capability of characterizing the shower and lead to a better γ/hadron discrimination. Moreover, the use of a trigger system which registers the signal only if it is seen by more than one telescope, largely reduces the rate of accidental triggers (not induced by a shower).

Another important feature of IACTs is their *energy threshold*, which is the energy above which the telescope can efficiantly detect γ-rays. Typical value is around hundreds of GeV. Following Longair (1992), for this kind of telescopes, it can be written as:

$$E_{th} \propto \sqrt{\frac{\phi \Omega \tau}{\epsilon A}} \tag{4.17}$$

with A the mirror surface, ϵ the light detection efficiency (which includes the mirror reflectivity and the efficiency of the light detectors), τ the integration time of the Cherenkov signals, Ω the solid angle subtended by the collection mirror. The background flux from the night sky, ϕ, also enters in the formula as parameter since it varies from site to site. Equation 4.17 suggests that a low energy threshold telescope needs a large mirror surface (with high reflectivity), high efficiency light detectors, small FoV and fast readout electronics to minimize the background light integration time.

Finally, another important parameter to be taken into account for the design of an IACT is its angular resolution: the accuracy in the reconstruction of the primary incoming direction. Typical value is of the order of 0.1°. As for the sensitivity, the use of multiple telescopes improves significantly this parameter.

4.5.1 IACTs in the world

Figure 4.14 illustrates the location of the three major IACTs: MAGIC, H.E.S.S. and VERITAS, located respectively in La Palma (Canary Islands), Namibia (Africa), and Arizona (U.S.).

The main characteristics of the instruments (Colin et al., 2009; Chaves, 2009; Holder, 2007), are listed in Table 4.2: while H.E.S.S. and VERITAS are arrays of four telescopes with relatively small reflective surfaces, MAGIC is a 2-telescopes system with a large mirror area.

Name	Location	N_{Tel}	Ref. Surface Diam.	E_{th}	FoV
MAGIC	N	2	17 m	60 GeV	3.5°
H.E.S.S.	S	4	12 m	100 GeV	5°
VERITAS	N	4	12 m	100 GeV	3.5°

Table 4.2: Main Characteristics of three main IACTs in the world.

Thanks to the large field of view coupled with its favourable location, H.E.S.S. is the ideal instrument for the observation of the galactic center region, while MAGIC and VERITAS are more indicated for other galactic regions or extra-galactic nothern sources, see Fig. 4.15.

The three collaborations have already started to work on a common project for the development of next generation of IACTs. The current plan involves the

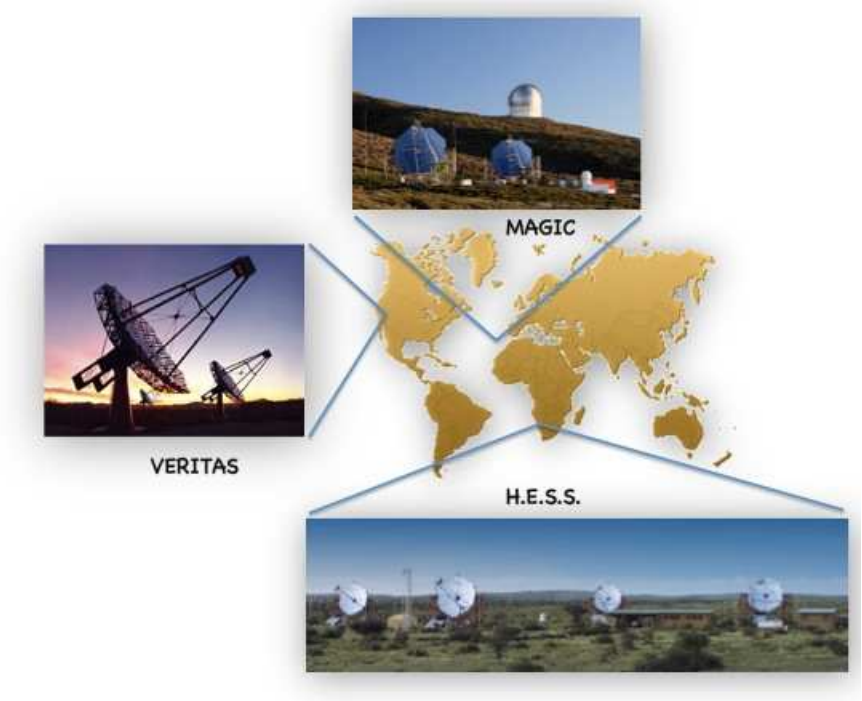

Figure 4.14: Location of the three major IACTs: MAGIC, H.E.S.S. and VERITAS.

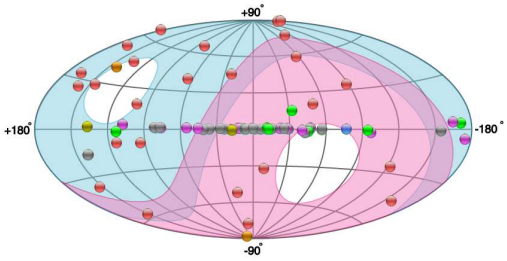

Figure 4.15: Comparison of the visibility of MAGIC (Northern emisphere) and H.E.S.S. (Southern emisphere). From http://tevcat.uchicago.edu/.

construction of a giant array of Cherenkov telescopes, called Cherenkov Telescope Array (CTA), of different sizes, see Fig 4.16. The main purposes of the project include the attainment of a low energy threshold and a high sensitivity, one order of magnitude better than the current generation of IACTs (CTA Consortium, 2010).

At the moment, many different designs are being studied, and we are close to

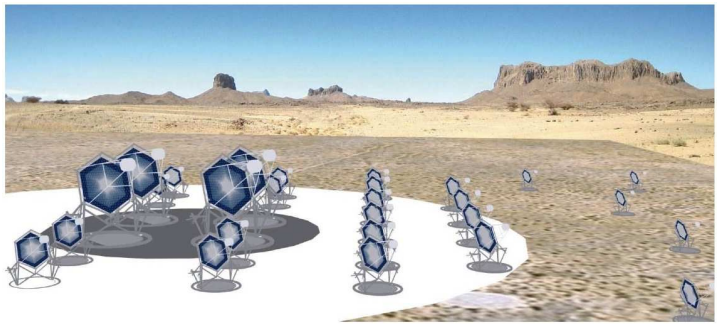

Figure 4.16: A possible realiziation of the CTA, from CTA Consortium (2010).

Figure 4.17: The site MAGIC telescopes, in La Palma, with MAGIC I on the left, MAGIC II on the right, close to the counting house. In the background the Gran Telescopio Canarias, on the right, and the Telescopio Nazionale Galileo, on the left. Picture from R. Wagner.

the prototype construction phase[8].

4.6 The MAGIC Florian Goebel telescopes

Since fall 2009, MAGIC is a fully operative stereoscopic imaging Cherenkov telescopes system. It is installed at the Roque de los Muchachos on the Canary Island of La Palma at 2200 m altitude. The telescopes have been recently renamed *MAGIC Florian Goebel Telescopes* in memory of our colleague and friend, the project manager of MAGIC II, who accidentally died in 2008.

A group of more than 150 people, among physicist, engineers and astronomers, called the MAGIC Collaboration, is working for the set up, mantainance and data analysis of the two telescopes. They come from different countries spread all over Europe, mainly from Germany, Spain and Italy. Figure 4.17 shows the MAGIC telescopes site, with the two telescopes, located at approximatively 85 m away, and the counting house, hosting the electronic and the datataking rooms.

MAGIC I overview

Between August 2004 and November 2009, MAGIC (Major Atmospheric Gamma Imaging Cherenkov telescope) was the largest Cherenkov telescope of the world, with its 17 m of diameter, operating in single telescope mode.

Thanks to its unique characteristics (low energy threshold, light structure and fast electronics), it has been the suitable instrument for the observation of a wide range of objects. In particular, during its five years of operation, its highlight results have been:

- The discovery of a significant γ–ray emission from 8 AGNs. One of the most important was probably the FSRQ 3C 279, so far the most distant object detected at VHE (Albert et al., 2008c).

[8]See for details: http://www.cta-observatory.org .

- The discovery of a variable emission from the microquasar object LS I +61 303 (Albert et al., 2006c).

- The discovery of a pulsed signal from the Crab Nebula pulsar (Aliu et al., 2008), thanks to the develpment of a special trigger, which ensured an energy threshold of 25 GeV.

Moreover, MAGIC carried out other important observation campaigns, which include the observation of GRBs, such as the one described in Aleksić et al. (2010a), and the search for DM from promising objects, such as the dwarf spheroidal galaxy Draco (Albert et al., 2008b).

MAGIC II is the second telescope of the MAGIC array and is basically an improved version of MAGIC I. In order to minimize the time and the resources required for design and production, in fact, the second MAGIC telescope is in its most fundamental parameters a clone of the first telescope.The improvements reside in the camera and in the readout. Since its start-up, MAGIC II has almost always worked in stereoscopic mode. For this reason we don't have any specific result related to this instrument alone.

4.6.1 The *stereo* "vision"

The big technical improvement adopted by the MAGIC Collaboration when passing from the mono to the stereo system is evident: in less than one year, four new sources (4C +21.35, MAGIC J2001+435, B3 2247+381, NGC 1275)[9] have been easily detected within few hours of observations, thanks to the good sensitivity achieved by the instrument.

Figure 4.18 shows the comparison between the integral sensitivity of MAGIC I compared to that achieved with the upgraded stereoscopic system. The improvment at all energies is evident.

[9]For an updated list of TeV instruments discoveries, see: http://www.mppmu.mpg.de/∼rwagner/sources/.

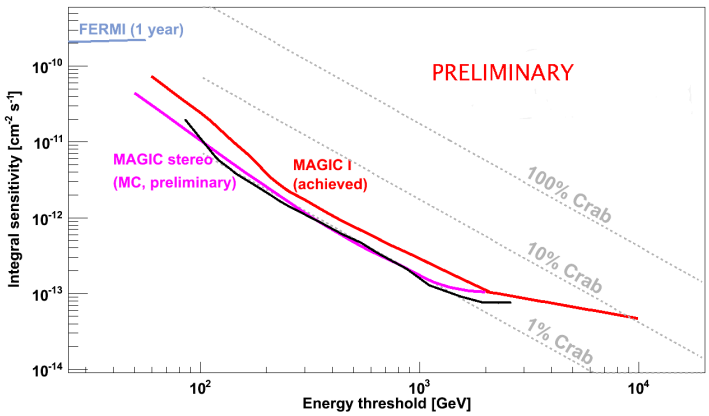

Figure 4.18: Comparison between the integral sensitivities of MAGIC in mono and stereo mode.

4.7 Hardware components

In the following Sections, the main harware characteristics of the MAGIC telescopes are outlined. Since the second instrument has been built 5 years after the first one, some technical solutions adopted for MAGIC II are different. In particular, the camera and readout system have been changed in a substantial way, as introduced above. Regarding other details, the second telescope is a clone of MAGIC I. When not explicitely mentioned, the details explained should be considered valid for both instruments.

In Summer 2011, an upgrade of MAGIC I is scheduled: the camera and readout system will be changed to match the MAGIC II components. After this upgrade, the two instruments will be almost identical, with a greate advantage for the data analysis and simplicity of manteinance.

4.7.1 Structure and drive system

The structure which holds the mirrors, in both telescopes, is a very lightweight carbon fiber space frame, which permits very fast movements of the instrument needed for the GRBs observation: either telescope can do a complete turn–around in less than 45 s. By design, in fact, MAGIC was conceived as a fast pointing system: lightness was one of the goals achieved during the telescope construction.

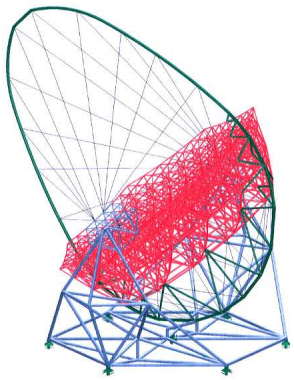

Figure 4.19: MAGIC frame.

The carbon fiber guarantees a good resistance to atmospheric agents, particularly aggressive in the island. The total weight of the frame is 5.5 tons. The tubes are joined with aluminum knots as shown in Figure 4.20(c).

MAGIC telescope have an *alt-azimuth* mounting: the whole structure can move in the azimuth and in the altitude directions. There is an access tower in front of the instrument which permits the experts to access the camera both from the rear and the front part. The camera is sustained by a metallic arch, which is supported by narrow steel cables connected to the main structure. These cables are narrow for minimizing the surface obscuration.

The structure is mounted on a circular rail of 19 m ⌀. Both telescopes can be moved from $-80°$ to $105°$ in declination and $450°$ in azimuth. The camera is located at a distance of around 17 m from the reflector, and is carried by a single aluminum tubular arc. The weight of the camera is around half a ton, and the small bending, unavoidable during the telescope tracking, is corrected via a re-orientation of the mirrors. Two motors control the motion in azimuth and one motor the zenith motion with a maximum power consumption of ~ 7 kW per motor, see Figure 4.20(a), 4.20(b). The angular positions are controlled by absolute shaft-encoders of 14-bit precision/360°. In addition, a starguider camera, shown in Figure 4.20(d), mounted at the centre of the reflector, monitors the positioning of the telescope by viewing both the camera of the telescope and the corresponding section of the sky star-field Mirzoyan et al. (2007). The lightweight structure allows for very fast repositioning of the telescope to any position in the sky within ~ 30 s. This challenging feature was designed to instantly react to Gamma–Ray Burst (GRB) alerts from dedicated satellites detecting GRBs in the

(a) Azimuth motor

(b) Zenith motor

(c) CFRP tubes

(d) SBIG camera

Figure 4.20: The mount and drive system. In figure (*a*) one can see the azimuthal motor, mounted on the circular rail. In figure (*b*), the zenith motor drives the elevation and is mounted on the aluminum arc. Figure (*c*) shows the joints between the tubes and the aluminum knots and figure (*d*) shows the open box of the SBIG camera, which controls the active mirror repositioning system. From Doro (2009).

KeV/MeV domain.

4.7.2 Reflective surface

The overall shape of the reflector dish is parabolic to minimize the time spread of the Cherenkov light flashes on the camera plane. This is of particular importance to mantain the temporal evolution of the shower image. Moreover, the preservation of the time structure of the Cherenkov flashes is important to allow the reduction of the signal integration window (both in the trigger and in the analysis), reducing the number of random coincidence trigger due to the night sky background, and also to increase the signal to noise ratio.

The parabolic tessellated reflector consists of 247 individually movable $1\,\mathrm{m}^2$ mirror units, which are adjusted by an Active Mirror Control (AMC) system depending on the orientation of the telescope. The position of panels is on–line corrected, so that the light emitted by lasers situated in the center of each panel is correctly positioned on the camera plane. The radius of curvature of each mirror is adequate for its position on the paraboloid. The total area of the reflecting surface is then 234 m^2.

Three different mirror types are installed:

1 m^2 aluminum mirrors: motivated by the demand of keeping the weight of the telescope as small as possible, the MAGIC Collaboration adopted this

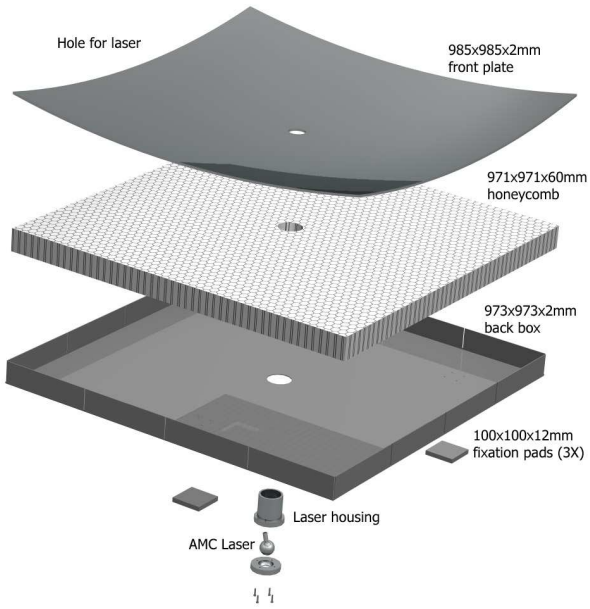

Figure 4.21: Design of the MAGIC II aluminum mirrors. The structure is a sandwich of an aluminum skin $985 \times 985 \times 2$ mm made highly reflective by surface diamond milling, a honeycomb hexcell panel $971 \times 971 \times 60$ mm to provide rigidity, and an aluminum back box $973 \times 973 \times 61.9$ mm (2 mm thick) to close the structure. In addition, a hole is drilled at the center to house the laser for mirror repositioning control and three aluminum inserts inside the panel are inserted for mounting. Schematic from M. Zago.

inovative kind of technology. Aluminum mirrors, whose structure is sketched in Fig. 4.21, are composed of an aluminum box open on the upper side where an honeycomb aluminum structure is inserted in order to guarantee the necessary rigidity of the mirror. A thin aluminum plate is located on the top of the mirror and glued to the honeycomb. The upper side of the plate is finally polished using a special diamond milling machine which makes the surface reflective. The reflecting surface, spherically shaped, is protected by a final layer of quartz-based material which coats the mirror and protects the surface from scratches and the aluminum from oxidation. The reflectivity has been measured to be around 87%, while the radius of the circle containing 90% of the spot light is of the order of 30 mm. The weight of a mirror of this type is of 3.5 kg. Out of the 247 mirror tiles, in MAGIC II 143 are aluminum mirrors.

0.25 m^2 aluminum mirrors: are analogous to the $1\,m^2$ mirrors described in the previous point, except for the dimensions. MAGIC I telescope was originally built with this kind of mirrors, located four per panel, as shown in Fig. 4.22. The passage to 1 m^2 mirror reduced cost and manpower (it is no longer necessary to align all four mirrors individual tiles inside one panel before installing the panels at the telescope).

1 m^2glass mirrors: the remaining 104 mirror tiles of MAGIC II are produced as a sandwich of 2 mm glass plates around a aluminum honeycomb layer using a cold slumping technique. The frontal glass surface is coated with a reflecting aluminum layer and a protecting quartz coating. This kind of

Figure 4.22: MAGIC I reflective surface. The mirrors are grouped in fours into panels. At the center of each panel there is a laser that allows for a fine focusing, through the on–line *Active Mirror Control*.

mirrors shows a PSF which almost doubles that of the aluminum mirrors but the light spot is still well inside the size of a camera pixel (Cortina et al., 2009).

4.7.3 Camera

The MAGIC camera is a key element to improve the gamma sensitivity and γ/hadron separation.
The camera of MAGIC I is 1.5 m diameter, covers 3.5° of Field of View (FoV), and is composed of 577 pixels. Each pixel collects the incoming light by a high Quantum Efficiency (QE) PhotoMulTiplier (PMT): 577 hemispherical tubes, out of which 397 are 0.1° FOV 1″ diameter surrounded by 180 0.2° FOV 1.5″ diameter. The pixels are ordered in a hexagonal board.

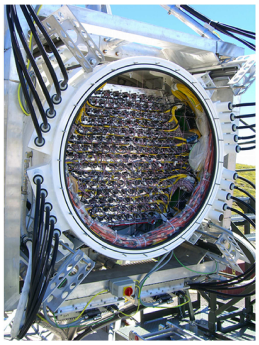

Figure 4.23: MAGIC II camera.

The use of two different PMT sizes is mainly due to a compromise between the telescope performances and its cost. A picture of the MAGIC I camera structure is shown in Fig. 4.24, left panel. On the front side the pixels are equipped with Winston cone type light guides to minimize light losses due to the dead area between the PMTs and to reject large angle background light. Both the input and the output pupils of the light catchers have a hexagonal shape.

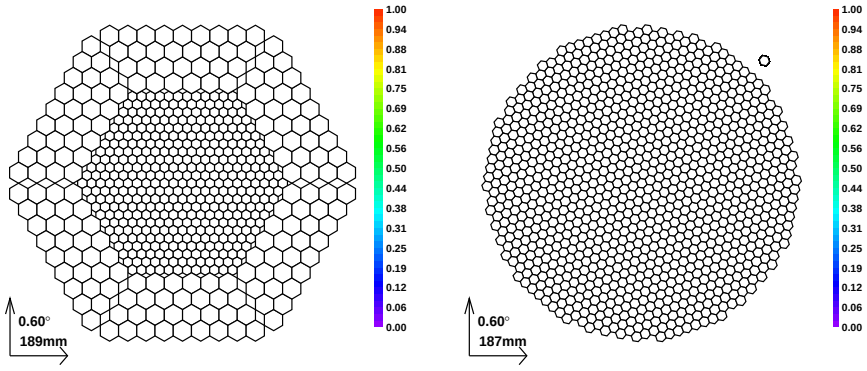

Figure 4.24: The two cameras of MAGIC telescopes.

The typical time response FWHM of each PMT is below 1ns. The photocatode QE reaches up to 30% peak value. Each PMT is connected to an ultrafast low-noise transimpedance pre-amplifier. The camera has two lids which open during

data–taking and protect the camera from daylight during the day. In addition, there are the water and air cooling and heating systems, which prevent the camera from getting too hot and reaching the dew point. The whole camera housing can be moved forward and backward with respect to the mirror dish in order to get different focuses, ranging from some meters to infinity.

MAGIC-II camera, Fig. 4.24 right panel, has a circular shape and the same field of view of the camera of MAGIC I. It is equipped uniformly with 1039 pixels of 0.1°, grouped in different clusters. Each cluster comprises seven pixels sorted in a hexagonal configuration. The modular design allows an easier control and maintenance of the camera. Besides the larger number of pixels, the ulterior improvement of the second camera is the installation of increased QE PMTs. The Hamamatsu R10408 6 stage PMTs with hemispherical photocathode typically reach a peak QE of 34%, see Fig. 4.25. The typcal response is of the order of ∼1 ns FWHM.

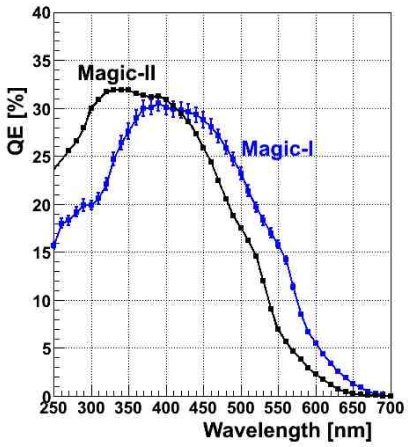

Figure 4.25: QE of Magic II PMT compared to the one of MAGIC I. From Borla Tridon et al. (2009).

The flexible cluster design allows field tests of new technology within the MAGIC II camera without major interference with the rest of the camera. For example 7-pixel modules in the outermost ring of MAGIC-II have been equipped with HPDs (high QE hybrid photo–detectors) and read out by the acquisition electronics. These HPDs feature peak QE values of 50%.

4.7.4 Readout chain

PMT signals are amplified by ultrafast and low-noise transimpedance pre-amplifiers in the camera housing. The amplified analog signals are transmitted via optical fibers using Vertical Cavity Surface Emitting Lasers (VCSELs, $\lambda = 850\,\mathrm{nm}$). Transmission over optical links drastically reduces the weight and size of the cables and protects the Cherenkov signal from ambient electromagnetic noise in the line.

Since the γ–ray signals are very short in time, a very fast readout electronics is required. The pulses have to be first processed to generate the trigger signal and then digitized at ultra-fast speed. Afterwards they have to be stored for the subsequent analysis. In the receiver board the signal is converted back to electric and, if passing the trigger requirements, digitized.

The digitization system is also referred as the FADCs (Flash Analog to Digital Converters) in virtue of the high speed of digitization. Pulses are sampled at the speed of 2 GSample/s. Both the MAGIC I and MAGIC II readouts digitize

at the same sampling speed but with very different electronics. A custom made multiplexed system (MUX) which uses commercial FADC for the final digitization is used in MAGIC-I, see Fig. 4.26, whereas a completely new approach is used in MAGIC-II. The new 2 GSamples/s digitization and acquisition system for the

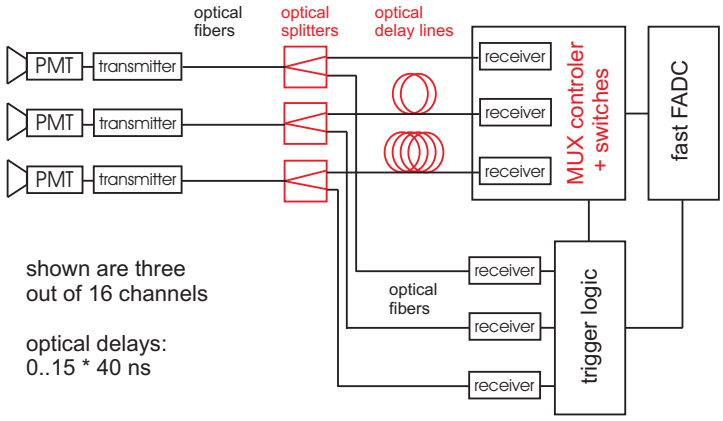

Figure 4.26: Readout system scheme for MAGIC I (F. et al., 2007).

second telescope is based upon a low power analog sampler chip called Domino Ring Sampler. The analog signals are stored in a multi capacitor bank that is organized as a ring buffer, in which the single capacitors are sequentially enabled by a shift register driven by an internally generated 2 GHz clock locked by a PLL to a common synchronization signal. Once an external trigger has been received, the sampled signals in the ring buffer are read out at a lower frequency of 40 MHz and digitized with a 12 bits resolution ADC.

4.7.5 Trigger system

The *trigger* of each telescope is a multi level decisional system. Its purpose is to set out the beginning of the image acquisition process simultaneously with the shower detection.

The trigger system should discriminate the signals arriving from Cherenkov flashes from the accidental fluctuations of the light of the night sky. Therefore, it selects very fast events that happen in compact regions of the camera. Operationally, the trigger system is based on a compact next neighbor logic. In MAGIC I, the trigger area covers 1.9° diameter FoV, while the uniform camera design of MAGIC II allows an increased trigger area of 2.5° diameter FoV, as sketched in Figure 4.27. This increases the potential to study extended sources and to perform sky scans. Moreover, it enhances of ∼15 % the efficiency of point–like sources observation.

The MAGIC trigger has the following decisional levels:

level zero trigger (L0T): this is the first decisional level. Its task is to check if the signal in every PMT is greater than a fixed threshold. If this happens, a very fast digital signal is generated with a standard duration of $\sim 3ns$ (the typical duration of a Cherenkov flash). A pixel is considered illuminated when its signal passes the level zero trigger.

level one trigger (L1T): this level requires a temporal coincidence (multiplicity) of the signals selected in the level 0. It's then introduced a *topology*,

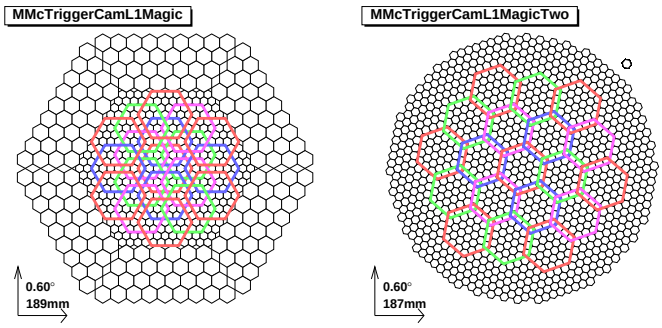

Figure 4.27: The two trigger systems of the MAGIC telescopes and their trigger areas.

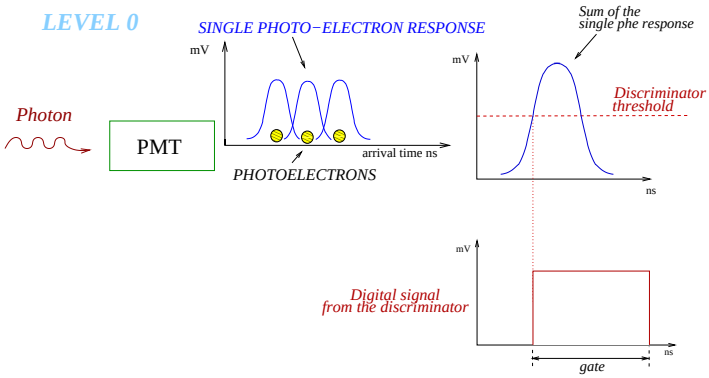

Figure 4.28: Schematic view of the level 0 trigger.

with the aim of combining temporal and spatial informations. The condition adopted is to accept only those signals which have a certain amount of adjacent illuminated pixels, and in a *compact* configuration (meaning that if a pixel is taken away, the others are still connected). This topology is called CCNN (Close Compact Next Neighbors). This trigger level was developed by the Padova MAGIC group.

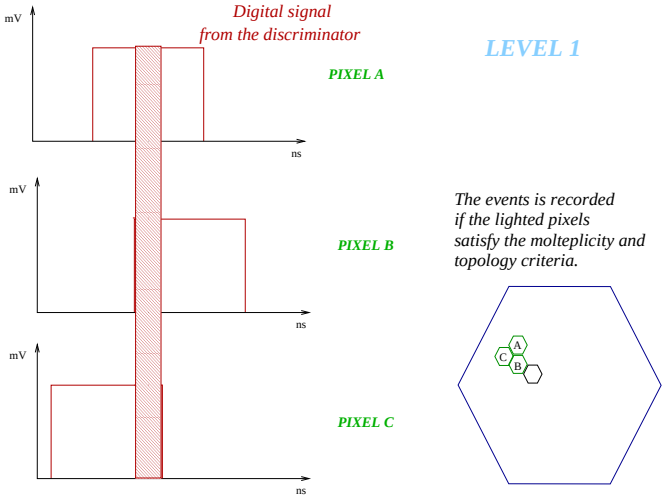

Figure 4.29: Schematic view of the level 1 trigger.

level two trigger (L2T): can be used to perform a rough analysis and to apply topological constraints on the event images. It consists of a set of Look Up Tables, enabled from L1, and acting on the trigger cells with a tree–structured set of programmable fast memories. Up to now the second level trigger has been used just in flag-mode: the events are tagged with L2 selection criteria but not rejected yet.

level three trigger (L3T): used when the two telescopes are operated in stereo mode. This coincidence trigger between the two telescopes rejects events triggered by only one telescope. In order to minimize the coincidence gate in the level 3 trigger, the triggers produced by the individual telescopes are delayed by a time which depends on the pointing direction. This reduces the overall trigger rate to a rate which is manageable by the data acquisition system.

Starting in 2007, an additional trigger can run in parallel with the standard next neighbour trigger in first telescope: the *sumtrigger*. This trigger operates on the analog sum of groups of 18 pixels and has allowed to lower the trigger threshold of the MAGIC telescope by a factor of two to 25 GeV.

After passing the trigger conditions, events are digitized using an FADC, and stored. The time and the trigger information for each event are also recorded by dedicated digital modules which are read out together with the FADC modules.

4.7.6 Other instrumentation

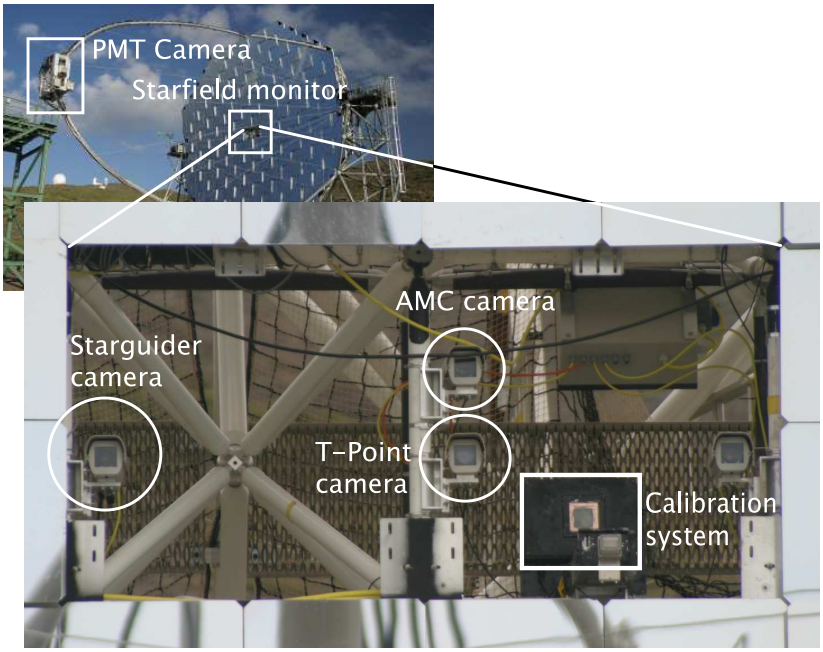

Figure 4.30: MAGIC-I central dish instrumentation. Similar devices are mounted also in MAGIC II. From Errando Trias (2009).

Calibration system

The calibration of the signals from each channel is done to translate the information recorded by the FADCs into incident light flux in the camera. This is

accomplished by calculating a conversion factor between the number of recorded FADC counts and the number of photo–electrons (`phe`) in the PMT. The final calibration must be in terms of incident photons, so that also the different quantum efficiency of the PMTs is taken into account. The MAGIC calibration system provides fast light pulses at different wavelengths and variable intensity in order to calibrate the whole dynamic range of the camera photosensors and their readout chain.

The system consists of a box located at the center of the telescope mirror dish, see Fig. fig:calibration, which houses 64 LEDs emitting at three different wavelengths: 370nm (UV LEDs), 460nm (blue LEDs) and 520nm (green LEDs). The light pulses have about 3-4 ns FWHM duration. Fastness is important for the calibration pulses in order to correctly resemble the real pulses from a shower.

The calibration of the signals recorded by each pixel of the camera is done basically in two steps: first a relative calibration and then an absolute calibration. The relative calibration equalizes the response of different channels when exposed to the same input signal. An absolute calibration is needed in order to convert the signal recorded by a pixel in FADC counts into physical quantities more related to the flux of photons arriving at the camera. Details about the calibration of MAGIC signal can be found in Gaug (2006).

Starguider system

The accuracy of the pointing is guaranteed by the starguider system. It is appointed to monitor the exact pointing position and to correct for a possible mispointing. This is done though a sensitive CCD camera mounted on the center of the mirror dish (see Figure 4.30. The starguider camera points to the camera of MAGIC but its FoV is large enough (4.6°) to see also directly some of the stars in the FoV of the MAGIC camera. The actual pointing position can then be reconstructed by software and recovered. The starguider information is actually used off–line during the data analysis to correct for possible mispointings during the observations.

4.8 MAGIC data taking

MAGIC collects the data during night; the sunlight, in fact, is a dominating background that makes it impossible to register the faint Cherenkov flashes, centered in the optical wavelenghts. Therefore, the ideal data-taking is during dark nights; however, MAGIC electronics have been conceived to take data also in moderate light conditions, such as in presence of moon light and during twilight.

The weather conditions are an essential factor which influence the quality of MAGIC datasets. Main causes of bad–quality data are the presence of clouds in the sky, high humidity, wind and *calima*, the sand from the desert typical for Canary islands.

Since fall 2009, MAGIC is a stereoscopic system; the standard data-taking procedure is therefore the stereo observation mode, in which the two telescopes observe at the same time, and only events seen by both telescopes (under a different viewing angle) are recorded by the L3T. Each telescope can take data individually, in the so-called mono observation mode. This was the standard data-tacking mode of MAGIC I before the stereo upgrade.

Due to the reduced field of view, MAGIC can only be operated with the tracking approach, in which each telescope follows a given position in the sky while recording air shower images. There are two different data-taking modes: the *On/Off* mode, in which the signal and background events are collected separately pointing to different sky regions, and the *wobble* mode (Fomin et al., 1994), in which each telescope is alternated every 20 minutes between two sky positions at 0.4° offset from the source. This technique allows On and Off to be collected simultaneously. Hence, the required observation time for one source is almost halved if we observe in wobble mode: this is the reason why MAGIC in the last years has been observing almost all the sources in this way.

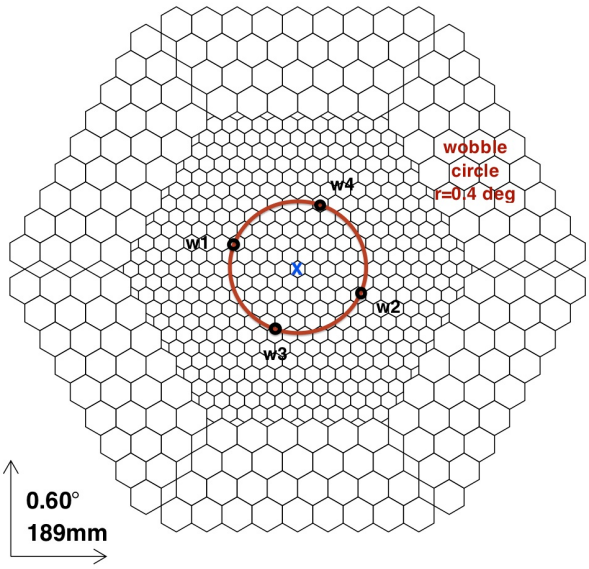

Figure 4.31: Geometry of the wobble mode. The W1, W2, W3 and W4 positions are marked, as well as the camera center (cross).

Figure 4.31 shows the geometry of the wobble data-taking mode: we have two positions, called wobble-1 (W1) and wobble-2 (W2), and two additional positions, named W3 and W4. All these regions are located at a distance of 0.4° from the camera center. When we track a source in wobble mode, we point it not at the camera center, but alternatively in the W1 and W2 position, and we switch from one pointing position to the other every 20 minutes. Therefore the source location in camera coordinates the wobble center (W1 or W2), while it is the camera center in case of On/Off mode of observation. In this way, when we extract the signal we can extract the Off from the remaining region. For example, when we point the source in W1, W2 can be used for the background extraction. The additional two regions can be used to extract additional Off, on order to increase the background statistics, and consequently increase the source significance.

L' essentiel est invisible pour les yeux

Le Petit Prince – Antoine de Saint-Exupéry

5

VHE γ-rays from 5 years of MAGIC observations of PG 1553+113

The BL Lac object PG 1553+113 was discovered as VHE γ–rays emitter in 2006 by the MAGIC and H.E.S.S. Cherenkov Telescopes. After the discovery, MAGIC regularly observed the source in order to monitor its activity. In this Chapter the analysis of the data taken from 2007 to 2009 is presented and the corresponding results combined with previous observations.
We describe in detail the signal search, and present the main physical results related to the differential and integral spectrum analyses. Power law fits of the differential energy spectrum of the individual years are compatible with a steady mean photon index. In the last three years of observations, the flux level above 150 GeV shows a marginal variability, in the range from 4% to 11% of the Crab Nebula flux. Simultaneous optical data also show only a modest variability which seems to be correlated with the VHE γ–ray variability. In addition, we perform a temporal analysis of all available *Fermi*/LAT data of PG 1553+113 above 1 GeV, which reveals a clear variability in the 2008–2009 sample. Finally, we present a combination of the mean spectrum measured at VHEs with archival data available for other wavelengths. The mean spectral energy distribution can be modeled with a one–zone SSC model, as usual for BL Lac objects, which gives the main physical parameters governing the VHE emission in the blazar jet.

Part of this work has been published in Aleksić et al. (2011).

5.1 The source PG 1553+113 and its detection as VHE γ–rays emitter

PG 1553+113 is a BL Lac discovered by Green et al. (1986) during an optical survey. It is located at Ra 15 h 55 m 43.0 s and Dec +11 d 11 m 24 s, and can be observed from the Northern hemisphere. The large X-ray to radio flux ratio makes this source a typical HBL. While the radio flux is quite weak and stable, at the level of a few tens of mJy at 5 GHz, the X-ray emission is very strong and variable. A comparative study among many data collected by various satellites from 1998 to 2006 (BeppoSax, XMM/*Newton*, *Suzaku*, *Swift* and RXTE), carried out by Reimer et al. (2008), has shown a peculiar stability of the X-ray spectrum despite a variability factor larger than 5. Regarding the optical range, the flux in the

R band was monitored by the Tuorla Observatory Blazar Monitoring Program[1] (Takalo et al., 2007) starting from 2005, and so far shows only modest variations changing from 1 to 8 mJy. Indeed, the synchrotron peak of this source is located between the UV and X-ray bands (Nieppola et al., 2006), as shown in Fig. 5.1.

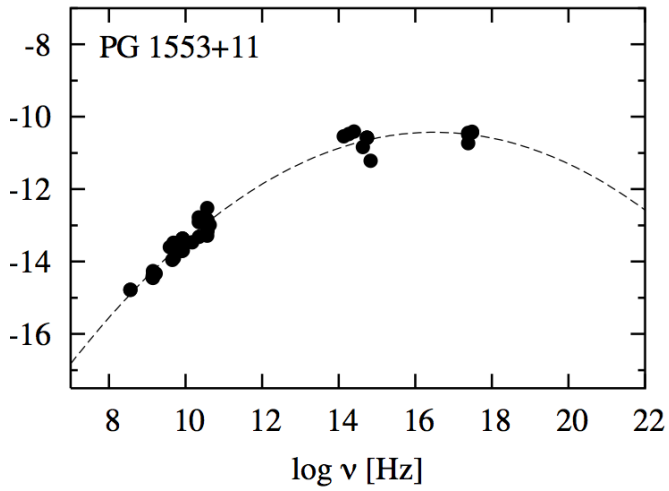

Figure 5.1: Spectral Energy Distribution (SED) of PG 1553+113, from Nieppola et al. (2006). The synchrotron peak estimated from a parabolic fit is at 0.4 keV (corresponding to $10^{16.5}$ Hz).

Due to its spectral features, PG 1553+133 was listed in the Costamante and Ghisellini (2002) catalog of TeV candidate BL Lac objects and in 2005 it has been discovered as a VHE emitters by H.E.S.S. (Aharonian et al., 2006) and MAGIC (Albert et al., 2007a), with a flux of approximately 2% of that of the Crab Nebula one above 200 GeV in 2005 and 2006. Despite the different energy ranges and observation periods, the spectral measures of the two IACTs are in very good agreement, as can be noted from Figure 5.2(b). The spectrum appears extremely soft (photon index $\Gamma \sim 4$), as expected by the absorption of VHE photons through interaction with the EBL if the source is located at relatively large redshift (Stecker et al., 1992).

In the HE range, at MeV-GeV energies, PG 1553+113 was not detected by EGRET, whereas it has been well observed by *Fermi*/LAT, with a significance above $10\,\sigma$ in the first three months of observations (Abdo et al., 2009). A reported in Abdo et al. (2010a), the LAT spectrum is surprisingly constant over ~ 200 days both in normalization and slope, with a spectrum well described by a pure power law of index 1.68 ± 0.03, as drawn in Figure 5.2(a). Interestingly, a stability of the spectrum was also suggested in the TeV range by the H.E.S.S. and MAGIC observations, which showed rather marginal variability during 2005–2006 observations. This stability is in contrast with the behavior commonly observed in the other TeV emitting BL Lacs, showing rather pronounced variations at all timescales.

5.1.1 The redshift

The featureless optical spectrum of PG 1553+113, outlined in Fig. 5.3, has prevented the direct determination of its redshift. Up to now, in fact, nor emission

[1] more information at http://users.utu.fi/kani/1m/

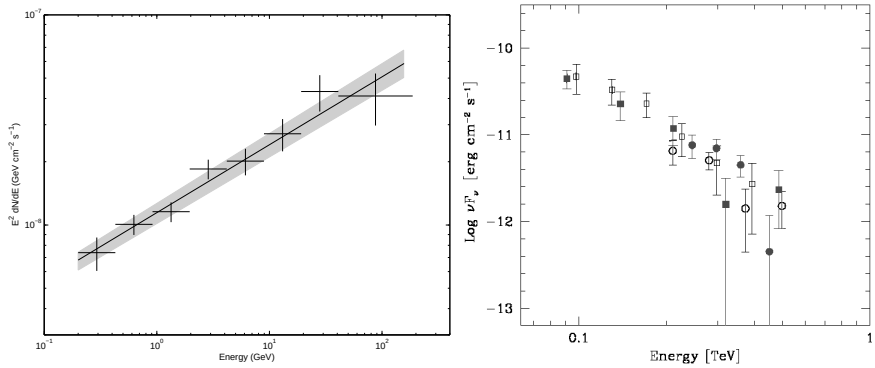

(a) HE spectrum. (b) VHE spectrum.

Figure 5.2: Differential energy spectra of PG 1553+113. Left panel: spectrum measured by *Fermi*/LAT in the HE regime. Right panel: VHE spectrum measured by H.E.S.S. in 2005 (open circles) and 2006 (filled circles) and MAGIC in 2005 (open squares) and 2006 (filled squares) from Reimer et al. (2008). Image from Abdo et al. (2010a).

neither absorption lines has been observed, except for those associated to the telluric absorption.

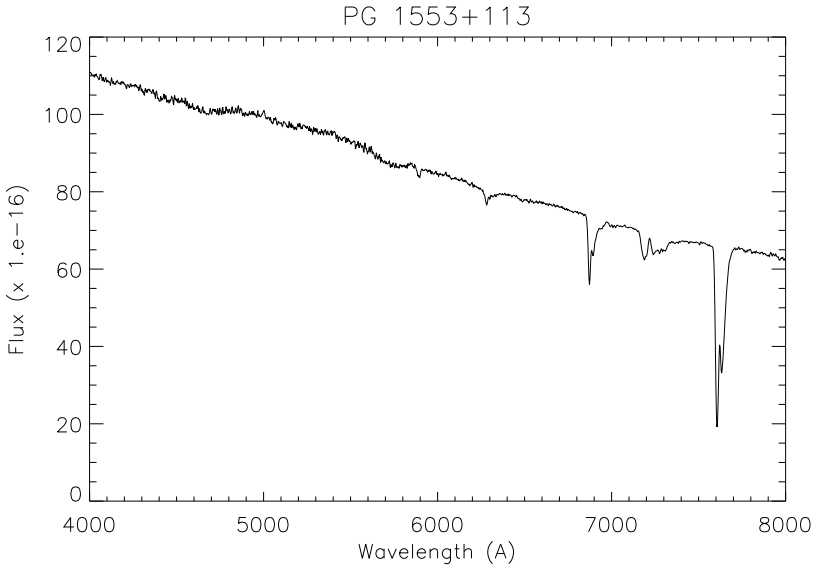

Figure 5.3: Optical spectrum of PG 1553+113, from Treves et al. (2007). No characteristic emission or absorption lines are identified from the thermal continuum, apart from the telluric absorption.

Roughly half of the AGNs classified as BL Lacs have unknown or uncertain redshift. Such behavior is typical of BL Lacs: the largely enhanced jet emission hides any feature of the system. The extreme nature of these objects prevents an easy determination of their distance, based on the detection of non continuum structures in the spectrum. The situation is changing in the last years thanks to very good instruments and improved spectrometric and photometric techniques. In some cases, long exposures have led to the detection of spectral lines, as for the case of PKS 0426–380 shown in Figure 5.4 observed with ESO Very Large Telescope (Sbarufatti et al., 2005a). The problem to obtain deep observations of

the emission lines in some blazars with non–thermal continuum is enhanced so much to hide the thermal emission leaded to the misclassification of some objects as BL Lacs (Ghisellini et al., 2010a).

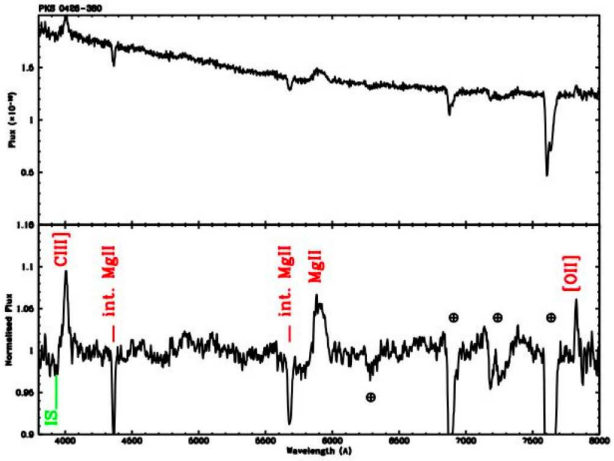

Figure 5.4: Optical spectrum of PKS 0426–380. The high S/N obtained with VLT allowed the detection of several emission lines at $z = 1.105$. Adapted from Sbarufatti et al. (2005b).

Concerning PG 1553+113, the only direct redshift determination was carried out by Miller and Green (1983) that reported the value $z = 0.36$. Unfortunately, this value was found later on to be spurious by Falomo and Treves (1990). Since then, different indirect methods based on optical and near-IR observations have provided limits on the source distance. The absence of evidence of the host galaxy in *Hubble Space Telescope* (*HST*) images (Scarpa et al., 2000) was used to set a lower limit of $z > 0.78$ by Sbarufatti et al. (2005a), with the underlying assumption of small evolution of BL Lac host galaxies. The lack of characteristic lines in VLT spectra, instead, leads to a lower limit of $z > 0.09$ (Sbarufatti et al., 2006). With a different approach, but strong hypothesis on the host galaxy luminosity, Treves et al. (2007) estimated the redshift of PG 1553+113 to lie in the range 0.3–0.4.

Recently, a new method to constraint the distance of such lineless blazars has been applied by Danforth et al. (2010) on PG 1553+113. The method makes use of the absence of intrinsic features in the spectrum to search for signatures of absorption lines arising in the interstellar medium (ISM) and intergalactic medium (IGM). In particular, it consists of looking for evidences of weak metal-line systems and thermally broadened H I absorbers, in order to set confident lower limits to blazar distances. For the case of PG 1553+113, far UV spectra collected with the HST/Cosmic Origin Spectrograph in the wavelength range $1135\,\text{Å} < \lambda < 1795\,\text{Å}$ were used to set the new limit: $z > 0.4$, which can be seen as the first *direct* lower limit to the source distance. The absence of lines above a certain redshift has constrained the distance of the source in the range $0.4 < z < 0.58$.

Finally, VHE observations have been used as alternative methods to constraint the distance of blazars as will be presented in Chapters 7 and 8. Such methods are based on the assumptions that the VHE intrinsic spectrum cannot be harder than a fixed value predicted by the theory (Aharonian et al., 2006) or measured

at lower energies (Prandini et al., 2010). Other methods require the absence of a pile up at high energies (Mazin and Goebel, 2007). In the case of PG 1553+113 the upper limits obtained with these methods are in the range of the limits set by optical measures.

PG 1553+113 VHE γ–ray emission has been monitored with the MAGIC telescope since 2005. Before reporting the results of the analysis, we give a brief introduction on MAGIC data analysis.

5.2 MAGIC data analysis

Since fall 2009, MAGIC (Cortina et al., 2009) has upgraded to a stereo system composed of two new generation Imaging Atmospheric Cherenkov Telescopes (IACTs).

Raw data collected by each telescope have to be reduced in order to get physical information about the observed source. The main ingredients of the data reduction are the real and the simulated, or montecarlo (MC) data, along with a dedicated software, called *MARS* (*Magic Analysis and Reconstruction Software*), which works in the *ROOT* framework. The analysis of MAGIC data can be divided into the following steps:

Signal extraction and calibration The program `callisto` performs the signal extraction from the FADC slices, recorded in the raw files. The charge of a triggered event collected by each PMT is then calibrated and converted into number of photo-electrons (phel). At this stage, pixels affected by hardware problems, called *bad–pixels*, are excluded from further analysis. More details can be found in Gaug (2006).

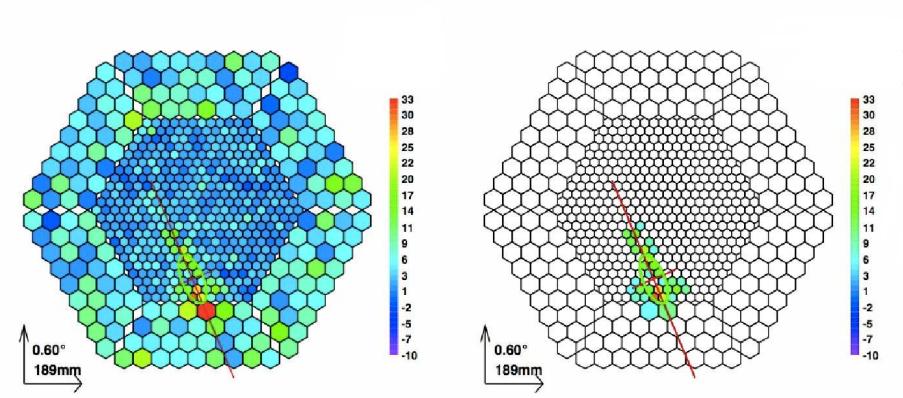

Figure 5.5: Event recorded by MAGIC before (left panel) and after (right panel) the image cleaning procedure. Superimposed to the images, the ellipse which parametrizes the cleaned event is plotted.

Image cleaning At this stage, the diffuse background that surrounds each shower image after the calibration is rejected. In this way, all the information regarding the pixels not involved in the shower image is lost and the file dimension greatly reduced. After this step, the cleaned image is parametrized with the so–called *Hillas Parameters* (Hillas 1985; see Sec. 4.4), plus some additional parameters useful for the signal to noise extraction. These operation are done by a program called `star`.

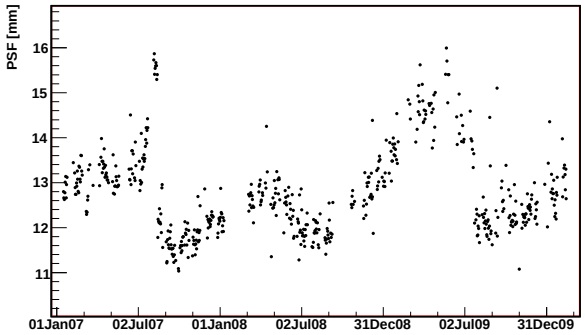

Figure 5.6: Evolution of the PSF of MAGIC I from early 2007 to late 2009.

First data quality selection After the image cleaning, bad quality data are usually rejected; a data selection based on its quality is essential for a correct data reduction.

Main effects which influence data quality are:

- bad weather: it affects our data in a non–trivial way. Since we do not have a model predicting the shower development in every atmospheric condition, we cannot correct the data a posteriori, therefore we have to reject the sample collected during bad weather[2].

  In La Palma, besides normal clouds, another peculiar event can affect the sky: the dust from the desert, called *calima*. When this dust fills the atmosphere, the sky transparency decreases and the opacity is therefore increased. As a result, the threshold of the analysis increases, since low energy events are strongly reduced. Part of PG 1553+113 data were taken under such circumstances.
- hardware problems or changes, related to the telescope subsystems state. Mirrors reflectivity, pointing accuracy (i.e the mirrors point spread function (PSF), of Figure 5.6), number of bad pixels are some of the typical parameters affected by common problems. As a side effect, *camera inhomogeneities* may arise, affecting severely the data quality. For a detailed treatment, see Appendix A.

In MAGIC analysis, the data selection is not standardized in a dedicated software, since the mean values of the Hillas parameters characterizing our events are largely variable. For example, they depend strongly on the data taking conditions, such as the region of the sky observed. At this level, it is common to use the *rate after image cleaning* parameter to do a first quality selection on single file basis.

Stereoscopic images reconstruction Up to the former step, the analysis chain is applied to the data collected, independently if taken in single or stereoscopic mode. Therefore, in case of stereo observations, the analysis is performed on the data of each telescope separately. At this point, in case of stereoscopic observations, two sets of files which contain two different views of the same cleaned showers are available, one per telescope. The stereo

[2]The definition of *bad weather* depends on the source under study: for pulsar observations, for example, we need very low energy threshold. Hence, even few clouds prevent us to carry on the observations. In general, the two parameters considered are the sky transparency and the wind.

analysis then proceeds with the aid of a new program called `superstar`, which reduces the two sets of files in a single one, containing all the necessary information. The aims are to identify the matching pairs of images belonging to the same event from the two data streams, based on the L3 Trigger numbering, to update the names of the image parameters of each telescope according to the telescope number (e.g. `size1, size2, width1, width2`, etc.) and to calculate further image parameters which refer to the stereoscopic view of the showers, such as the primary incoming direction, the ground impact point with respect to the two telescopes (`impact1` and `impact2`) and the height of the shower maximum (`maxheigth`).

Energy reconstruction and γ–hadron separation These fundamental tasks of the analysis are both performed through the Random Forest (RF) method (Albert et al., 2008a), which is composed of a training and a test phase.

In the *training* phase, two specific matrices, one for the reconstructed energy and one for the `hadronness` reconstruction are created, the last parameter being a real number between 0 to 1 related to the probability that the event is hadron–like (`hadronness` = 1) or γ–like (`hadronness` = 0). In order to create the matrices, MC data simulating γ–like events are used together with, in the `hadronness` case, real data.

Those matrices are then applied, in the *test* phase, to both real and simulated events, which are assigned two new parameters: their reconstructed energy and their `hadronness`. In Figure 5.7 the `hadronness` distribution of γ–like events (from simulated data) is compared to that of real events. While the former is peaked at zero, the latter is peaked at `hadronness` = 1. This behavior underlines that the hadron–induced showers are the large majority of the collected events. Hence, a cut in the `hadronness` parameter can be used to reject the hadron–like showers and select the events most likely induced by γ–rays.

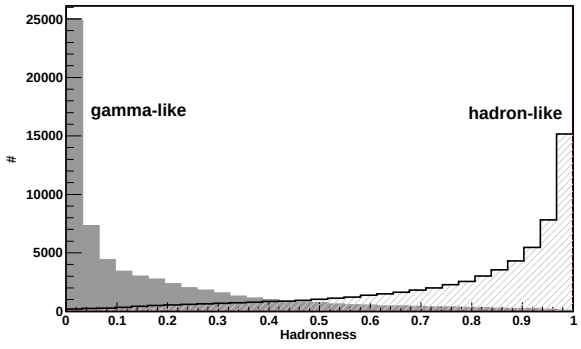

Figure 5.7: Distributions of the parameter `hadronness` for γ–like events (peaked in zero) and hadrons (peaked at 1).

Figure 5.8 shows the energy resolution obtained with the RF method. The resolution achieved if we apply a cut in the parameter `size`, defined in Sec. 4.4, at 80 phel, which is the usual cut applied in the analysis and corresponds to an energy threshold below 100 GeV, is compared with the resolution achieved with a cut at 200 phel, which is a more conservative cut, useful for example in analysis affected by bad data quality. In former case, the resolution is worse, especially between 150 GeV to 400 GeV, while it is better in the low energy range, below 150 GeV. In both cases, the mean reconstructed energy above 200 GeV has value of $\sim 20\,\%$.

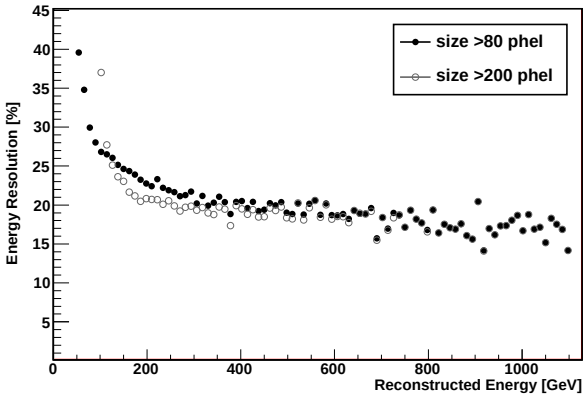

Figure 5.8: Energy resolutions corresponding to a `size` cut at 80 phel and 200 phel.

The energy threshold of the analysis, usually estimated from the peak of the reconstructed energy distribution of γ–like MC data surviving all the cuts applied, is strictly dependent, among others, on the cut in the `size` parameter. The threshold is also related to other factors, such as the `zenith angle` of the observation and the status of the telescope hardware.

As of now, the reconstruction of the energy of the stereo events is not performed by using the RF method as in case of single telescope data. Instead, for each telescope the energy is reconstructed using lookup-tables based on the values of some selected image parameters. Combination of these two energy estimations provides the final reconstructed energy of the event. Although the method is simpler than the RF method, it provides a better energy resolution, especially at low energies; this is due to the 3D parameters of the shower which are well reconstructed by stereoscopy.

Signal search For the signal search, there are two different approaches, namely the `alpha` and the θ^2 techniques, as shown in Figure 5.9.

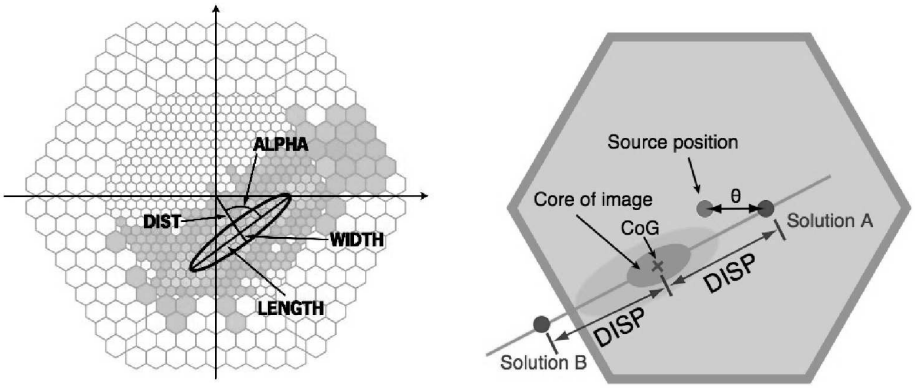

Figure 5.9: Signal search methods. Left plot: `alpha` technique, from Albert et al. (2008); right plot: θ^2 technique principle.

In the former, the distribution of the `alpha` parameter is studied. `alpha` represents the angle between the image major axis and the line linking the image center with the pointing position (camera center in ON–OFF mode, wobble center otherwise). This parameter is one of the best separator known so far between hadronic and electromagnetic showers: while the `alpha` pa-

rameter is randomly distributed for former events, it is peaked around zero in latter events.

A possible way to extract the signal is that of plotting the distribution of `alpha` for the On and Off samples after the selection cuts and an appropriate `hadronness` cut[3], as shown for example in Figure 5.10. The γ–ray like events, if any, appear as an excess in the region at small `alpha` values. The Off distribution, instead, is quite flat.

An analogue behaviour is followed by the parameter θ^2, the distance in camera coordinates between the reconstructed shower origin (`DISP`) and the pointing position, that can be used as well for the signal extraction. In particular, this is the method of signal extraction in case of stereoscopic observations (see for example Chapter 6).

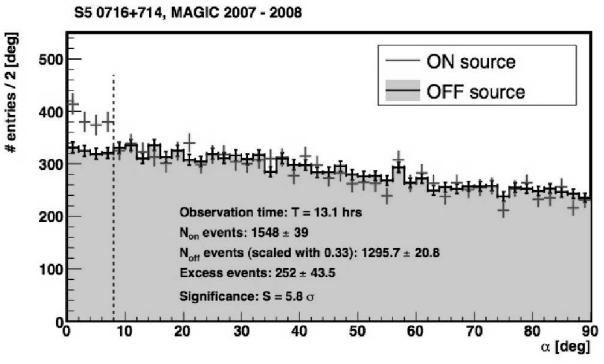

Figure 5.10: Example of distributions of the parameter `alpha` for the On data (empty histogram) and Off data (filled histogram), after the selection cuts. Adapted from Anderhub et al. (2009a).

A source is considered **detected at VHE** if the excess events are detected above **5 sigma** of significance defined according to the formula 17 of Li and Ma (1983).

Finally, another useful tool for the signal search is the skymap, done with the program `caspar`. It is a bidimensional map of the reconstructed incoming direction of each event and can be very useful to check the extent of the signal (usually point–like, especially in the extragalactic sources case). It is used, as well, to estimate the resolution of the analysis and to point out an eventual mispointing during the data taking.

Integral and differential flux estimate After the detection of a significant signal from a given source, the ultimate scope of the analysis is the characterization of the VHE γ–ray emission. This is done through the determination of the integral and differential energy flux emitted by the source, performed with a dedicate program called `fluxlc`.

The *differential energy spectrum* is, by definition:

$$\frac{dN}{dE}(E) = \frac{N_\gamma}{dE \cdot dA_{eff} \cdot dt_{eff}}, \tag{5.1}$$

where, in the real case, N_γ are the excesses in the finite energy bin dE estimated from the corresponding `alpha` or θ^2 plot, A_{eff} is the *effective collection area* and t_{eff} the *effective observation time*.

[3]Even for the strongest sources, such as for example the blazar Mkn 501 or the Crab Nebula, a `hadronness` cut must be applied to the sample in order to extract the signal, due to the very low signal to background ratio.

The effective collection area, A_{eff}, is the area in which air showers can be potentially observed by the telescope, folded by the detection efficiency, after all analysis cuts. The detection efficiency can be estimated from the ratio between the number of simulated γ-ray showers surviving all the cuts and the total number of γ-ray showers. Figure 5.11 shows the effective collection area before and after cuts, as a function of the energy of the simulated γ-ray shower.

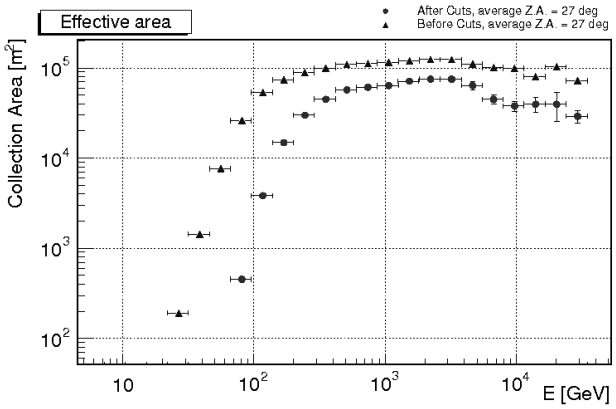

Figure 5.11: Effective collection area, in m^2, before (triangles), and after cuts (filled dots).

Below 300 GeV, the effective area is a function rapidly decreasing with decreasing energy, while above this threshold it is pretty constant around a mean value of the order of $10^5\,\mathrm{m}^2$ before any cut, and almost half of this value after the specific cuts applied in this case (`size` >80 phel, energy dependent `hadronness` cut).

Therefore, taking onto account these elements the differential flux can be investigated, and the upper part of the Spectral Energy Distribution (SED) can be characterized. In parallel to this study, the integral flux emitted by a source is also investigated. This quantity is essential to put in evidence an eventual variability of the emission.

Effects on the spectrum determination introduced by the limited energy resolution are usually corrected by *unfolding* the final spectra (performed with the macro `CombUnfold.C`).

5.3 PG 1553+113: the dataset

PG 1553+113 was observed with the MAGIC telescope for nearly 19 hours in 2005 and 2006 (Albert et al., 2007a); it was also the subject of a multiwavelength campaign carried out in July 2006 with optical, X-ray and TeV γ–ray telescopes (Albert et al., 2009). Here, we present the results of follow-up observations carried out for 14 hours in March-April 2007, for nearly 26 hours in March-May 2008, some of those simultaneously with other instruments (Aleksić et al., 2010c), and for about 24 hours in March-July 2009, which are partly taken in moderate light conditions (moon light). Unfortunately, both 2008 and 2009 observations are severely affected by bad weather (including *calima*, i.e. Saharan sand-dust in the atmosphere) that reduces the final dataset and results in an increased energy threshold. For the detailed list of data see Appendix B.

Cycle	Date	Eff. Time [min]	Zd [°]	Mean Rate [Hz]	DC [μA]
	23/03/2007	58	19 - 29	164	dark night
	19/04/2007	32	22 - 28	155	dark night
	20/04/2007	150	17 - 29	163	dark night
III	21/04/2007	115	17 - 24	155	dark night
	22/04/2007	101	17 - 23	162	dark night
	23/04/2007	143	17 - 27	161	dark night
	24/04/2007	92	17 - 23	160	dark night
	17/03/2008	58	17 - 19	150	dark night
	18/03/2008	26	18 - 19	150	dark night
	01/04/2008	43	20 - 26	167	dark night
	05/04/2008	109	17 - 31	167	dark night
IV	13/04/2008	97	17 - 22	147	dark night
	29/04/2008	44	27 - 36	151	dark night
	03/05/2008	24	26 - 31	146	dark night
	04/05/2008	40	28 - 36	155	dark night
	05/05/2008	38	26 - 33	150	dark night
	07/05/2008	40	28 - 36	153	dark night
	16/04/2009	93	17 - 27	133	2.8 - 3.7
	17/04/2009	103	17 - 28	151	1.6 - 2.4
V	18/04/2009	126	17 - 28	168	0.7 - 1.7
	20/04/2009	73	19 - 35	171	0.9 - 1.4
	21/04/2009	57	23 - 34	177	0.8 - 1.0
	15/06/2009	57	24 - 35	125	0.8 - 2.1

Table 5.1: PG 1553+113 final dataset from 2007 to 2009 used in this study. From left to right: MAGIC Cycle of observation (first column) and corresponding dates in dd/mm/yy (second column); effective time of observation in minutes and zenith angle range in degrees (third and fourth columns). In the last two columns, the rate of the events after the image cleaning, in Hz, and the mean DC current in the camera, in unit of μA, are reported. The night is considered as dark night if the DC current during observations of extragalactic objects is less than indicatively 1.2 μA.

All the data analyzed here are taken in wobble mode (see Section 4.8). The zenith angle of 2007 observations distributes between 17° to 30°, in 2008 it extends up to 36°, while in 2009 it covers the range from 17° to 35°.

5.3.1 The quality selection

Severe quality cuts based on event rate after night sky background suppression are applied in order to select good quality samples: 28.7 hours of data remain after these cuts, out of which 11.5 hours are taken in 2007, 8.7 hours in 2008 and 8.5 hours in 2009. In Figures 5.12 the rate distributions of the selected cleaned data are shown. More details about the final dataset can be found in Table 5.1. For the signal study, a cut in the parameter `size` removes events with a total charge less than 80 photo-electrons (phel) in the 2007 dataset, and 200 phel in 2008 and 2009 datasets. In the latter case, this cut reduces the effect of the moon light (Britzger et al., 2009).

The threshold of the analysis[4] is 80 GeV in 2007, 150 GeV in 2008 and 160 GeV in 2009, as displayed in Fig. 5.13.

Due to changes in the telescope performance, the *sigma* of the PSF of 2007 and 2008 is measured to be 13.0 mm, while in 2009 it is 14.9 mm. To take all

[4]The threshold of the analysis reported here is the peak of the `reconstructed energy` of the simulated gamma events surviving the cuts.

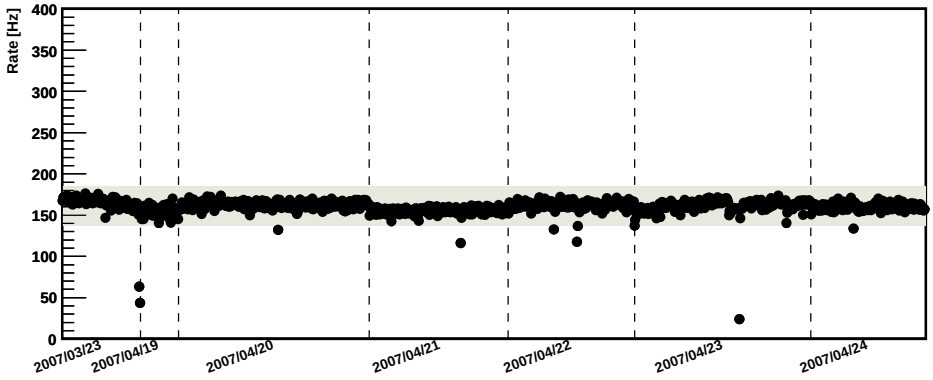

(a) 2007 sample.

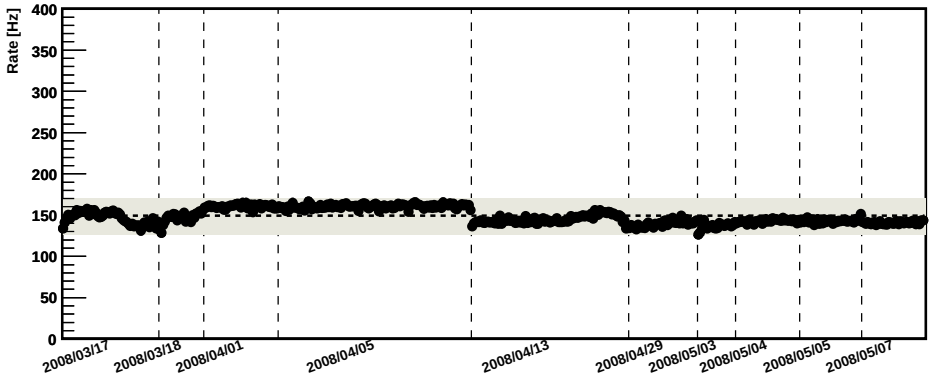

(b) 2008 sample.

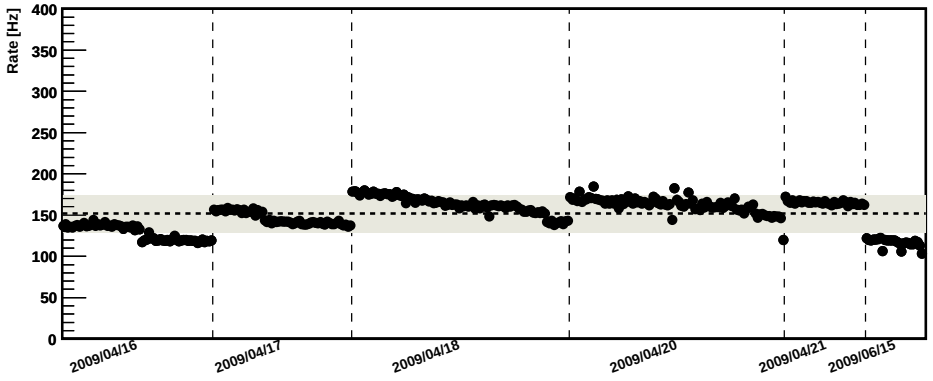

(c) 2009 sample.

Figure 5.12: PG 1553+113 rate distributions of the selected data after the image cleaning with a pre–cut in the parameter `size` at 80 phel for the 2007 (a), 2008 (b), and 2009 (c) samples.

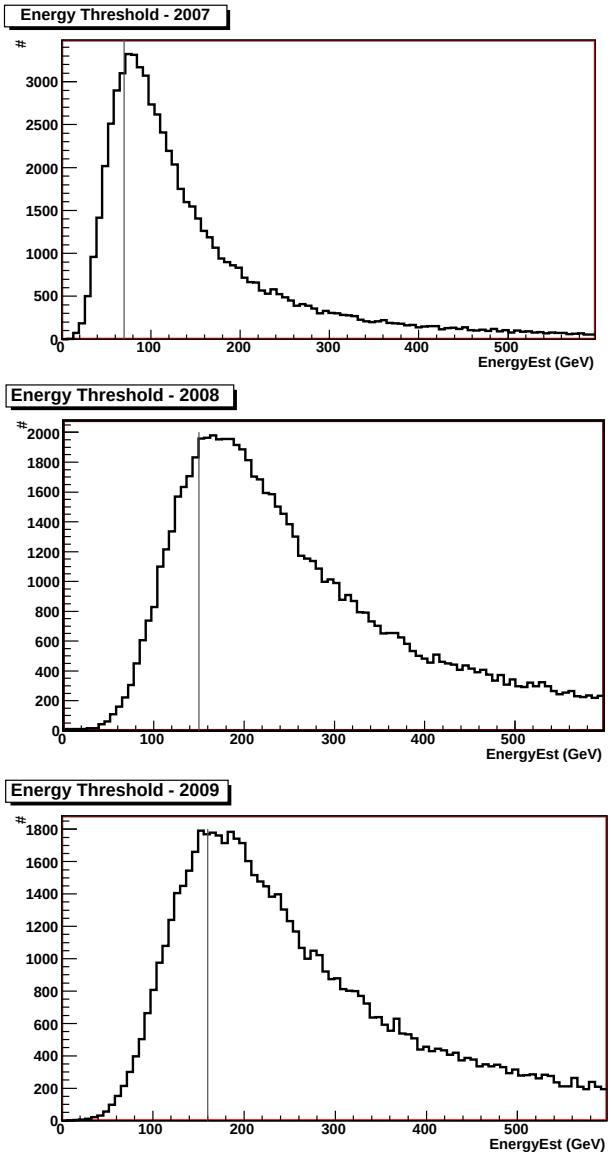

Figure 5.13: Energy thresholds of PG 1553+113 during 2007 to 2009 observations.

these differences into account data are analysed separately using dedicated sets of simulated data. Effects on the spectrum determination introduced by the limited energy resolution are corrected by unfolding the final spectra (Albert et al., 2007e).

5.4 Detection of the signal

For the signal extraction, we analyze the distribution of the parameter `alpha`, related to the incoming direction of the primary cosmic ray inducing the atmospheric shower. As mentioned above, images induced by primary gammas have this parameter close to zero because of their preferential direction, while images due to hadrons have a random distribution of alpha (the direction of hadrons is nearly isotropic).

Since all the data were taken in wobble mode, the background is extracted from the data themselves. In particular, we use 1 Off region for 2007 sample, due to the low cut in `size` adopted, which ensures a low energy threshold but does not eliminate the camera inhomogeneities which affect severely the results when adopting 3 Off regions, as explained in Appendix A. In 2008 and 2009 samples, instead, we applied a safer cut in the parameter `size`, at 200 phel, due to the weather and light conditions, and thus we can use 3 Off regions for the background determination.

Year	Time [h]	PSF [mm]	`size` cut [phel]	`had` cut eff. [%]	E_{th} [GeV]	N_{exc}	Signif. [σ]
2007	11.5	13.0	80	50	80	1400 ± 242	5.8
2008	8.7	13.0	200	60	150	542 ± 69	8.1
2009	8.5	14.8	200	60	160	212 ± 52	4.2

Table 5.2: PG 1553+113 signal study. From left to right: year of observation, effective time of good quality data used for the signal analysis, PSF, cut in the parameter `size` adopted in the analysis, efficiency of the `hadronness` cut applied, energy threshold of the analysis, number of excess events observed and significance of the signal.

The typical γ–ray emitting blazar ejects a differential energy photon spectrum of the form:

$$\frac{dN}{dE} \propto E^{-\Gamma}, \tag{5.2}$$

with Γ ranging from 2.5 to 4.5. Hence, the shape of the emitted spectrum is largely dependent on the energy range considered. In particular, the emission is stronger at low energies, where the telescope is less sensitive (see Fig. 4.18), and it rapidly decreases for increasing energies.

The capability of recognizing the γ–like events from the dominating background, i.e. the distribution of the `hadronness` parameters for the simulated gammas, is also a function of energy. The behaviour of the `hadronness` parameter for (simulated) γ–like events as a function of the reconstructed energy, is shown in Figure 5.14. It is evident that at low energies the `hadronness` parameter has a large spread around a mean value of 0.4. Therefore, at these energies it is more difficult with a cut in the `hadronness` parameter to separate gammas from hadrons, which are characterized by a mean `hadronness` of 0.6. At higher energies, instead, the mean `hadronness` for gammas thins to small values while that for hadrons approaches to 1, and a `hadronness` cut becomes an efficient separator between gamma and hadrons. This behavior depends also on the `size` cut applied in the analysis, as shown in the Figure.

In order to take all this into account, we apply a so–called dynamical `hadronness` cut to the `alpha` plot. This means that for the signal extraction in the *integral energy band*, an energy dependent `hadronness` cut is applied, based on the efficiency estimated with simulated γ events. In particular, we require an efficiency of `hadronness` cut of 60 % and 50 % when a `size` cut at 200 and 80 phel is applied, respectively. In addition, we set a minimum `hadronness` and `alpha` cut at 0.07 and 8°, respectively.

From the comparison of the last two Figures, we can conclude that the `size` cut:

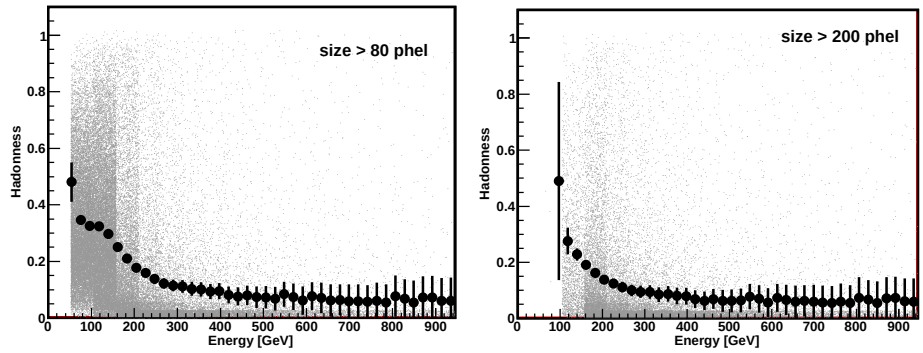

Figure 5.14: Profiles of the `hadronness` parameter for γ–like events and a `size` cut of 80 phel (left plot), and 200 phel (right plot).

- strongly influences the energy threshold of the analysis, which is $\sim$80 GeV for a cut at 80 phel, and more than 150 GeV in case of a cut at 200 phel;
- influences the `hadronness` distribution: a lower `size` cut corresponds to a higher value of the `hadronness` parameter for γ–like events, especially at low and mean energies. For example, at 200 GeV the mean `hadronness` is 0.15 in case of events with `size` above 200 phel, and 0.2 in the other cases.[5]

Figure 5.15 reports the integral `alpha`–plots resulting from our study. The significance of the signal is 5.8 σ in 2007, 8.1 σ in 2008 and 4.2 σ in 2009, according to eq. 17 of Li and Ma (1983), as reported in Table 5.2. Hence, the source is detected by MAGIC every year (actually a more than 4 *sigma* signal for a well established source can be considered a detection), indicating that PG 1553+113 is a stable presence in the VHE sky. The combined signal has 8.8 σ of significance.

Due to a large difference in the energy thresholds and changes in the experimental conditions, we cannot extract any further information from the obtained integral significance; a detailed spectral analysis is necessary in order to study the source emission.

5.5 Differential energy spectrum

The differential spectrum observed by MAGIC between 2007 and 2009 is studied in detail in this Section. First we present the results from individual years, thus we combine all the spectra and compare the average spectrum obtained with the previous determinations.

For the spectrum reconstruction we study the emission in intervals of reconstructed energy (or true energy in the case of unfolded spectrum), also called energy bins. We set 29 and 25 bins in logarithmic scale between 5 GeV to 50 TeV for the individual 2007/08 and 2009 spectra, respectively. The unfolded spectrum is characterized by the same bins scaled by a factor 1.4, which allows to perform

[5]This fact indicates that the presence of low energy (i.e. `size`) events during the training phase of RF, influences the performance of the gamma/hadron separation and suggests to apply a cut in the `size` parameter for obtaining better performances of the analysis above 300 GeV. Unfortunately, the large majority of extragalactic objects presents a cut–off in the energy spectrum at relatively low energies, sometimes below 400 GeV, making the energy region between 100 to 300 GeV the most important for the study of such objects.

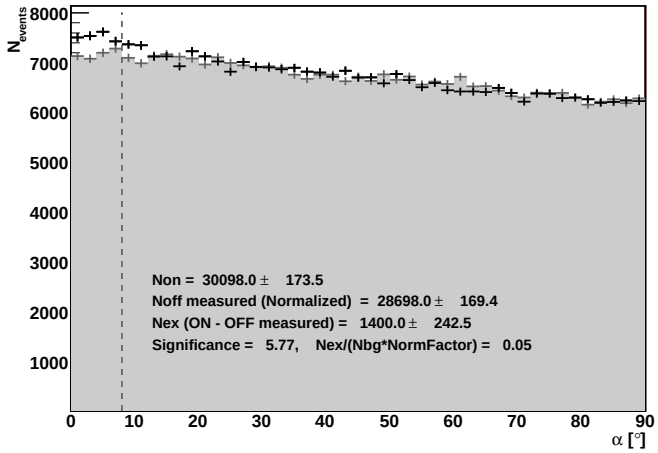

(a) PG 1553+113 Alpha plot of 2007 data, 1 Off region, size cut 80 phel.

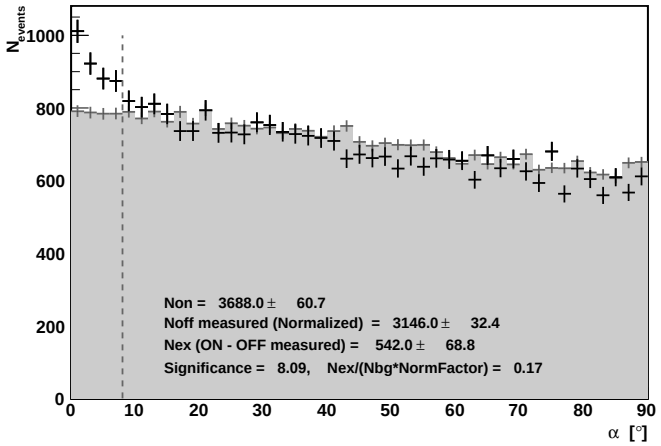

(b) PG 1553+113 Alpha plot of 2008 data, 3 Off regions, size cut 200 phel.

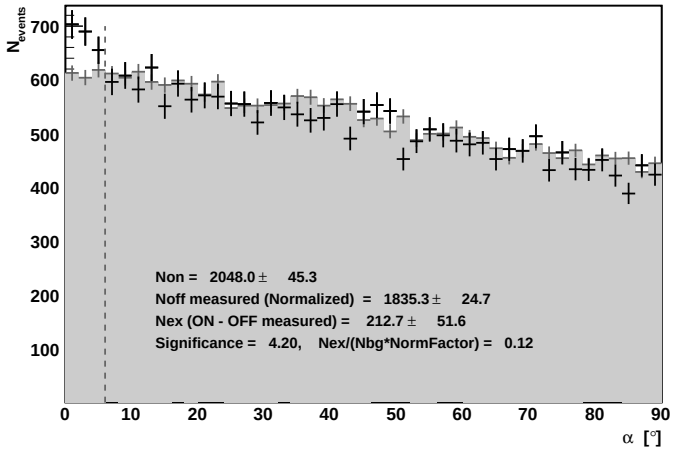

(c) PG 1553+113 Alpha plot of 2009 data, 3 Off regions, size cut 200 phel.

Figure 5.15: Signal detection of PG 1553+113during 2007 (a), 2008 (b), and 2009 (c) observations.

the true energy reconstruction procedure. For the final mean spectrum, we unfold all together the differential spectra obtained with a binning set to 29.

2007

The main characteristic of 2007 sample is that the good quality of the data collected allows the achievement of a low energy threshold analysis. In terms of spectrum determination, this means low energy spectral points (below 100 GeV).

For the differential spectrum estimation, we perform the signal search with the `alpha` technique in bins of energy. The bins considered for the study are listed in Table 5.3, along with the corresponding cuts in the parameters `hadronness` and `alpha`. The last column reports the mean flux measured, which is obtained by dividing the number of excess events measured in the `alpha` plot by the corresponding effective area and time (see Eq. 5.1). The measured excesses and overall spectrum are drawn in Figure 5.16.

Finally, the spectrum unfolded for the finite energy resolution is computed. Figure 5.17 shows the differential energy spectrum of PG 1553+113 after this correction procedure, performed with the Tikhonov method (Tikhonov and Arsenin, 1977). The spectrum in the energy range 80 GeV–500 GeV can be well fitted by a quite steep power law with an index of 4.1 ± 0.3, in agreement with previ-

Mean energy [GeV]	`had` cut	`alpha` cut [°]	Flux [cm^{-2} s^{-1} TeV^{-1}]
75	0.33	14	$(2.3 \pm 2.4) \times 10^{-09}$
103	0.30	14	$(3.7 \pm 0.8) \times 10^{-09}$
142	0.20	12	$(1.2 \pm 0.2) \times 10^{-09}$
195	0.07	10	$(1.7 \pm 0.4) \times 10^{-10}$
268	0.07	8	$(3.3 \pm 1.8) \times 10^{-11}$
368	0.07	8	$(2.8 \pm 8.7) \times 10^{-12}$
506	0.07	8	$(2.9 \pm 3.2) \times 10^{-12}$
695	0.07	8	$(1.4 \pm 1.5) \times 10^{-12}$

Table 5.3: Mean energy of the bin (first column), `hadronness` and `alpha` cuts applied for the spectrum determination of 2007 data (central columns), and mean flux before unfolding (last column).

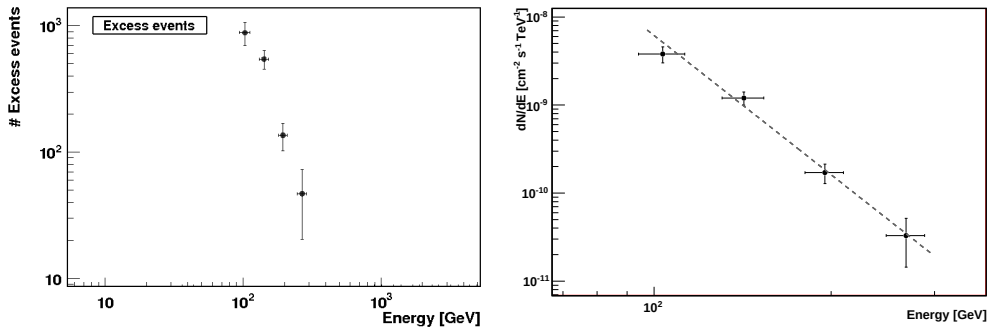

(a) Excess events of PG 1553+113 2007 subsample in each energy bin considered for the spectrum estimation.

(b) Differential energy spectrum of PG 1553+113, 2007 subsample.

Figure 5.16: Differential energy spectrum of PG 1553+113 for the 2007 sample.

ous determinations of the source spectrum (Aharonian et al., 2006; Albert et al., 2007a).

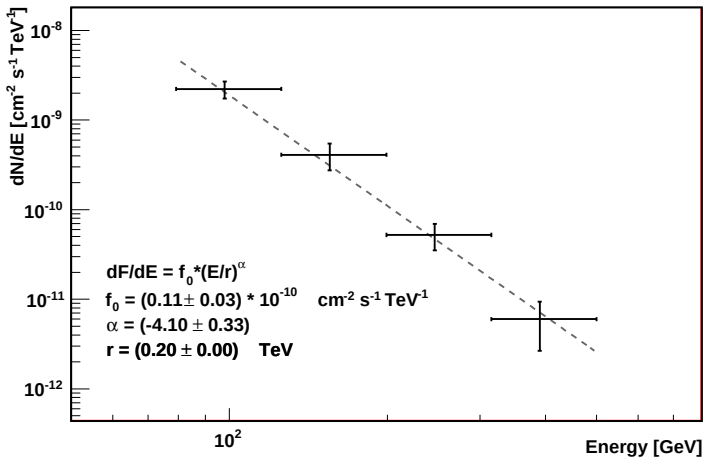

Figure 5.17: Unfolded differential energy spectrum of PG 1553+113 for 2007 data.

2008

As said, the large `size` cut at 200 phe applied to the 2008 and 2009 samples induces a higher energy threshold in the analysis. On the other side, thanks to this cut we get an better energy resolution above 150 GeV, as noticed above, and we can use of 3 Off regions for the signal search.

Table 5.4 reports the results of 2008 spectrum determination. For the sake of completeness, we report also the first bin, whose energy center is 103 GeV, even if the flux level registered is not significant and will be rejected from further analysis steps[6]. The corresponding excess events and differential energy flux, before the unfolding, are shown in Figure 5.18.

Mean energy [GeV]	`had` cut	`alpha` cut [°]	Flux [cm^{-2} s^{-1} TeV^{-1}]
103	0.34	8	$(4.9 \pm 6.8)\times10^{-10}$
142	0.25	10	$(1.1 \pm 0.3)\times10^{-09}$
195	0.13	12	$(4.6 \pm 0.7)\times10^{-10}$
268	0.07	10	$(1.0 \pm 0.2)\times10^{-10}$
368	0.07	8	$(1.8 \pm 0.9)\times10^{-11}$
506	0.07	8	$(8.4 \pm 4.2)\times10^{-12}$
695	0.07	8	$(0.2 \pm 1.8)\times10^{-12}$

Table 5.4: Mean energy of the bin (first column), `hadronness` and `alpha` cuts applied for the spectrum determination of 2008 data (central columns), and mean flux (last column).

The final spectrum, corrected for the finite energy resolution with the unfolding procedure is drawn in Figure 5.19. The lack of low energy spectral points with

[6]This behavior can be explained by observing that the mean energy of this bin is well below the energy threshold.

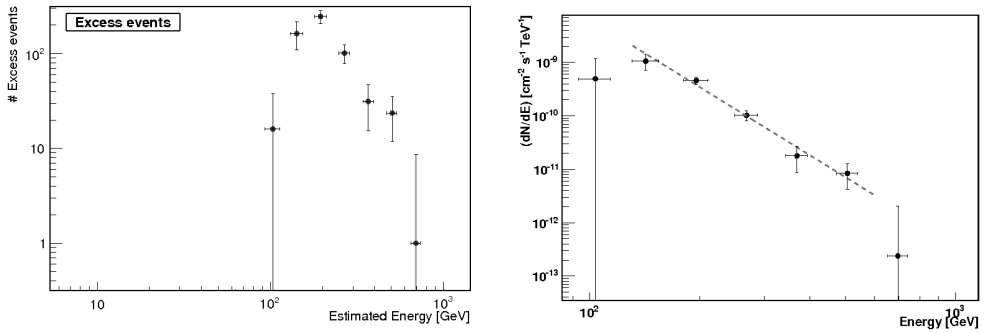

(a) Excess events of PG 1553+113 2008 subsample.

(b) Differential energy spectrum of PG 1553+113, 2008 subsample.

Figure 5.18: Differential energy spectrum of PG 1553+113 for the 2008 sample.

respect to 2007 spectrum is in a sense compensated by the presence of points up to 600 GeV, probably due to the increased sensitivity. Also in this case the spectrum is well fitted by a power law. We obtain in the energy range from 140 GeV to 800 GeV an index of $\Gamma = 4.27 \pm 0.43$.

Part of this subsample has been the subject of a multi-frequency campaign, published in Aleksić et al. (2010c). In that paper, the reported power law fitting

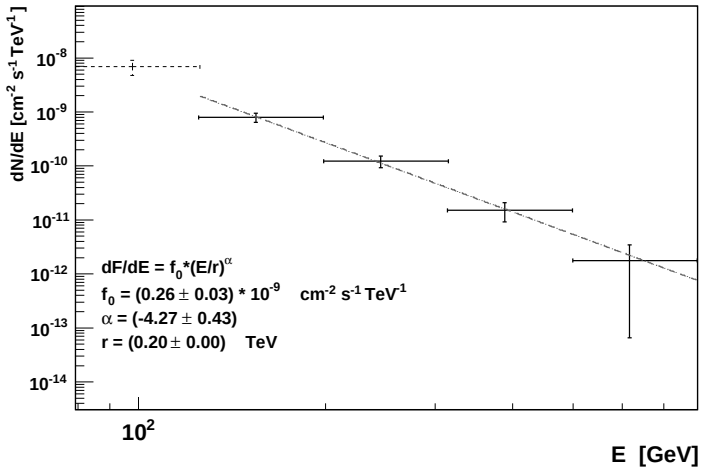

Figure 5.19: Unfolded differential energy spectrum of PG 1553+113 for 2008 data.

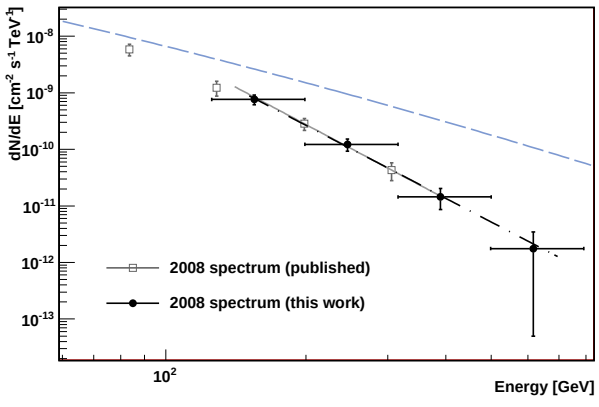

Figure 5.20: Comparison of 2008 spectrum obtained in this work with that published in Aleksić et al. (2010c), partially simultaneous. Superimposed to the spectra, the fit of published data above 150 GeV (continuous line) and the fit of the spectrum obtained with our analysis (dashed–dotted line). For comparison, the Crab Nebula spectrum is reported (dashed line).

the data has an index of 3.4 ± 0.1, which is apparently in disagreement with our result. The mismatch, however, is only apparent, and is due to a different set of cuts applied in the analyses, which led to different energy thresholds, and ultimately to different energy ranges of the fits. In the published spectrum, the points are mainly concentrated at lower energies, below 350 GeV, and the spectral slope reported is obtained by fitting the spectrum in the range 70–350 GeV. If we fit above 140 GeV, the two slopes become perfectly compatible, as shown in Figure 5.20.

2009

For the determination of 2009 spectrum an additional cut in PMT DC current, namely above 2.5 μA, is applied to the data. This cut reduces the systematics due to the moon light (Britzger et al., 2009), and resulted in 6.9 hours of good quality data. In Table 5.5, the individual bins results are listed.

The excess events and differential energy spectrum of PG 1553+113 resulting from 2009 data analysis are shown in Figure 5.21. The high energy threshold, $\sim$160 GeV, combined to the low significance of the signal (that could be related to a lower emission state of the source), to a too short exposure time or both effects combined together, leads to large error bars in the spectral points and corresponding large uncertainties in the differential energy spectrum determination.

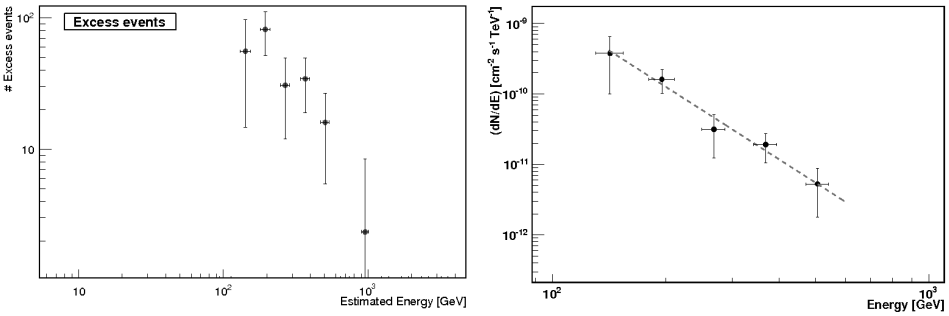

(a) Excess events of PG 1553+113 2009 subsample.

(b) Differential energy spectrum of PG 1553+113, 2009 subsample.

Figure 5.21: Differential energy spectrum of PG 1553+113 2009 for the 2009 sample.

The unfolded spectrum, shown in Figure 5.22, is composed of only three reliable spectral points above 150 GeV, compatible with a power law of index 3.43. ± 0.50

Mean energy [GeV]	`had` cut	`alpha` cut [°]	Flux [cm^{-2} s^{-1} TeV^{-1}]
116	0.26	8	$(6.7 \pm 5.6)\times10^{-10}$
168	0.15	10	$(2.1 \pm 1.4)\times10^{-10}$
243	0.07	8	$(8.2 \pm 2.9)\times10^{-11}$
351	0.07	8	$(3.2 \pm 1.1)\times10^{-11}$
508	0.07	8	$(4.2 \pm 3.8)\times10^{-12}$

Table 5.5: Mean energy of the bin (first column), `hadronness` and `alpha` cuts applied for the spectrum determination of 2009 data (central columns), and mean flux (last column).

in the energy range 120–600 GeV.

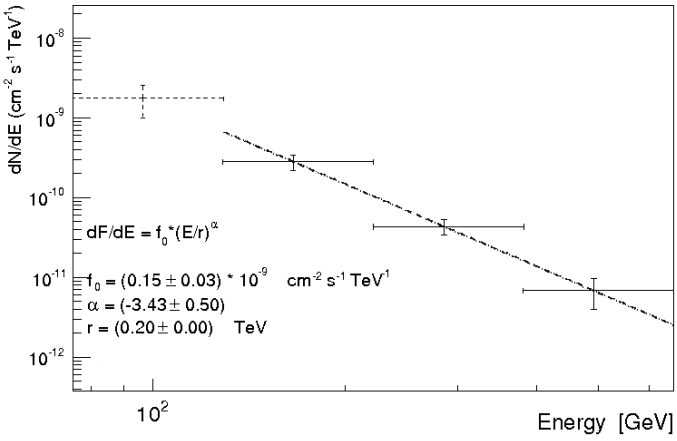

Figure 5.22: Unfolded differential energy spectrum of PG 1553+113 for 2009 data.

5.5.1 Combined spectrum

The comparison between the differential spectra observed from PG 1553+113 by MAGIC every year from 2007 to 2009 is shown in Figure 5.23.

In summary, we can notice that, as for other blazars, each spectrum can be well fitted with a power law function of the form

$$\frac{dF}{dE} = f_0 * \left(\frac{E}{200\,\mathrm{GeV}}\right)^{-\Gamma} \tag{5.3}$$

where f_0 is the flux at 200 GeV, also called normalization factor, and Γ is the power law index. The resulting indices are listed in the last column of Table 5.6. The systematic uncertainty is estimated to be 35% in the flux level and 0.2 in the power index (Albert et al., 2008), and is the sum of many contributions, mainly due to the use of MC simulations instead of test beams.

Thanks to the low energy threshold of the analysis of 2007 data, the corresponding spectrum has a measured point below 100 GeV. This point is, within the errors, in good agreement with the low energy point measured in 2005 and 2006. The 2008 differential spectrum is in good agreement with the spectrum determined with a partially simultaneous sample taken during a multiwavelength

Year	time [h]	F > 150 GeV [10^{-11} cm^{-2} s^{-1}]	F > 150 GeV [Crab %]	Γ
2007	11.5 h	1.40 ± 0.38	4%	4.1 ± 0.3
2008	8.7 h	3.70 ± 0.47	11%	4.3 ± 0.3
2009	6.9 h	1.63 ± 0.45	5%	3.4 ± 0.5

Table 5.6: Individual years spectra of PG 1553+113. From left to right: year of MAGIC observations; effective time in hours; integral flux above 150 GeV in units of 10^{-11} cm^{-2} s^{-1} and Crab Nebula flux %; in the last column the Γ indices obtained by fitting the observed differential spectra with a power law are listed.

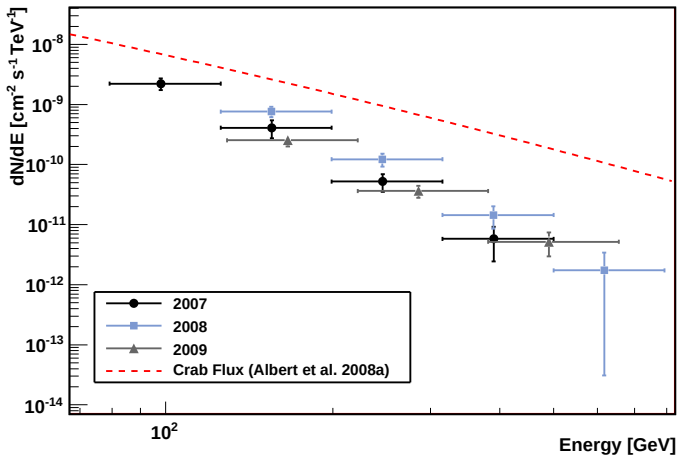

Figure 5.23: Differential energy spectra from PG 1553+113: comparison between 2007, 2008 and 2009 spectra. The fit of the Crab Nebula spectrum measured by MAGIC (Albert et al., 2008) is superimposed for comparison.

campaign with other instruments (Aleksić et al., 2010c). Finally, the 2009 differential spectrum is scarcely determined due to the limited signal. Except for the latter sample, whose significance is rather low and corresponding errors noticeably large, the power law indices describing the spectra are compatible. This indicates that the shape of the emitted spectrum does not change, even if the total flux shows hints of (small amplitude) variability, as also noted for other BL Lacs such as 1ES 1218+304 (Acciari et al., 2010).

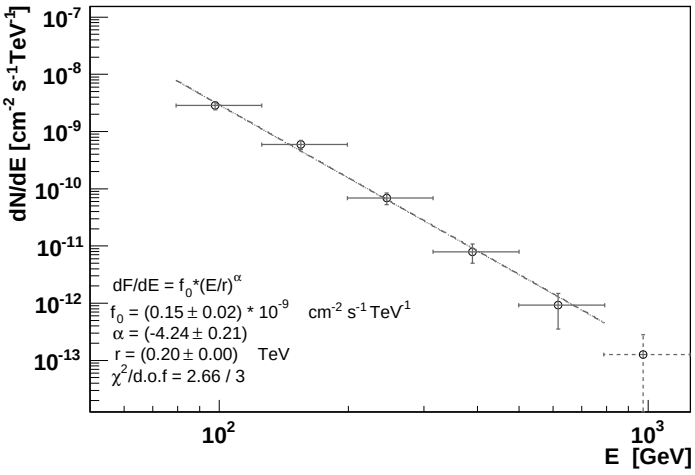

Figure 5.24: PG 1553+113 2007/09 combined unfolded spectrum.

The results of the unfolded 2007/09 combined spectrum are listed in Table 5.7. The last point is excluded from further analysis due to its low statistical significance. Figure 5.24 shows the overall determination characterized by a mean index of slope 4.24 ± 0.21, together with the mean fit to the data.

Figure 5.25 displays the comparison between the mean deabsorbed spectrum measured from 2007 to 2009, with that measured by MAGIC in 2005/06 ($\Gamma = 4.21 \pm 0.25$, Albert et al. 2007a). The good agreement among these mean determinations suggests that, despite the (small) variability seen on yearly scale, the

Mean Energy [GeV]	Flux [cm^{-2} s^{-1} TeV^{-1}]
97	$(2.85 \pm 0.45) \times 10^{-9}$
155	$(5.91 \pm 1.05) \times 10^{-10}$
245	$(6.88 \pm 1.59) \times 10^{-10}$
389	$(7.91 \pm 2.92) \times 10^{-11}$
617	$(9.22 \pm 5.67) \times 10^{-12}$
974	$(1.27 \pm 1.54) \times 10^{-13}$

Table 5.7: Results of the 2007/09 combined unfolded spectrum analysis of PG 1553+113.

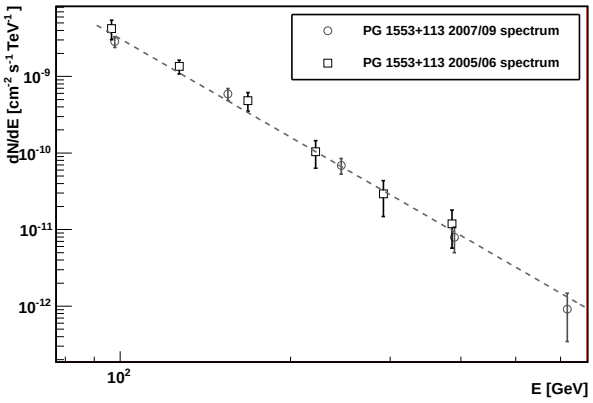

Figure 5.25: Comparison between PG 1553+113 mean spectrum estimated in this work (circles) with previous observations carried out in 2005/06 by MAGIC (squares) from Albert et al. (2007a). The dashed line represents the fit of the data.

overall mean flux emitted by this source is stable. A power law fit gives the values of $\Gamma = 4.27 \pm 0.14$ for the index and $f_0 = (1.61 \pm 0.14) \times 10^{-10}$ s^{-1} cm^{-2} TeV^{-1} for the normalization factor, with a $\chi^2/\mathrm{dof} = 5.68/9$ and a corresponding probability of 77%. The integral flux above 150 GeV is at the level of 8% of the Crab Nebula flux.

VHE photons from cosmological distances are absorbed in the interaction with the EBL (Chapter 3). This effect will be deeply discussed in Chapter 7. Here, we

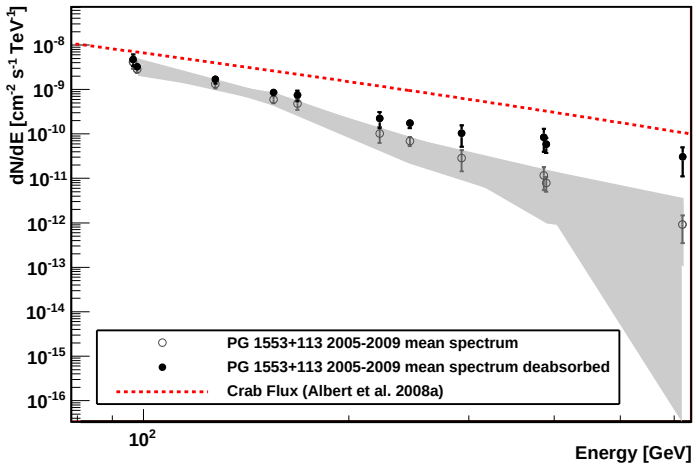

Figure 5.26: Superimposition of 2005-2006 spectrum, from Albert et al. (2007a), to 2007-2009 mean spectrum and corresponding deabsorption for $z = 0.4$ using the EBL model of Domínguez et al. (2011). The continuous line is the power law fit to the deabsorbed spectrum. The fit of the Crab Nebula spectrum measured by MAGIC (Albert et al., 2008) is superimposed for comparison.

simply mention that this effect induces a deformation in the detected spectrum, F_{obs} of a source, which is related to the emitted spectrum, F_{em}, by the formula:

$$F_{obs} = F_{em} \cdot e^{-\tau(E,z)}, \tag{5.4}$$

where τ is the optical depth associated with the interaction.

Figure 5.26 shows the combined differential spectrum of PG 1553+113 from 2005 to 2009, observed (open circles) and deabsorbed (filled circles). The gray band represents the systematic effect on the combined spectrum resulting from different unfolding methods. Taking into account the EBL absorption (Domínguez et al., 2011), the intrinsic spectrum is compatible with a power law of index 3.09 ± 0.20, if we assume a redshift $z = 0.40$, superimposed to the figure.

5.6 Integral flux

In order to explore the VHE γ–ray emission of PG 1553+113 from each year, we compare the integral flux above 150 GeV. This value is a safe compromise taking into account the different energy thresholds. The final samples and the results of the spectral analyses are shown in Table 5.6.

The integral fluxes measured above 150 GeV lie in the range from 4% to 11% of the Crab Nebula flux measured by MAGIC (Albert et al., 2008): the highest flux level recorded is in 2008 (0.11 Crab units), a factor 2-3 larger than the one measured in 2007 (0.04 Crab units[7]) and 2009 (0.05 Crab units). Such changes in the flux level observed in PG 1553+113 are quite moderate in comparison to other monitored TeV blazars. For example, in Mkn 421 a flux variation exceeding one order of magnitude have been observed (Fossati et al., 2008).

A detailed study about possible flux level variations on short timescale is then carried out with the limiting condition that the signal is not strong enough to allow for a detailed sampling on sub-day timescale. The upper panel of Figure 5.27 displays the lightcurve of PG 1553+113 measured from 2007 to 2009 by MAGIC with a variable binning. For comparison, the daily flux levels measured in 2005 and 2006 are shown, as extrapolated from the published data (Albert et al., 2007a), and rescaled according to the power law interpolating that differential flux. Furthermore, the 2006 mean integral flux above 150 GeV taken during the multiwavelength campaing and reported in Albert et al. (2009) is shown. The former data have not been used for the integral flux study, due to very large uncertainties related to the extrapolation procedure. We set 2-days, daily and monthly binning for the 2007, 2008 and 2009 datasets respectively, according to the significance of the signal (for the daily signal analysis, see Appendix B.1). Table 5.8 reports the integral flux values measured above 150 GeV. We find a hint of variability within a factor of 4 during the period monitored in 2008. However, a constant fit to 2008 data drawn in Figure 5.28 has a probability of 50%.

In 2007, the flux values resulting from the temporal analysis are in good agreement with the hypothesis of constant flux (93% of probability). Nothing can be concluded about 2009 sample, since the significance of the signal is too low and prevents a detailed temporal study.

[7] A Crab unit is an arbitrary unit obtained by dividing the integral energy flux measured above a certain threshold by the Crab Nebula flux (which is a stable VHE photons emitters) measured above the same threshold.

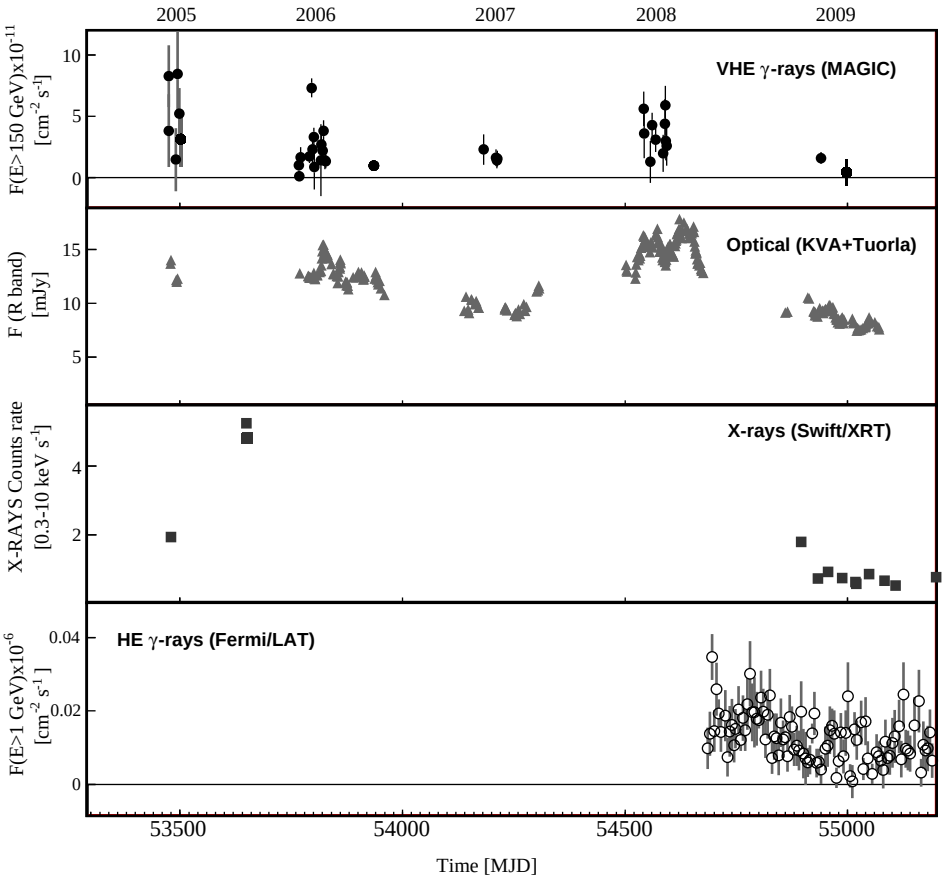

Figure 5.27: Multiwavelength lightcurve of PG 1553+113 from 2005 to late 2009. From upper to lower panel: VHE γ–rays above 150 GeV measured by MAGIC (filled circles), optical flux in the R-band (triangles), X–rays counts rate (squares) and HE γ–rays above 1 GeV (open points).

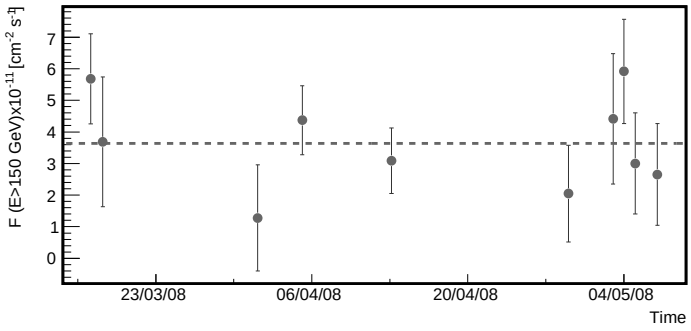

Figure 5.28: Zoom of Figure 5.27 around 2008 MAGIC observations.

In general, the high energy threshold of the analysis together with the weakness of the PG 1553+113 signal and its very steep spectrum make any variability study at small timescale difficult and might have hided the detection of an increased activity on very short timescale. In order to detect or exclude TeV flares from this source, a more sensitive instrument should be used. For this purpose, PG 1553+113 is regularly monitored by the upgraded MAGIC stereo system.

Year	Day	Time [min]	Signif. [σ]	Integral LC ($>$ 150 GeV) [cm^{-2} s^{-1}]
	23/03	58	1.9	$(2.3 \pm 1.2)\times10^{-11}$
2007	19+20/04	182	2.4	$(1.6 \pm 0.6)\times10^{-11}$
	21+22/04	217	2.2	$(1.4 \pm 0.6)\times10^{-11}$
	23+24/04	235	2.4	$(1.6 \pm 0.6)\times10^{-11}$
	17/03	58	4.2	$(5.6 \pm 1.4)\times10^{-11}$
	18/03	26	1.8	$(3.6 \pm 2.0)\times10^{-11}$
	01/04	43	0.8	$(1.3 \pm 1.7)\times10^{-11}$
	05/04	109	4.1	$(4.3 \pm 1.0)\times10^{-11}$
2008	13/04	97	3.1	$(3.1 \pm 1.0)\times10^{-11}$
	29/04	44	1.3	$(2.0 \pm 1.5)\times10^{-11}$
	03/05	24	2.2	$(4.4 \pm 2.0)\times10^{-11}$
	04/05	40	3.7	$(5.9 \pm 1.6)\times10^{-11}$
	05/05	38	1.8	$(3.0 \pm 1.6)\times10^{-11}$
	07/05	40	1.7	$(2.6 \pm 1.6)\times10^{-11}$
2009	17-21/04	359	3.3	$(1.6 \pm 0.4)\times10^{-11}$
	15/06	57	0.4	$(0.4 \pm 1.1)\times10^{-11}$

Table 5.8: PG 1553+113 integral flux study; year of observation (first column), day and duration of the observations (second and third columns), significance of the signal (fourth column) and integral lightcurve above 150 GeV detected (last column).

5.7 PG 1553+113 as seen at other wavelengths

Figure 5.27 displays the lightcurve of PG 1553+113 in different wavelengths. The MAGIC data shown cover five cycles of TeV observations at energies above 150 GeV. The time bins used are variable, as described in the previous Section.

The simultaneous optical R-band data are outlined in the second panel. These data are collected on a nightly basis by the Tuorla Observatory Blazar Monitoring Program[8] (Takalo et al., 2007) using the KVA 35 cm telescope at La Palma and the Tuorla 1 meter telescope in Finland. The public X-ray data, results of an automatic analysis performed by the *Swift*/XRT Monitoring Program[9], are shown in the third panel.

In the lower panel, the *Fermi*/LAT lightcurve of PG 1553+113 above 1 GeV computed in bins of 5 days is displayed. The lightcurve is derived from the publicly available data[10], which are processed using Science Tools 9.15.2, including the Galactic diffuse and isotropic background and the Instrument Response Function (IRF) P6 V3 DIFFUSE. We select the photons of class 3 (DIFFUSE) with energy in the range 1–100 GeV collected between the beginning of *Fermi* data acquisition on 2008 August the 4th (MJD 54682) and 2010 January the 4th (MJD 55200), for a total of $\sim$17 months of elapsed time. In each 5–days time bin, we select photons in the good–time intervals and within a region of interest (ROI) with radius of 10° from the position of the source in the radio band, applying a cut on the zenith angle parameter ($<$ 105°) to avoid the Earth's albedo. Then we calculate the live–time, the exposure map and the diffuse response.

[8] More information at http://users.utu.fi/kani/1m/

[9] http://www.swift.psu.edu/monitoring/

[10] Accessible from `http://fermi.gsfc.nasa.gov`

Taking all this into account, we perform an analysis of the high energy emission in each separate time bin, by using an unbinned likelihood algorithm `gtlike` (Abdo et al., 2009). The model includes the isotropic and Galactic diffuse backgrounds, the source of interest and all the all the sources included in the 1^{st} year *Fermi* catalog (Abdo et al., 2010b) located within the ROI. For all point sources, we assume a power law spectrum, with flux and photon index as a free parameter and calculate the corresponding test statistic (TS; $\sqrt{TS} \simeq \sigma$, see Mattox et al. 1996).

As already noted, during the five years of monitoring the source generally shows a marginal activity in the VHE γ–ray band. The same behavior is followed by the optical flux, whose variations are limited within a factor of four, with a maximum flux reached in 2008 and a minimum value in 2009. A low emission in 2009 is also registered at all the other wavelengths (Figure 5.29) suggesting that the source entered in a low activity state during that year, with a minimum reached a few days after MAGIC observations.

Figure 5.30 shows the result of a correlation study between optical and TeV simultaneous observations. The VHE γ–ray flux above 150 GeV is plotted as a function of the optical flux. In order to increase statistics, we used for 2007–2009 samples the daily lightcurve values; however, since the optical measurements have a different time coverage, in some cases we estimate the mean VHE flux from two or more consecutive days. 2005 and 2006 data, from Albert et al. (2007a), are rejected from this study due to the large uncertainty on the extrapolated flux in the VHE band. The mean flux value from 2006 multiwavelength campaign reported in Albert et al. (2009) is included. A linear relation among the two components has 76% of probability, which suggests a correlation between these two extreme energetic bands. This result is in good agreement with the SSC model, which predicts a correlation between the synchrotron and the IC emission, related to the same electron population. Due to the poor coverage at other wavelengths, the same study has not been performed in X-rays and HE γ–rays.

The X-ray lightcurve shows a pronounced variability, in contrast to optical and VHE bands. The X-ray flux spans an interval of about one order of magnitude (with maximum in 2005 and minimum in 2009), larger than that observed in the TeV, optical and GeV bands. The different variability displayed by the synchrotron (X-ray) and inverse Compton (GeV-TeV) components seems to be somewhat in contrast with the typical behavior observed in TeV BL Lacs, showing, in general, a coordinated variability (Fossati et al., 2008)[11]. However, the sparse sampling of the observations and the lack of a truly simultaneous monitoring prevents any strong conclusion. Coordinated multi-frequency monitoring is necessary to further investigate this important issue.

In a dedicated paper (Abdo et al., 2010a), the *Fermi*/LAT collaboration reports the analysis of the first year of PG 1553+113 data. They find that during the monitoring period the emission above 200 MeV is almost steady. This is in contrast with the behavior of the source at larger energies (> 1 GeV). In our analysis of 2008 and 2009 LAT data drawn in lower panel of Figure 5.27, in fact, a steady emission above 1 GeV has a probability smaller than 0.1% and is ruled out (see Figure 5.31). The lowest flux observed in June 2009 is compatible with zero, while the highest flux, detected in August 2008, has a value of

[11] Rare exceptions to this rule are the so called “orphan" TeV flares, e.g. Krawczynski et al. (2004).

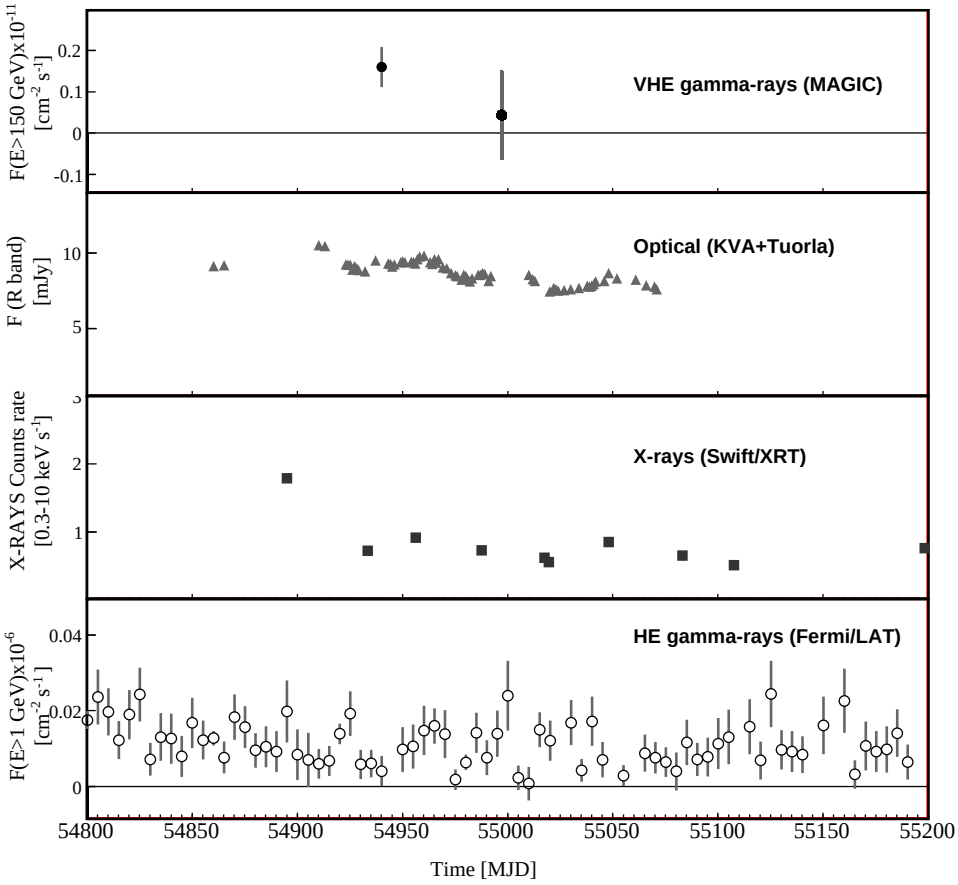

Figure 5.29: Zoom of Figure 5.27 around the Cycle V campaign carried out in 2009. From upper to lower panel: VHE γ–rays above 150 GeV measured by MAGIC (filled circles), optical flux in the R-band (triangles), X–rays counts rate (squares) and HE γ–rays above 1 GeV (open circles).

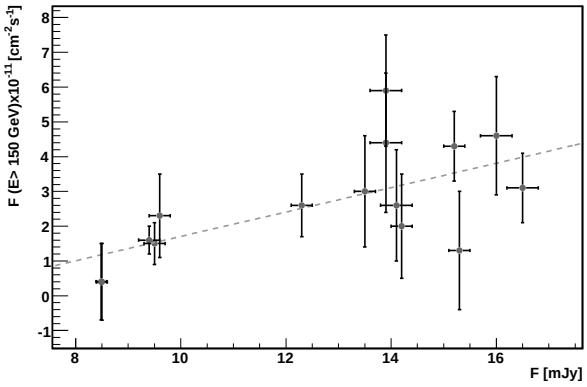

Figure 5.30: Correlation study between PG 1553+113 optical R–band flux and VHE γ–ray integral flux above 150 GeV observed from 2006 to 2009.

$(0.035 \pm 0.006) \times 10^{-6}$ cm^{-2}s^{-1}, a factor 3 higher with respect to the mean flux, $(0.0106 \pm 0.0004) \times 10^{-6}$ cm^{-2}s^{-1}. In our case, we are looking only at the upper edge of LAT band, probably close to the IC peak, while the integral flux above 200 MeV reported by Abdo et al. (2010a) is dominated by lower energies, due to

larger statistics. Therefore, we conclude that while at low energies the IC continuum shows marginal variability, this is not the case in the vicinity of the peak. In fact, small variability at GeV energies is a common feature of HBLs (Abdo et al., 2010b).

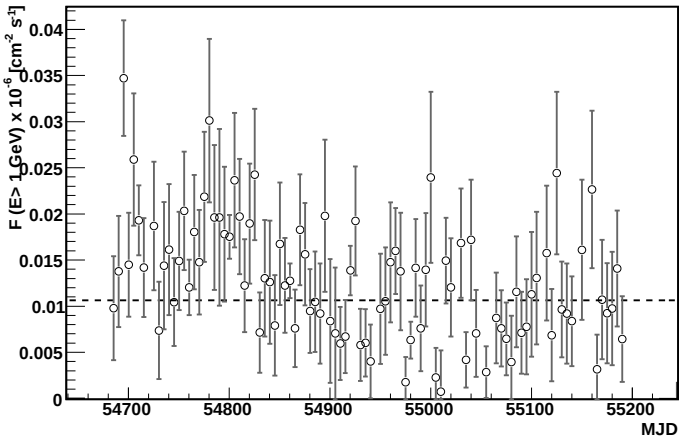

Figure 5.31: Zoom of Figure 5.27 around Fermi/LAT observations.

5.8 Modeling the SED

In Figure 5.32, we assemble the SED of PG 1553+113 using historical data and the MAGIC spectra described in the previous Sections. Open black squares displaying radio-optical data are from NED[12]. In the optical band, we also show (red diamonds) the KVA minimum and maximum flux measured in the period covered by MAGIC 2005-2009 observations together with optical-UV fluxes from *Swift*/UVOT (filled black triangles, from Tavecchio et al. 2010). For the X-ray data, two *Swift*/XRT spectra taken in 2005 (high flux state, red crosses, and intermediate state, black asterisks, from Tavecchio et al. 2010) are given, and a *Suzaku* spectrum taken in 2006 (continuous red line, from Reimer et al. 2008). In addition, the average 14-150 keV flux measured by *Swift*/BAT during the first 39 months of survey (Cusumano et al., 2010) is shown (black star), and the average *RXTE*/ASM flux between March 1 and May 31, 2008 (small black square), from quick–look results provided by the ASM/RXTE team[13].

The green triangles correspond to the LAT spectrum averaged over ~ 200 days (2008 August-2009 February) from Abdo et al. (2010a). As discussed in that paper, the flux above 200 MeV is rather stable, showing very small variability over the entire period of LAT observations. However, it is possible that variability at the highest energies is not detected due to the limited statistics, but is important in determining the averaged spectrum at the highest energies, as suggested in the previous Section.

For MAGIC, we report the 2005-2006 and 2007-2009 observed spectra (filled circles) and the same spectra corrected for the absorption by the EBL using the model of Domínguez et al. (2011) (red open circles).

[12] http://nedwww.ipac.caltech.edu/
[13] http://xte.mit.edu/asmlc/

Table 5.9: Input model parameters for the model reported in Fig.5.32. We report the minimum, break and maximum Lorentz factors, and the low and high energy slope of the electron energy distribution, the magnetic field intensity, the electron density, the radius of the emitting region and its Doppler factor. We also report the derived power carried by electrons, magnetic field, protons (assuming one cold proton per emitting relativistic electron), and the total radiative luminosity.

Parameter		Value
$\gamma_{\rm min}$	$[10^3]$	2.5
$\gamma_{\rm b}$	$[10^4]$	3.2
$\gamma_{\rm max}$	$[10^5]$	2.2
n_1		2.0
n_2		4.0
B	[G]	0.5
K	[10^3 cm^{-3}]	5.35
R	[10^{16} cm]	1
δ		35
$P_{\rm e}$	[10^{44} erg/s]	2.2
P_B	[10^{44} erg/s]	1.5
$P_{\rm p}$	[10^{44} erg/s]	0.34
$L_{\rm r}$	[10^{44} erg/s]	6.3

We model the SED with the one-zone SSC model fully described in Maraschi and Tavecchio (2003), and reported in Chapter 2. The emission zone is supposed to be spherical with radius R, in motion with bulk Lorentz factor Γ at an angle θ with respect to the line of sight. Special relativistic effects are described by the relativistic Doppler factor, $\delta = [\Gamma(1-\beta\cos\theta)]^{-1}$. The electron energy distribution of the relativistic emitting electrons is described by a smoothed broken power law function, with limits $\gamma_{\rm min}$ and $\gamma_{\rm max}$ and break at $\gamma_{\rm b}$. To calculate the SSC emission, we use the full Klein–Nishina cross section.

Given the large variations of the X-ray synchrotron flux, we decid to use the average level of the synchrotron bump as measured by XRT, including also ASM and BAT fluxes to constrain the model. The corresponding input parameters are listed in Table 5.9. We also report the derived powers carried by the different components, relativistic electrons, P_e, magnetic field, P_B, and protons, P_p (assuming a composition of one cold proton per relativistic electron), and the total radiative luminosity $L_{\rm r} \simeq L_{\rm obs}/\delta^2$.

The derived value of the total jet power, $P_{\rm jet} = P_{\rm e} + P_B + P_{\rm p} = 4 \times 10^{44}$ erg/s, is consistent with the typical values inferred modelling similar sources (Ghisellini et al., 2010b). We use a relatively large minimum electron Lorentz factor, $\gamma_{\rm min} \sim 10^3$ in order to reproduce the hard MeV-GeV continuum observed by LAT. The high value of $\gamma_{\rm min}$ implies that, as commonly derived in TeV BL Lacs, the relativistic electrons (and the magnetic field, almost in equipartition) carry more power than the cold proton component. Another characteristics that PG 1553+113 shares with the other TeV BL Lacs is that the total luminosity $L_{\rm r}$ is larger than the power supplied by electrons, magnetic field and protons. As discussed in Celotti and Ghisellini (2008), this implies that either only a small fraction of leptons is accelerated at relativistic energies (leaving a reservoir of cold pairs and/or protons) or that the jet is dissipating a large fraction of its power as radiation, eventually leading to the deceleration of the flow, as in fact observed at VLBI scales (Piner et al., 2010) and envisaged in the models of structured jets (Georganopoulos and Kazanas, 2003; Ghisellini et al., 2005).

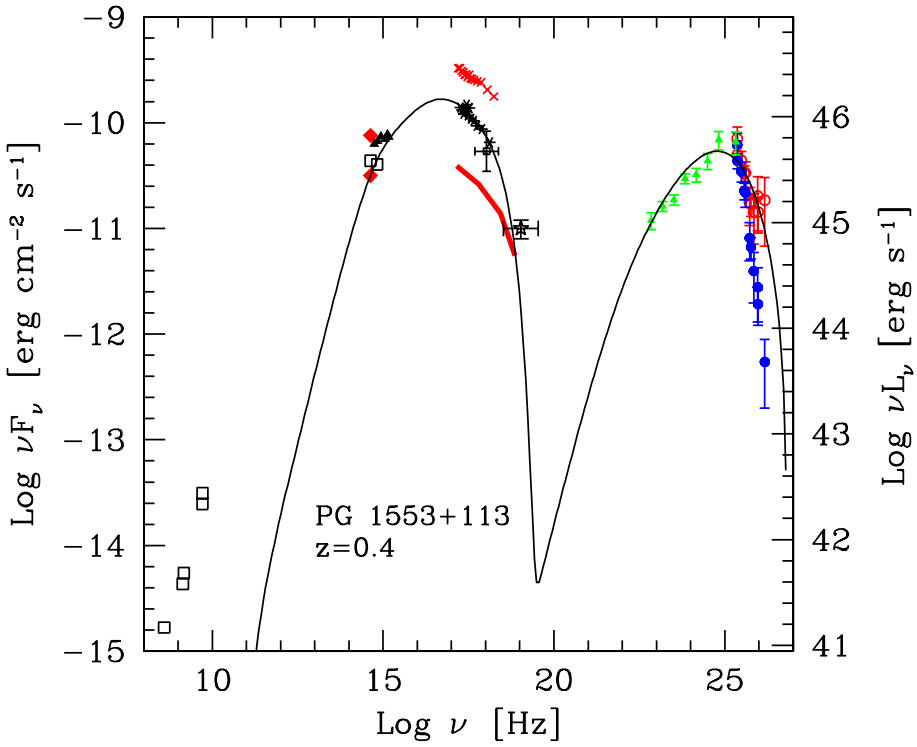

Figure 5.32: SED of PG 1553+113. Open black squares are radio-optical data from NED, red diamonds represent the KVA minimum and maximum flux measured in the period covered by MAGIC observations, together with optical-UV fluxes from *Swift*/UVOT (filled black triangles). For the X-ray data, two *Swift*/XRT spectra taken in 2005 (high flux state, red crosses, and intermediate state, black asterisks) are given, and a *Suzaku* spectrum taken in 2006 (continuous red line). The average 14-150 keV flux measured by *Swift*/BAT (black star) and the average *RXTE*/ASM flux between March 1 and May 31, 2008 (small black square), are also represented. The LAT spectrum averaged over $\sim$200 days (2008 August-2009 February) is given (green filled triangles). For MAGIC, we display the 2005-2006 and 2007-2009 observed spectra (blue filled circles) and the same spectra corrected for the absorption by the EBL (red open circles). The SED is modeled with a one-zone SSC model (continuous black line). Detailed references are addressed in the text.

5.9 Conclusions

In this Chapter, we have presented the analysis of three years of VHE γ–ray data of PG 1553+113 collected by MAGIC from 2007 to 2009. The dataset has been divided into individual years, and a significant signal was found in every sample, confirming PG 1553+113 as a stable presence in the VHE sky. The overall flux above 150 GeV from 2007 to 2009 shows only a modest variability on yearly time-scale, within a factor 3, corresponding to a variation between 4% to 11% of the Crab Nebula flux. No clear variability on smaller time-scale is evident in the

sample.

For the spectral analysis, the dataset was combined with previous observations carried out by MAGIC during the first two Cycles of operations, from 2005 to 2006, for a total of five years of monitoring. This sample was excluded from the temporal study due to very large systematics related to the flux extrapolation procedure. Despite the hints of variability on the flux level, the differential flux from each year is in very good agreement with a power law of constant index 4.27 ± 0.14. This behavior has been already observed in other blazars, such as the HBL 1ES 1218+304 (Acciari et al., 2010).

PG 1553+113 was also monitored in optical, X-ray and HE γ–ray frequencies, but only the former data could be used for correlation studies thanks to the good time coverage. Interestingly, a hint of correlation with probability of 76% was found between MAGIC and R-band optical flux levels, which in turn shows only a modest variability within a factor 4. A clear variability is seen in X-rays and γ–rays above 1 GeV. The latter outcome, exploring the energies close to the IC peak, is only apparently in contradiction with previous results stating a quite stable spectrum for this source in the HE (> 200 MeV) γ–ray band (Abdo et al., 2010a). The different energy thresholds used in the two studies can, in fact, explain very well the discrepancy, as discussed in the Chapter.

Finally, for the study of the SED, the mean differential spectrum measured by MAGIC an corrected for EBL absorption, assuming a redshift of $z = 0.4$, was combined with historical data at other wavelengths. Due to the large variations observed in X–rays and characterizing the synchrotron peak, we decided to use for the SED modeling the high energy bump, and the average level of the low energy bump. A more precise model requires coupling the VHE γ–ray part of the spectrum with simultaneous coverage of the synchrotron peak, in particular at optical-X-ray energies. An interesting feature of PG 1553+113 is the narrowness of the SSC peak derived from the LAT and MAGIC spectra, implying a relatively large value of the minimum Lorentz factor of the emitting electrons, 2.5×10^3. This is also required by other HBLs with hard GeV spectra (e.g. Tavecchio et al. 2010).

The MAGIC stereo system, with its increased sensitivity and low energy threshold, is the suitable instrument to further investigate an eventual daily scale TeV variability, as well as provide a good differential spectrum determination below 100 GeV.

El que busca la verdad corre el riesgo de encontrarla.

Isabel Allende

6

VHE γ–ray emission from the unknown distance blazar PKS 1424+240

THE UNKNOWN DISTANCE BLAZAR PKS 1424+240 is another extragalactic object monitored by MAGIC since 2006, only recently discovered as VHE γ–rays emitter. In this Chapter, we present the analysis of the data collected by MAGIC in 2009 in single telescope mode, observation triggered by an optical outburst, and with the MAGIC stereoscopic system in 2010. In 2009 a hint of signal of more than $4\,\sigma$ of significance is found, which comes mainly from the low energy region, below 400 GeV. In 2010 instead a clear signal of $5.7\,\sigma$ is seen. The mean differential flux is compatible with a power law of steep index $\Gamma = 4.0 \pm 0.6$. The integral flux recorded above 150 GeV is at the level of 0.06 Crab units in 2009, and 0.01 Crab units in 2010. Moreover, in 2009 there are hints of monthly flux variations. Dedicated analyses of PKS 1424+240 data in other frequencies show a marginal variability at almost all frequencies. Thanks to a partial overlap between optical and TeV data, a correlation study is performed, and a hint of correlation is found.

Part of this work will be included in Aleksić et al. (2011), in preparation.

6.1 Introduction

The blazar PKS 1424+240, located at Ra 14 h 27 m 00.4 s and Dec +23 d 48 m 00 s, was first discovered in the late seventies as a radio source. Recently, thanks to the discovery led by the VERITAS Collaboration, it has entered the family of VHE γ–rays emitters (Acciari et al., 2010a). VERITAS observations were triggered by the report of its detection at HE by *Fermi*/LAT. This fact confirmed the key role of *Fermi* satellite as a source of information for finding promising sources at higher energies.

As for many BL Lacs, such as PG 1553+113, the distance of PKS 1424+240 is still unknown. Despite several observing campaigns with optical instruments, no emission or absorption lines have been detected. Moreover, the observed jet emission from this source, largely enhanced by relativistic effects, is so bright that prevents optical observation of the host galaxy. Past measurements resulted in the lower limit on the redshift of $z > 0.06$ (Scarpa and Falomo, 1995) and more recently of $z > 0.67$ (Sbarufatti et al., 2005a).

The source PKS 1424+240 was observed in single-telescope mode (using only MAGIC I) in May–June 2006, February 2007 and from April to June 2009, when MAGIC II was in the commissioning phase, and re-observed in stereo mode in Spring 2010.

In particular, 2009 observations were triggered by an optical outburst in the R band, revealed by the Tuorla/KVA telescopes. Figure 6.1 shows the optical lightcurve of PKS 1424+240 from 2006 to 2010. In March 2009 (MJD 54900), the flux increased significantly with respect to previous observations, suggesting that the source underwent a flaring state at these frequencies.

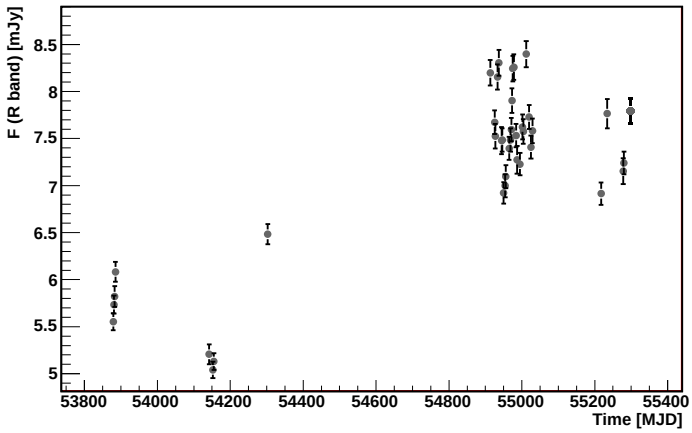

Figure 6.1: Optical lightcurve, from Tuorla/KVA telescopes.

According to SSC models, a variability in the low energy peak, as that observed in PKS 1424+240, should be mimicked by the high energy bump of the SED (see Chap. 2). It follows that if this is the case, a strong correlation between the optical and VHE γ–rays should be found. This is in agreement with recent experimental findings, such as those presented in last Chapter (i.e. 5.7). A successful strategy for the discovery of new VHE γ–rays emitters is that of monitoring the optical state of promising sources and observe them with Cherenkov telescopes in correspondence to high optical states. The HBL Mkn 180 was discovered as VHE γ–ray emitter by MAGIC thanks to this approach (Albert et al., 2006b). This was also the strategy which led to the detection, in 2009, of a significant signal from PKS 1424+240.

Here, we present the results of MAGIC observations of PKS 1424+240 in 2009 and 2010, and perform a study of the source emission, applying a multiwavelength approach.

6.2 Dataset and signal search

PKS 1424+240 was observed in 2009 for 23 hours with MAGIC, operating in single telescope mode. Out of this sample, described in detail in Appendix B, we selected 13.2 h of good quality data for the analysis. MAGIC re-observed the source in stereoscopic mode[1] for ∼16.6 hours in early 2010, between March to April. The quality of this sample is surprisingly good, and we used all the data for the successive steps of the analysis.

The zenith angle of the observations, reported in Table 6.1 along with the daily time coverage and the mean rate after cleaning, ranges from 4°to 32°. All the data were taken in wobble mode.

[1] i.e. MAGIC I and MAGIC II simultaneously.

Cycle	Date	Eff. Time [min]	Zd [°]	Mean Rate [Hz]
	17/04/2009	30	5–9	174
	18/04/2009	96	5–13	177
	19/04/2009	70	5–10	173
	21/04/2009	67	5–10	172
	22/04/2009	92	5–13	177
	23/04/2009	70	5–11	176
V	24/04/2009	69	5–11	174
	20/05/2009	23	5–26	160
	12/06/2009	18	9–12	152
	15/06/2009	88	6–24	152
	20/06/2009	34	22–30	143
	21/06/2009	79	8–28	163
	22/06/2009	17	10–13	155
	23/06/2009	42	20–30	150
	14/03/2010	66	5–11	95
	18/03/2010	83	6–11	78
	20/03/2010	154	5–29	79
	21/03/2010	98	8–29	82
VI	22/03/2010	92	5–14	88
	23/03/2010	69	9–31	72
	24/03/2010	169	5–32	83
	25/03/2010	121	6–31	84
	06/04/2010	29	11–14	91
	07/04/2010	66	5–14	76
	18/04/2010	69	12–26	113

Table 6.1: PKS 1424+240 2009 and 2010 datasets used in this study after data quality selection. From left to right: MAGIC Cycle of observation (first column) and corresponding dates in dd/mm/yy (second column); effective time of observation in minutes and zenith angle range in degrees (third and fourth columns). In the last column, the rate of the events after the image cleaning, in Hz, is reported.

The analysis of both datasets is performed with the standard MAGIC analysis and reconstruction software, described in previous Chapters. Also in this case, dedicated MC files, simulating γ–like events, are employed. We use the θ^2 approach for the signal search, which, as anticipated in previous Chapter, consists in plotting the squared angular distance between the estimated and the true source position (camera center in case of On/Off observations, the wobble center otherwise). Regarding the estimated source position, it is reconstructed during the data analysis steps. Precisely, what is reconstructed is the angular distance between the center of gravity of the image and the shower direction, the so–called `DISP`.

In the analysis of stereo data of PKS 1424+240 we take advantage of a new direction reconstruction method based on the `DISP` RF method, described in Aleksić et al. (2010b) and adapted to the stereo observations. In order to combine information from both the geometrical and timing properties of images in the most efficient way, the Random Forest method is used also for the `DISP` reconstruction.

Figure 6.2 shows the rate after cleaning distributions of the 2009 and 2010 samples. The event rate has a significantly higher value in 2009 sample w.r.t. 2010. Namely, it is $\sim$170 Hz for 2009 and only $\sim$90 Hz for 2010 sample. This difference is mainly related to the stereo data taking mode adopted in 2010 observations (see next Section for a detailed explanation).

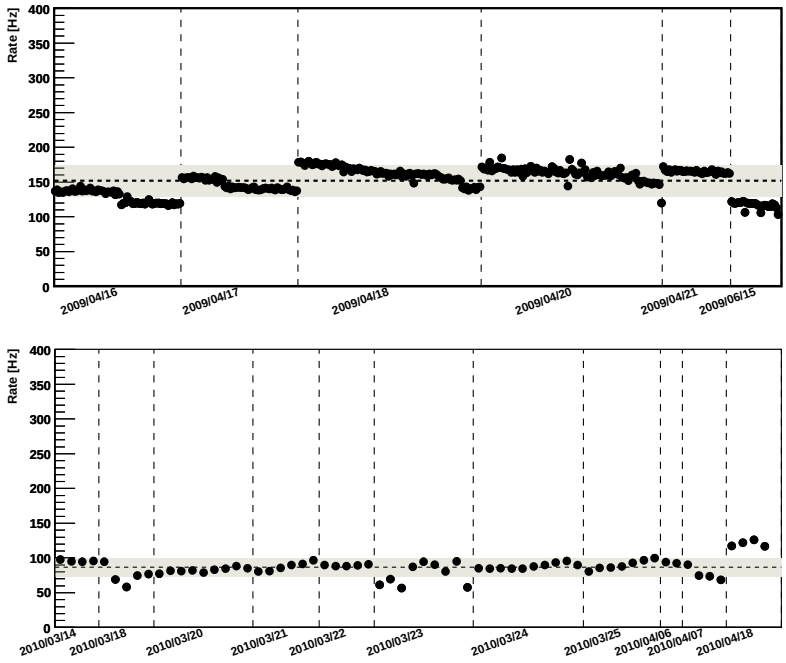

Figure 6.2: Event rate distributions after data quality selection of 2009 and 2010 PKS 1424+240 data registered by MAGIC. An area corresponding to $\pm$10% of the mean value is superimposed to both plots.

6.2.1 θ^2 plots

For the signal search, we present the analysis of the distribution of the θ^2 parameter:

2009 results the θ^2 distribution of 2009 sample drawn in Figure 6.3(a) indicates the presence of a hint of signal, which seems to originate from the low energy region (below 300 GeV), Figure 6.3(b). The distribution shows a weak excess of 418 events of 4.2 σ of significance, calculated according to Eq. 17 of Li and Ma (1983). The significance of the signal becomes 4.5 σ if we reduce our analysis to the events with reconstructed energy below 300 GeV. In both distributions we have used three Off regions for the signal extraction. To do so, we applied a cut in `size` at 200 phel. The corresponding energy threshold is 150 GeV, (Fig. 6.4). In addition, we applied a dynamical `hadronness` cut for the selection of the γ–like events.

If we apply a lower `size` cut at 80 phel, and use only one Off region, the significance of the signal drops significantly (below 3 σ), despite the lower energy threshold. Therefore, in this case, the improved sensitivity of the instrument that we reach if we apply a higher `size` cut, combined with the possibility of using three Off regions, is essential for the signal detection.

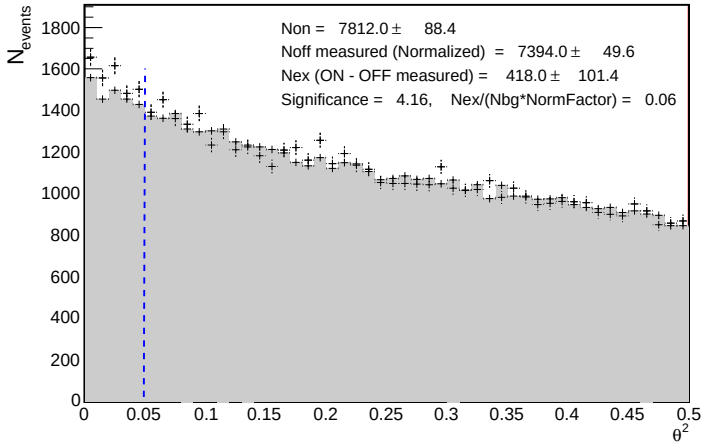

(a) Integral energy plot.

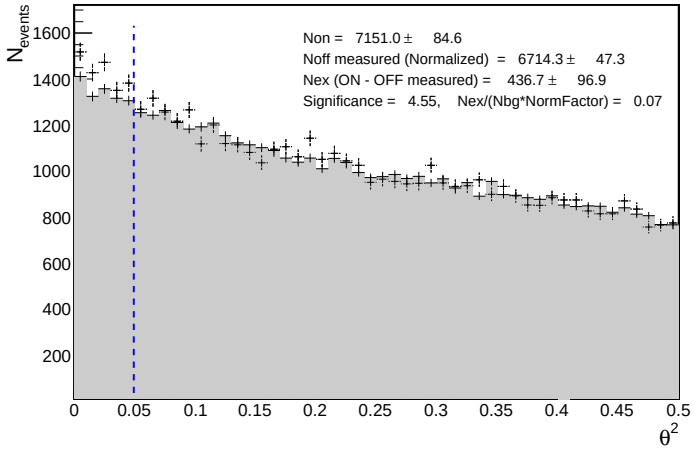

(b) θ^2 plot of the events with energy below 300 GeV.

Figure 6.3: Integral θ^2 plot of PKS 1424+240 data taken in 2009.

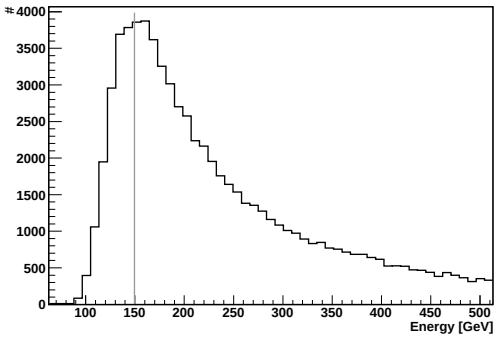

Figure 6.4: Energy threshold of 2009 PKS 1424+240 data analysis.

2010 results The θ^2 plot of 2010 sample in the integral energy range shows the presence of a clear signal of significance 5.75 σ as displayed in Fig. 6.5, obtained by applying a `hadronness` cut at 0.28.

Conversely to what we observe in the 2009 sample, in this case a better significance is obtained by applying a very low `size` cut, at 50 phel, and using only one Off region. This could be related to the lower background

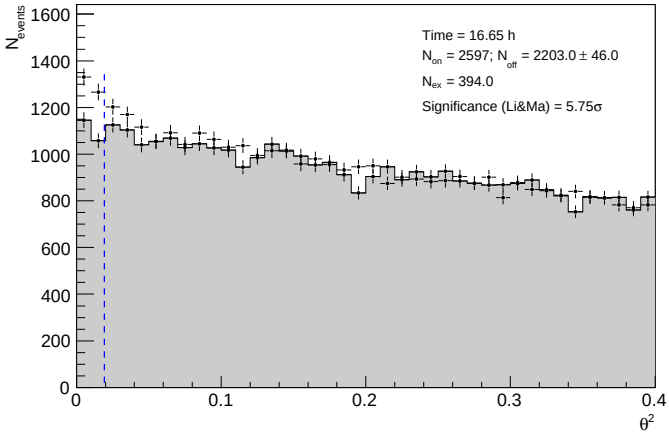

Figure 6.5: θ^2 plots of PKS 1424+240 data registered in 2010.

level registered when observing in stereoscopic mode. The corresponding energy threshold is 100 GeV, Figure 6.6.

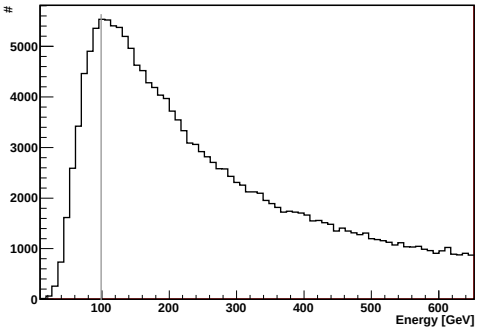

Figure 6.6: Energy threshold of 2010 PKS 1424+240 data analysis.

The comparison of the background levels of the two distributions shows that despite the longer exposure time, the 2010 θ^2 plot has 33 % less background events. This is due to the data taking mode: when working as stereoscopic system, MAGIC registers only data collected by both telescopes (L3 trigger), leading to a pronounced reduction of the background. This is also the reason of the difference between the two event rate distributions.

Period	Obs. Time	N_{exc}	Signif.
2009	13.0 h	437	$4.2\,\sigma$
2010	16.6 h	275	$5.7\,\sigma$

Table 6.2: PKS 1424+240 signal study

6.3 Differential energy spectrum

In this Section, we report the results of the differential spectrum analyses performed on PKS 1424+240 samples. Individual year results are described and finally compared and combined; we set 25 energy intervals between 5 GeV to

50 TeV. In both cases, the spectra can be well fitted with a simple power law of the usual form:

$$\frac{dF}{dE} = f_0 \cdot (\frac{E}{200\,\mathrm{GeV}})^{-\Gamma} \tag{6.1}$$

The small significances of the signals detected, which could be improved by extended observations, prevent the estimation of the individual unfolded spectra.

2009 sample For the spectrum determination of the 2009 sample, we perform a θ^2 analysis in bins of energy. We adopt a `size` cut at 200 phel, like in the signal search case. The cuts in `hadronness` and θ^2, along with the significance of the signal found in each energy bin, are listed in Table 6.3.

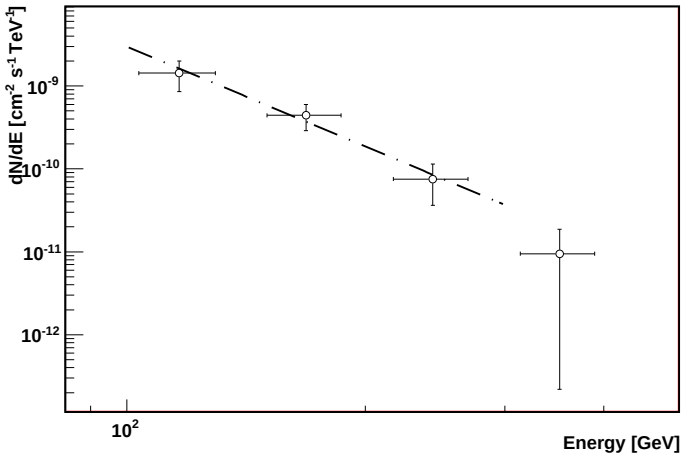

Figure 6.7: Differential energy spectrum of PKS 1424+240 2009 dataset.

The cuts applied are selected according to the corresponding efficiency on MC data. In both cases, we set the cuts such that the 70% of the simulated events survive. The last column lists the measured flux, in each bin, obtained by dividing the number of excess event by the effective area and time (Sec. 5.2). A significant signal, between $2\,\sigma$ to $3\,\sigma$ significance, is found in three energy bins, between 100 GeV to 250 GeV, while a hint of signal of $1\,\sigma$ significance is obtained in the energy bin centered at 350 GeV. This result confirms what we have already noticed in the signal search analysis: the emission is concentrated at low energies, below 400 GeV.

The differential spectrum is drawn in Figure 6.7. A power law fit of the data

Mean energy [GeV]	`had` cut	θ^2 cut	Significance [σ]	Flux [cm^{-2} s^{-1} TeV^{-1}]
116	0.36	0.050	2.5	$(1.4 \pm 0.6)\times10^{-09}$
168	0.30	0.040	2.9	$(4.4 \pm 1.5)\times10^{-11}$
243	0.21	0.030	1.9	$(7.5 \pm 3.9)\times10^{-11}$
351	0.15	0.020	1.0	$(9.5 \pm 9.2)\times10^{-12}$

Table 6.3: Spectral analysis of the PKS 1424+240 2009 sample. Mean energy of the bin, first column, `hadronness` and θ^2 cut applied in in the θ^2 plots and corresponding significance, central columns, mean flux before unfolding, last column.

(limited to the first three significant bins) is characterized by a soft index of $\Gamma = 4.0 \pm 1.3$, and a factor $f_0 = (1.9 \pm 0.8)\times10^{-10}$ cm^{-2}s^{-1}TeV^{-1}.

2010 sample The results of the spectral analysis for this dataset are listed in Table 6.4. The efficiency on MC data of the θ^2 cuts is, like in previous sample, set to 70%. Regarding the `hadronness`, instead, we had to apply very loose cuts (efficiency 90%), in order to avoid some systematics related to hardware inefficiencies of MAGIC II.

Mean energy [GeV]	`had` cut	θ^2 cut	Significance [σ]	Flux [cm^{-2} s^{-1} TeV^{-1}]
116	0.44	0.045	1.7	$(2.2 \pm 1.3)\times10^{-10}$
168	0.43	0.030	2.0	$(7.2 \pm 3.6)\times10^{-11}$
243	0.40	0.020	1.8	$(1.9 \pm 1.1)\times10^{-11}$
351	0.37	0.015	1.2	$(4.5 \pm 3.8)\times10^{-12}$

Table 6.4: Spectral analysis of the 2010 sample. Mean energy of the bin, first column, `hadronness` and θ^2 cut applied in in the θ^2 plots and corresponding significance, central columns, mean flux before unfolding, last column.

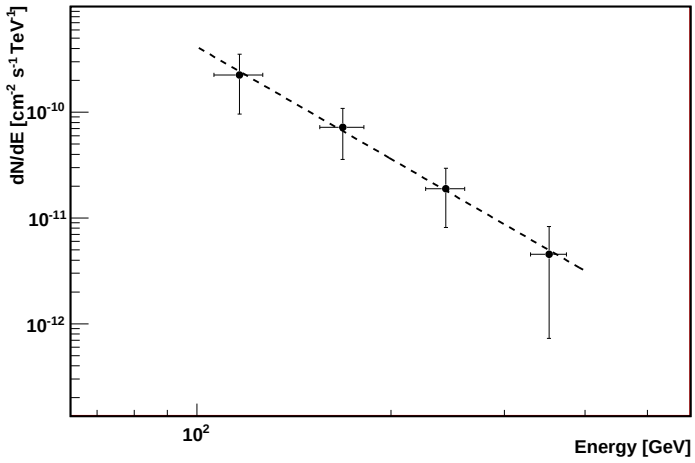

Figure 6.8: Differential energy spectrum of the PKS 1424+240 2010 dataset.

Figure 6.8 shows the differential spectrum measured. A power law fit to the data in the range 100–400 GeV has a slope of $\Gamma = 3.5 \pm 0.8$, in agreement, within the (very large) errors, with the slope measured in 2009. Regarding the normalization factor, its value if $f_0 = (0.4 \pm 0.1)\times10^{-10}$ cm^{-2}s^{-1}TeV^{-1}.

Combined sample Table 6.5 summarizes the outcome of the fits of the differential energy spectra. The results obtained by VERITAS are reported for comparison and will be discussed in the next Section. Regarding MAGIC results, while the slopes of the two measurements are well compatible, as noticed above, the normalization factor of 2010 is significantly lower than that fitting 2009 spectrum. This difference could be due to a different emission state of the source during the two observation periods, and will be further analyzed in Section 6.4. The relevance of this result, however, is mitigated by the large error bars affecting 2009 parameters, which in turn

Period	f_0 [cm^{-2} s^{-1} TeV^{-1}]	Γ
2009	$(1.9 \pm 0.8)\times10^{-10}$	4.0 ± 1.2
2010	$(0.4 \pm 0.1)\times10^{-10}$	3.5 ± 0.8
Mean spectrum (09+10)	$(0.56 \pm 0.14)\times10^{-10}$	4.0 ± 0.6
2009 (VERITAS)	$(0.51 \pm 0.09)\times10^{-10}$	3.8 ± 0.5

Table 6.5: Parameters of PKS 1424+240 power law fit of the spectra.

are due to the small significance of the signal. In addition the spectra cannot be unfolded, as noticed before. Therefore, we cannot perform a conclusive comparison between the two spectral determinations, and we cannot directly compare these individual years spectra with VERITAS spectrum. For the comparison we will adopt, instead, the mean spectrum measured by MAGIC in 2009/10, which, thanks to the improved significance of the combined signal, can be unfolded.

Mean energy [GeV]	Flux [cm^{-2} s^{-1} TeV^{-1}]
96	$(1.03 \pm 0.27)\times10^{-09}$
165	$(1.3 \pm 0.39)\times10^{-10}$
282	$(1.3 \pm 0.66)\times10^{-11}$
488	$(2.2 \pm 3.7)\times10^{-12}$

Table 6.6: Results of the unfolded spectrum analysis of PKS 1424+240.

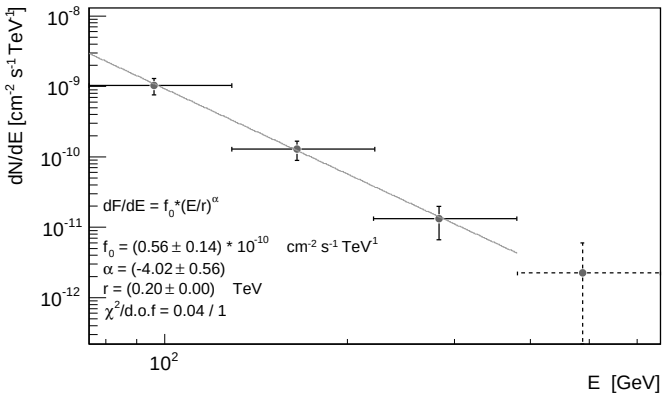

Figure 6.9: Combined unfolded spectrum of PKS 1424+240 measured by MAGIC in 2009 and 2010.

The mean spectrum obtained by combining 2009 and 2010 spectra through the unfolding procedure is displayed in Figure 6.9. The individual energy bins results are listed in Table 6.6. A power law fit to the data in the range 80–400 GeV gives a spectral index of $\Gamma = 4.0 \pm 0.6$, in line with the individual measurements, while f_0 is $(0.56 \pm 0.14) \times 10^{-10}\,\mathrm{cm^{-2}s^{-1}TeV^{-1}}$, value which is much closer to the 2010 normalization factor. Due to its low significance, the point above 400 GeV is excluded from the fit.

The systematic uncertainty of the unfolded MAGIC spectrum is estimated

to be 35% in the flux level and 0.2 in the power index, analogously to the the case of PG 1553+113.

6.3.1 Comparison with VERITAS spectrum

Figure 6.10 shows the comparison between the mean unfolded spectrum of PKS 1424+240 measured in 2009 and 2010 by MAGIC, and that measured by VERITAS in 2009. The parameters resulting from the fits are listed in Table 6.5.

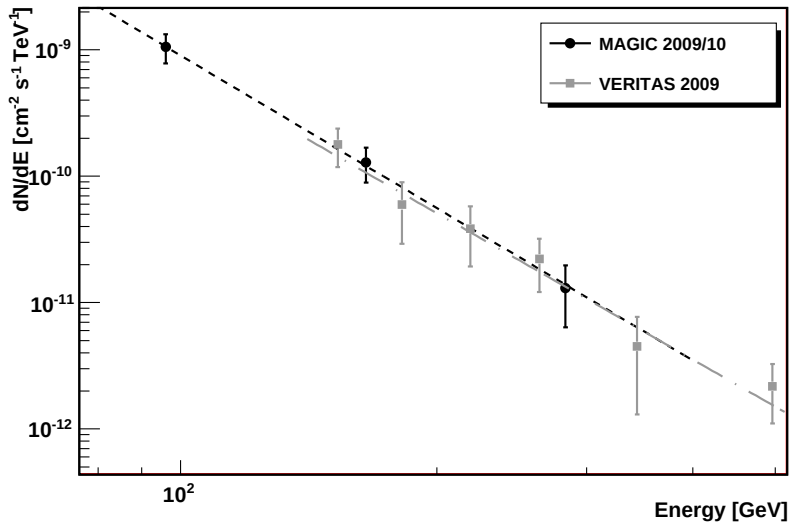

Figure 6.10: Mean differential energy spectrum of PKS 1424+240 measured by MAGIC (filled circles) superimposed to the spectrum measured by VERITAS (filled squares) in 2009 (Acciari et al., 2010a), partially simultaneous to MAGIC observations.

The good agreement between the two determinations is evident. Both the spectral slopes, $\Gamma_V = 3.8 \pm 0.5$ while $\Gamma_M = 4.0 \pm 0.6$, and the normalization factor at 200 GeV, which in in units of 10^{-10} cm^{-2}s^{-1}TeV^{-1} are $f_{0(V)} = 0.51 \pm 0.09$ and $f_{0(M)} = 0.56 \pm 0.14$, are well compatible, within the (large) error bars.

This result could be an evidence that the mean spectrum emitted by PKS 1424+240 in 2009/10 is stable. However, the individual years results found by MAGIC, suggest a higher state of the source during MAGIC observations in 2009. This possibility will be analyzed in the next Section.

6.4 Temporal analysis

In order to investigate the temporal evolution of PKS 1424+240 emission, we study the individual years integral flux emission above 150 GeV as a function of time. Due to technical reasons, we have to exclude from the lightcurve analysis 4.2 hours from 2009 sample and 2.4 hours in 2010 sample. Therefore, the datasets that we use in this study are composed of 7.8 h of MAGIC data collected in 2009 and of 14.2 h of data collected in 2010. We selected the temporal bins according to the significance of the signal. For completeness, the daily values are reported in Appendix B.

2009 sample The integral flux study of 2009 sample, we set a 2–days binning for

Year	Period	Time [min]	Signif. [σ]	F ($>$ 150 GeV) [cm^{-2} s^{-1}]
2009	17/04–19/04	99	1.7	$(2.4 \pm 1.4)\times10^{-11}$
	21/04–22/04	106	1.1	$(1.6 \pm 1.4)\times10^{-11}$
	23/04–24/04	87	3.4	$(5.4 \pm 1.6)\times10^{-11}$
	12/06–22/06	187	0.5	$(0.5 \pm 1.0)\times10^{-11}$
2010	14/03–25/03	710	1.9	$(0.3 \pm 0.2)\times10^{-11}$
	06/04–18/04	147	1.5	$(0.6 \pm 0.4)\times10^{-11}$

Table 6.7: PKS 1424+240 integral flux study. The year of observation (first column), the period covered (second column), the exposure time (third column), the significance of the signal detected (fourth column) and the integral flux measured (last column) are reported.

the April subsample, while a monthly binning for the June subsample. In April, the source emission above 150 GeV is at the level of 0.09 ± 0.03 Crab units, and seems in a higher state with respect to June (0.015 ± 0.031 Crab units). In particular, at the end of the month we see an increased activity, at the level of 17% ± 5% Crab Nebula flux. The large error bars involved, however, due to the small signal detected, prevent any strong conclusion about a possible variability of the source emission.

The MAGIC lightcurve of 2009 VHE γ–rays observations above 150 GeV is drawn in Figure 6.11, superimposed to the mean flux registered by VERITAS during the observations (dashed horizontal line) carried out in the days marked with the gray bands. This value has been estimated from the power law fitting the spectrum and is affected by large error bars related to the extrapolation procedure.

During its observations, VERITAS registered above 150 GeV a mean flux at the level of 2% ± 0.1% of that of the Crab Nebula flux. This flux level is significantly lower the mean flux observed by MAGIC in 2009 (6% ± 2% of the Crab flux). Moreover, VERITAS reported a flux compatible with

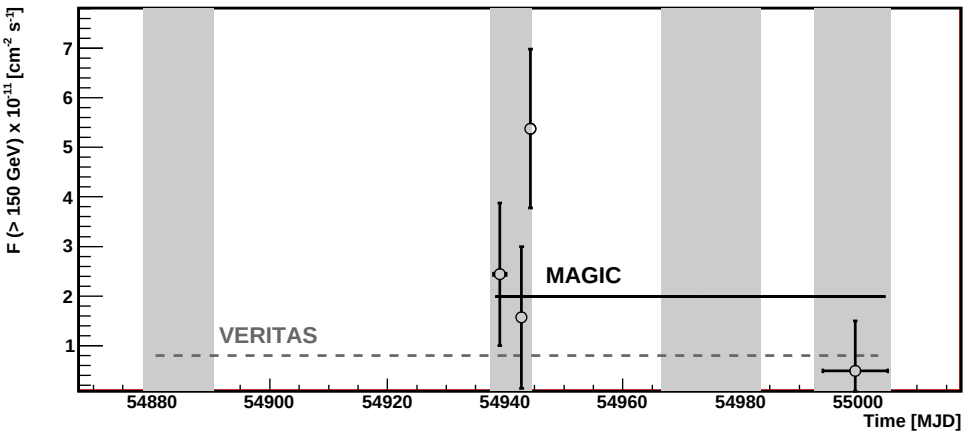

Figure 6.11: Daily lightcurve of PKS 1424+240 2009 sample. The gray bands represent the time slots of VERITAS observations.

a steady emission, in contradiction with the hint of variability found by MAGIC in 2009 data. It is evident, however, that VERITAS monitored the source for a longer period, and only part of the data collected overlap with MAGIC observations. In particular, it seems that VERITAS did not observe PKS 1424+240 during the apparently "higher" state detected at the end of March. Therefore, the controversial result found could be due to a different sampling of the two observations.

2010 sample Due to the small significance of the daily integral flux above 150 GeV registered in 2010 sample (see Appendix B), we set a monthly binning for the lightcurve. The significance of the signal from the individual months, reported in Table 6.7, is $1.5\,\sigma$ in April and $1.9\,\sigma$ in May. Figure 6.12 displays the corresponding VHE lightcurve of PKS 1424+240 above 150 GeV. The flux is compatible with a steady (faint) flux at the level of 1.2% Crab flux. No significant flares are evident at monthly scale. The flux observed is in agreement with the flux detected from the source in 2009 by VERITAS, and, compared to previous results, significantly lower than that observed by MAGIC in 2009.

Final remarks Table 6.8 summarizes the integral flux emitted by PKS 1424+240 measured by MAGIC during the biennium 2009/10, compared to that observed in 2009 by VERITAS. In the 2009 sample collected by MAGIC the mean flux registered above 150 GeV is at the level of 6% of the Crab Nebula flux above the same threshold, and there are traces of monthly variation. Interestingly, this behaviour has not been observed by VERITAS, which monitored the source for a longer period and found a mean integral flux at the level of 2% of Crab Nebula flux. This flux state is somehow similar to that registered by MAGIC in 2010, which stabilizes at the level of 0.01 Crab units.

A possible explanation for the results found is that PKS 1424+240 experienced an increased activity at VHE γ–rays at the end of March 2009, period better covered by MAGIC dataset. This caused a higher mean flux state

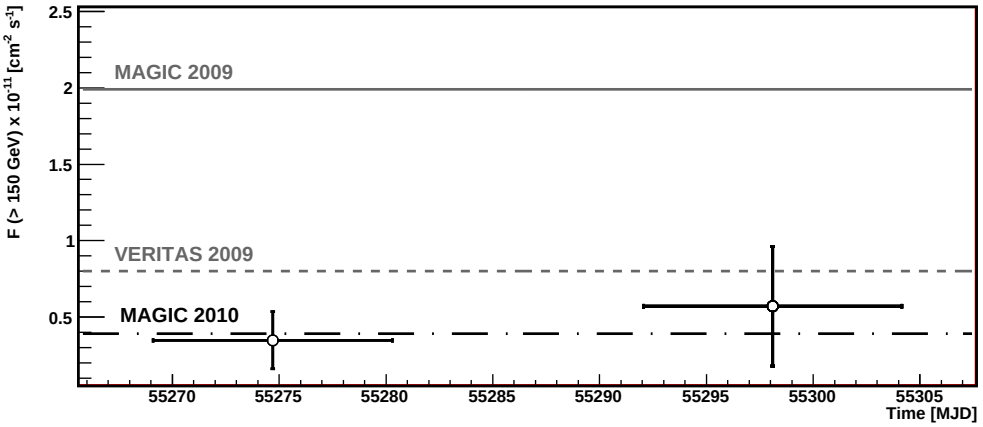

Figure 6.12: Monthly lightcurve of PKS 1424+240 2010 sample measured by MAGIC, along with the mean flux (dashed–dotted line). The mean flux detected by MAGIC in 2009 (continuous line) and that found by VERITAS (dashed line) are superimposed for comparison.

registered in 2009 by MAGIC (and corresponding higher mean spectrum). The flux state observed by MAGIC in June 2009, instead, as well as that observed in 2010, are compatible with the mean flux reported by VERITAS in 2009 obtained with a wide sample, and suggests that the mean (*reference*) emission of PKS 1424+240 above 150 GeV is at the level of few percentage of Crab.

Period	Time [h]	F>150 GeV [cm^{-2} s^{-1}]	Crab Nebula fraction
2009 (MAGIC)	8.0	$(1.99 \pm 0.65) \times 10^{-11}$	$6.2\% \pm 2.0\%$
2009 April (MAGIC)	4.9	$(2.99 \pm 0.86) \times 10^{-11}$	$9.3\% \pm 2.7\%$
2009 June (MAGIC)	3.1	$(0.49 \pm 1.01) \times 10^{-11}$	$1.5\% \pm 3.1\%$
2010	14.3	$(0.39 \pm 0.17) \times 10^{-11}$	$1.2\% \pm 0.1\%$
2009 (VERITAS)	28.5	$(0.8 \pm 0.2) \times 10^{-11}$	$2.0\% \pm 0.1\%$

Table 6.8: PKS 1424+240 VHE γ–rays integral flux measured by MAGIC. In addition, VERITAS results are reported for comparison.

6.5 Lightcurve: the multiwavelength view

6.5.1 Optical

The optical behaviour of PKS 1424+240 has already been described in the introduction of this Chapter, where we have noticed that the source emission is variable at optical frequencies. The optical activity in 2009 and 2010, drawn in Figure 6.1, fluctuates between 7 mJy to 8.5 mJy, and is almost a factor 1.5 higher w.r.t. previous years. Moreover, during the last biennium, there is clear evidence for flux variations at daily scale. The amplitude of the variations, however, is quite modest in comparison with that observed in other blazars. This behaviour is similar to that found in PG 1553+113, where the optical flux, between 2005 to 2010, varied in the limited range from 1 mJy to 8 mJy.

Since the exposure of the observations is partially coincident with VHE observations, we present a correlation study between these two extreme energetic bands.

Optical –TeV correlation study

Figure 6.13 shows the results of the correlation study between daily significant detections of VHE γ–rays, above 150 GeV, and optical observations, listed in Table 6.9. In total, eight nights could be included in the study, which span from April 2009 to March 2010.

Indeed, the highest flux states have been observed, in both cases, in April 2009. A linear fit to the data distribution, superimposed to the Figure, has a probability of 83% and suggests a correlation between these extreme frequencies. However, the poor statistics involved together with the large error bars, prevent any definitive conclusion from this study.

Day	F(>150 GeV) [$cm^{-2}s^{-1}$]	F (R band) [mJy]
17/04/2009	6.4 ± 3.5	8.31 ± 0.14
22/04/2009	2.6 ± 1.8	7.40 ± 0.14
23/04/2009	7.3 ± 2.3	7.48 ± 0.14
24/04/2009	3.6 ± 2.2	7.58 ± 0.12
20/06/2009	4.6 ± 3.5	7.57 ± 0.12
23/03/2010	0.9 ± 0.8	7.15 ± 0.14
24/03/2010	0.5 ± 0.4	7.16 ± 0.12
25/03/2010	0.5 ± 0.5	7.24 ± 0.12

Table 6.9: Correlation study between daily flux measured by MAGIC above 150 GeV and optical flux.

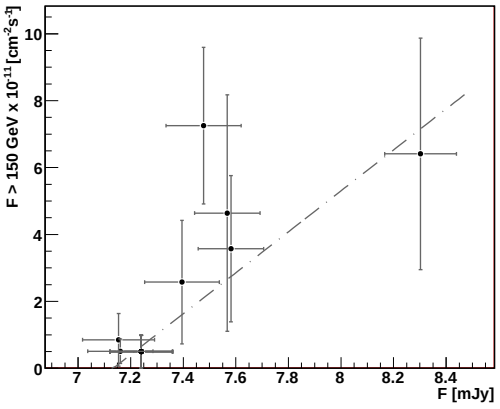

Figure 6.13: PKS 1424+240 correlation study between the VHE component and the optical. The daily values of truly simultaneous data (open circles) show no evident correlation, while the mean values (filled squares), shows some hints of correlation.

6.5.2 X–rays

PKS 1424+240 is regularly monitored in X–rays by the XRT instrument on-board *Swift*. This campaign is part of the *Swift*/XRT monitoring of *Fermi*/LAT sources of interest[2]. Figure 6.14 displays the X–ray lightcurve of the available data, in count rate units.

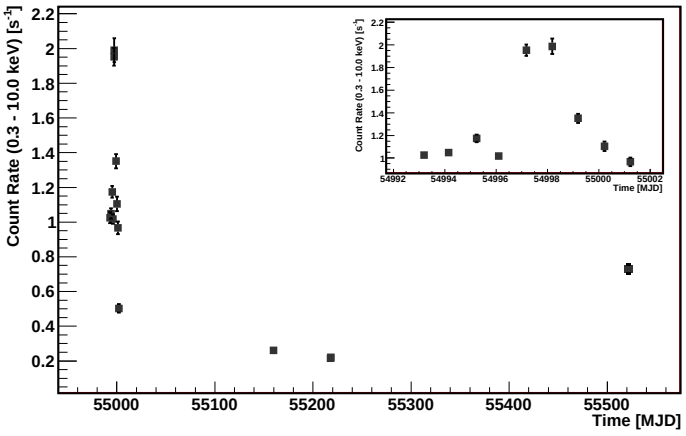

Figure 6.14: X–ray lightcurve of PKS 1424+240, from *Swift*–XRT monitoring

The monitoring started in June 2009 (MJD 54990), when a count rate at $1\,s^{-1}$ was registered. Soon after, the source underwent a flaring state (inset in the

[2]http://www.swift.psu.edu/monitoring/

Figure): within one day the count rate doubled (from $1.02\,s^{-1}$ to $1.95\,s^{-1}$). This result is a strong evidence of fast flux variations of PKS 1424+240, at least at X–ray frequencies. The lightcurve shows also that in November 2009 the count rate was very low, at the level of $0.26\,s^{-1}$, while in April 2010 it increases of a factor $\sim$3 ($0.72\,s^{-1}$).

Unfortunately, the lack of truly simultaneous VHE–X-ray data has prevented a dedicated correlation study, which would have been of great interest, especially if during a flaring state, for testing blazars models of VHE γ–ray emission. According to the SSC model, in fact, as outlined in Chap. 2, fast variations of the emission of a HBL blazar at X–ray wavelenghts (associated with the synchrotron peak), would suggest the same behavior at higher energies (in the IC peak).

6.5.3 γ–rays

PKS 1424+240 is one of the blazars regularly monitored by *Fermi*, as mentioned in previous Section. The source was already present in the *Fermi* bright sources list, indicating that it is very bright at γ–rays below 100 GeV. The detailed analysis of the source emission after the first year of data taking in the HE range[3] shows that the source is likely to be variable at monthly scale at these energies. However, the analysis of simultaneous *Fermi* and VERITAS (2009) data, carried out in Acciari et al. (2010a), shows that the HE emission is compatible with a steady flux during the covered period, as shown in Figure 6.15.

Therefore, the hint of variability suggested by MAGIC observations in 2009 seems to be not correlated with the lower energy γ–rays counterpart.

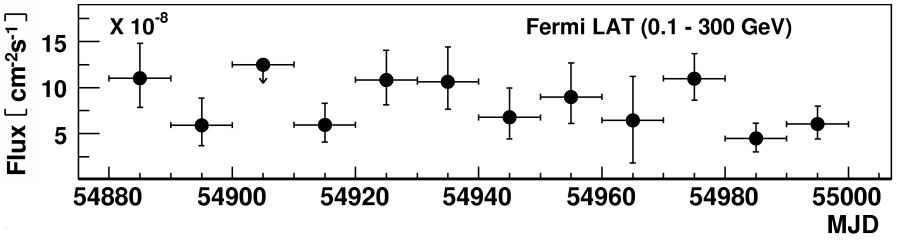

Figure 6.15: γ–ray lightcurve of PKS 1424+240 in 2009. Courtesy of Acciari et al. (2010a).

6.5.4 Final remarks

The comparison between the multiwavelength lightcurves presented is finally displayed in Figure 6.16. Except for optical data, which were collected also in 2006 and 2007, the available measurements concentrates in the last two years.

In general, the source emission is variable at all wavelenghts, with evidence of flares on daily scale at optical and, according to the LAT first year catalog, also at γ–ray frequencies at least on monthly scale. The correlation study between VHE γ–ray and optical frequencies suggests hints of correlation between these extreme wavelengths, while the same study could not be performed between the VHE γ–ray and X–ray frequencies, due to the scarce overlap of the observations. Further coordinated multi–frequency campaigns are strongly encouraged to investigate this important issue.

[3] available at http://heasarc.gsfc.nasa.gov/

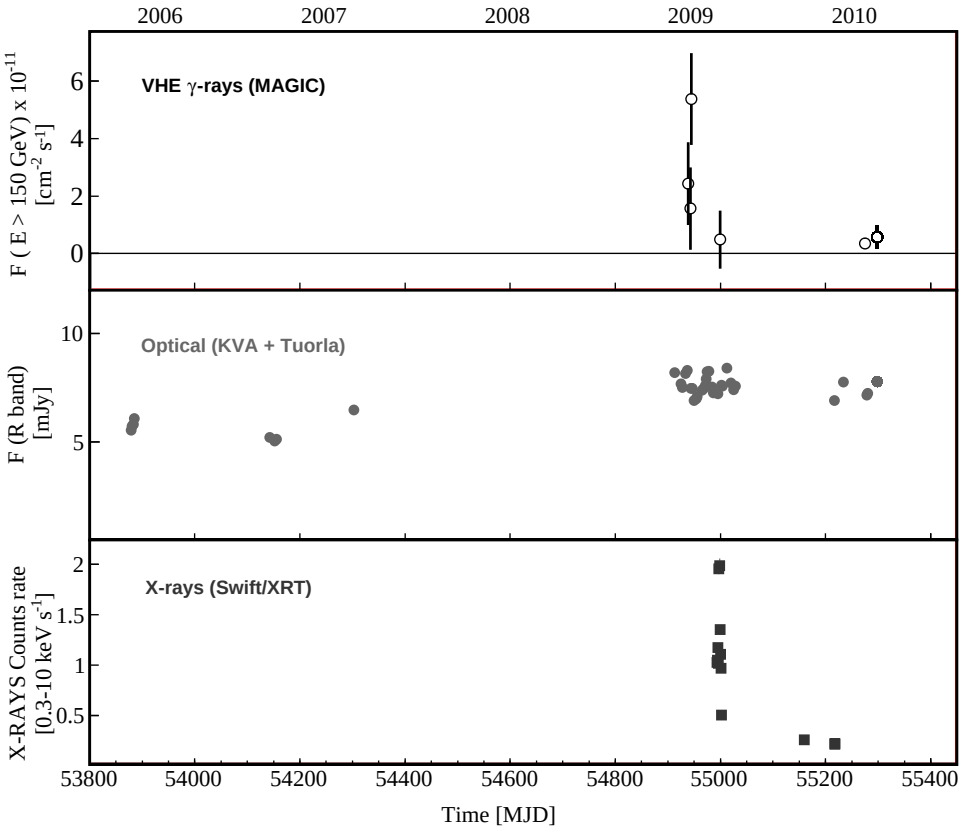

Figure 6.16: PKS 1424+240 multiwavelength view.

6.6 PKS 1424+240 SED

In order to study the overall SED emitted by the blazar, we have to correct the VHE γ–ray spectrum for the effect of EBL absorption, due to electron positron pairs production. A complete study of this absorption will be presented in the next Chapter. This effect is related to the photon–photon opacity, which in turn is coupled to the redshift, z, of the source. However, as noticed above, the distance of this source is still unknown. Here, anticipating the results presented in Chapter 8, we adopt for PKS 1424+240 a redshift of $z = 0.26$. This value will be estimated with a new empirical technique, based on the properties of the combined GeV and TeV spectra.

Figure 6.17 shows the mean spectrum observed by MAGIC reported in Section 6.3 (open circles), and the spectrum corrected for EBL absorption (filled circles), obtained using a mean energy density EBL model (Domínguez et al., 2011). This is our measure of the intrinsic source emission. The spectrum can be well described by a power law fit (probability 92%) with a soft index of $\Gamma = 3.51 \pm 0.50$, and normalization factor $f_0 = (0.8 \pm 0.2)\times10^{-10}$ cm^{-2}s^{-1}TeV^{-1}.

Figure 6.18 displays a collection of PKS 1424+240 spectral determinations, from radio to γ–ray frequencies. In addition to historical data (open squares), extracted from NED[4], optical-UV and X-ray data from *Swift* (Tavecchio et al., 2010) are represented, and characterize the synchrotron peak. On the other hand, 2009 *Fermi*/LAT data (filled triangles), from Abdo et al. (2009), together with the

[4]http://nedwww.ipac.caltech.edu/ .

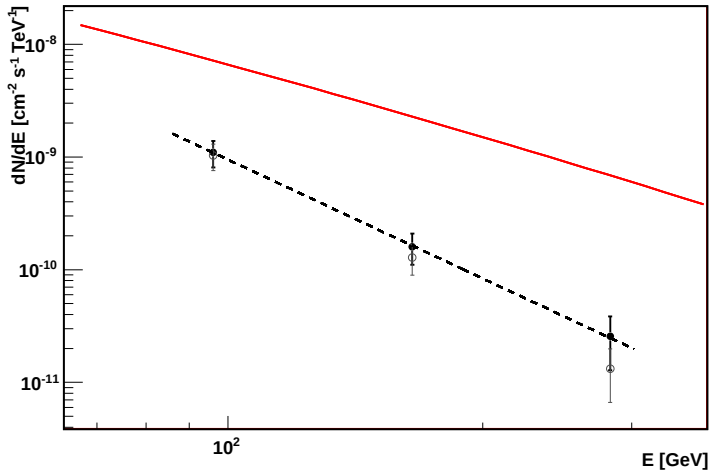

Figure 6.17: PKS 1424+240 mean spectrum observed (open marks) and deabsorbed (filled marks) adopting a mean energy density EBL model (Domínguez et al., 2011).

partially simultaneous mean 2009/10 VHE γ–ray data (filled circles), obtained by deabsorbing the VHE spectrum seen by MAGIC (open circles) assuming a redshift of $z = 0.26$, contribute to the definition of the second peak of the SED.

Conversely to what observed in PG 1553+113 , between HE and VHE observations there is still a gap, which will be probably filled in the next years. Extended

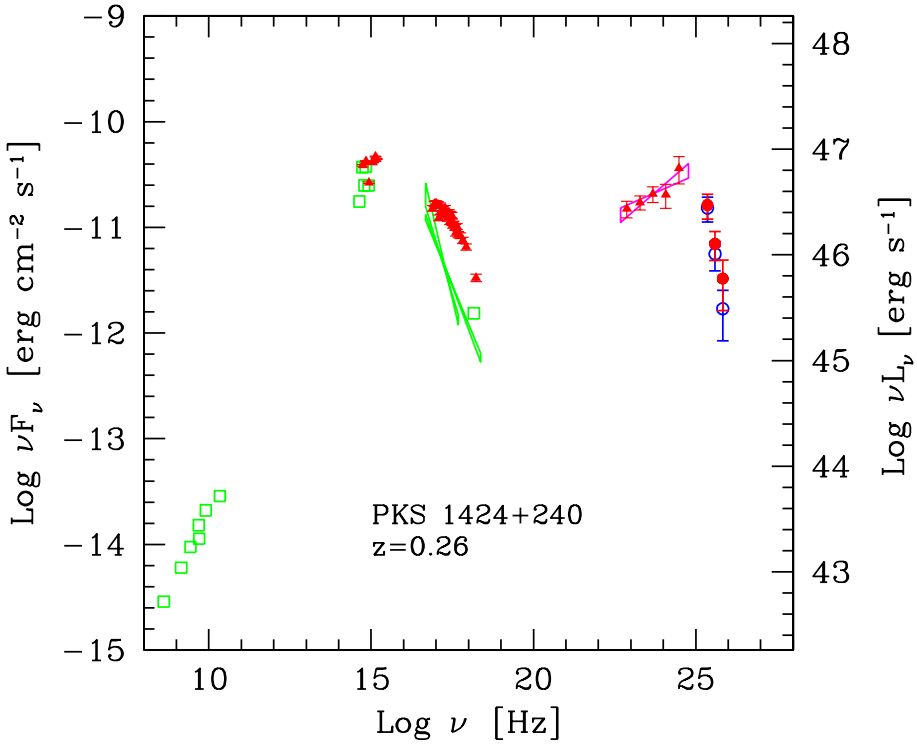

Figure 6.18: SED of PKS 1424+240. Historical data (open squares) are from NED. Optical-UV and X-ray data from Swift are from Tavecchio et al. (2010). *Fermi*/LAT data (filled triangles) are from Abdo et al. (2009). At the highest energies, the observed (open circles) and deabsorbed spectrum (filled circles) assuming a redshift $z = 0.26$ are represented.

Fermi/LAT exposures, in fact, will probably lead to the detection of γ–rays up to 100 GeV. Moreover, prolonged exposures of IACTs, in good data taking conditions will contribute to measure the low energy part of the VHE spectra ($\sim$100 GeV). Despite the incomplete coverage of the second bump, we can constrain the peak of the high energy emission to lie in the 50 GeV–100 GeV energy range.

6.7 Conclusions

In this Chapter, we have presented the analysis of VHE γ–ray data the unknown distance blazar PKS 1424+240, collected by MAGIC in 2009 and 2010. The former observation was triggered by an optical outburst in the R-band, revealed by the Tuorla/KVA telescopes.

The differential spectrum observed is compatible with a mean photon index of 4.0 ± 0.6. If we assume for the source a redshift $z = 0.26$, the slope of the deabsorbed mean spectrum becomes 3.51 ± 0.50.

The mean flux registered above 150 GeV by MAGIC in 2009 is at the level of 6% of the Crab Nebula flux above the same threshold. In that dataset there are traces of monthly variation. In particular, the flux registered in March is higher than that observed in June. Interestingly, this behaviour has not been observed by VERITAS, which monitored the source for a longer period and found a mean integral flux at the level of 2% of Crab Nebula flux. This flux state is somehow similar to that registered by MAGIC in 2010, which is at the level of 0.01 Crab units. A possibility that we have proposed to explain this apparent disagreement between the two measures is that PKS 1424+240 could have experienced an increased activity at VHE γ–rays at the end of March 2009, period better covered by MAGIC dataset. This would have caused a higher mean flux state registered in 2009 by MAGIC. The flux state observed by MAGIC in June 2009, instead, as well as that observed in 2010, are compatible with the mean flux reported by VERITAS in 2009 obtained with a larger sample. This fact suggests that the existence of a *reference* emission state at the level of few percentage of Crab above 150 GeV.

Dedicated analyses of PKS 1424+240 data at other frequencies show a marginal variability at almost all frequencies. In particular, the partial overlapping optical and TeV data allowed a correlation study. We found, in agreement with what observed in other blazars such as PG 1553+113, hints of correlation between these two extreme bands, in agreement with the predictions of the SSC model.

Finally, the study of the overall spectral energy distribution, from radio to VHE γ–rays, allowed us to define the location of the synchrotron and high energy peak, at UV–X-rays frequencies and between 50 GeV to 100 GeV respectively. More detailed studies, which could constrain the physical conditions inside the blazar jet, would require truly simultaneous data, collected for example in dedicated multiwavelength campaigns.

Equipped with his five senses, man explores the universe around him and calls the adventure Science.

Edwin Hubble

7 Limits on blazars distance from VHE spectra

In the first part of the Chapter, we investigate the effect of EBL absorption on the VHE spectra of TeV blazars, taking onto account different EBL models. The second part is dedicated to the description of two different methods to set upper limits on the distance of a blazar, based on the spectral properties measured. Both methods use the EBL absorption as a tracer of the distance of the emitting object. We finally apply the methods described to set a limit on the distance of PG 1553+113 and PKS 1424+240.

The work presented here is an extended and updated version of Prandini et al. (2009) and Prandini (2010).

7.1 The effect of EBL on blazars spectra

As first pointed out by Nikishov (1962), the Universe is partially opaque to VHE γ–rays due to the interaction with low photons and the subsequent electron positron pair production. Photons with energy above 100 TeV traveling in space interact with the CMB, and have a very short mean free path before decaying, of about 10 kpc for PeV γ–rays (Kifune, 1999). Due to the large CMB photon density, extragalactic sources are essentially undetectable above this energy. Below hundreds of TeV, the detectability of a source depends on its distance, and is governed by the photon–photon opacity induced by extragalactic backgrounds other than the CMB (see Chap 3). Between tens of GeV to 100 TeV, extragalactic γ–rays interacts with the optical/near-infrared photons of the EBL, and can be partially or totally absorbed. The amount of such absorption depends on the *energy* of the VHE photon and on the *distance* of the emitting blazar. As a result, only relatively nearby objects, below redshift 0.6, have been detected in this energy range. Moreover, a partial absorption causes a deformation in the spectra observed: indeed, if we analyze the distribution of TeV blazars slopes, drawn in Fig. 7.1, we see a clear evidence for a dependence of the Γ_{TeV} slope of the power law fitting the spectrum measured by IACTs above 100 GeV, with the distance z of the source.

Finally, at lower energies, the background photon density is too faint to cause

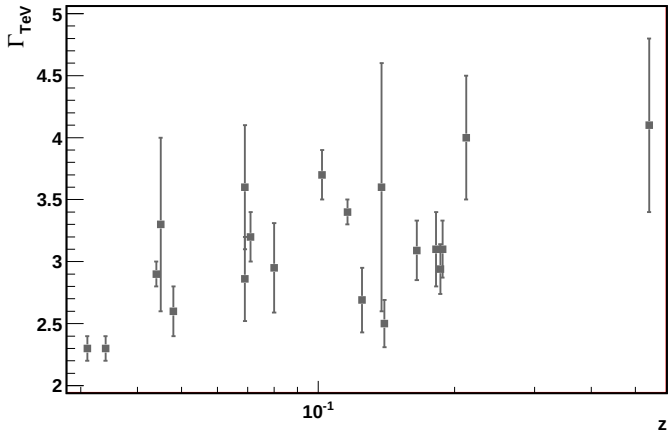

Figure 7.1: Spectral indices of TeV blazars as a function of their distance. All the blazars with well known distance are taken into account.

a significant absorption of photons below some GeV; the corresponding gamma–gamma opacity gets negligible and the Universe becomes transparent to keV-GeV photons (Figure 7.2).

7.1.1 The γ-γ opacity

The absorption of energetic photons traveling in a medium can be described by the parameter $\tau(E, z)$, called *optical depth*. It is defined as the path length before the radiation emitted by a source is attenuated by a factor e, and is a function of both photon energy and source distance.

The observed flux from a source, F_{obs}, located at distance z, is related to the emitted one through the equation:

$$F_{obs} = F_{em} \cdot e^{-\tau} \tag{7.1}$$

In our case, following Franceschini et al. (2008), the opacity is dominated by electron-positron pair creation. For a VHE photon of energy E_γ traveling from a

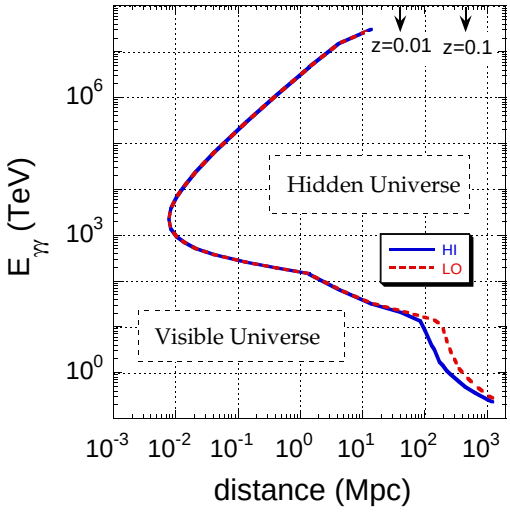

Figure 7.2: Low redshift ($z \ll 1$) γ–ray horizon giving the relationship between photon energy and z for the distance where $\tau_{\gamma\gamma}(E,\ z) = 1$ for a low and high EBL models. From Dermer (2007).

E_γ	λ_{EBL}	Energy Range
$\leq$ 300 GeV	$\leq 0.3\,$nm	UV
300-600 GeV	$\sim 0.5\,\mu$m	Optical
0.6 - 2 TeV	0.8 - 2.5 μm	Near-infrared
$\sim$ 10 TeV	$12\,\mu$m	Far-infrared
$\geq$100 TeV	$\geq 0.1\,$mm	Microwaves

Table 7.1: Wavelength of the EBL photons corresponding to the maximum absorption of VHE photons due to $\gamma - \gamma$ pair production, as a function of the energy of the energetic photons.

source at redshift z_s to an observer at present time, and passing through a medium filled with low energy (EBL) photons with density $n_\gamma(z)$, the corresponding optical depth is:

$$\tau(E_\gamma, z_s) = c \int_0^e dz \frac{dt}{dz} \int_0^2 dx \frac{x}{2} \int_{\frac{2m_e^2c^4}{E_\gamma \epsilon x(1+z)}} d\epsilon \frac{dn_\gamma(\epsilon, z^*)}{d\epsilon} \sigma_{\gamma\gamma}(\beta) \tag{7.2}$$

where ϵ is the energy of the background photon, $\sigma_{\gamma\gamma}$ the photon-photon cross section, and:

$$\beta \equiv \left(1 - 4m_e^2c^4/s\right);\ s \equiv 2E_\gamma \epsilon x;\ x \equiv (1 - cos\theta)\,, \tag{7.3}$$

with θ angle between the two photons. For a flat Universe, the differential time in Eq. 7.2 is:

$$\frac{dt}{dz} = \frac{1}{H_0\,(1+z)} \left[(1+z)^2\,(1+\Omega_m z) - z\,(z+2)\,\Omega_\Lambda\right]^{1/2} \tag{7.4}$$

Finally, the photon-photon cross section for pair production is (Heitler (1960)):

$$\sigma_{\gamma\gamma}(E_\gamma, \epsilon, \theta) = \frac{3\sigma_T}{16} \cdot (1-\beta^2)x \left[2\beta(\beta^2 - 2) + (3 - \beta^4) ln\left(\frac{1+\beta}{1-\beta}\right)\right] \tag{7.5}$$

Thus, the energy of maximum absorption is:

$$\epsilon_{max} \simeq \frac{2\left(m_e c^2\right)^2}{E_\gamma} \simeq 0.5 \frac{1TeV}{E_\gamma} eV, \tag{7.6}$$

that, in term of wavelength, becomes:

$$\lambda_{max} \simeq 1.24\,(E_\gamma[TeV])\,\mu m \tag{7.7}$$

This relation between the energy, E, and the corresponding wavelength of absorbing photons is made possible by the fact that the the cross section of the interaction has a narrow and well defined peak. This means that, following Table 7.1, low energy photons of the CMB interact mainly with photons of energy above 100 TeV, causing a total absorption due to the large density of this background. At larger energies of the background photons, the absorption cross section has a maximum at lower E_γ values.

Therefore *VHE photons above 1 TeV probe the infrared part of the EBL*, as underlined in Aharonian et al. (2007b), *while below 600 GeV we are investigating the optical/UV energy band.*

Figure 7.3 shows the behaviour of the absorption coefficient, $e^{-\tau}$, as a function of the energy, E_γ, of the energetic photon. This coefficient represents the suppres-

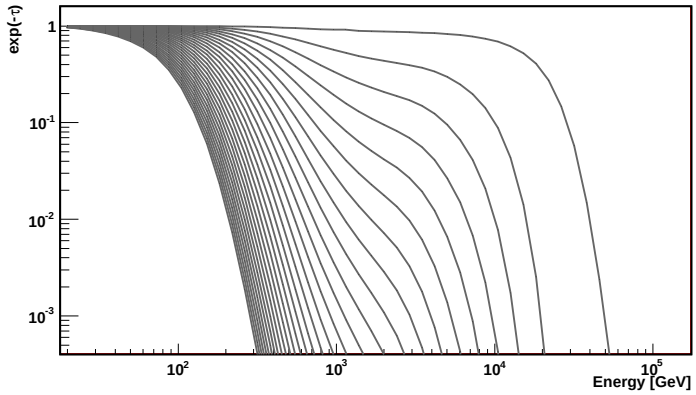

Figure 7.3: Absorption coefficient, $e^{-\tau}$, as a function of the energy, E_γ, for redshift from 0.01 to 1.5, from top to bottom, with the Franceschini et al. (2008) EBL model.

sion factor of the differential energy flux, defined in Eq. 7.1. It is evident that for nearby sources, upper curves, the Universe is rather transparent to photons up to energies above tens TeV. This means that for objects located at redshift smaller than 0.05, the spectrum observed below 10 TeV is almost unaffected by the interaction with the EBL. At larger redshifts, the absorption increases rapidly, and the spectrum is strongly suppressed at energies ranging from 10 TeV to 100 GeV. This is the reason why, up to now, IACTs have not detected any blazar at distances much larger than $z = 0.5$.

The distance effect becomes evident if we compare the plots reported in Figure 7.4. The observed and deabsorbed TeV spectra for three sources located at different distance (upper panels), are shown together with the corresponding absorption factor, e^{τ} (lower panels).
For Mkn 501, which is a prototype of nearby blazars and is located at redshift 0.03, the absorption becomes significant only at energies larger than 10 TeV, Fig. 7.4(a).
As an example of intermediate distance blazar, we show in Fig. 7.4(b) the emission of 1ES 1218+304, a HBL discovered by the MAGIC telescope and recently observed by VERITAS, at redshift 0.182. For this object, the absorption is significant already at some hundreds of GeV.
The extreme example is the FSRQ 3C 279 (Fig. 7.4(c)), at redshift of $z = 0.534$, discovered by MAGIC at VHEs during a flaring state in 2006. In this case the observed spectrum is strongly affected by interaction with EBL already at 100 GeV, as expected for sources located at such large distances.
For all the cases considered, we have adopted a mean energy density EBL model (Franceschini et al., 2008).

7.1.2 Comparison between models

We have seen in Chap 3 that there are few different models describing the EBL and its evolution. As a result, also the the attenuation factor, $e^{-\tau}$, is affected by uncertainties, and is model dependent. In order to investigate this dependence, we display in Figure 7.5 the value of this factor as a function of the energy, E_γ for four EBL models and different redshift values.

The models taken into account are: Franceschini et al. (2008), Domínguez et al. (2011), Kneiske and Dole (2010), and Stecker et al. (2006), hereafter called Frances-

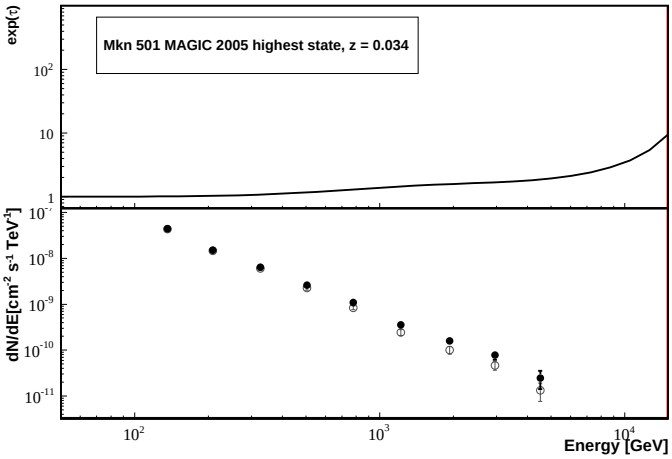

(a) Mkn 501, located at redshift 0.03.

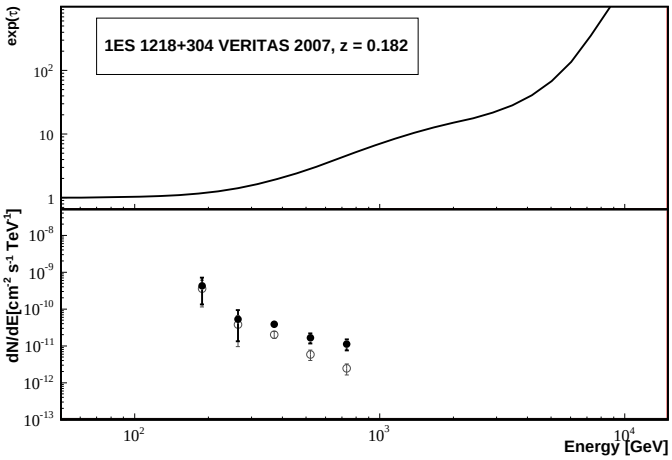

(b) 1ES 1218+113, located at redshift 0.182.

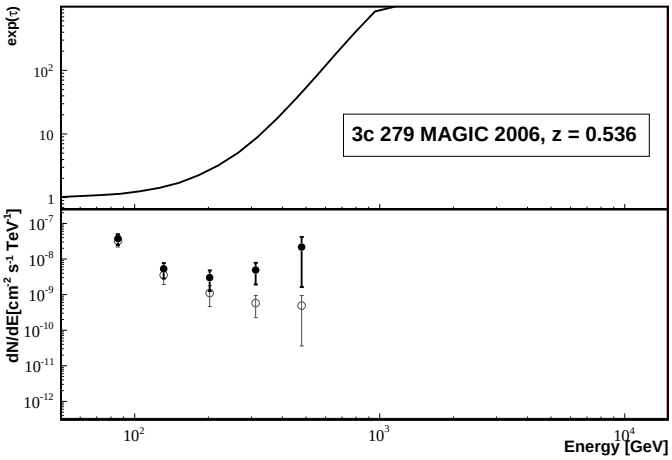

(c) 3C 279, the most distant blazar discovered by Cherenkov instruments, located at redshift 0.536.

Figure 7.4: Upper panels: absorption factor e^{τ} for three blazars located at different redshift. Lower panels: observed (open circles) and deabsorbed (filled circles) spectra.

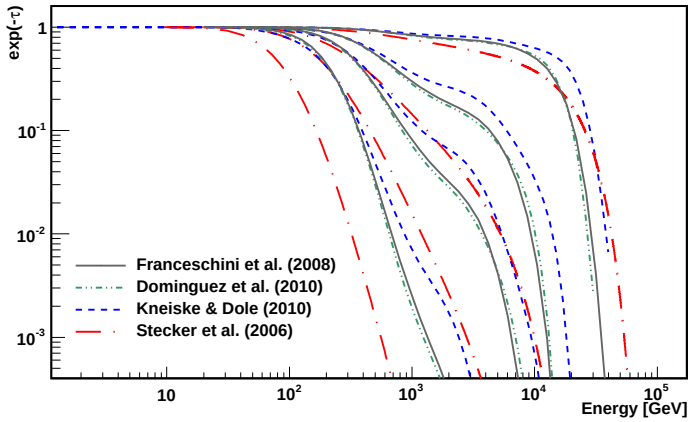

Figure 7.5: Comparison of the absorption coefficient, $e^{-\tau}$, for four different EBL models, and redshifts $z = 0.019$, 0.118, 0.226, and 0.475 (from upper to lower curves).

chini, Dominguez, Kneiske and Stecker model, respectively. From the direct comparison it is evident that the difference between the values of the attenuation obtained with the first two models is almost negligible, for every distance considered. This outcome suggests that the Franceschini and Dominguez models foresee a similar optical/infrared background level and evolution, at least below z=0.5. The absorption obtained with the Kneiske model, instead, is less pronounced, especially for redshift about 0.2, where the difference with the Franceschini and Dominguez models reaches a factor 3. On the other side, the Stecker model predicts a high background level, which corresponds to a large absorption already at small distances. For example, while the absorption at redshift 0.118 is almost negligible below 500 GeV for the first three models, this is no longer valid in the latter case, which foresee a flux reduction larger than 50%. It is important to underline that the EBL model suggested by Stecker et al. (2006) has been recently ruled out by an investigation performed with the *Fermi*/LAT data (Abdo et al., 2010a), based on the observation of the photons of energy above 30 GeV from distant objects (both from GRBs and blazars). If this result was confirmed, as it seems also from studies on spectra of TeV blazars, the uncertainty on the EBL would be significantly reduced.

7.2 Methods

Conversely to the majority of the works present in literature, that use the TeV observations and some basic hypotheses on the intrinsic spectrum in order to set limits on the EBL density, we use the of spectral information for setting a limit on the *distance* of the emitting object.

The study is motivated by the experimental statement that the distance of many blazars is unknown or largely uncertain. This is in particular true for a class of objects, called BL Lacs (presented in Chap. 2), characterized by very faint or absent emission and absorption lines in the optical spectrum. Since the method to constraint blazars distance is based on the detection of spectral lines, for such objects it is intrinsically difficult to make this measure, as discussed for PG 1553+113 and PKS 1424+240.

For the determination of an upper limit on the redshift of blazars from the

observed VHE γ–rays spectrum, two elements are needed. First, we necessitate an EBL model describing the light content and its evolution. For this purpose we use the Franceschini model. The second element is an assumption on the shape of the emitted spectrum. Two different approaches can be used in order to discriminate physical and unphysical emitted spectra:

- The first method consists in requiring a minimum value given by theory for the power law index of the deabsorbed spectrum (straight dotted line of fig.7.6), as proposed in Aharonian et al. (2006);
- The second method is based on the hypothesis that the SED of a blazar does not show a third peak at VHE (curved line of Fig.7.6).

Both techniques use the fact that the absorption increases with distance. Therefore, if the spectrum is "over-corrected" its shape becomes unphysical.

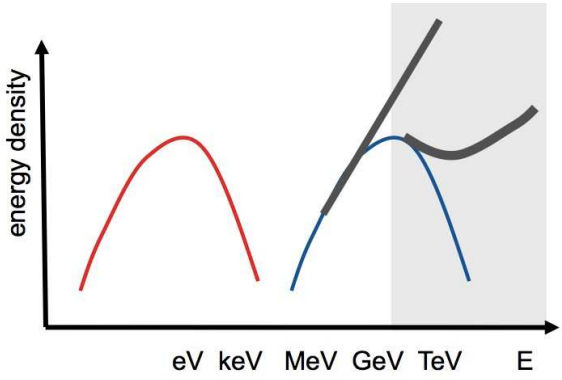

Figure 7.6: A graphical representation of the two possible criteria for constraining the deabsorbed spectrum of a blazar.

7.2.1 Maximum intrinsic photon index

According to the standard scenario of particle acceleration, the minimum allowed index in AGN spectra is $\Gamma_{int}^{st} = 1.5$, that is the hardest index for the accelerated particles foreseen by shock acceleration models (see e.g. Malkov and O'C Drury 2001). Following Aharonian et al. (2006), for the case of electrons, the spectrum of the γ–ray component emitted via IC scattering is expected to be steeper than $\Gamma_{int} = 1.5$ under most circumstances. Only if radiative cooling is not effective and the blazar Compton emission is wholly within the Thomson limit, one finds $\Gamma_{int} = 1.25$. However, this is widely unlikely at such high energies. On the other hand, for the case of protons interacting with ambient plasma, the resulting γ–ray spectrum has the same slope, $\Gamma_{int} = 1.5$.

As an indirect probe of the limit of 1.5 in the spectral slopes pf blazars, it can be noticed that in none of the nearby blazars detected at TeV energies such hard spectra have been ever observed. For example, close blazars such as Mkn 501 and 1ES 1959+650, located at redshift smaller than 0.05, and consequently almost unaffected by EBL absorption below 10 TeV, have a VHE spectrum compatible with a power law of index $\Gamma = 2.3$ and $\Gamma = 2.6$, respectively. Another experimental probe in favour of the expectations of the acceleration model is the distribution of the power law indices of blazars detected by *Fermi*/LAT in the 200 MeV-300 GeV energy range, reported in Abdo et al. (2010) and Finke and Razzaque

(2009). Figure 7.7 shows the distribution of the photon index as a function of the peak frequency of the synchrotron component of the SED for the *Fermi* detected blazars. Interestingly, only for few sources, almost all HBLs, the power law index fitting the spectrum has a value smaller than 1.5, and in all cases still compatible with it at a $1\,\sigma$ level. In the next Chapter we will investigate more in detail the possibilities opened by the *Fermi*/LAT spectral measurements, in particular regarding the spectral slope mentioned here.

We can conclude by remarking that the experimental evidences are in favour of the presence of a maximum possible hardness value, around 1.5, as expected from the standard model of particle acceleration. Despite this, it cannot be ignored that several theoretical possibilities have been proposed to create harder spectra (e.g. Aharonian et al. 2008). As an "extreme case" the value of $\Gamma_{int}^{ex} = 2/3$ can be taken, as discussed in Katarzyński et al. (2006).

Therefore, the maximum hardness criterion can be used to set an upper limit on the distance of TeV blazars. The method is straightforward: we correct the blazar TeV spectral points for the absorption, given a specific EBL model, and fit every time the deabsorbed spectrum with a power law. The resulting index, Γ, is a decreasing function of the distance. According to our requirement that the maximum allowed slope is 1.5, we can consider the redshift, z, at which the deabsorbed spectrum has such power law index as an upper limit on the distance[1].

Recently, this criterion has been used by a number of authors for constraining the EBL energy density. If the redshift of the source is known, in fact, the EBL energy density can be constrained by applying the same procedure described above for the redshift. The method has been proposed in Aharonian et al. (2006); Mazin and Raue (2007); Aharonian et al. (2007b); Albert et al. (2008c), and more recently in Finke and Razzaque (2009); Georganopoulos et al. (2010); Yang and Wang (2010); Mankuzhiyil et al. (2010).

[1]More precisely, the upper limit on the distance is given by the redshift z plus twice its error (σ).

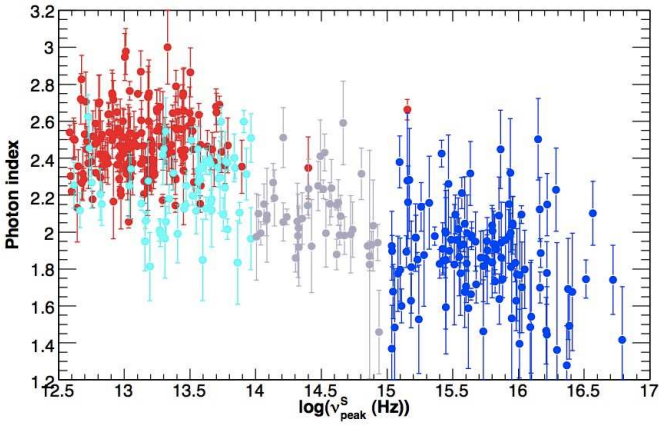

Figure 7.7: Photon spectral index vs. peak frequency of the synchrotron component of the SED for FSRQs (red) and BL Lacs (cyan: LBLs, gray: IBLs, blue: HBLs). From Abdo et al. (2010).

7.2.2 Absence of a third peak in the intrinsic spectrum

The second criterion used to constrain the distance of a blazar, which, in some cases, can be more limiting than the one described above, is based on the shape of the deabsorbed spectrum, as first suggested by Mazin and Goebel (2007) for the source PG 1553+113. The basic idea moves from the empirical fact that all the TeV blazars observed show a simple two–peaked SED structure: the low energy peak being related to the synchrotron emission by accelerated electrons, the second peak probably due to IC scattering. Since the EBL absorption is energy dependent, and it increases with increasing energy, if the VHE spectrum is over-corrected a third peak may arise in the SED.

As extreme example, we have plotted in Figure 7.8 the observed and deabsorbed spectrum of Mkn 501 measured by MAGIC, assuming a redshift of 0.35 (instead of 0.03). The effect of the over-correction at the highest energies is evident. A possible way to quantify this anomaly is to fit the spectrum with a *curved power law* of the form:

$$\frac{dN}{dE} = F_0 \left(\frac{E}{E_0} \right)^{-\Gamma+\beta lnE} \tag{7.8}$$

which, in first approximation, can be used as an indicator of a pile–up at the highest energies.

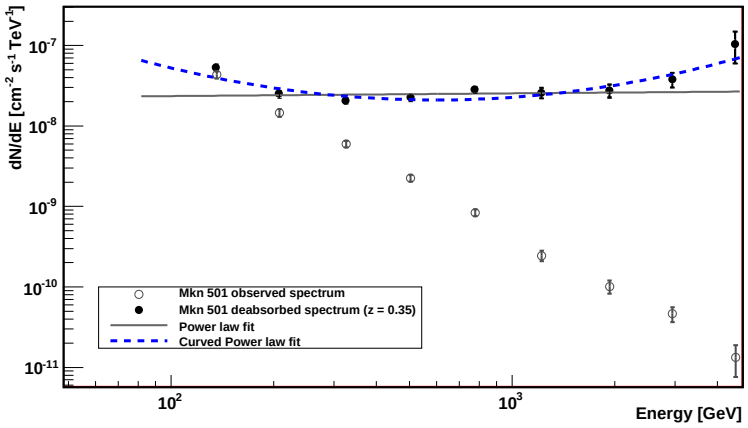

Figure 7.8: Observed (open circles) and deabsorbed (filled circles) spectrum of the blazar Mkn 501 assuming a distance $z = 0.35$. The two lines represent the power law (continuous line) and curved power law fits (dashed line).

In order to test the absence of a third peak in the deabsorbed spectrum, a likelihood ratio test can be used. This test, proposed by Eadie et al. (1988), is a statistical tool to evaluate between two hypotheses whether an improvement to a fit quality, quantified by the corresponding χ^2 values, is significant, taking into account the different degrees of freedom. More details about this method can be found in Mazin and Goebel (2007). In our case, the test consists in a comparison between the hypothesis A, data fitted with a simple power law, and hypothesis B, data fitted with a curved power law, corresponding to a parabolic law in a $\log(dN/dE)$ vs $\log(E)$ representation. When the probability that the curved power law fits better the data than the simple power law is larger than our confidence level, set to 95%, then it means that the a pile–up, i.e. a third peak in the spectrum, becomes statistically significant. The redshift at which this

happens can be safely considered as an upper limit on the source distance.

7.3 Results

In this Section, the methods are applied to the blazar PG 1553+113, discussed in detail in Chapter 5, and to PKS 1424+240 presented in Chapter 6.

7.3.1 PG 1553+113

PG 1553+113 has been monitored by the MAGIC telescope for 5 years (from 2005 to 2009). Despite the indication of flux variability, the spectral indices are consistent within the errors. Here, we use the measured spectrum to infer the distance of this object, still affected by large uncertainties. Since the methods of finding the limit on the source redshift are based on the shape of the spectrum, and not its normalization, we use the combined dataset, in order to increase statistics. The overall measured spectrum is well described by a simple power law fit of index 4.27 ± 0.14, presented in Section 5.5.

We calculate a first upper limit on the distance of PG 1553+113, based on the assumption that the slope of the deabsorbed spectrum cannot be harder than 1.5. Figure 7.9(a) shows the dependence of the slope with the redshift, z, of the source. Indeed, while the redshift increases the absorption becomes more and more effective and the slope decreases. The redshift at which the power law index equals the limit, 1.5, is $z_{\Gamma=1.5} = 0.81 \pm 0.08$. Hence, the upper limit on the distance based on this method, at a $2\,\sigma$ level, i.e. 95% of confidence level, is $z <$0.97.

We realize the second method, based on the requirement that the intrinsic spectrum does not show a pile–up at the highest energies, using the likelyhood ratio test among the simple and curved power law. The resulting probability of the likelihood ratio test is shown in Fig. 7.9(b), thick line. For $z = 0.67$, the curved fit is better than the straight fit with a confidence level of 95%. The deep minimum of the probability, at z=0.28, indicates that at this redshift the intrinsic spectrum is a strict power law. Below this value, the curved fit of the deabsorbed spectrum presents the concavity downward, whereas the rise at redshifts above 0.28 corresponds to a curved spectrum with concavity upward. The likelyhood probability becomes 95% at $z = 0.67$. Hence, the requirement that the intrinsic spectrum from PG 1553+113 does not show a pile–up at high energies, leads to an upper limit of $z < 0.67$ on its distance.

From the comparison between the two methods, we can conclude that in case of PG 1553+113, the demand of no pile–up at high energies leads to the most stringent upper limit on the source redshift, which is constrained below redshift 0.67. The corresponding spectrum is shown in Figure 7.10.

The limit obtained here is less constraining than that resulting from an analogue study applied to a smaller sample of data from the same source (Mazin and Goebel, 2007), where the same procedure led to the upper limit of $z < 0.42$. The reason for this discordance is probably due to the presence, in our spectrum, of points at low energy (~ 100 GeV). Such points, characterized by small error bars, constrain the fit of the deabsorbed spectrum, and are the main cause of the discrepancy found. However, since based on a larger sample of data, we consider the result presented here is more conservative and stable.

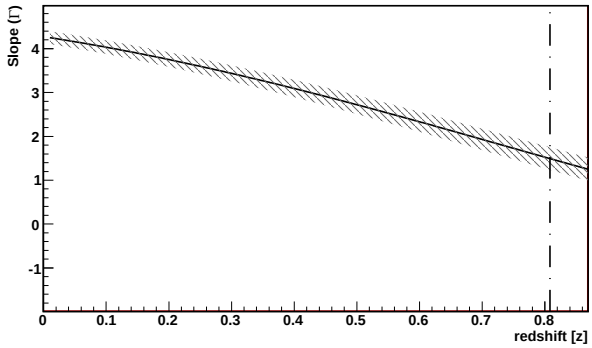

(a) Limit on PG 1553+113 distance from the deabsorbed spectrum power law fit.

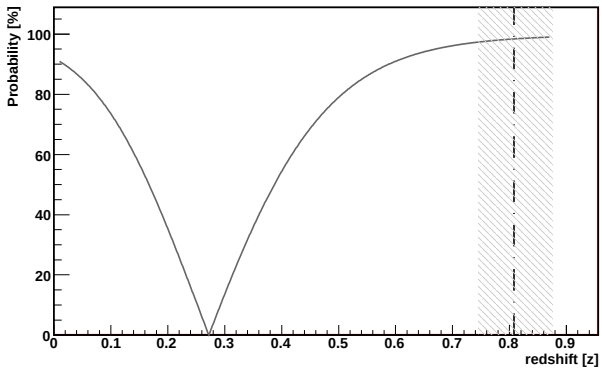

(b) Limit on PG 1553+113 distance from the likelihood ratio test.

Figure 7.9: Result of the distance study on PG 1553+113. We assume Franceschini EBL model.

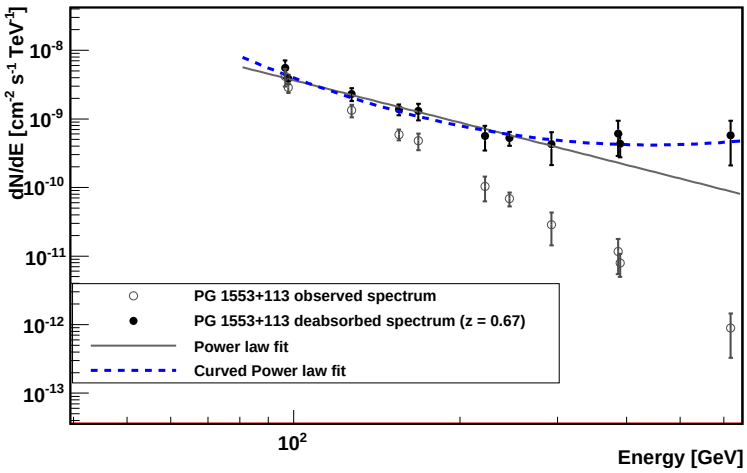

Figure 7.10: Deabsorbed spectrum of PG 1553+113 for a distance $z = 0.67$.

7.3.2 PKS 1424+240

Thanks to the longer exposure of VERITAS observations of PKS 1424+240 in the VHE range, the spectrum, even if compatible with the MAGIC mean spectrum

obtained from combined 2009/10 data, is better determined. For this reason we use the VERITAS data to estimate the limit on the distance of this blazar.
The result of the maximum hardness study is shown in Figure 7.11. The redshift at which the slope becomes 1.5 is $z_{\Gamma=1.5}= 0.51 \pm 0.15$, Fig. 7.11(a). The corresponding redshift limit resulting with this method is $z < 0.81$, at a $2\,\sigma$ level. Figure 7.11(b) reports the results of the likelihood ratio test. In this case, the observed spectrum does not show any significant curvature corresponding to a negative concavity in the spectrum. Therefore, the probability resulting from the χ^2 ratio test is a monotonic function of the redshift, and becomes 95% at values larger than 1.

Clearly, for this source the most constraining method is the maximum hardness one, conversely to the PG 1553+113 case. The reason could be related to the lack of low energy points in the spectrum. Hence, from our study the redshift is constrained below 0.81. The corresponding spectrum is shown in Figure 7.12.

For the sake of completeness, we report the results of the study applied using the MAGIC determination of the spectrum reported in Chapter 6. As expected, the redshift at which the slope of the deabsorbed spectrum becomes 1.5 is $z = 0.88 \pm 0.19$, well above the determination obtained with VERITAS data. If we adopt the no pile–up criterion, the z at a which the third peak becomes evident is larger than 1.2, again well above the determination obtained with the VERITAS spectrum (Figure 7.13).

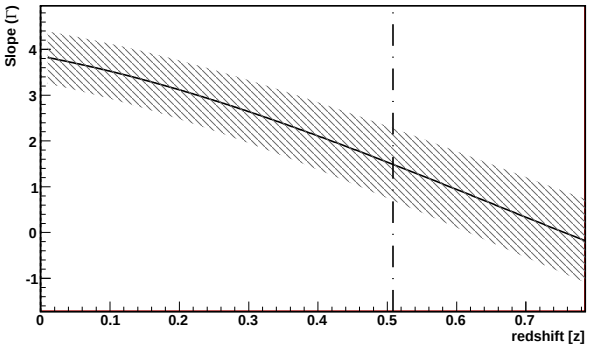

(a) Limit on PKS 1424+240 distance from the deabsorbed spectrum power law fit.

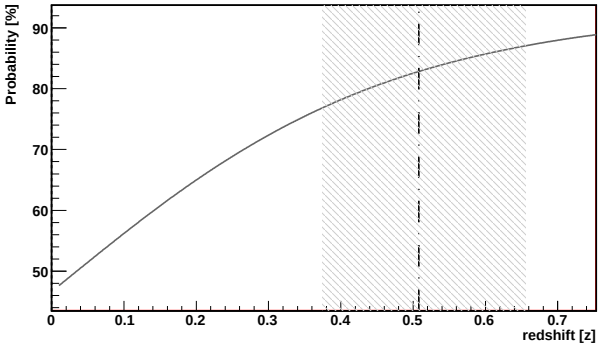

(b) Limit on PKS 1424+240 distance from the likelihood ratio test.

Figure 7.11: Result of the distance study on PKS 1424+240.

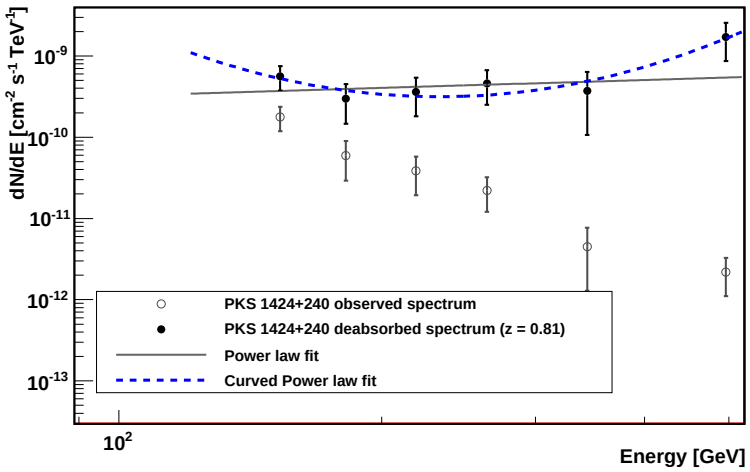

Figure 7.12: Deabsorbed spectrum of PKS 1424+240 in the limit hypothesis of redshift $z = 0.81$. We assume Franceschini EBL model.

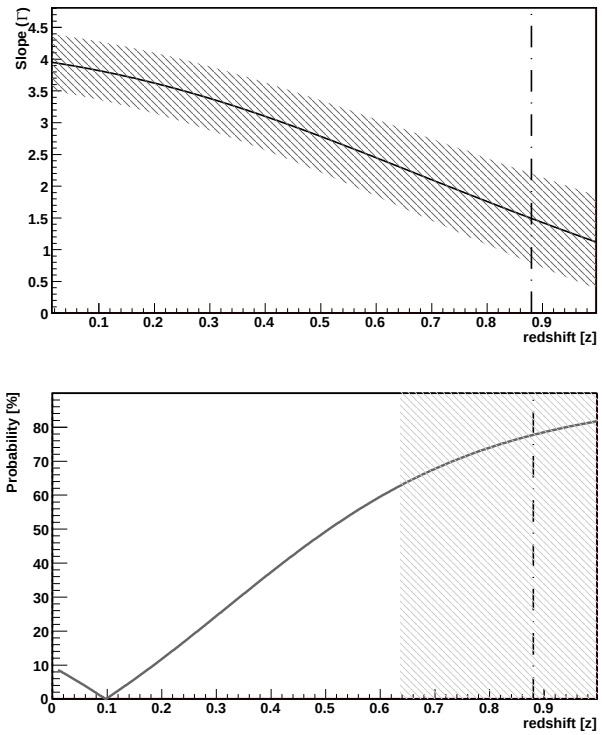

Figure 7.13: Results of the study on PKS 1424+240 distance, using PKS 1424+240 the mean 2009/10 spectrum estimated in Chapter 6.

7.4 Conclusions

In this Chapter, the effect of EBL on blazars spectra has been investigated. In particular, it has been shown how, starting from the observed VHE spectrum of a blazar and an EBL model, it is possible to set a limit on its distance. This is of particular interest since many BL Lac objects have unknown redshift, due to the relativistically enhanced emission from the jet.

Two different methods have been proposed, based on the properties of the deabsorbed spectrum, and applied to the blazars PG 1553+113 and PKS 1424+240. In the first case, the requirement that the deabsorbed spectrum does not show a pile–up at high energies leads to the most stringent limit on the source distance ($z < 0.67$). In the second case, on the contrary, it is the demand of a spectral index softer than 1.5 to better constrain the source redshift ($z < 0.81$). To calculate this limit we adopted the VHE γ–rays spectrum measured by VERITAS. The same analysis performed on the MAGIC spectra reported in Chapter 6, gives less strict limits.

Everything we see hides another thing, we always want to see what is hidden by what we see

René Magritte

8

Constraining blazars distances with combined GeV and TeV data

We discuss a method to constrain the distance of blazars with unknown redshifts using combined observations in the GeV and TeV regimes. It is based on the assumption that the VHE spectrum corrected for the absorption through the interaction with the EBL can not be harder than the spectrum in the *Fermi*/LAT band. The method is successfully tested on a preliminary sample of TeV blazars detected by *Fermi*/LAT after 5.5 months of data taking. Using different EBL models leads to systematic changes in the derived upper limits. We have also derived an empirical law describing the relation between the constrains found and the true redshifts, that can be used to give an estimate of the distance of unknown redshift blazars. The method is then tested on an updated sample of blazars based on the latest GeV and TeV results. The case of PG 1553+113 is discussed in detail, and, finally, we use the empirical law to infer the distance of the unknown redshift blazar PKS 1424+240.

This work has been published in Prandini et al. (2010), Prandini et al. (2011a), and Prandini et al. (2011b).

8.1 Introduction

In the previous Chapter we have discussed how VHE photons emitted by cosmological sources are effectively absorbed, through the pair production process $\gamma\gamma \rightarrow e^{+-}$, by the interaction with the EBL (Stecker et al., 1992). We have shown that, if we make reasonable hypotheses on the intrinsic spectrum of a blazar at VHE and assume a model for the EBL energy density and its evolution, an upper limit on the redshift of unknown distance blazar can be estimated.

In this Chapter we continue the study and discuss a new method to derive an upper limit on the redshift of a source based on the comparison between the spectral index at GeV energies as measured by LAT, which is unaffected by the cosmological absorption up to redshifts far beyond those of interest here, and the deabsorbed TeV spectrum. We will show that a solid upper limit to the distance can be inferred deriving the redshift at which the slope of the deabsorbed spectrum coincides with that measured by LAT.

With respect to the methods presented in previous Chapter, this approach is

based on direct observations. It can be considered complementary to those used by Stecker and Scully (2010) and Georganopoulos et al. (2010) (see also Abdo et al. 2009), where the comparison of the spectral slopes at GeV and TeV energies of blazars at known distances is used to derive limits on the EBL.

Starting from the derived limits, we find a simple law relating these values to the real redshifts, that can be used to give an estimate on the distance of unknown redshift blazars. In the second part of the Chapter, the same study is performed using an updated blazar sample, based on the latest published *Fermi* catalog (Abdo et al., 2010).

The work can be sub–divided into two parts:

- *Preliminary study*: where we test the idea of using the slope of the power law fitting the blazar spectrum in the HE energy range as a limit on the unabsorbed TeV spectrum. This is an empirical version of the maximum hardness hypothesis, presented in Sec. 7.2.1. The maximum value, in this case, is not a constant set by theory but it is related to a measured quantity.

  The sample used is composed of all TeV blazar detected by *Fermi*/LAT after 5.5 months of operation. We will show that the results obtained are satisfactory. Moreover, we propose an empirical law that allows the determination of the distance of a TeV emitting blazar.

- *Follow–up study*: where we perform the same study on an enlarged sample of TeV blazars, from the 1-year *Fermi* catalog. We also adopt a new EBL model.

We assume a cosmology with $h = 0.72$, $\Omega_M = 0.3$ and $\Omega_\Lambda = 0.7$.

8.2 Blazars sample

For the preliminary study, we consider all the extragalactic TeV emitters observed with the new generation of Cherenkov instruments (H.E.S.S., MAGIC and VERITAS) located at redshift larger than $z = 0.01$, detected by *Fermi*/LAT after 5.5 months of data taking, as reported in Abdo et al. (2009). All the sources forming the sample are blazars (see Chap. 2). The photon flux emitted by a blazar, in both GeV and TeV regimes, can be usually well approximated with power laws, of the form $dN/dE = f_0(E/E_0)^{-\Gamma}$, where Γ is the power law index. In total, the sample is composed of the sixteen sources listed in Table 8.1, along with their spectral slopes, in the $0.2 - 300$ GeV, Γ_{HE} and TeV, Γ_{VHE}, regimes.

NOTE ON PG 1553+113 – In order to increase statistics, in this work we assume the redshift of PG 1553+113 to be 0.40, as listed in Table 8.1. This hypothesis is strongly supported by recent optical observations of the Ly–α forest (Danforth et al., 2010). Moreover, it is in agreement with both lower and upper limits provided by other studies. In Section 8.7.1 a detailed study on this assumption is done.

Source Name	z_{true}	Γ_{HE}	Γ_{VHE}
Mkn 421	0.030	1.78 ± 0.03	$2.3 \pm 0.1^{(1)}$
Mkn 501	0.034	1.73 ± 0.06	$2.3 \pm 0.1^{(2)}$
1ES 2344+514	0.044	1.76 ± 0.27	$2.9 \pm 0.1^{(3)}$
Mkn 180	0.045	1.91 ± 0.18	$3.3 \pm 0.7^{(4)}$
1ES 1959+650	0.047	1.99 ± 0.09	$2.6 \pm 0.2^{(5)}$
BL Lacertae	0.069	2.43 ± 0.10	$3.6 \pm 0.5^{(6)}$
PKS 2005−489	0.071	1.91 ± 0.09	$3.2 \pm 0.2^{(7)}$
W Comae	0.102	2.02 ± 0.06	$3.7 \pm 0.2^{(8)}$
PKS 2155−304	0.116	1.87 ± 0.03	$3.4 \pm 0.1^{(9)}$
1ES 0806+524	0.138	2.04 ± 0.14	$3.6 \pm 1.0^{(10)}$
1ES 1218+304	0.182	1.63 ± 0.12	$3.1 \pm 0.3^{(11)}$
1ES 1011+496	0.212	1.82 ± 0.05	$4.0 \pm 0.5^{(12)}$
S5 0716+714	$0.310^{a,b}$	2.16 ± 0.04	$3.4 \pm 0.5^{(13)}$
PG 1553+113	0.400^{c}	1.69 ± 0.04	$4.1 \pm 0.2^{(14)}$
3C 66A	0.444^{a}	1.93 ± 0.04	$4.1 \pm 0.4^{(15)}$
3C 279	0.536	2.34 ± 0.03	$4.1 \pm 0.7^{(16)}$

Table 8.1: List of TeV blazars used in the study. In the first column the list of sources, their redshift (second column), their *Fermi*/LAT slope (third column) and the VHE slope of the observed spectrum fit (fourth column). [a]: uncertain. [b]: from Nilsson et al. (2008). [c]: Danforth et al. (2010). 1: Acciari et al. (2009); 2: Albert et al. (2007e); 3: Albert et al. (2007d); 4: Albert et al. (2006b); 5: Tagliaferri et al. (2008); 6: Albert et al. (2007b); 7: HESS Collaboration et al. (2010); 8: Acciari et al. (2009b); 9: Aharonian et al. (2009); 10: Acciari et al. (2009a); 11 Acciari et al. (2009); 12: Albert et al. (2007c); 13: Anderhub et al. (2009a); 14: Prandini et al. (2009); 15: Acciari et al. (2009); 16: Albert et al. (2008c)

8.2.1 Blazars spectral break

Figure 8.1 displays the comparison between the power law indices Γ_{HE} and Γ_{VHE} listed in Table 8.1: while the former distribute from 1.63 to 2.43, with a peak around 2, the VHE spectral slopes show a larger distribution, ranging from 2.28 to 4.12.

The systematic difference between the two distributions is primarily due to an intrinsic break in the spectrum emitted by the source. In fact, the peak of the HE component in the SED of TeV blazars is commonly located between GeV and thousands of GeV (e.g. Tavecchio et al. 2010): LAT observes mainly the photons of energy below the energy of the IC peak, in the hard portion of the spectrum, while Cherenkov instruments probe the steeper part of the peak (e.g. Aharonian et al. 2009).

A second effect influencing the distribution of TeV slopes is the interaction of VHE photons with EBL and the consequent reduction of the flux which depends on the distance (see also Sec. 7.1). This dependence is likely responsible for the observed spread of the TeV spectral indices not present in the well peaked GeV indices distribution.

In principle, as largely debated in previous Chapter, it is possible to derive the emitted (or intrinsic) spectrum by deabsorbing the observed spectrum. This procedure depends on the absorption coefficient $\tau(E, z)$ and the redshift z of the source. Viceversa, if the intrinsic source spectrum is known, given the absorption coefficient τ, the redshift z can be estimated comparing the absorbed spectrum

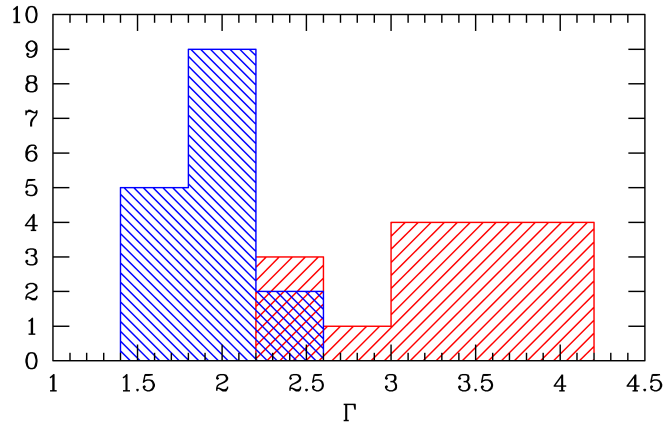

Figure 8.1: Spectral indices distributions of blazars listed in table 8.2 as measured by *Fermi*/LAT after 5.5 months of operations (left histogram) and Cherenkov instruments (right histogram).

with the observed one.

Here, we use the second approach, developing an empirical method to estimate a safe upper limit to the source distance based on the reasonable assumption that the intrinsic spectrum at TeV energies cannot be harder than that in the adjacent GeV band. Indeed, from the brightest objects studied at both GeV and TeV energies it appears that the SED is continuous with a broad peak not requiring additional spectral components (e.g. Aharonian et al. 2009). Hence, a natural assumption is to require that the slope measured in the GeV energy range is a limit value for the power law index of the deabsorbed TeV spectrum. This condition, satisfied when the IC peak maximum extends beyond the VHE spectral points, has never been observed in nearby blazars, for which the EBL absorption effect is negligible.

8.3 Results

In order to test the maximum hardness hypothesis, we estimate the redshift, z^*, for which the TeV spectral slope equals the GeV one, the measured spectral points of each source have been corrected for the corresponding absorption factor starting from $z = 0.01$, and the resulting spectrum fitted with a power law. This procedure, applied in fine steps of redshift, is iterated until the slope of the deabsorbed spectrum equals the one measured by LAT. The corresponding redshift, z^*, is the limit value on the source distance.

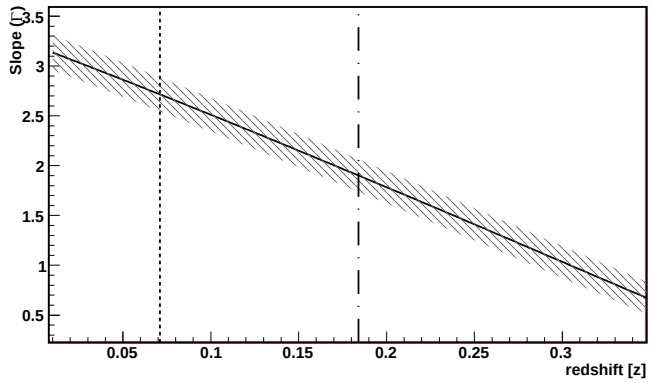

Figure 8.2: TeV slope of PKS 2005-489 as a function of the redshift with a $1\,\sigma$ error bar, using the Franceschini EBL model. The vertical dotted line corresponds to the true redshift value of the source, the dashed-dotted one to z^*.

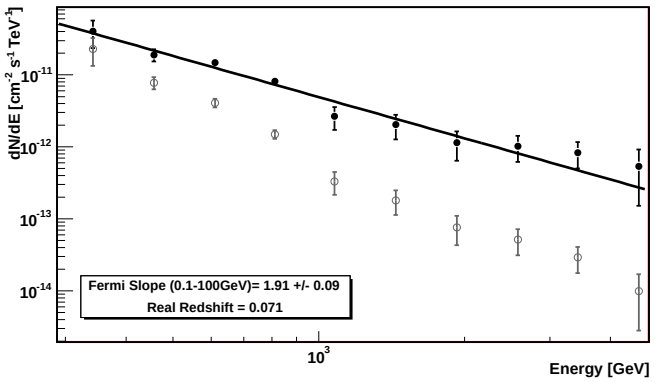

Figure 8.3: The measured (open circles) and deabsorbed (filled circles) spectrum of PKS 2005-489 assuming the redshift z^*, deabsorbed with the Franceschini EBL model.

Source Name	z_{true}	z^* low EBL model	z^* mean EBL model	z^* high EBL model
Mkn 421	0.030	0.10 ± 0.02	0.08 ± 0.02	0.05 ± 0.01
Mkn 501	0.034	0.12 ± 0.02	0.10 ± 0.02	0.07 ± 0.01
1ES 2344+514	0.044	0.25 ± 0.08	0.20 ± 0.06	0.14 ± 0.04
Mkn 180	0.045	0.25 ± 0.15	0.20 ± 0.13	0.15 ± 0.09
1ES 1959+650	0.047	0.11 ± 0.05	0.09 ± 0.04	0.06 ± 0.02
BL Lacertae	0.069	0.30 ± 0.16	0.26 ± 0.13	0.17 ± 0.09
PKS 2005−489	0.071	0.24 ± 0.05	0.18 ± 0.03	0.13 ± 0.03
W Comae	0.102	0.30 ± 0.06	0.24 ± 0.05	0.18 ± 0.03
PKS 2155−304	0.116	0.28 ± 0.02	0.22 ± 0.01	0.16 ± 0.01
1ES 0806+524	0.138	0.28 ± 0.19	0.24 ± 0.16	0.18 ± 0.12
1ES 1218+304	0.182	0.26 ± 0.11	0.22 ± 0.09	0.17 ± 0.07
1ES 1011+496	0.212	0.67 ± 0.19	0.62 ± 0.18	0.35 ± 0.09
S5 0716+714	0.310[a]	0.26 ± 0.11	0.22 ± 0.10	0.16 ± 0.07
PG 1553+113	0.400	0.78 ± 0.07	0.74 ± 0.08	0.39 ± 0.03
3C 66A	0.444[a]	0.45 ± 0.08	0.38 ± 0.06	0.26 ± 0.04
3C 279	0.536	1.09 ± 1.07	-	0.44 ± 0.42

Table 8.2: Redshift values obtained by deabsorbing the VHE spectra until the slope is the one observed by LAT, using three different EBL models. [a]: uncertain.

An example is illustrated in Figure 8.2, where the procedure is applied to the blazar PKS 2005-489. The plot represents the value of the slope of the power law fitting the VHE deabsorbed spectrum (corrected for EBL, using the Franceschini model) as a function of the redshift z. As expected, the value of the slope Γ decreases as the redshift increases. For this source, of redshift $z = 0.071$, the slope reported by LAT in the 0.2–300 GeV energy range is 1.91 ± 0.09, Table 8.1. The value of the redshift, z^*, for which the deabsorbed spectrum at TeV energies assumes this slope is 0.18 ± 0.03, Figure 8.3, well above the real distance.

8.3.1 Test on maximum hardness hypothesis

Of the sixteen sources considered in this study, 14 blazars have well known redshift and are used to test the method, while the remaining two blazars (3C 66A and S5 0716+714) have uncertain redshift, and are considered separately. The last

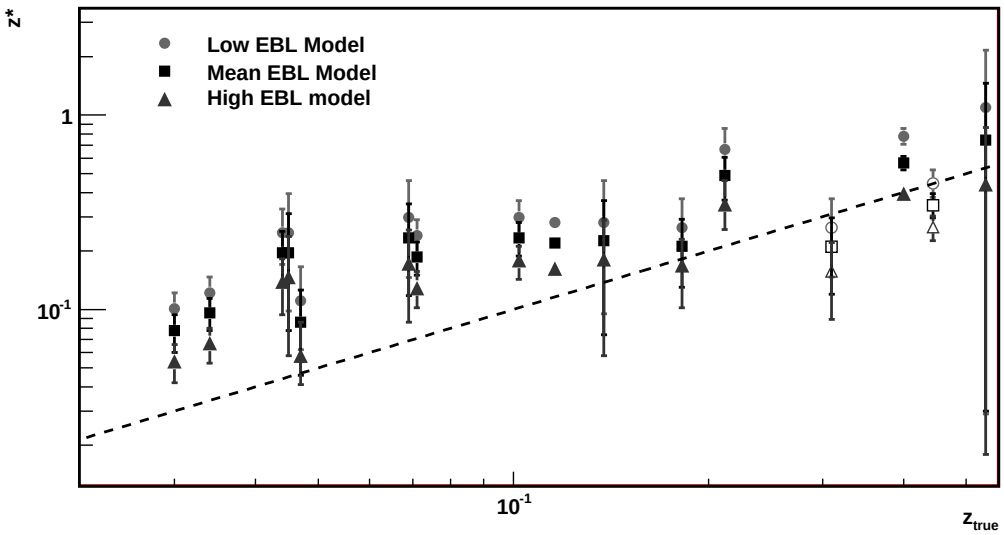

Figure 8.4: True redshifts vs z^* derived with the procedure described in the text for the three different EBL models. The open circles represent the sources with uncertain redshift (3C 66A and S5 0716+714). The dashed line is the bisector: only for the sources 3C 66A and S5 0716+714 the limits on the redshift estimated are below the true (even if uncertain) redshifts.

three columns of Table 8.2 list the z^* values calculated following the method described above, using three different EBL models: a low limit model (Kneiske and Dole, 2010), a mean (Franceschini et al., 2008)[1] and a high level one (Stecker et al. 2006, baseline model). The absorption coefficients of the last model were obtained from a simple extrapolation of the values given for fixed redshifts in Stecker et al. 2006 (F. Stecker, private communication). The errors on z^* are estimated taking into account both errors on the TeV and LAT slopes. For the distant source 3C 279, the slope of the spectrum deabsorbed with the Franceschini et al. (2008) EBL model does not reach the LAT value at redshift lower than z = 1.2, where the last point of the spectrum diverges. Hence, in this case it is not possible to estimate z^*.

Figure 8.4 shows the comparison between the real redshift, x-axis, and the estimated one, y-axis, obtained with the three different EBL models. It is evident that different levels of extragalactic background light lead to significantly different values for z^*. A high EBL level (Stecker et al., 2006) implies more absorption and corresponds to small values for z^*. Viceversa, large z^* values are obtained with an EBL model which foresees less absorption. The difference between the mean z^* values of the two extreme models is of the order of 56%. This result underlines the large uncertainty still existing on EBL. Recently, the *Fermi* Collaboration has investigated the effect of gamma-ray flux attenuation by the EBL in distant blazars and GRBs (Abdo et al., 2010a). The study correlates the photons above 10 GeV with the distance of the emitting source. As a result, the baseline model of Stecker et al. (2006) is ruled out with high confidence, due to its large EBL

[1]The values of z^* reported are slightly different from the published ones in Prandini et al. (2010). This difference is due to a variation in the extrapolation method of the absorption coefficients of Franceschini et al. (2008) EBL model. The numbers reported in this work should be considered as the final ones.

intensity in the optical-ultraviolet wavelengths. This conclusion is in line with other experimental findings, such as the spectrum of the FSRQ 3C 279 observed by MAGIC Albert et al. (2008c).

The difference between the z^* values estimated with the other two models is less evident, especially at higher redshifts. The mean relative dispersion is less than 20%.

For the low and mean level EBL models, all the z^* values are larger than the real redshifts, i.e. they lie above the bisector (dashed line) of Figure 8.4. This is expected since we are not considering the presence of the intrinsic break in the blazar spectra and *confirms that the method can be used to set safe upper limits on blazars distance*, if we use a mean EBL density model. Conversely, the values estimated using Stecker et al. (2006) EBL model are approximately at the level of the true redshifts, suggesting that this model cannot be used to set safe upper limits on the blazars distance with the method presented here.

The only exceptions are the two sources with uncertain distance, S 0716+714 and 3C 66A (open markers). The behaviour of Γ_{VHE} as a function of the redshift, for 3C 66A is displayed in Figure 8.5, while that of S5 0716+714 is shown in Figure 8.6. In both cases, the z^* values are well below the presumed values, for all EBL models. This is an evidence in favour of a wrong estimate of their distances. However, we cannot rule out the possibility that these sources are peculiar; in particular, the *Fermi*/LAT slope of S5 0716+714 is well above the usual value observed in other blazars. This fact could lead to an underestimation

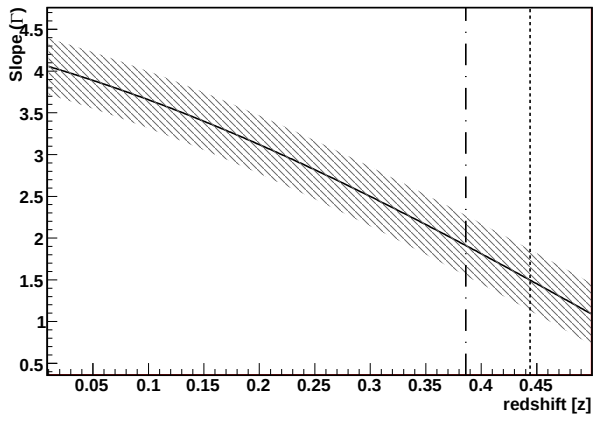

Figure 8.5: Γ_{VHE} obtained by deabsorbing the VHE γ–rays spectrum of 3C 66A as a function of the redshift, z. The vertical dashed line represents the (uncertain) redshift of the sources, while the dashed–dotted line is the z^* estimated with our method.

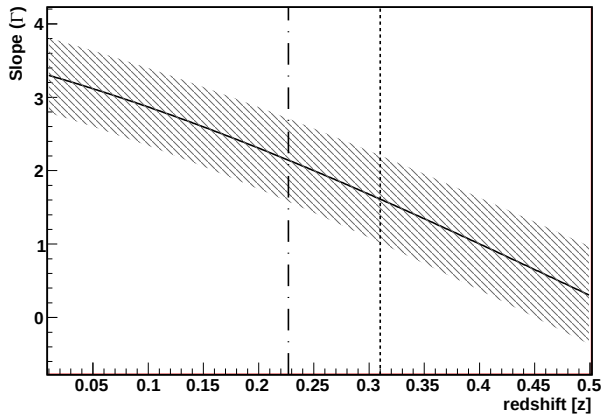

Figure 8.6: Γ_{VHE} obtained by deabsorbing the VHE γ–rays spectrum of S5 0716+714 as a function of the redshift, z. The vertical dashed line represents the (uncertain) redshift of the sources, while the dashed–dotted line is the z^* estimated with our method.

of the quantity z^*. Nevertheless, even if we assume, for this source, a $\Gamma_{HE} = 1.8$, in line with the mean value measured in other blazars, we obtain $z^* = 2.82 \pm 0.10$, still above the (uncertain) value of $z = 0.31$ reported in literature.

8.3.2 Linear relation

Stecker and Scully (2010) derived a linear expression for the steepening of the observed TeV slope due to EBL absorption. Since in our procedure z^* is related to this steepening, it would be natural also for z^* and z_{true} to be related by a linear function, $z^* = A + Bz_{true}$.

In order to check this possibility, we interpolate with a linear function the z_{true}–z^* distribution of the data with well known distance, estimated with the mean EBL model. The result of the interpolation is drawn in Figure 8.7. The linear fit (continuous line) describes very well the data, as confirmed by the reduced chi-squared value of the fit, $\chi^2/d.o.f. = 9.5/11$, and corresponding probability of 58%. The parameters of the fit are listed in Table 8.3, together with the results obtained with of the other two EBL models. Even if the optical depth evolution is different between the EBL models, a linear behaviour is evident also in the two extreme cases.

The meaning of the coefficients is rather transparent: basically A is a measure of the intrinsic spectral break of the sources, while, following Stecker and Scully (2010), B is a measure (increasing values for decreasing EBL level) of the optical depth of the EBL model used.

Table 8.3: Parameters of the linear fitting curves (z^*=$A + Bz_{true}$).

EBL Model	A	B
Low level	0.062 ± 0.017	1.86 ± 0.17
Mean level	0.036 ± 0.014	1.69 ± 0.15
High level	0.040 ± 0.009	0.96 ± 0.08

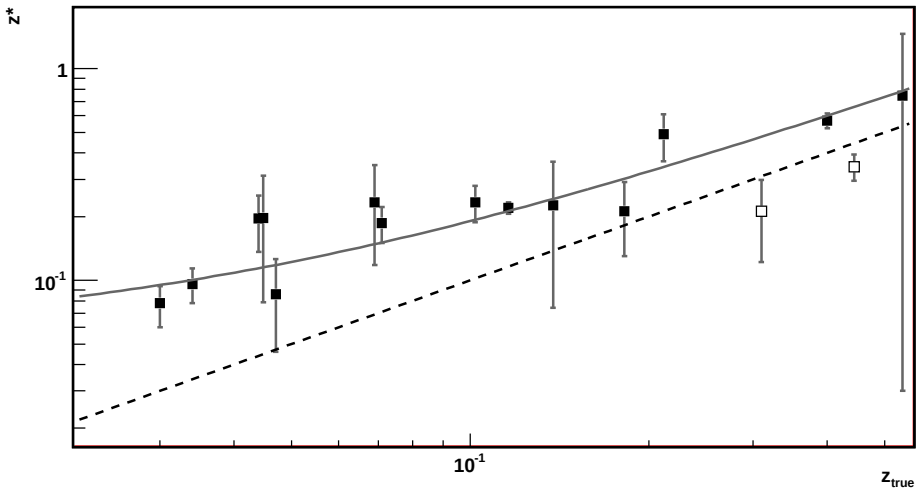

Figure 8.7: True redshifts vs z^* derived with the procedure described in the text for the Franceschini EBL model. The open circles were not used in the fit calculation (continuous line) since their redshift is uncertain (sources 3C 66A and S5 0716+714). The dashed line is the bisector: only for the sources 3C 66A and S5 0716+714 the limits on the redshift estimated in this work are below the true (even if uncertain) redshifts.

Source Name	z_{true}	z_{rec}
Mkn 421	0.030	0.02
Mkn 501	0.034	0.04
1ES 2344+514	0.044	0.10
Mkn 180	0.045	0.10
1ES 1959+650	0.047	0.03
BL Lacertae	0.069	0.13
PKS 2005−489	0.071	0.09
W Comae	0.102	0.12
PKS 2155−304	0.116	0.11
1ES 0806+524	0.138	0.12
1ES 1218+304	0.182	0.11
1ES 1011+496	0.212	0.35
S5 0716+714	0.310^a	0.11
PG 1553+113	0.400	0.42
3C66A	0.444^a	0.20

Table 8.4: Reconstructed redshift values obtained by applying the inverse formula to the linear fit of Fig. 8.7. ^{a}: uncertain.

Having derived this empirical relation we can use it to *derive the redshift* of sources with uncertain distance. This can be done under the assumption that the source of interest shares similar spectral properties with the sources used to derive the fit (basically they have similar values of the spectral break measured by A).

To demonstrate the feasibility of such a method, in Table 8.4 we report the values of the *reconstructed* redshift, z_{rec}, obtained by applying the inverse formula $z_{rec} = (z^* - A)/B$ to the z^* estimated with the Franceschini EBL model. The distribution of the differences between the real and the reconstructed redshifts, Δz, is drawn in Figure 8.8 (filled area). Despite the low statistics involved, the distribution can be roughly described (probability of 35%) by a Gaussian centered in zero with a σ of 0.04. The separated shaded histogram represents the Δz of the uncertain redshift sources.

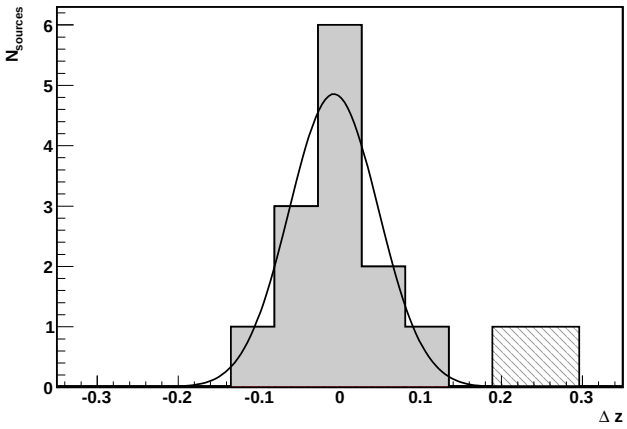

Figure 8.8: Δz plot ($z_{true} - z_{rec}$) (filled histogram) and superimposed the two sources with uncertain redshift (S5 0716+714 and 3C 66A), not used for the Gaussian fit.

8.4 Discussion

In previous Sections, we have presented a method that allows the estimation of the quantity z^*, and demonstrated that this value can be considered as an upper limit on the redshift of a TeV emitting blazar with a GeV counterpart.

In order to use the largest sample of spectra for this study, we made several assumptions: first of all we combined GeV and TeV data even if the observations in the different energy bands were not simultaneous. The impact of this choice, however, is probably moderated by fact that we do not use the flux but only the values of the slopes, less variable than the flux (unless in extreme states). For example the spectral slope of the HBL 1ES 1218+304 recently measured by the VERITAS Collaboration (Acciari et al., 2010) during a high flux level, matches within the errors the slope determined during its quiescent state.

Secondly, in this work we use TeV spectra observed with various Cherenkov experiments, characterized by different sensitivities. This difference, especially at high energies, could affect the result, leading to systematic effects in the distance limit determination. Another possible cause of systematics could be the use of all the blazar sample, independently from the nature of the source: we didn't apply any distinction between HBL, LBL and FSRQ, characterized by a different position of the IC peak. For a detailed treatment of the systematics, see Section 8.6.

Despite all these approximations, the method presented, applied to a sample of test sources, gave satisfactory results. The z^* values obtained by correcting the spectra from the EBL absorption, are, in fact, all above the real redshift values if we use a low and a mean background photon level. This suggest the use of this method for constraining the distance of unknown redshift sources.

We applied the z^* estimate also to two sources with uncertain distance: in both cases the limit lies below the quoted values. This result could be due to some intrinsic properties of the sources (specifically, a more moderate intrinsic spectral break between the GeV and TeV bands than that of the other sources), or to a wrong estimate of their distances. In the latter case, our method would constrain the redshift of S5 0716+714 below 0.22 ± 0.10 and that of 3C 66A below 0.38 ± 0.06. It can be pointed out that for the case of S5 0716+714, the redshift of 0.31 used in this work, recently reported by Nilsson et al. (2008), is estimated by assuming the luminosity of its host galaxy. Another estimate on the blazar distance, based on the spectrography of the three galaxies close to this source, gives the value of $\sim$0.26 for its redshift, more in agreement with our derived limit.

The same procedure was applied to our sample using two extreme EBL models. The low density one gives even safer upper limits on the sources distance, while the z^* obtained with the high density model are very close to the real redshift values. Except for this model, recently ruled out by other works, all the estimates are well above the bisector, confirming our assumption that the deabsorbed TeV slope cannot be harder than the GeV slope reported by *Fermi*/LAT.

Following previous works, we tested the possibility of a linear relation between our z^* estimates and the real distance of the sources. We found that the linear fit describes quite well our results, independently on the EBL model considered, although the slope and intercept of the fits are different in the three cases (Table 8.3).

The relation found suggests to use the z^* estimate not only to set an upper limit on unknown distances of blazars, but also, via the inverse formula, to try an

evaluation of this distance. In order to investigate this opportunity, we tested it on our sample of sources using the mean EBL model, paying a special attention to avoid biases in the calculation. The distribution of the difference Δz between the reconstructed and the real redshift can be approximated by a Gaussian peaked in zero with a σ of 0.04. Once again, the uncertain redshift sources are outside the expected interval.

The value of the redshift of S5 0716+714 obtained with this method is 0.11 ± 0.04, where the error quoted is the σ of the Δz distribution. For 3C 66A, the same procedure leads to a redshift estimate of 0.20 ± 0.04.

8.5 Follow–up study

In previous Section, we presented a new method for constraining the redshifts of TeV blazars, based on the power law index measured at lower energies. We tested this method on all the TeV sources discovered before December 2009 and present in the *Fermi* catalog of the first 5.5 months of observations.

As a follow–up of that work, we test the same method on an *updated sample* of objects and with a new EBL model.

The main characteristic of this study is the use of:

- *New TeV sources* - Recently the H.E.S.S. and VERITAS collaborations published the previously unknown spectra of PKS 0548-322 (Aharonian et al., 2010) and RGB J0710+591 (Acciari et al., 2010b), respectively. However, only the latter source has been detected at lower energies by *Fermi* and is included in the sample.

  Despite many TeV emitters, listed in Table 8.5, have been discovered since late 2009 by IACTs, none of the new sources can be included in our sample since the corresponding TeV spectra are not published, yet.

- *1-year Fermi Catalog* - The public on–line catalog[2] of *Fermi* sources, published in Abdo et al. (2010), has been updated with the data collected after the first year of operations. Here we will adopt this new catalog whose exposure time is more than doubled with respect to the 5.5 months catalog used in previous study. Thanks to the longer coverage, new sources have been detected in the HE range; moreover new measures of the spectra of known sources have been performed. With respect to the 5.5 months catalog, the new LAT determinations of the spectral slopes are characterized by smaller errors, due to the increased statistics.

- *Latest EBL model* - The new Dominguez model, which takes into account updated results from recent surveys, is considered, in addition to the Franceschini model.

8.5.1 Results

The updated sample, listed in the first column of Table 8.6, is composed of 17 sources with well known redshift[3] and two additional sources with uncertain red-

[2] available at $http://fermi.gsfc.nasa.gov/ssc/data/access/lat/1yr\_catalog/$

[3] The source 1H 1426+428 is not included in the sample since never detected by the last generation of Cherenkov instruments (VERITAS, H.E.S.S. or MAGIC).

Table 8.5: New TeV sources discovered starting from late 2009 by Cherenkov Telescopes. None of these sources is included in the new sample since the TeV spectra are still unpublished. [a]: z uncertain.

Source Name	redshift	Type
NGC 1275	0.0176	Center of Perseus cluster
IC 310	0.0189	Unidentified Object
AP Lib	0.049	BL Lac
SHBL J001355.9	0.0948	HBL
B3 2247+381	0.119	BL Lac
1ES 1215+303	0.13[a]	LBL
1ES 1440+122	0.162	BL Lac
RBS 0413	0.19	BL Lac
PKS 0447-439	0.2	BL Lac
1ES 0414+009	0.287	BL Lac
1ES 0502+675	0.341	BL Lac
PKS 1510-08	0.36	FSRQ
4C +21.35	0.432	FSRQ
RGB 0648+152	unknown	Unidentified Object
VER J0648+152	unknown	Unidentified Object
MAGIC J2001+435	unknown	BL Lac
VER J0521+211	unknown	Unidentified Object

shift, namely 3C 66A and S5 0716+714. The second and third columns represent the slopes measured by LAT after 5.5 months (between 0.2 GeV to 300 GeV) and 1-year (between 0.1 GeV to 100 GeV). Three new sources are included in the sample: RGB J0710+591, H 2356−309 and 1ES 1101−232, located at redshifts 0.125, 0.165 and 0.186, respectively. The last two sources were not detected by LAT in the first 5.5 months, while the spectrum of RGB J0710+591 has only recently been published by the VERITAS collaboration, as already mentioned.

With this enlarged data set, we estimate the quantity z^*, redshift at which the deabsorbed TeV spectrum exhibits the same slope measured by LAT at lower energies. We adopt the Franceschini EBL model, and the Dominguez model. The values obtained are listed in the last two columns of Table 8.6. In case of 3C 279, the slopes of deabsorbed spectrum do not converge to the LAT value for any redshift. As will be discussed at the end of this Chapter for PG 1553+113, probably also in this case the presence of points in the spectrum with energy below 100 GeV, is the main cause of this result.

Figure 8.9(a) represents the distribution z^* versus z_{true} obtained with the Franceschini model. All the z^* values distribute above or on the bisector. This confirms that z^* can be considered an upper limit on the source redshift, hence the maximum hardness hypothesis is validated also in this study. The linear curve drawn represents the fit of the data. The linear trend of the distribution is less evident here than in the first study. The probability of the fit is, in fact, ∼11%, well below the previous value (58%). The reason for this behaviour can be related to the new sources introduced, but also to the new LAT determination of the slopes. In order to investigate such alternatives, we have fitted the distribution excluding the three new sources. The new fit returns a probability of 14%, close to the value obtained with the full sample. This result suggests that the low probability found is mainly due to the smaller error bars which characterize the determination of the new slopes in the HE band with respect to previous estimates.

Figure 8.9(b) represents the z^* distribution obtained with the more recent EBL model. The linear fit has a slope of 1.58 and and intercept of 0.03; the probability

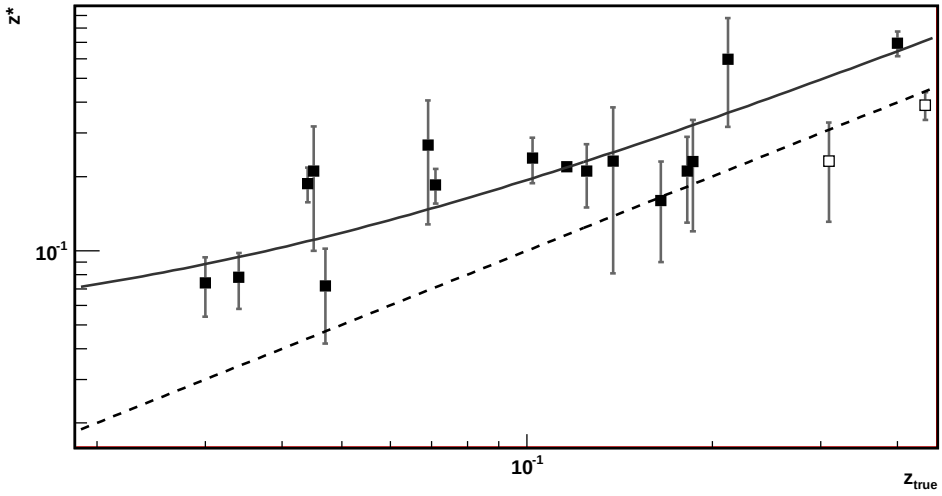

(a) z^* obtained with the Franceschini EBL Model; open markers refer to the two sources with uncertain redshift, excluded from the fit (continuous line).

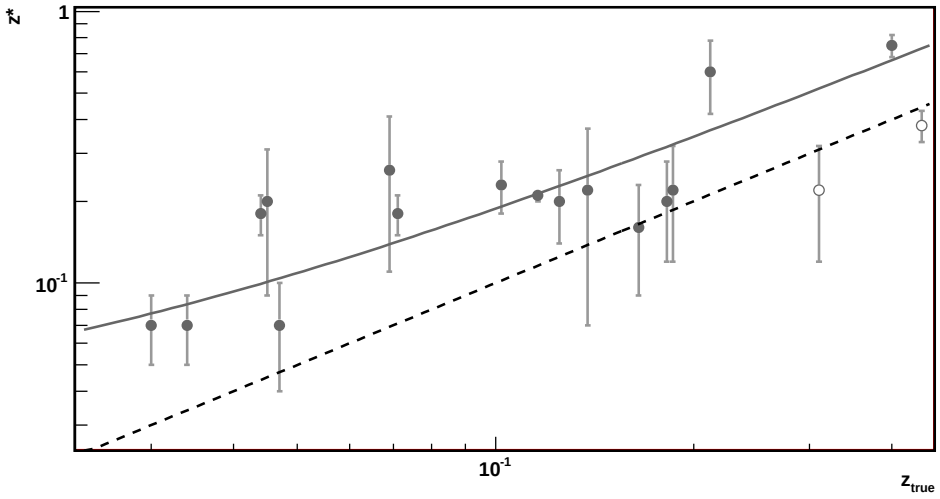

(b) z^* obtained with Domínguez et al. (2011) EBL Model.

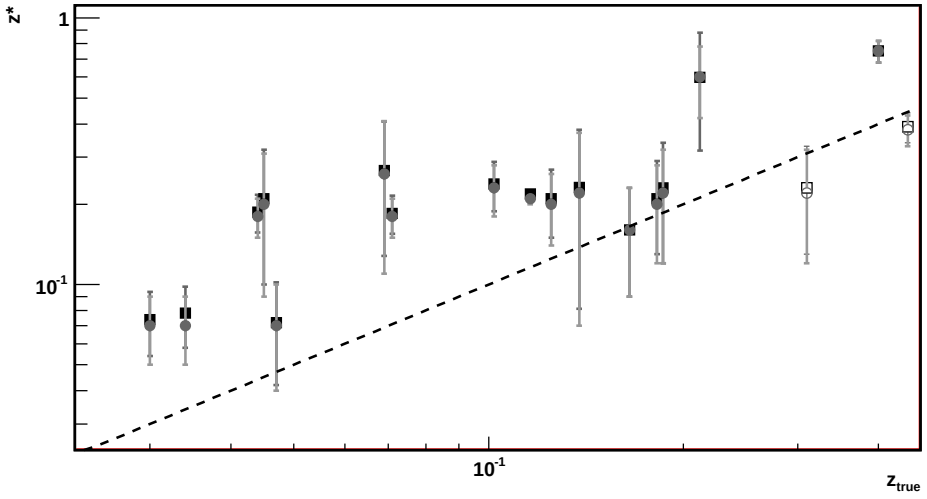

(c) Comparison between the two models.

Figure 8.9: z^* vs z_{true} plots, result of the follow–up study.

Source Name	z_{true}	Γ_{HE} (5.5 m)	Γ_{HE} (1 y)	z^*_{Fra}	z^*_{Dom}
Mkn 421	0.030	1.78 ± 0.03	1.81 ± 0.02	0.07 ± 0.02	0.07 ± 0.02
Mkn 501	0.034	1.73 ± 0.06	1.85 ± 0.04	0.08 ± 0.02	0.07 ± 0.02
1ES 2344+514	0.044	1.76 ± 0.27	1.57 ± 0.17	0.19 ± 0.03	0.18 ± 0.03
Mkn 180	0.045	1.91 ± 0.18	1.86 ± 0.11	0.21 ± 0.11	0.20 ± 0.11
1ES 1959+650	0.047	1.99 ± 0.09	2.09 ± 0.05	0.07 ± 0.03	0.07 ± 0.03
BL Lacertae	0.069	2.43 ± 0.10	2.37 ± 0.04	0.27 ± 0.14	0.26 ± 0.15
PKS 2005−489	0.071	1.91 ± 0.09	1.90 ± 0.06	0.18 ± 0.03	0.18 ± 0.03
W Comae	0.102	2.02 ± 0.06	2.06 ± 0.04	0.24 ± 0.05	0.23 ± 0.05
PKS 2155−304	0.116	1.87 ± 0.03	1.91 ± 0.02	0.22 ± 0.01	0.21 ± 0.01
RGB J0710+591	0.125	1.21 ± 0.25	1.28 ± 0.21	0.21 ± 0.06	0.20 ± 0.06
1ES 0806+524	0.138	2.04 ± 0.14	2.09 ± 0.10	0.23 ± 0.15	0.22 ± 0.15
H 2356−309	0.165	-	2.10 ± 0.17	0.16 ± 0.07	0.16 ± 0.07
1ES 1218+304	0.182	1.63 ± 0.12	1.70 ± 0.08	0.21 ± 0.08	0.20 ± 0.08
1ES 1101−232	0.186	-	1.36 ± 0.58	0.23 ± 0.11	0.22 ± 0.10
1ES 1011+496	0.212	1.82 ± 0.05	1.93 ± 0.04	0.60 ± 0.28	0.60 ± 0.18
S5 0716+714	0.310[a]	2.16 ± 0.04	2.15 ± 0.03	0.23 ± 0.10	0.22 ± 0.10
PG 1553+113	0.400	1.69 ± 0.04	1.66 ± 0.03	0.75 ± 0.07	0.75 ± 0.07
3C 66A	0.444[a]	1.93 ± 0.04	1.92 ± 0.02	0.39 ± 0.05	0.38 ± 0.05
3C 279	0.536	2.34 ± 0.03	2.32 ± 0.02	-	-

Table 8.6: List of TeV blazars used in the follow–up study. Source name (first column), Γ_{HE} reported in the 5.5 months catalog (second column) and in the 1-year catalog (third column), z^* value, as described in the text, obtained with the Franceschini model (fifth column) and the Dominguez model (sixth column). [a]: uncertain.

Table 8.7: Parameters of the linear fitting curves (z^*=A + Bz_{true}), obtained with the updated sample.

EBL Model	A	B
Franceschini	0.036 ± 0.014	1.59 ± 0.14
Dominguez	0.030 ± 0.014	1.58 ± 0.14

of the fit is 6%. The difference of the z^* values obtained with the two models is quite modest, as drawn in Fig. 8.9(c).

Following the first study, now we investigate the distribution Δz, difference between the values z_{rec} listed in Table 8.8 and obtained by applying the inverse formula, and the true redshifts z_{true}. The histogram obtained with Franceschini EBL model is displayed in Figure 8.10, and is approximated by a Gaussian of $\sigma = 0.05$, which can be assumed as the error on the reconstructed redshift, z_{rec}, estimated with this method. The probability of the fit, in this case, has a value of 65%, well above the probability found in the preliminary study (35%). Analogous results are achieved if we adopt Dominguez EBL model. In both cases the two sources with uncertain redshifts, not used for the Gaussian fits, lie outside the expected interval. This result confirms that the behaviour of S5 0716+714 and 3C 66A is different from that found for other sources, and suggests that or these sources are peculiar, or their redshift is wrong.

In conclusion, we can say that with an enlarged data set the results previously found are confirmed. However, the linearity of the z_{true}–z^* relation has a smaller probability, due to the reduced errors of the new Γ_{HE} determinations. Moreover, the error on the reconstructed redshift assumed as the σ of the Gaussian describing

Source Name	z_{true}	$z_{rec(Fra)}$	$z_{rec(Dom)}$
Mkn 421	0.030	0.02	0.02
Mkn 501	0.034	0.03	0.02
1ES 2344+514	0.044	0.09	0.09
Mkn 180	0.045	0.11	0.11
1ES 1959+650	0.047	0.02	0.02
BL Lacertae	0.069	0.14	0.14
PKS 2005−489	0.071	0.09	0.09
W Comae	0.102	0.13	0.12
PKS 2155−304	0.116	0.11	0.11
RGB J0710+591	0.125	0.12	0.12
1ES 0806+524	0.138	0.11	0.11
H 2356−309	0.165	0.08	0.08
1ES 1218+304	0.182	0.11	0.11
1ES 1101−232	0.186	0.12	0.12
1ES 1011+496	0.212	0.35	0.36
S5 0716+714	0.310^a	0.12	0.12
PG 1553+113	0.400	0.45	0.45
3C 66A	0.444^a	0.22	0.22

Table 8.8: Reconstructed redshift, z_{rec}, with the Franceschini and Dominguez background models. The error on the values, determined a posteriori, is 0.05 in both cases. See text for details. ^{a}: uncertain.

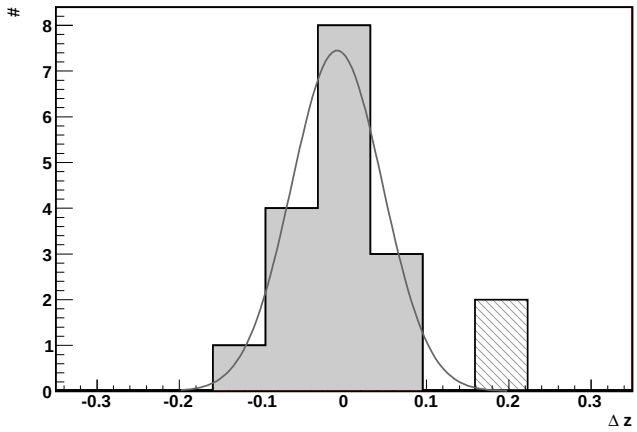

Figure 8.10: Dispersion plot (z_{true}-z_{rec}) obtained adopting Franceschini EBL model. The shaded area represents the two sources with uncertain redshift (S5 0716+714 and 3C 66A), not used in the Gaussian fit.

the residuals from the linear fit is larger with this enlarged sample. The probability of a Gaussian distribution of these residuals, however, is much larger here than in previous study. This could an evidence that despite the linearity of the sample with the new HE spectral determinations is less evident, the procedure that leads to the estimate of the sources distances works well, and is statistically consistent. Taking all this into account, we consider the results of this updated study more reliable with respect to those found in the preliminary work.

8.6 Systematics

In Section 8.4 we have presented a detailed analysis of the assumptions done in the study carried on in this Chapter in order to use the largest possible sample of sources.
Shortly, the basic assumptions are related to the use of:

- not simultaneous *Fermi* and TeV data;
- data from different Cherenkov experiments;
- sources of different nature;

Here, we would like to investigate the role of these assumptions and give an estimate on the order of magnitude of the systematics involved. A more precise quantification of the numbers is almost impossible to give, considering the nature of this type of errors.

8.6.1 Not simultaneous data

Blazars spectra are characterized by fast variability at all wavelengths (see Chap.2). Thus, the use of not simultaneous data in the HE and VHE ranges can lead to systematics in the z^* calculation. Significant changes in the spectral shape (and not only in the flux normalization) of TeV blazars have been observed in the VHE range, while the Γ_{HE} is more stable. Therefore, in what follows we will further investigate the Γ_{VHE} variability.

In some cases, the variability detected at VHE does not correspond to a change in the spectral slope. This is the case, for example, of 1ES 1218+304 (Acciari et al., 2010). In such circumstances, the value of z^* is not affected by the flux change (since related only to the slopes, Γ_{HE} and Γ_{VHE}), and the systematic is negligible.

Conversely, if the spectral slope changes significantly among different source states, the value of z^* can be strongly affected. An evidence of this effect can be obtained by comparing the value of z^* obtained from two distinct spectral states of Mkn 501, observed by the MAGIC telescope.

The spectrum used in the study, and reported in Table 8.6, refers to the highest state ever detected (Albert et al., 2007e). We compare it with the low state measured in 2006 an reported in Anderhub et al. (2009b). Figure 8.11 shows the comparison between the two states, superimposed with other determinations of the source spectrum. It is evident that the source in the two emission states shows a completely different spectral shape. This can be associated to a change in the peak position of the source. The limit on the redshift estimated using the low state is $z^* = 0.17 \pm 0.03$, using Franceschini background model. The value obtained with the high state, instead, is $z^* = 0.08 \pm 0.02$. The difference between the two determinations, a factor larger than 2, underlines the dependence of z^* on the source spectral shape, and suggests this as a significant contribution to the overall a systematic error.

8.6.2 Different instruments

In the study presented, we have used indifferently data collected by instruments with different characteristics. This could lead to systematic errors affecting the z^* determination, related to consistent changes in the experimental conditions.

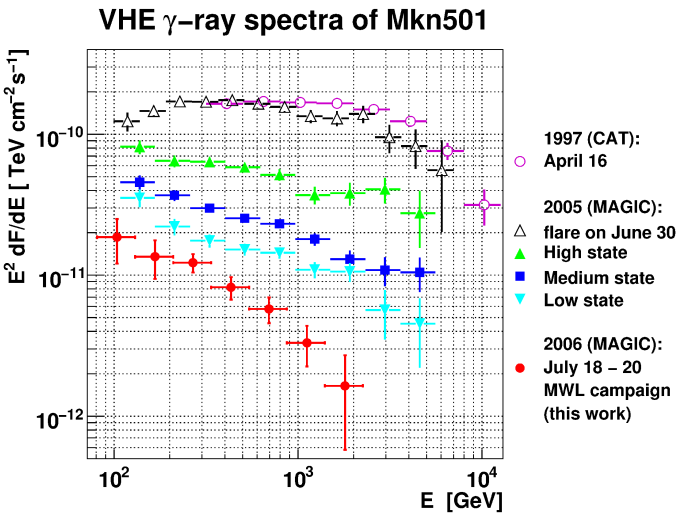

Figure 8.11: Comparison between differential spectra of Mkn 421. Triangles refer to MAGIC spectral determination of a high state, taken in 2005, and used in our study. The spectral slope measured is $\Gamma = 2.28 \pm 0.05$. For comparison, the lowest flux level reported, filled dots, has a slope of $\Gamma = 2.8 \pm 0.1$. Figure from Anderhub et al. (2009b).

In order to test this influence, we compare the value z^* obtained by deabsorbing the spectrum of 1ES 1218+304 taken with MAGIC (Albert et al., 2006a) with the one detected by VERITAS (Acciari et al., 2009) when the source was in the same state. In the former case we have $z^* = 0.38 \pm 0.16$, while in the latter $z^* = 0.21 \pm 0.08$. The reason of this large difference between the two values has to be charged to the presence of low energy points, below 150 GeV, in MAGIC spectrum, obtained thanks to its lower energy threshold. If we interpolate the deabsorbed spectrum above 150 GeV we obtain $z^* = 0.23 \pm 0.14$, well in agreement with VERITAS result.

Hence, the instrument used for the spectral measure, or more precisely its energy threshold, has an important effect on z^* determination. We conclude that this effect is probably an important source of systematics in our study.

8.6.3 Nature of the source

According to the current model of AGNs, blazars can be divided into FSRQ and BL Lac objects, subdivided themselves into HBL, IBL or LBL depending on the position of the synchrotron peak (see Chapter 2). In principle this differentiation, done on spectral properties basis, could affect our analysis.

A careful look into the objects used in our study, reveals that almost all the sources of known redshift used are catalogued as HBL[4]. The only exception is W Comae, classified as IBL. Hence, we can conclude that the sample used in the study is quite homogeneous, and probably not affected by systematics related to the classification.

It can be noticed, however, that the source state can affect the position of the peak, as for the case of Mkn 501 described above. A change of this type induces a large systematic error, especially if the IC peak position moves from below 100 GeV to higher energies, affecting strongly the TeV slope.

[4]Values taken from http://tevcat.uchicago.edu/

8.7 Conclusions

8.7.1 The case of PG 1553+113

Throughout this Chapter, we have assumed for PG 1553+113 a redshift of 0.40. This value is in good agreement with both optical limits and TeV observations (see previous Chapter). Moreover, we have used for the study the spectrum published in Prandini et al. (2009), which includes only part of the dataset presented in Chapter 5.

Here we check what happens to the relation found if we remove PG 1553+113 from the list of sources. In addition, we perform an estimate of the reconstructed redshift z_{rec} using the 2005/09 combined spectrum presented in Chapter 5, that is the most detailed determination of the VHE source spectrum.

Figure 8.12, from the follow–up study of Sec. 8.5, shows the $z^* - z_{true}$ plot of the sources with well known redshift plus PG 1553+113 (open marker). The linear fit obtained without this source is shown as a dashed line, and compared to the fit of all the data. The good agreement between the two fits is evident. Therefore we can conclude that the use of PG 1553+113 has not strongly influenced our study.

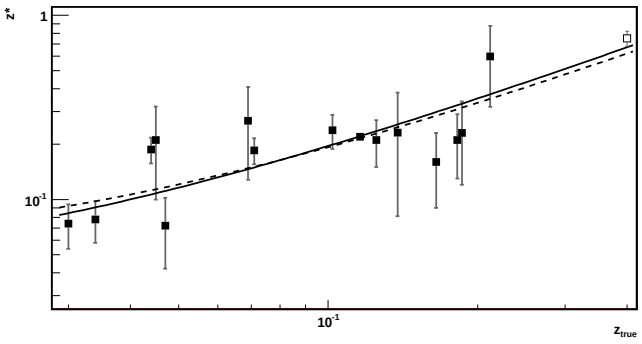

Figure 8.12: $z^* - z_{true}$ plot. The continuous line is the linear fit of all the data, while the dashed line is the fit obtained excluding PG 1553+113 (open marker).

Regarding the redshift, z^*, obtained for this source in the follow–up study, it is $z^* = 0.75 \pm 0.07$ with both EBL models. The reconstructed redshift is $z_{rec} = 0.45 \pm 0.05$ in both cases, well in agreement with the current upper and lower limits.

We perform now the same study using the new spectrum that we have estimated in Section 5.5.1, combination of the mean 2005/06 and 2007/09 spectra. This is characterized by very small error bars, especially in the energy points below 100 GeV. This feature is very important for understanding the results found. The redshift z^* that we obtain is 0.77 ± 0.07. It must be noticed, however, that this value is well above the limit, $z = 0.67$, reported in Sec. 7.3.1, representing the redshift above which a power law fit cannot be considered as a good fit with respect a curved power low. Therefore, in this situation, we cannot consider the results of our method reliable. A similar outcome is found if we use Dominguez model. A possible way to overcome the problem could be that of fitting the deabsorbed spectra only at energies above 100 GeV. In this case, we obtain for z^* a value of 0.70 ± 0.08 with the Franceschini model, and of 0.71 ± 0.08 with the Dominguez model, much closer to the limit of 0.67. The use of these z^* values yields to $z_{rec} = 0.44 \pm 0.05$ and $z_{rec} = 0.43 \pm 0.05$, respectively.

Figure 8.13 shows the deabsorbed spectrum (filled circles) of PG 1553+113 if we assume a redshift z of 0.43 ± 0.05. It is compatible with a power law of index

3.0 ± 0.2.

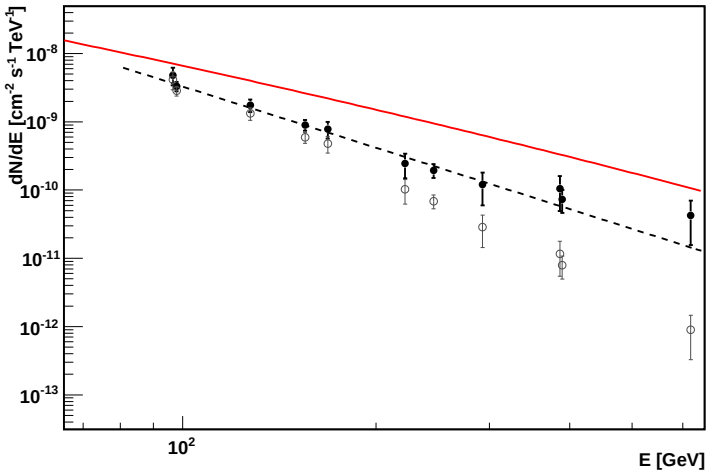

Figure 8.13: PG 1553+113 spectrum measured by MAGIC from 2005 to 2009 determined in Section 5.5.1(open circles) and deabsorbed with Dominguez EBL model (filled circles), assuming a redshift $z = 0.43$. A simple power low to the deabsorbed spectrum (dashed line) has a slope Γ of 3.0. The Crab Nebula spectrum is superimposed for comparison (continuous line).

The values obtained here are quite consistent with those derived from the former spectral determination. Therefore we can conclude that according to our study, and adopting the recent Dominguez EBL model, the redshift of PG 1553+113 is likely $z = 0.43 \pm 0.05$.

8.7.2 The redshift of PKS 1424+240

As a final application, we use our procedure on the blazar PKS 1424+240. For the z_{rec} determination, we use the VHE spectrum observed in 2009 by VERITAS (Acciari et al., 2010a). As shown at the end of previous Chapter, thanks to the longer exposure time this spectrum is more detailed with respect to the MAGIC spectra reported in Chapter 6, especially at high energies.

The slope of the *Fermi*/LAT spectrum, between 0.2 to 300 GeV, reported in the 5.5 months catalog is 1.85 ± 0.05, while the slope reported in the 1-year *Fermi* catalog between 0.1 to 100 GeV is $\Gamma = 1.83 \pm 0.03$. The values of the redshift, z^*, at which the deabsorbed TeV spectrum slope equals the lower energy one, for both *Fermi* slopes and different EBL models considered in the study, are listed in the fourth column of Table 8.9. It spans from 0.28 ± 0.08 to 0.5 ± 0.16. Excluding the one obtained with the Stecker model, the results are in agreement with the value of 0.5 ± 0.1, reported by Acciari et al. (2010a), and calculated applying the same procedure but only simultaneous *Fermi* data.

The deabsorbed spectrum obtained with the Franceschini EBL model, assuming the 5.5 months *Fermi* slope, is drawn in Figure 8.15.

In the fifth column of the Table, the upper limit determinations, at a $2\,\sigma$ confidence level, are reported. They spread from 0.82, obtained adopting a low energy density EBL model, to 0.44, using the high energy density EBL model. We can conclude that the redshift of PKS 1424+240 is, at high confidence level, lower than 0.82, and more likely below 0.75.

EBL Model	*Fermi* Catalog	Γ_{HE}	z^*	$z_{ul}(2\sigma)$	z_{rec}
Kneiske	5.5 months	1.85 ± 0.05	0.50 ± 0.16	0.82	0.24 ± 0.04
Franceschini	5.5 months	1.85 ± 0.05	0.45 ± 0.10	0.75	0.24 ± 0.04
Stecker	5.5 months	1.85 ± 0.05	0.28 ± 0.08	0.44	0.25 ± 0.04
Franceschini	1 year	1.83 ± 0.03	0.45 ± 0.15	0.75	0.26 ± 0.05
Dominguez	1 year	1.83 ± 0.03	0.45 ± 0.15	0.75	0.26 ± 0.05

Table 8.9: Comparison between the different determinations of the limit on the redshift, z^*, the upper limit and the reconstructed redshift, z_{rec}, of the source PKS 1424+240.

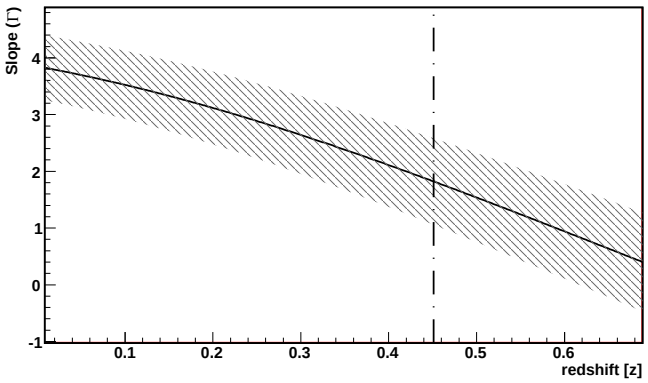

Figure 8.14: VHE γ–ray slope of PKS 1424+240 as a function of the redshift with a 1σ error bar, using the Franceschini EBL model. The vertical dashed-dotted line corresponds to $z^* = 0.45$.

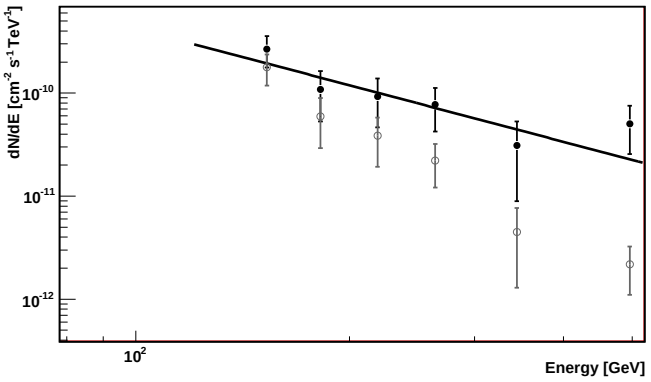

Figure 8.15: Measured differential energy spectrum of PKS 1424+240 (open circles) and deabsorbed with a mean density EBL model (filled circles) for a redshift z = 0.45 (corresponding to z^*).

We finally use the previous limits to estimate the most probable distance of PKS 1424+240. The z_{rec} values are listed in the last column of Table 8.9, where the error, as usual, is assumed as the σ of the Gaussian fitting the Δz distributions. The value of the reconstructed redshift obtained adopting the HE slope reported in the latest *Fermi* catalog is $z_{rec} = 0.26 \pm 0.05$ for both EBL models, that is our best estimate on the distance of this blazar.

The good agreement between the z_{rec} values obtained with different methods is quite impressive, taking into account the large difference existing between the EBL models, and suggests that the redshift estimation performed with this technique is almost background model independent.

Black hole sun won't you come?
And wash away the rain...
Black hole sun won't you come?
Won't you come?

Black Hole Sun – Soundgarden

9 Conclusions and Outlook

This thesis was focused on the characterization of the distances of blazars starting from the properties of the detected TeV emission. The research activity presented, carried out in the field of extragalactic VHE γ–ray astrophysics, is composed of an *experimental* and a *phenomenological* part, the former carried out as a member of the MAGIC Collaboration.

The first part of the work was dedicated to the purely experimental results: we have presented the detailed analysis of the VHE γ–ray radiation emitted by the two blazars with uncertain redshift observed with MAGIC: PG 1553+113 and PKS 1424+240. For each source we have measured the differential energy spectrum and studied the temporal evolution of the integral flux detected. In the former case, we have combined the new sample presented, composed of the data collected from 2007 to 2009, with previous observations (2005/06). This large sample made PG 1553+113 one of the longest studied sources at energies above 100 GeV.

Concerning PKS 1424+240, we have presented the analysis of 2009 and 2010 datasets. The main feature of the 2010 sample is that it was collected in stereoscopic mode, using the upgraded MAGIC stereoscopic system.

Both sources revealed a modest variability in the VHE γ–rays, and a steep spectrum of power law index ~ 4. The results obtained have been, in both cases, combined with partially simultaneous observations carried out in other frequencies, from optical to γ–rays. Correlation studies between the integral fluxes at optical and TeV energies suggested a correlation between these two extreme components for the case of PG 1553+113. Conversely, the small significance of the signal detected from PKS 1424+240 prevented any definitive conclusion about an eventual correlation of TeV photons with optical, X–ray and γ–ray data. In general, the sparse sampling of the observations and the lack of truly simultaneous monitoring affected both observations, and prevented more detailed studies. Therefore, coordinated multi–frequency observations are strongly suggested to further investigate this important subject.

Finally, we have combined the mean spectra measured at VHE with archival data available for other wavelengths. In both cases, a clear two bump structure arose, in agreement with current models of blazar emission. In case of PG 1553+113,

we modeled the mean SED with a one–zone SSC model, and derived the main physical parameters governing the emission in the blazar jet. More precise studies would require coupling the VHE γ–ray part of the spectrum with simultaneous measurements of the synchrotron peak, in particular at optical/X–ray energies.

In the second part of the thesis we have reported the results of the phenomenological work, aimed to set constraints on TeV blazars distances. This work is of particular interest for current VHE γ–rays astrophysics, since many new TeV sources have unknown/uncertain redshifts.

First we have described the existing techniques, which make use of reasonable hypotheses on the VHE γ–rays intrinsic spectra emitted by blazars to set an upper limit on their distances. These methods were applied to PG 1553+113 and PKS 1424+240 spectra. In the first case, the requirement that the deabsorbed spectrum did not show a pile up at VHE led to the most stringent limit on the source distance of $z < 0.67$ at a two sigma level. In the second case, on the contrary, it was the demand of a spectral index softer than 1.5 (also called maximum hardness criterion) to better constrain the source redshift at $z < 0.81$.

Starting from these procedures, we developed a new method based on combined GeV and TeV observations. This technique can be seen as a sort of experimental version of the maximum hardness criterion, in which instead of assuming a limiting slope given by theory for the deabsorbed spectrum, we used the slope measured by *Fermi*/LAT at lower energies. Since almost all of these slopes are above the limiting value 1.5, the upper limits obtained with this method are below the previous limits. Therefore, in principle, this technique is more constraining. In order to check its validity, we tested it on a large sample of TeV blazars detected also at lower energies using different EBL models. The results obtained are satisfactory, and we could conclude that, for a TeV blazar, the redshift, z^*, at which the deabsorbed slope equals the slope measured at HE can be considered as an upper limit on the source distance, at least with mean and low energy density EBL models.

Adopting the recent Dominguez EBL model we obtained for the blazars PG 1553+113 and PKS 1424+240 the redshift values of $z^* = 0.75 \pm 0.07$ and $z^* = 0.45 \pm 0.15$, respectively, corresponding to the $2\,\sigma$ upper limits of $z < 0.89$ and of $z < 0.75$.

As a spin–off, we applied the same procedure to the two uncertain redshifts sources S5 0716+714 and 3C 66A, recently observed at VHE γ–rays. We got the values $z^* = 0.22 \pm 0.10$ and $z^* = 0.38 \pm 0.05$, respectively, in partial contradiction with the (uncertain) redshifts resulting from optical measurements. The results suggest that or the intrinsic properties of these sources are peculiar (specifically, they present a more moderate intrinsic spectral break between the GeV and TeV bands than that of the other sources), or the estimated (uncertain) distances are wrong. Therefore, further observations of S5 0716+714 and 3C 66A, both at optical frequencies and at combined GeV and TeV energies are recommended in order to discriminate between these alternatives.

Following previous works, we finally checked the possibility of a linear relation between the z^* estimates and the real distances of the sources. A linear fit was found to describe quite well the results, independently of the EBL model considered. The relation obtained suggested the use of the z^* estimate not only to limit the blazars redshifts, but also, via the inverse formula, to evaluate its distance. The distribution of the differences Δz between the reconstructed and the real redshifts of known distance sources, obtained using the most recent data, was

well fitted by a Gaussian peaked in zero with a σ of 0.05. This demonstrated that the method is statistically consistent. Therefore, we applied it to our sources in order to perform a first estimate of their distances.
The method applied to PG 1553+113 returned the value of 0.43 $\pm$ 0.05 for the reconstructed redshift, in agreement with both upper and lower limits found with other methods. For PKS 1424+240 the evaluated distance was 0.26 $\pm$ 0.05. In both cases, the use of a different EBL models did not influenced significantly the result. We found, instead, that the use of low energy points below 100 GeV can lead to inconsistent results. This was the case of PG 1553+113: we had to exclude these points from the fits in order to estimate the final result.

Regarding the uncertain redshift sources, the value of the redshift of S5 0716+714 that we obtained with this method was 0.12 $\pm$ 0.05, while for 3C 66A the same procedure led to a redshift estimate of 0.22 $\pm$ 0.05.

As a natural outlook of this work, given the large number of unknown redshifts blazars recently detected at VHE γ–rays, we foresee to apply our technique on these sources and infer their redshifts, as soon as their VHE spectra will be published.

APPENDIXES

Experience is simply the name we give our mistakes
Oscar Wilde

A Camera inhomogeneities in MAGIC I

CAMERA INHOMOGENEITIES are the consequence of hardware inefficiencies affecting the MAGIC camera and/or readout electronics. In this appendix, we show the dependence of such inhomogeneities on the `size` parameter. This study is of particular importance for the selection of reliable data, in particular in wobble data analysis.

A.1 Camera inhomogeneities

Among the different effects influencing the data quality, an important role is played by the homogeneity of the camera of the telescopes. Eventual inhomogeneities, in fact, cause a distortion in the final image registered by the DAQ, and result in a disagreement between real and simulated data. The discrepancy propagates in a non–linear way through the analysis, and can be a strong source of systematic errors affecting the physical results.

In order to avoid such systematics, we investigate the effect of inhomogeneities and propose a way, based on a cut in the parameter `size`, to remove them.

To study the homogeneity of the camera, a simple tool that can be used is

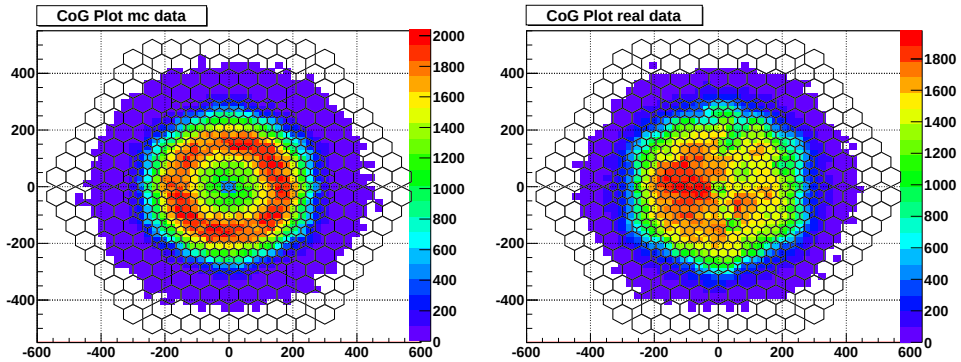

(a) CoG of MC γ events.

(b) CoG of real events.

Figure A.1: Comparison of CoG of real and simulated data.

the center of gravity (CoG) plot. The CoG is a bi-dimensional plot showing the centroid of each ellipse representing a shower image, as described in Sec. 4.4. If during the data taking the camera is homogeneous, we expect a symmetrical CoG distribution, with a characteristic shape related to the trigger efficiency. For example we compare in Figure A.1 the CoG plot for simulated γ events (whose distribution is clearly symmetrical, as expected) and real events collected with MAGIC I in 2009. The asymmetry in the real events case is evident.

The main causes for the deviation of the real data from the ideal case that we have identified, are:

- dead pixels;
- noisy pixels;
- stars in the FoV;
- DT and HV not set correctly;
- malfunctioning of the reflective surface (such as not correctly focused or degraded mirrors)
- trigger inefficiency.

Obviously, a correct treatment of camera inhomogeneities consists in investigating all these causes and, when possible, adjust the corresponding hardware component. This task is one of the priority of the hardware MAGIC group, which in the last year improved quite a lot the camera homogeneity. For example, we plot in Figure A.2 the comparison between the CoG of the data collected in January 2009 with those taken in July 2010. The improved homogeneity is evident. Hoverer, we are still far from a complete removal of all causes of inhomogeneities.

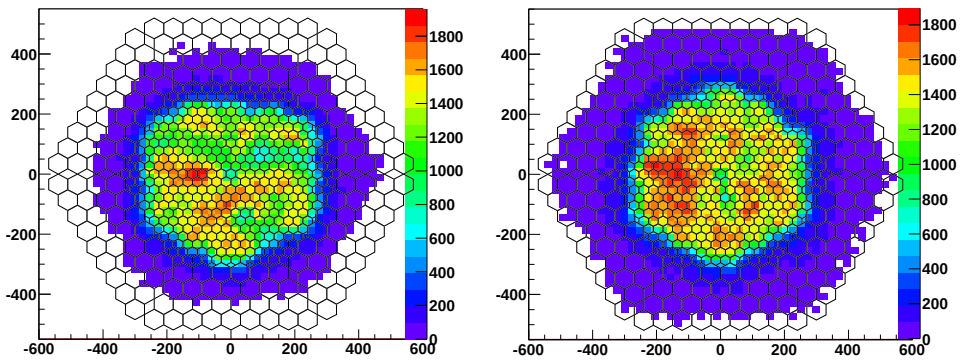

Figure A.2: Comparison of CoG distribution in January 2009 (left plot) and July 2010 (right plot).

A.2 Tools: CoG and ϕ–plot

In order to quantify the inhomogeneities, we propose the study the CoG distribution and its azimuthal projection, the so–called ϕ–plot, in differential `size` bins.

To do so, an useful approach is that of dividing the camera into six sectors, and then applying a cut in the parameter `dist`, in order to get rid of the fluctuations of the ϕ parameter, due to non azimuthal-symmetric trigger, depicted in Fig. A.3, which causes a sinusoidal–like behaviour in the CoG projection.

Figure A.4(a) shows the CoG plot divided into its six sectors (the so–called *hardware sectors* of the MAGIC I camera). The corresponding azimuthal projection is shown in the upper plot of Fig. A.4(b), where the dashed line represents the mean value, ϕ_{mean}, and the shaded area is the $\pm$ 10% range.

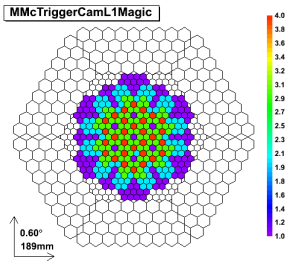

Figure A.3: MAGIC I trigger map.

The CoG projection is far from being constant, and shows fluctuations of the order of 20% of the mean value. As mentioned above, in part this behaviour is due to the trigger design. A possible way to exclude this component consists into applying a `dist` cut at the the ϕ-plot, and exclude all those events whose centroid lies in the outer regions of the camera, at `dist` larger than 200 mm. This is the distance, in camera coordinates, above which the trigger design causes the fluctuations visible in the ϕ–plot.

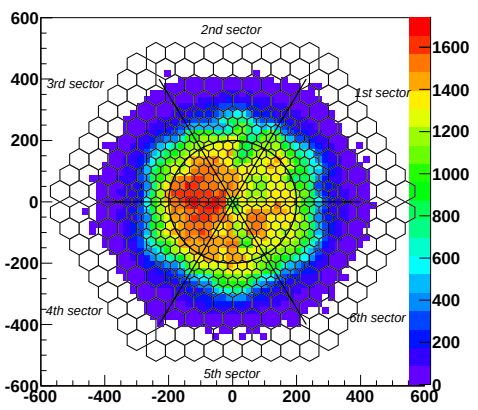

(a) Geometry of the camera sectors. The circle divides the events with `dist` greater and smaller than 200.

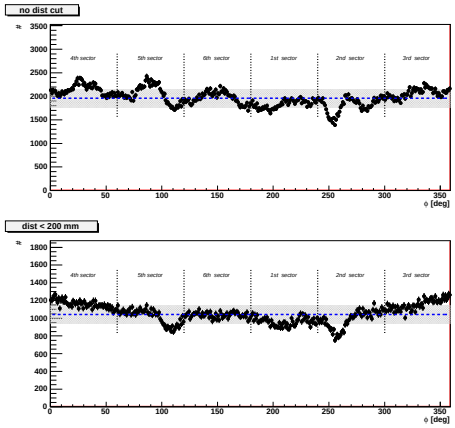

(b) ϕ–plot without and with `dist` cut.

Figure A.4: Graphical sketches illustrating the camera sectors and the effect of a cut in the `dist` parameter (circle in camera coordinates).

The lower panel of Figure A.4(b) shows the ϕ–plot with the `dist` cut applied. The number of events is almost halved with respect to the complete sample plot (upper panel), since many showers have their centroids at `dist` values above 200 mm. There are still significant deviations from the mean value. Conversely to the other plot, however, the deviations can be attributed as due to camera inefficiencies/dishomogeneities.

From the direct comparison between this ϕ–plot and its bi–dimensional representation, its is evident that for the case considered here:

- the left part of the camera has more events than the right part. The reason for this behaviour, however, is not obvious: it could be due to a better

efficiency of this part of the camera or to a zone of noisy pixels. In the ϕ–plot this corresponds to a large number of events with centroids located in the third and fourth sector.

- There are two zones, in the 2^{nd} and 5^{th} sectors, where there is an evident hole in the CoG distribution, corresponding to a dip in the ϕ–plot, around 250° and 100°, respectively.

In conclusion, the combination of the CoG plot and its projection is a useful diagnostic tool which allows to recognize and quantify the deviations from a homogeneous camera behaviour.

A.3 Dependence with the `size` parameter

It is intuitive to think that the camera inhomogeneities affects mainly small events: if an event involves few pixels, in fact, it is more sensitive to eventual inefficiencies of that region of the camera. Thus, in order to quantify camera dishomogeneities and their effect on the analysis, we will take into account the extension of the events.

A good estimator of the event extension is the parameter `size`, defined in Chapter 4. In order to study the relation between the dishomogeneities and such parameter, we divide the sample in four `size` bins, defined as:

30-50 phel: the very low `size` region;

50-100 phel: the low `size` region;

100-200 phel: the mean `size` region;

$>$ **200 phel:** the high `size` region.

To perform this study, we use a sample of 2 hours of Crab Nebula data collected with MAGIC I in September 2009, and compare the CoG distributions and ϕ–plots in the four `size` bins.

Figure A.5 reports the results of the study in different `size` bins. There is a noticeable dependence of the dishomogeneity to the `size` interval considered. At very low `size` values, the CoG distribution presents evident holes: there are regions, even close to the camera center, with almost no events. This is in particular true for the fifth sector, where the ϕ distribution reaches values close to 1/3 of the mean value, and in the transition region between the second and third sector.

At low size values, inhomogeneities are still very large, even if the holes in the ϕ distribution are less deep. In correspondence to `size` values comprise between 100 and 200 phel, the ϕ distribution becomes quite flat, with only few regions with ϕ values outside the 10% interval. Finally, in the high `size` values region, the camera can be considered homogeneous.

We can therefore conclude that there is a close correlation between the flatness of the CoG distribution and the `size` parameter. In a sense, high energy events[1] are less affected by camera inhomogeneities. Therefore, the distribution of the collected events in the camera can be made homogeneous "a posteriori", by

[1] The parameter `size` is highly correlated to the event energy.

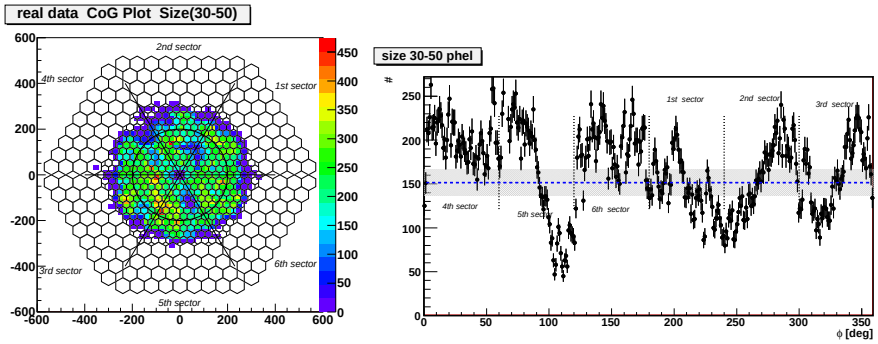

(a) CoG and ϕ–plot for the `size` bin 30-50 phel.

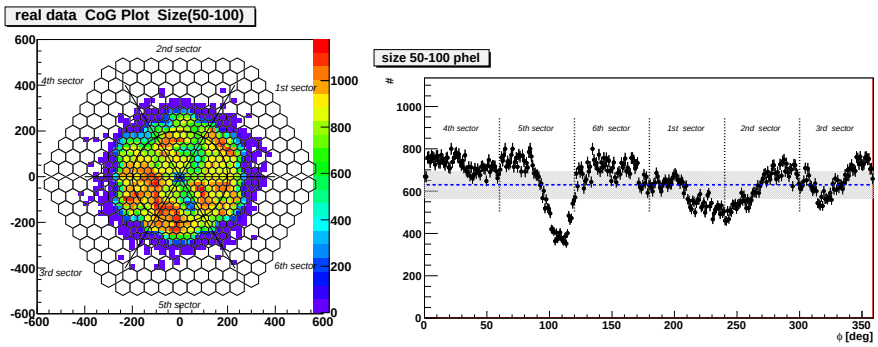

(b) CoG and ϕ–plot for the `size` bin 50-100 phel.

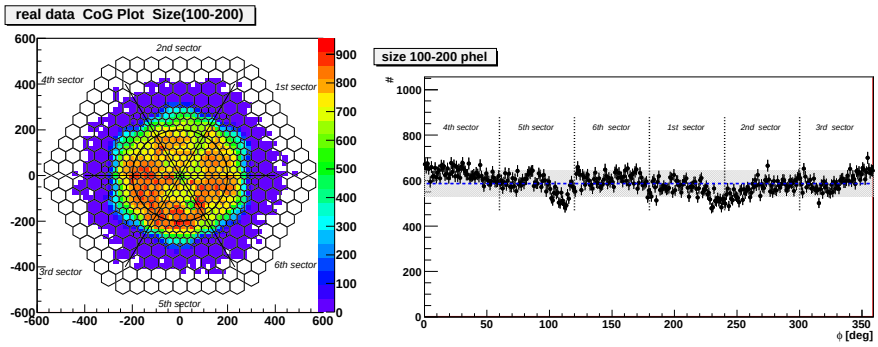

(c) CoG and ϕ–plot for the `size` bin 100-200 phel.

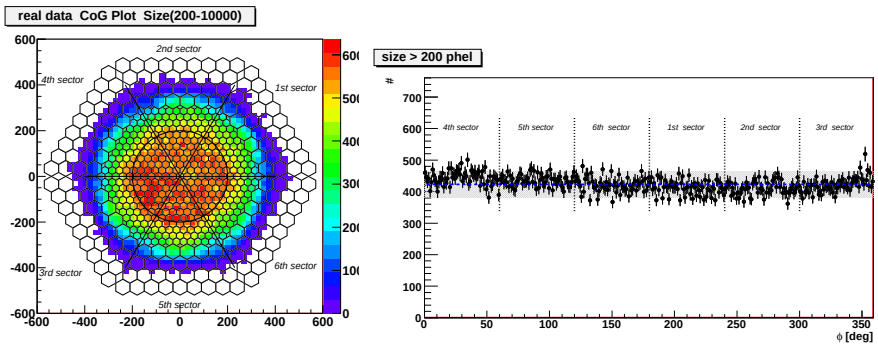

(d) CoG and ϕ–plot for `size` above 200 phel.

Figure A.5: CoG and ϕ plots for different size bins

applying a cut in `size`. In order to be in the *safe* zone, according to our study we must cut the events with `size` smaller than 200 phel.

Since 2006, MAGIC data taking has been performed in two different modes: *On–Off* mode and the *wobble* mode, as described in Sec 4.8. The effect of camera inhomogeneities on data, especially if taken in wobble mode, is that *fake signals* may arise if we don't take into account such inefficiencies. In particular, according to the results reported above, the use of the two additional Off regions should be limited to the analysis with a `size` cut above 200 phel. Moreover, if we use low `size` events, we must be careful that the temporal coverage of the source region in one wobble position equals the coverage in the other wobble position.

In case of observations carried out in On/Off mode, the problem is less dramatic, since On and Off data should be affected by the same inhomogeneities, if collected in the same period.

Vanno
vengono
per una vera
mille sono finte
e si mettono li tra noi e il cielo
per lasciarci soltanto una voglia di pioggia

Nuvole – Fabrizio De André

B

MAGIC data analysis: additional material

In this appendix, additional material to Chapters 5 and 6 is presented. In particular, the rate after cleaning distributions for all the recorded data of the sources PG 1553+113 and PKS 1424+240 before any quality selection are shown, along with a list of the daily significances obtained from the analysis of the good quality subsamples of data.

B.1 PG 1553+113

PG 1553+113 rate distributions

2007 sample PG 1553+113 was observed in 2007 in 8 different nights, Table B.1, from the end of March to late April. The rate distribution after the image cleaning, drawn in Figure B.1, shows that apart for one day, that will be excluded from further analysis, the mean rate is pretty stable.

2008 sample Table B.2 lists the PG 1553+113 dataset collected by MAGIC in 2008. The rate distribution after the image cleaning is drawn in Figure B.2, together with the `cloudiness`[1] distribution. The correlation between the two parameters is evident: in corresponding to high `cloudiness` values, the rate after cleaning drops. Since a large fraction of the sample is affected by bad weather, the final sample is greatly reduced, as described in Section 5.3.

2009 sample Finally, in Table B.3 the dataset collected in 2009 is drawn. In this case, the main cause of low rate is associated with the light conditions. Figure B.3 shows the rate distribution and the DC current of each night.

[1]The parameter *cloudiness* is a measure of the sky transparency, and is related to the sky temperature. Its value spans from 0 (clear sky) to 100 (completely opaque sky).

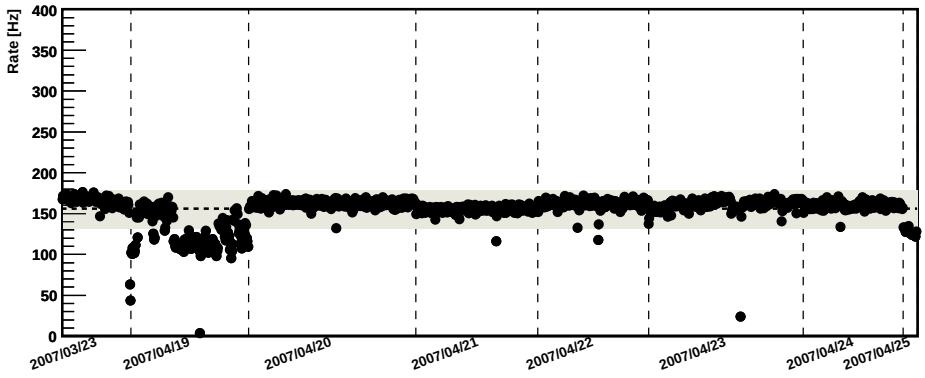

Figure B.1: Distribution of the event rate after image cleaning of 2007 data sample of PG 1553+113.

Cycle	Date	Rate
	23/03/2007	Decreasing $\sim$ 170 - 150 Hz
	19/04/2007	Fluctuating $\sim$ 120 - 150 Hz
	20/04/2007	Stable $\sim$ 165 Hz
III	21/04/2007	Stable $\sim$ 160 Hz
	22/04/2007	Stable $\sim$ 165 Hz
	23/04/2007	Stable $\sim$ 160 Hz
	24/04/2007	Stable $\sim$ 160 Hz
	25/04/2007	Stable $\sim$ 130 Hz

Table B.1: PG 1553+113 data collected by MAGIC in 2007.

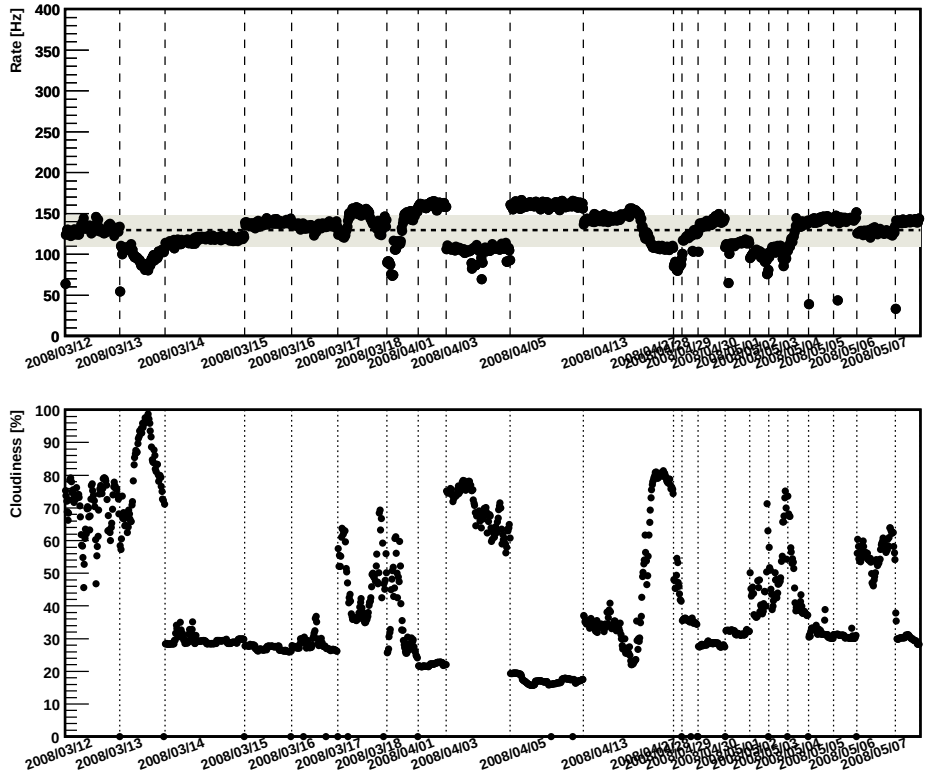

Figure B.2: Rate after cleaning and `cloudiness` distributions of 2008 data sample of PG 1553+113.

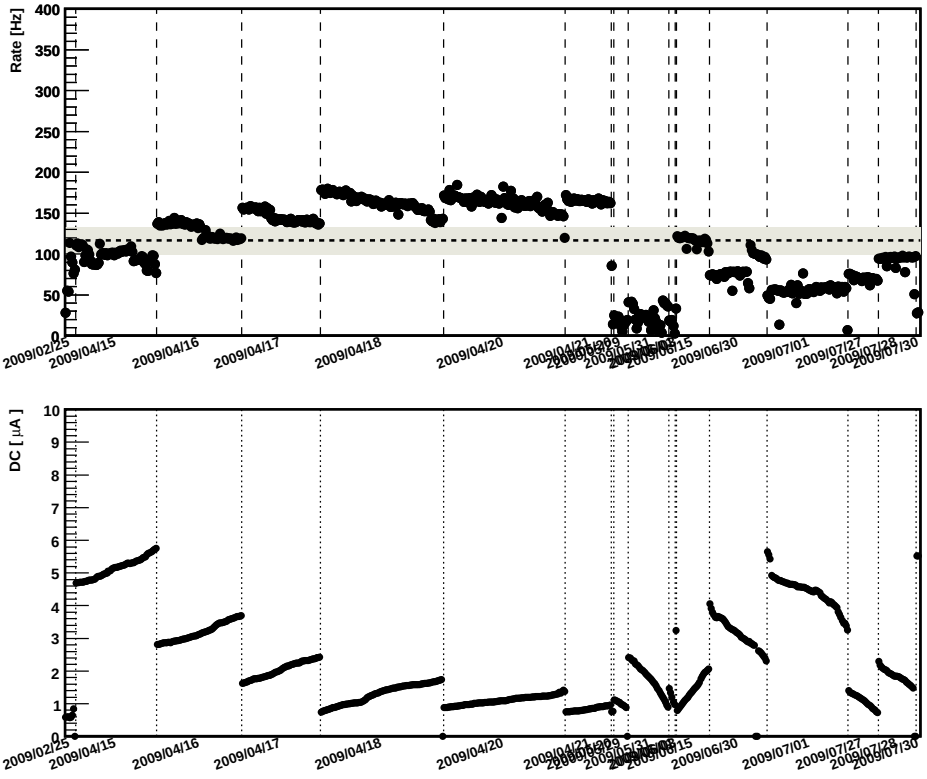

Figure B.3: Rate after cleaning and DC current distributions of 2009 data sample of PG 1553+113.

Cycle	Date	Rate
	12/03/2008	Affected by very high cloudiness
	13/03/2008	Affected by very high cloudiness
	14/03/2008	Stable $\sim$ 120 Hz
	15/03/2008	Stable $\sim$ 140 Hz
	16/03/2008	Stable $\sim$ 140 Hz
	17/03/2008	Fluctuates due to variable cloudiness (max value 150 Hz)
	18/03/2008	Fluctuates due to variable cloudiness (max value 150 Hz)
	01/04/2008	Stable $\sim$ 160 Hz
	03/04/2008	Affected by very high cloudiness
	05/04/2008	Stable $\sim$ 170 Hz
IV	13/04/2008	Fluctuates due to variable cloudiness (from 150 to 120 Hz)
	27/04/2008	Affected by very high cloudiness
	28/04/2008	Stable $\sim$ 140 Hz
	29/04/2008	Stable $\sim$ 150 Hz
	30/04/2008	Stable $\sim$ 130 Hz
	01/05/2008	Stable $\sim$ 110 Hz
	02/05/2008	Fluctuates due to variable cloudiness (around 120 Hz)
	03/05/2008	Fluctuates due to variable cloudiness (from 150 to 120 Hz)
	04/05/2008	Stable $\sim$ 150 Hz
	05/05/2008	Stable $\sim$ 150 Hz
	06/05/2008	Stable $\sim$ 140 Hz
	07/05/2008	Stable $\sim$ 150 Hz

Table B.2: PG 1553+113 data collected by MAGIC in 2008.

Cycle	Date	Rate
	02/25/2009	Very low and fluctuating (below 100 Hz)
	15/04/2009	$\sim$ 100 Hz: affected by high DC (above 4.5)
	16/04/2009	Stable $\sim$ 130 Hz
	17/04/2009	Stable $\sim$ 150 Hz
V	18/04/2009	Decreasing $\sim$ 180 - 150 Hz
	20/04/2009	Stable $\sim$ 170 Hz
	21/04/2009	Stable $\sim$ 170 Hz
	20/05/2009	Very low and fluctuations (below 100 Hz)
	29/05/2009	Very low and fluctuation (below 100 Hz)
	31/05/2009	Very low and fluctuation (below 100 Hz)
	01/06/2009	Very low and fluctuation (below 100 Hz)
	03/06/2009	Very low and fluctuation (below 100 Hz)
	15/06/2009	Stable $\sim$ 120 Hz
	30/06/2009	$\sim$ 50 Hz: affected by high DC (above 2.5 μA)
	01/07/2009	$\sim$ 50 Hz: affected by high DC (above 3.5 μA)
	27/07/2009	Stable $\sim$ 70 Hz
	28/07/2009	Stable $\sim$ 100 Hz
	30/07/2009	$\sim$ 30 Hz: affected by high DC (above 5)

Table B.3: PG 1553+113 data collected by MAGIC in 2009.

Daily lightcurve

The results of the good quality PG 1553+113 data daily signal analysis above 150 GeV are listed in Table B.4, where the year and day of observation (first and second column), exposure time (third column) and significance of the signal are reported. Except from 2008 sample, in which the significance of the signal exceeds $3\,\sigma$ in four days, in the other two years it is at the level of background fluctuations. These results explains the final binning chosen for the lightcurve study.

Year	Day [dd/mm]	Time [s]	Signif. σ
	23/03	58 min	1.9
	19/04	32 min	0.9
	20/04	150 min	2.2
2007	21/04	115 min	1.3
	22/04	101 min	1.8
	23/04	143 min	1.8
	24/04	92 min	1.6
	17/03	58 min	4.2
	18/03	26 min	1.8
	01/04	43 min	0.8
	05/04	109 min	4.1
2008	13/04	97 min	3.1
	29/04	44 min	1.3
	03/05	24 min	2.2
	04/05	40 min	3.7
	05/05	38 min	1.8
	07/05	40 min	1.7
	16/04	Excluded	(strong moon)
	17/04	103 min	3.5
2009	18/04	126 min	0.9
	20/04	73 min	3.1
	21/04	57 min	< 0
	15/06	57 min	0.4

Table B.4: Daily significance of PG 1553+113 signal.

B.2 PKS 1424+240

Rate distribution

Here, we present the rate after cleaning distribution of all the PKS 1424+240 data collected by MAGIC.

Table B.5 summarizes the sample collected in 2009, while in Figure B.4 the rate and `cloudiness` distributions are shown. For the `cloudiness` study the data collected on 20/05 had to be excluded from the sample since, due to technical reasons, the `cloudiness` parameter was not recorded.

Regarding 2009 sample, it can be noticed that part of the data characterized by a low rate of the events after the image cleaning were collected during high `cloudiness`. Therefore, in these cases this atmospheric condition clearly influenced the quality of the sample, as for 2008 PG 1553+113 case. In the other cases we observe a low event rate even if in presence of low `cloudiness`; probably other factors, such as the air humidity, its transparency (related for example to the presence of calima), or possible hardware inefficiencies have influenced the data quality.

Concerning 2010 dataset, the entire sample has been considered of good quality and used for the analysis.

Cycle	Date	Rate	Cycle	Date	Rate
	17/04/2009	~ 174 Hz		14/03/2010	~ 95 Hz
	18/04/2009	~ 177 Hz		18/03/2010	~ 78 Hz
	19/04/2009	~ 173 Hz		20/03/2010	~ 79 Hz
	21/04/2009	~ 172 Hz		21/03/2010	~ 82 Hz
	22/04/2009	~ 177 Hz		22/03/2010	~ 88 Hz
	23/04/2009	~ 176 Hz		23/03/2010	~ 72 Hz
V	24/04/2009	~ 174 Hz	VI	24/03/2010	~ 83 Hz
	26/04/2009	very low		25/03/2010	~ 84
	20/05/2009	~ 160 Hz		06/04/2010	~ 91
	21/05/2009	low (~ 130 Hz)		07/04/2010	~ 76
	22/05/2009	very low		18/04/2010	~ 113
	23/05/2009	very low			
	25/05/2009	fluctuating			
	26/05/2009	low (~ 135 Hz)			
	12/06/2009	~ 152 Hz			
	13/06/2009	low (~ 120 Hz)			
	15/06/2009	~ 152 Hz			
	20/06/2009	~ 143 Hz			
	21/06/2009	~ 163 Hz			
	22/06/2009	~ 155 Hz			
	23/06/2009	~ 150 Hz			

Table B.5: PKS 1424+240 overall data collected by MAGIC in 2009.

Daily lightcurve

In Table B.6 the results of the signal search on daily basis are listed. Except for few days, whose significance is above $1\,\sigma$, the daily significances are really

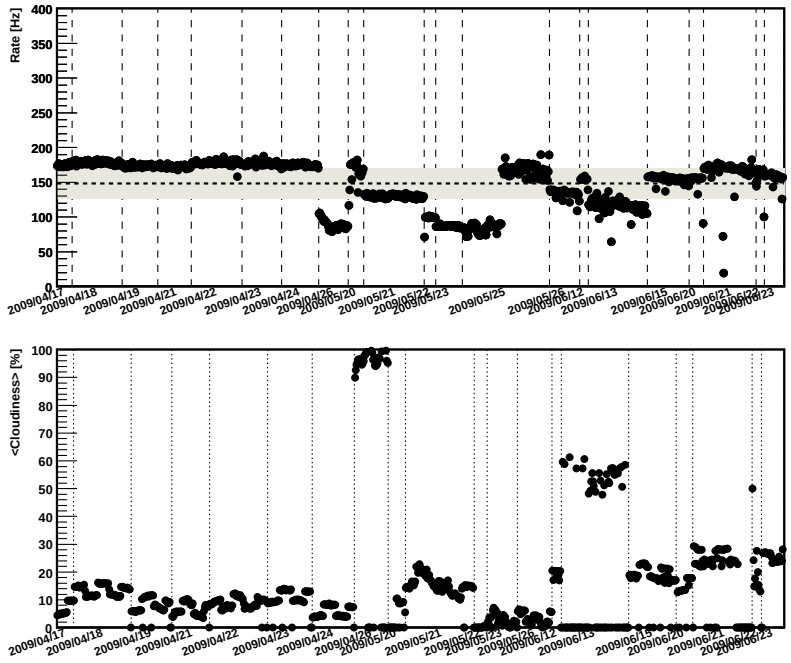

Figure B.4: Distribution of the event rate after image cleaning of 2009 data sample of PKS 1424+240 (upper plot) and distribution of the `cloudiness` parameter of the data (except for 25/05, see text for details).

low. This finding justifies the choice of adopting a larger temporal binning for the study of the temporal evolution of the signal, performed in Sec. 6.4.

Cycle	Date	Time [min]	Signif. [σ]	Cycle	Date	Time	Signif.
	17/04	18	1.9		14/03	63	<1
	18/04	38	<1		18/03	69	<1
	19/04	42	<1		20/03	104	<1
	21/04	42	<1		21/03	45	<1
2009	22/04	64	1.4	2010	22/03	89	<1
	23/04	42	3.2		23/03	53	1.1
	24/04	44	1.7		24/03	175	1.4
	12/06	17	<1		25/03	111	1.0
	15/06	85	<1		06/04	19	1.1
	20/06	31	<1		07/04	57	<1
	21/06	16	1.3		18/04	71	2
	22/06	16	<1				
	23/06	20	<1				

Table B.6: Daily significance of PKS 1424+240 signal in 2009 and 2010 samples.

Vedi mai una stella cadere
E non ricordi cosa desiderare?

Varanasi Baby – Afterhours

C

Constraints on blazars distances: additional material

In this Appendix, the Γ–z plots, relating the VHE γ–rays slope fitting the spectrum to the redshift, z, of the sources used in Chapter 8 are reported. First we present the results of the preliminary work, and then those of the follow–up study.

C.1 Preliminary study

In this Section, we present the plots of each source considered in the preliminary part of Chapter 8, and corresponding to the TeV slope as a function of the redshift with a $1\,\sigma$ error bar, using the Franceschini EBL model.

The vertical dotted line, when present, corresponds to the true redshift value of the source, while the dashed–dotted line is the redshift z^*. For simplicity, the sources considered, together with their redshift, z, and z^* resulting from the study, are listed in Table C.1.

Source Name	z	z^*
Mkn 421	0.030	0.08 ± 0.02
Mkn 501	0.034	0.10 ± 0.02
1ES 2344+514	0.044	0.20 ± 0.06
Mkn 180	0.045	0.20 ± 0.13
1ES 1959+650	0.047	0.09 ± 0.04
BL Lacertae	0.069	0.26 ± 0.13
PKS 2005−489	0.071	0.18 ± 0.03
W Comae	0.102	0.24 ± 0.05
PKS 2155−304	0.116	0.22 ± 0.01
1ES 0806+524	0.138	0.24 ± 0.16
1ES 1218+304	0.182	0.22 ± 0.09
1ES 1011+496	0.212	0.62 ± 0.18
S5 0716+714	0.310^a	0.22 ± 0.10
PG 1553+113	0.400	0.74 ± 0.08
3C 66A	0.444^a	0.38 ± 0.06
3C 279	0.536	-

Table C.1: Redshift values obtained by deabsorbing the VHE spectra until the slope is the one observed by LAT after 5.5 months of data taking, using Franceschini EBL model. ^{a}: uncertain. From Table 8.2.

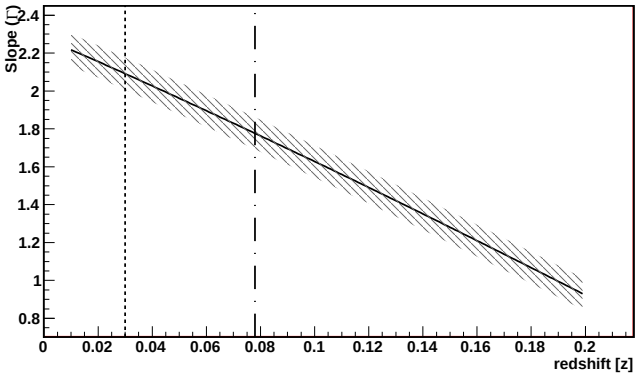

Figure C.1: Source Mkn 421 (real redshift 0.030).

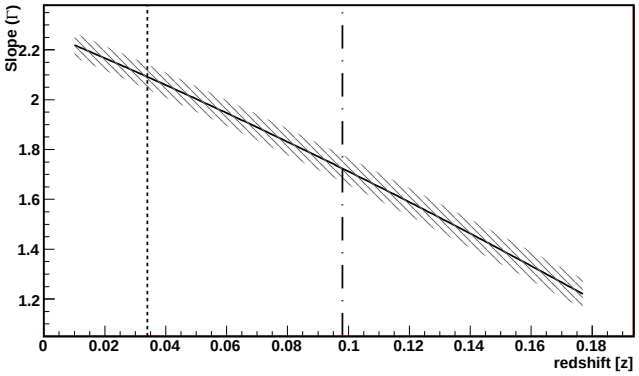

Figure C.2: Source Mkn 501 (real redshift 0.034).

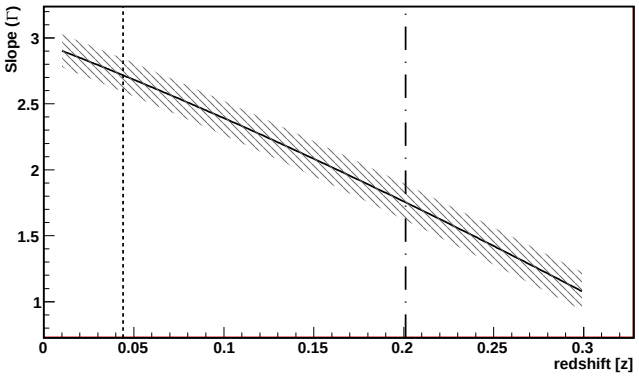

Figure C.3: Source 1ES 2344+514 (real redshift 0.044).

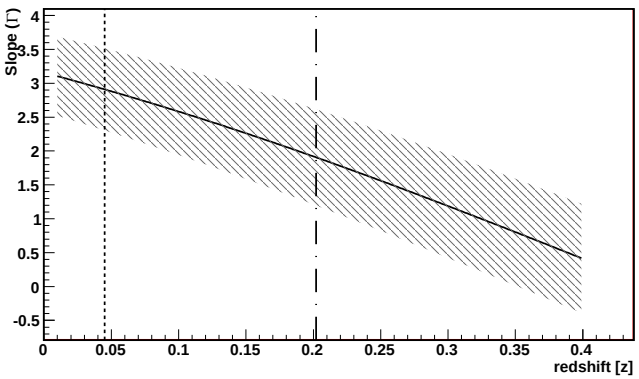

Figure C.4: Source Mkn 180 (real redshift 0.045).

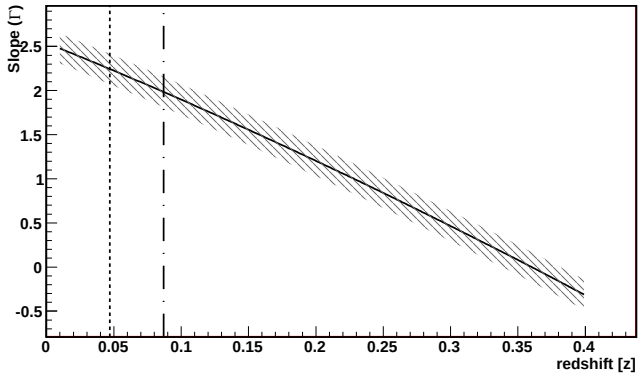

Figure C.5: Source 1ES 1949+650 (real redshift 0.047).

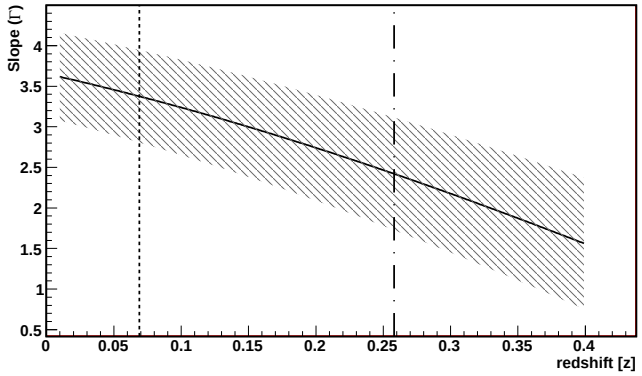

Figure C.6: Source BL Lacertae (real redshift 0.069).

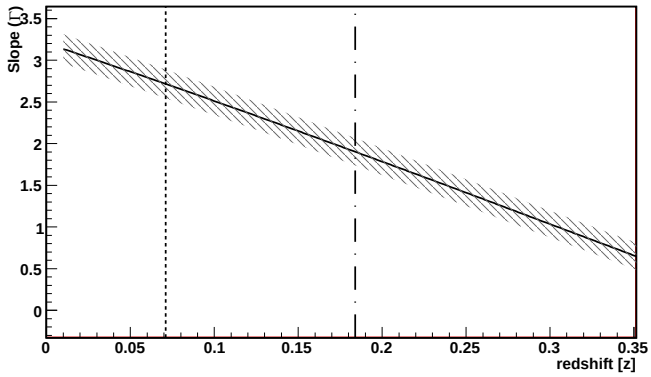

Figure C.7: Source PKS 2005−489 (real redshift 0.071).

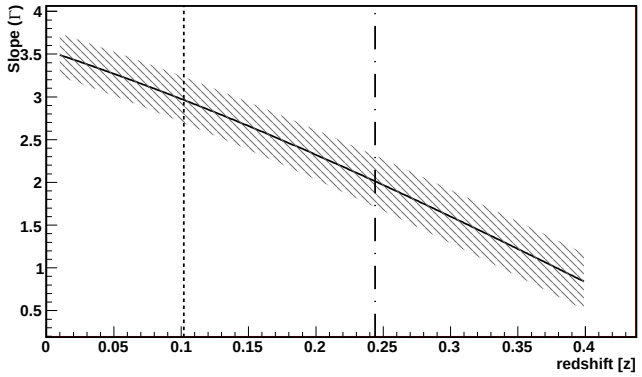

Figure C.8: Source W Comae (real redshift 0.102).

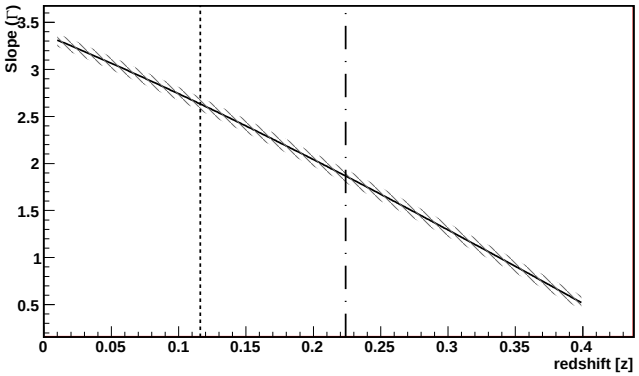

Figure C.9: Source PKS 2155−304 (real redshift 0.116).

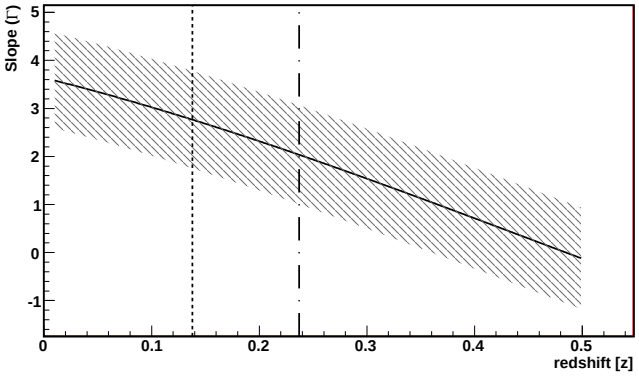

Figure C.10: Source 1ES 0806+524 (real redshift 0.138).

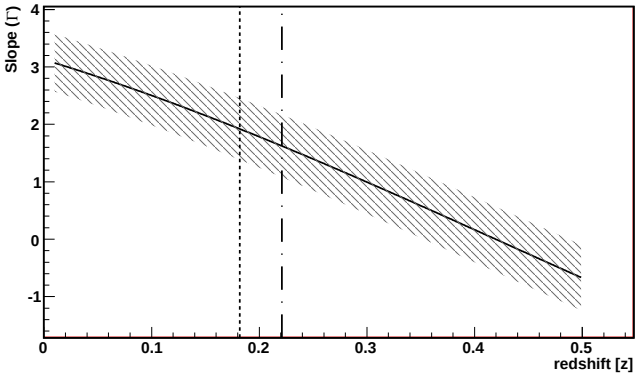

Figure C.11: Source 1ES 1218+304 (real redshift 0.182).

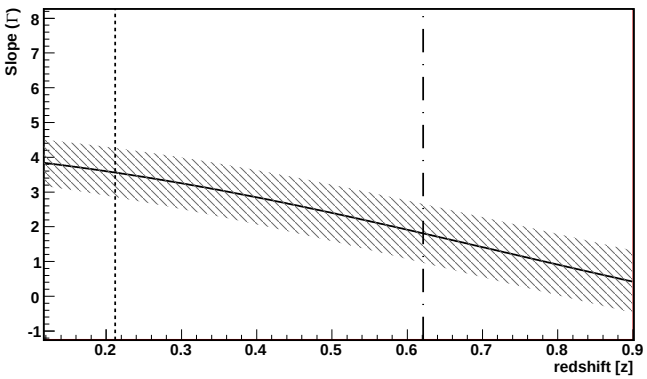

Figure C.12: Source 1ES 1011+496 (real redshift 0.212).

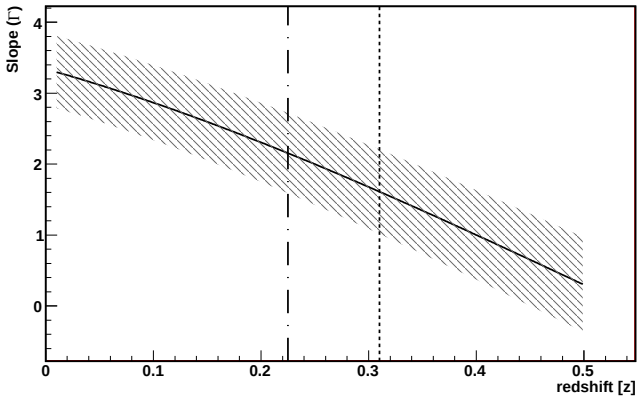

Figure C.13: Source S5 0716+714 (uncertain redshift, 0.310).

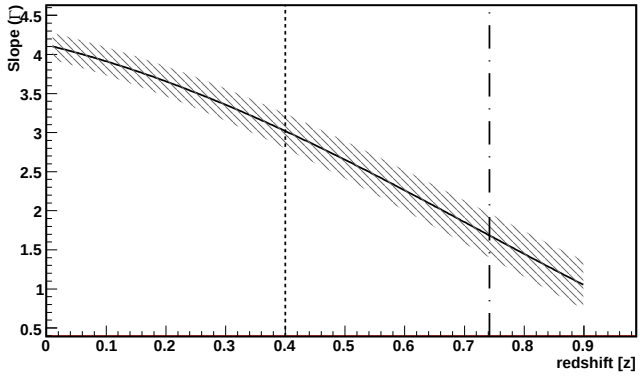

Figure C.14: Source PG 1553+113 (redshift assumed for this study 0.40, see discussion in Section 8.7.1).

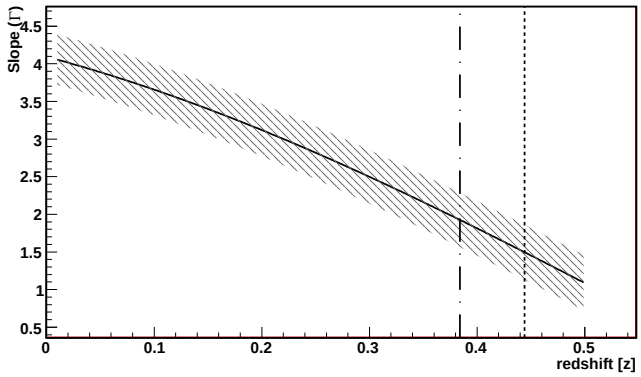

Figure C.15: Source 3C 66A (uncertain redshift, 0.444).

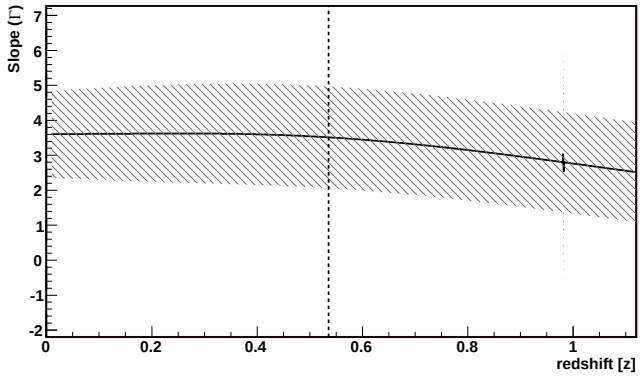

Figure C.16: Source 3C 279 (real redshift 0.536).

C.2 Follow—up study

In this Section, the Γ–z plots relative to the follow–up study presented in the second part of Chapter 8 are displayed. In this case, the blazars sample is enlarged and we adopt the slope measured by *Fermi*/LAT after 1 year of data taking.

The list of sources, along with their redshift, z, and the quantity z^* estimated with the Franceschini EBL model, are reported in Table C.2.

Source Name	z	z^*_{Fra}
Mkn 421	0.030	0.07 ± 0.02
Mkn 501	0.034	0.08 ± 0.02
1ES 2344+514	0.044	0.19 ± 0.03
Mkn 180	0.045	0.21 ± 0.11
1ES 1959+650	0.047	0.07 ± 0.03
BL Lacertae	0.069	0.27 ± 0.14
PKS 2005−489	0.071	0.18 ± 0.03
W Comae	0.102	0.24 ± 0.05
PKS 2155−304	0.116	0.22 ± 0.01
RGB J0710+591	0.125	0.21 ± 0.06
1ES 0806+524	0.138	0.23 ± 0.15
H 2356−309	0.165	0.16 ± 0.07
1ES 1218+304	0.182	0.21 ± 0.08
1ES 1101−232	0.186	0.23 ± 0.11
1ES 1011+496	0.212	0.60 ± 0.28
S5 0716+714	0.310[a]	0.23 ± 0.10
PG 1553+113	0.400	0.75 ± 0.07
3C 66A	0.444[a]	0.39 ± 0.05
3C 279	0.536	-

Table C.2: List of TeV blazars used in the follow–up study. [a]: uncertain.

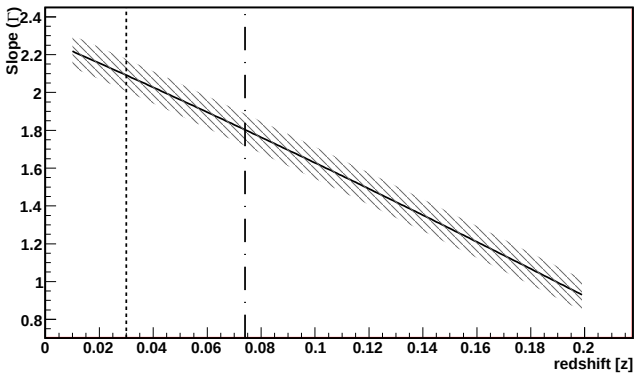

Figure C.17: Source Mkn 421 (real redshift 0.030).

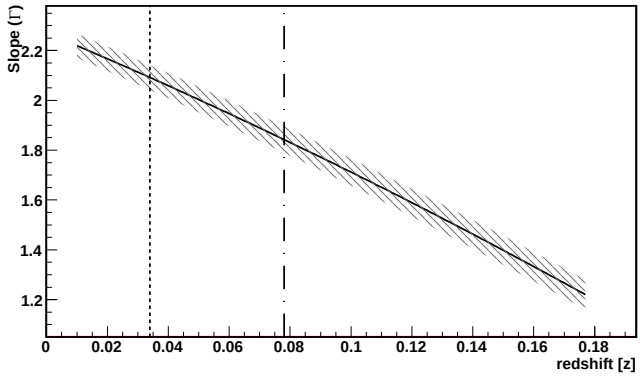

Figure C.18: Source Mkn 501 (real redshift 0.034).

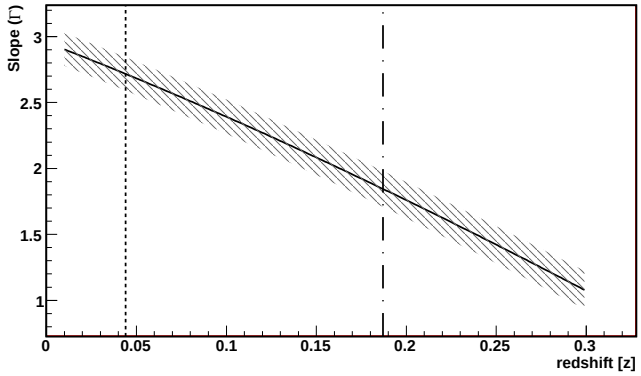

Figure C.19: Source 1ES 2344+514 (real redshift 0.044).

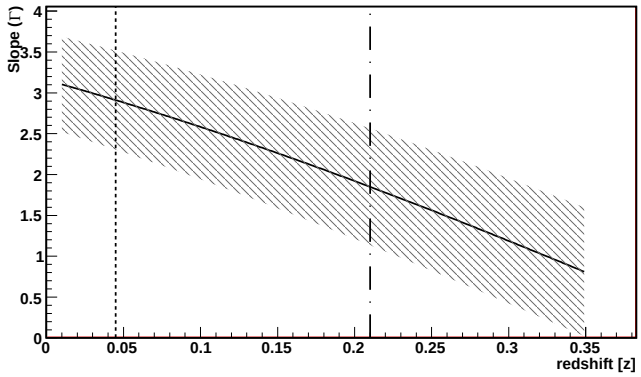

Figure C.20: Source Mkn 180 (real redshift 0.045).

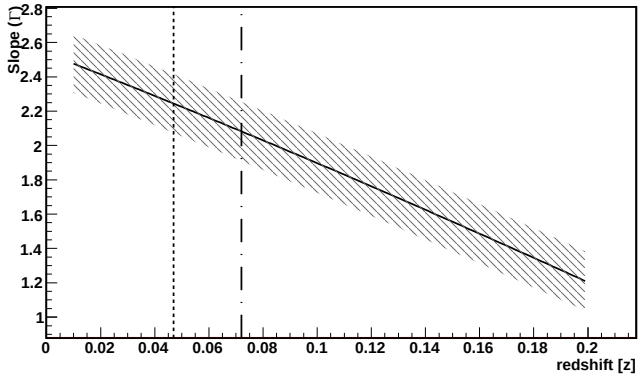

Figure C.21: Source 1ES 1949+650 (real redshift 0.047).

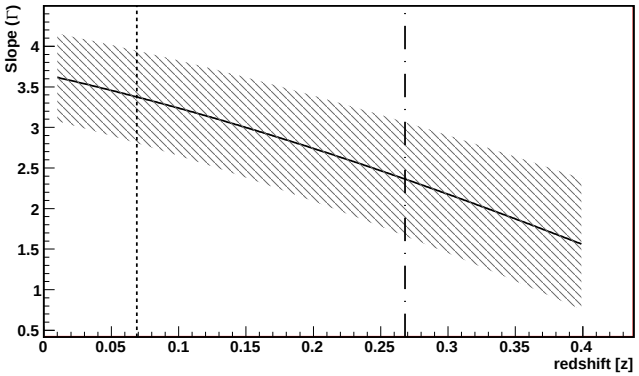

Figure C.22: Source BL Lacertae (real redshift 0.069).

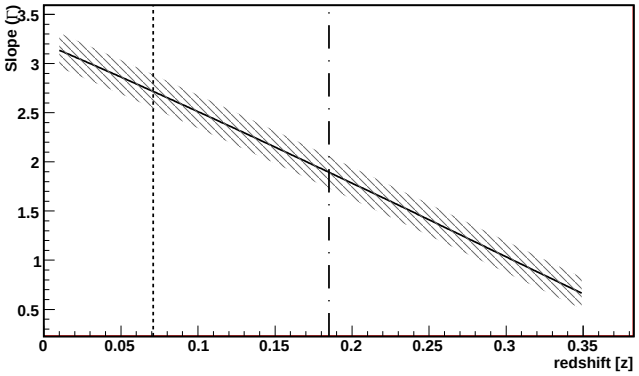

Figure C.23: Source PKS 2005−489 (real redshift 0.071).

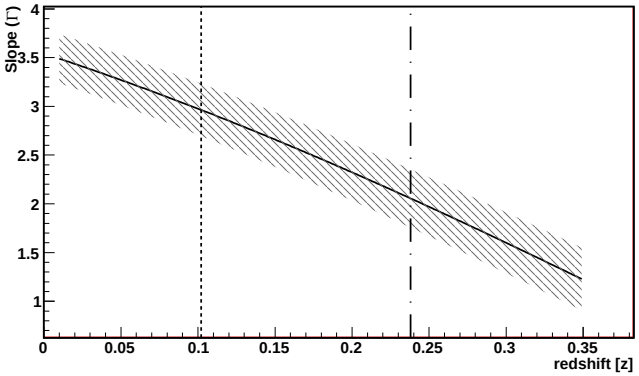

Figure C.24: Source W Comae (real redshift 0.102).

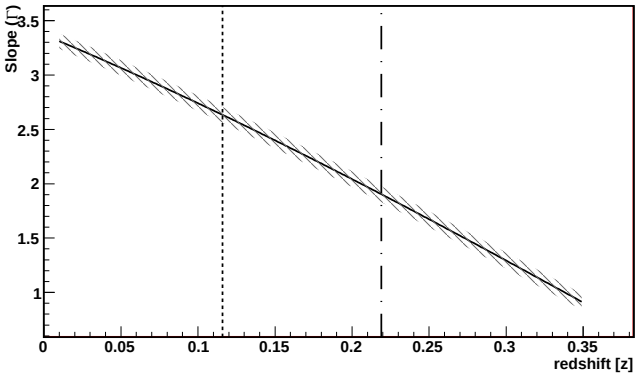

Figure C.25: Source PKS 2155−304 (real redshift 0.116).

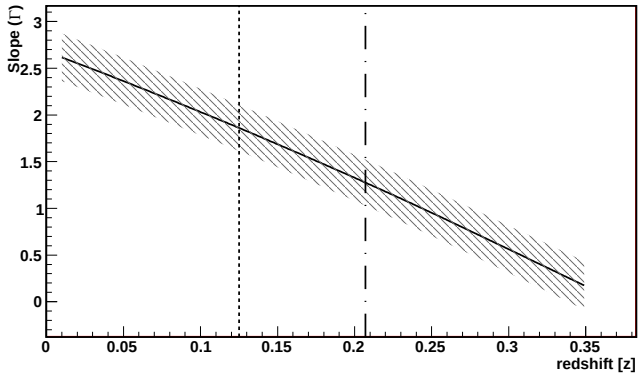

Figure C.26: Source RGB J0710+591 (real redshift 0.125).

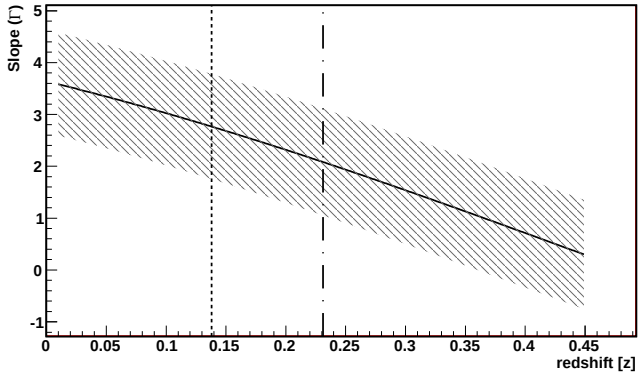

Figure C.27: Source 1ES 0806+524 (real redshift 0.138).

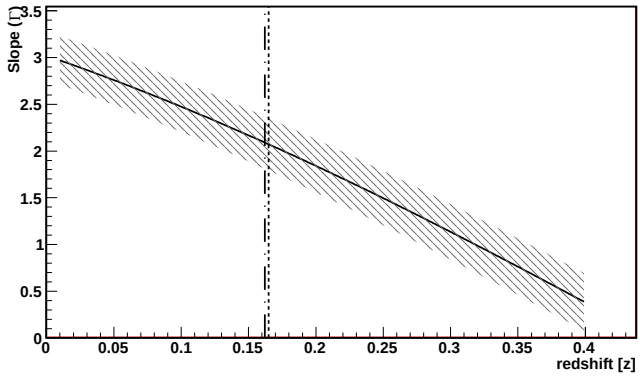

Figure C.28: Source H 2356−309 (real redshift 0.165).

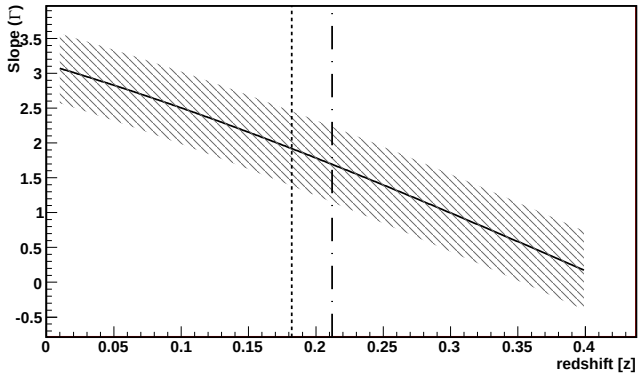

Figure C.29: Source 1ES 1218+304 (real redshift 0.182).

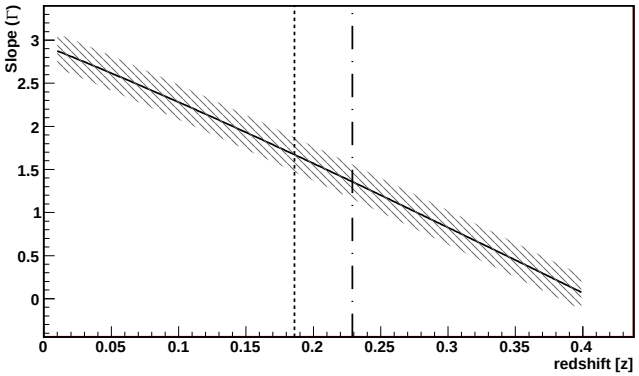

Figure C.30: Source 1ES 1101−232 (real redshift 0.186).

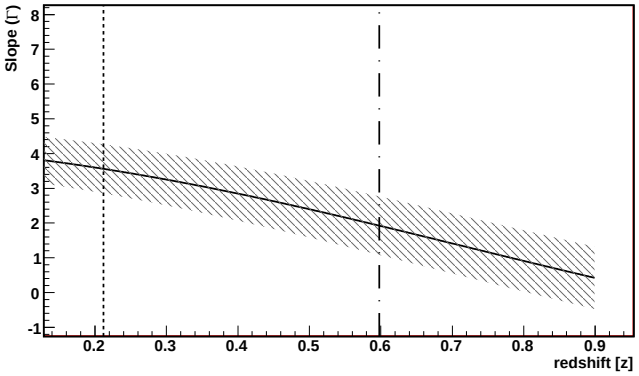

Figure C.31: Source 1ES 1011+496 (real redshift 0.212).

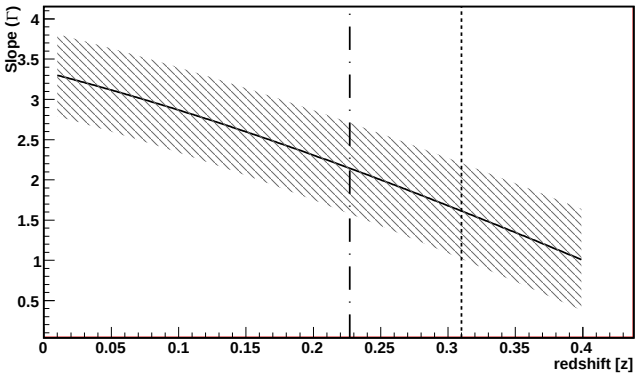

Figure C.32: Source S5 0716+714 (uncertain redshift, 0.310).

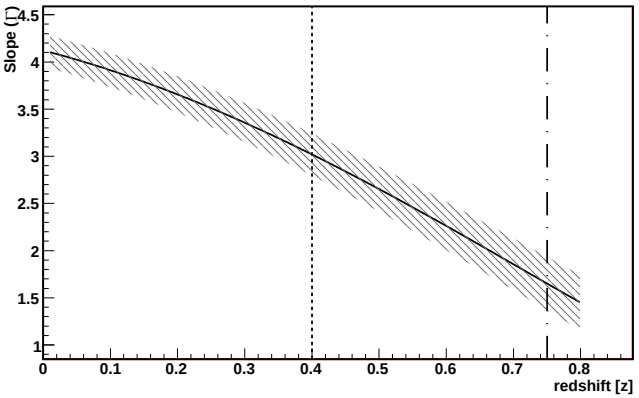

Figure C.33: Source PG 1553+113 (redshift assumed for this study 0.40, see discussion in Section 8.7.1).

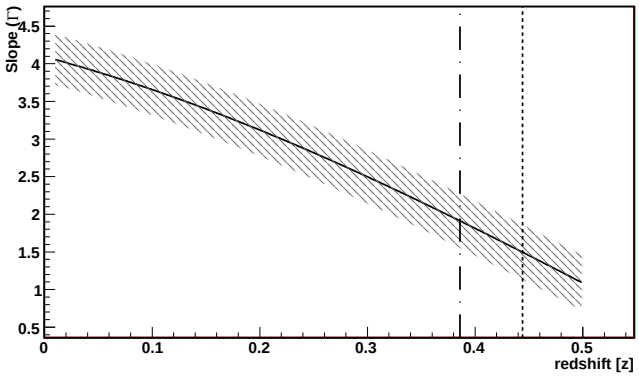

Figure C.34: Source 3C 66A (uncertain redshift, 0.444).

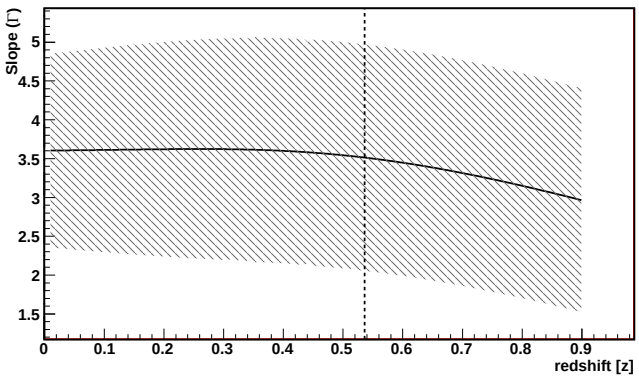

Figure C.35: Source 3C 279 (real redshift 0.536).

Bibliography

Abdo, A.A. et al., 2009. 'Bright active galactic nuclei source list from the first three months of the fermi large area telescope all-sky survey.' *ApJ*, **700**, 1, 597.

Abdo, A.A. et al., 2009. 'Fermi Observations of TeV-Selected Active Galactic Nuclei.' *ApJ*, **707**, 1310–1333.

Abdo, A.A. et al., 2009. 'Measurement of the cosmic ray $e^+ + e^-$ spectrum from 20 gev to 1 tev with the fermi large area telescope.' *Phys. Rev. Lett.*, **102**, 18, 181101.

Abdo, A.A. et al., 2010a. 'Fermi Large Area Telescope Constraints on the Gamma-ray Opacity of the Universe.' *ApJ*, **723**, 1082–1096. doi:10.1088/0004-637X/723/2/1082.

Abdo, A.A. et al., 2010b. 'Fermi Large Area Telescope First Source Catalog.' *ApJS*, **188**, 405–436.

Abdo, A.A. et al., 2010a. 'Fermi observations of the very hard gamma-ray blazar pg 1553+113.' *ApJ*, **708**, 2, 1310.

Abdo, A.A. et al., 2010b. 'Gamma-ray light curves and variability of bright fermi-detected blazars.' *ApJ*, **722**, 1, 520.

Abdo, A.A. et al., 2010. 'Spectral Properties of Bright Fermi-Detected Blazars in the Gamma-Ray Band.' *ApJ*, **710**, 1271–1285.

Abdo, A.A. et al., 2010. 'Spectrum of the isotropic diffuse gamma-ray emission derived from first-year fermi large area telescope data.' *Phys. Rev. Lett.*, **104**, 10, 101101.

Abdo, A.A. et al., 2010. 'The First Catalog of Active Galactic Nuclei Detected by the Fermi Large Area Telescope.' *ApJ*, **715**, 429–457.

Abdo, A.A. et al., 2011. 'Fermi/lat observations of markarian 421: the missing piece of its spectral energy distribution.' *Submitted to ApJ*.

Abramowicz, M.A., Bjornsson, G. and Pringle, J.E., editors, 1998. *Theory of Black Hole Accretion Disks*.

Acciari, V. et al., 2009a. 'Discovery of Very High Energy Gamma-ray Radiation from the BL Lac 1ES 0806+524.' *ApJ Letters*, **690**, L126–L129.

Acciari, V.A. et al., 2009b. 'Multiwavelength Observations of a TeV-Flare from W Comae.' *ApJ*, **707**, 612–620.

Acciari, V.A. et al., 2009c. 'Radio Imaging of the Very-High-Energy γ-Ray Emission Region in the Central Engine of a Radio Galaxy.' *Science*, **325**, 444.

Acciari, V.A. et al., 2009. 'Simultaneous multiwavelength observations of markarian 421 during outburst.' *ApJ*, **703**, 1, 169.

Acciari, V.A. et al., 2009. 'VERITAS Observations of the BL Lac Object 1ES 1218+304.' *ApJ*, **695**, 1370–1375.

Acciari, V.A. et al., 2010. 'Discovery of variability in the very high energy Îş-ray emission of 1es 1218+304 with veritas.' *AJ Letters*, **709**, 2, L163.

Acciari, V.A. et al., 2010a. 'Discovery of Very High Energy Gamma Rays from PKS 1424+240 and Multiwavelength Constraints on Its Redshift.' *ApJ Letters*, **708**, L100–L106.

Acciari, V.A. et al., 2010b. 'The Discovery of γ-Ray Emission from the Blazar RGB J0710+591.' *ApJ Letters*, **715**, L49–L55.

Acero, F. et al., 2009. 'Detection of Gamma Rays from a Starburst Galaxy.' *Science*, **326**, 1080–.

Ackermann, M. et al., 2010. 'Fermi observations of grb 090510: A short-hard gamma-ray burst with an additional, hard power-law component from 10 kev to gev energies.' *ApJ*, **716**, 2, 1178.

Adriani, O. et al., 2009. 'New Measurement of the Antiproton-to-Proton Flux Ratio up to 100 GeV in the Cosmic Radiation.' *Physical Review Letters*, **102**, 5, 051101–+.

Adriani, O. et al., 2010. 'PAMELA Results on the Cosmic-Ray Antiproton Flux from 60 MeV to 180 GeV in Kinetic Energy.' *Physical Review Letters*, **105**, 12, 121101–+.

Aharonian, F. et al., 2006. 'Evidence for VHE γ-ray emission from the distant BL Lac PG 1553+113.' *A&A*, **448**, L19–L23.

Aharonian, F. et al., 2006. 'A low level of extragalactic background light as revealed by gamma-rays from blazars.' *Nature*, **440**, 1018–1021.

Aharonian, F. et al., 2007a. 'H.E.S.S. Observations of the Supernova Remnant RX J0852.0-4622: Shell-Type Morphology and Spectrum of a Widely Extended Very High Energy Gamma-Ray Source.' *ApJ*, **661**, 236–249.

Aharonian, F. et al., 2007b. 'New constraints on the mid-IR EBL from the HESS discovery of VHE γ-rays from 1ES 0229+200.' *A&A*, **475**, L9–L13.

Aharonian, F. et al., 2008. 'Energy spectrum of cosmic-ray electrons at tev energies.' *Phys. Rev. Lett.*, **101**, 26, 261104.

Aharonian, F. et al., 2009. 'Simultaneous Observations of PKS 2155-304 with HESS, Fermi, RXTE, and Atom: Spectral Energy Distributions and Variability in a Low State.' *ApJ Letters*, **696**, L150–L155.

Aharonian, F. et al., 2010. 'Discovery of VHE γ-rays from the BL Lacertae object PKS 0548-322.' *A&A*, **521**, A69+.

Aharonian, F.A., 2000. 'TeV gamma rays from BL Lac objects due to synchrotron radiation of extremely high energy protons.' *New Astronomer*, **5**, 377–395.

Aharonian, F.A., 2002. 'Proton-synchrotron radiation of large-scale jets in active galactic nuclei.' *MNRAS*, **332**, 215–230.

Aharonian, F.A., Khangulyan, D. and Costamante, L., 2008. 'Formation of hard very high energy gamma-ray spectra of blazars due to internal photon-photon absorption.' *MNRAS*, **387**, 1206–1214.

Albert, J. et al., 2006a. 'Discovery of Very High Energy Gamma Rays from 1ES 1218+30.4.' *ApJ Letters*, **642**, L119–L122.

Albert, J. et al., 2006b. 'Discovery of Very High Energy γ-Rays from Markarian 180 Triggered by an Optical Outburst.' *ApJ Letters*, **648**, L105–L108.

Albert, J. et al., 2006c. 'Variable Very-High-Energy Gamma-Ray Emission from the Microquasar LS I +61 303.' *Science*, **312**, 1771–1773.

Albert, J. et al., 2007a. 'Detection of Very High Energy Radiation from the BL Lacertae Object PG 1553+113 with the MAGIC Telescope.' *ApJ Letters*, **654**, L119–L122.

Albert, J. et al., 2007b. 'Discovery of Very High Energy γ-Ray Emission from the Low-Frequency-peaked BL Lacertae Object BL Lacertae.' *ApJ Letters*, **666**, L17–L20.

Albert, J. et al., 2007c. 'Discovery of Very High Energy γ-Rays from 1ES 1011+496 at z = 0.212.' *ApJ Letters*, **667**, L21–L24.

Albert, J. et al., 2007d. 'Observation of Very High Energy γ-Rays from the AGN 1ES 2344+514 in a Low Emission State with the MAGIC Telescope.' *ApJ*, **662**, 892–899.

Albert, J. et al., 2007e. 'Variable Very High Energy γ-Ray Emission from Markarian 501.' *ApJ*, **669**, 862–883.

Albert, J. et al., 2008a. 'Implementation of the Random Forest method for the Imaging Atmospheric Cherenkov Telescope MAGIC.' *NIM A*, **588**, 424–432.

Albert, J. et al., 2008b. 'Upper Limit for γ-Ray Emission above 140 GeV from the Dwarf Spheroidal Galaxy Draco.' *ApJ*, **679**, 428–431.

Albert, J. et al., 2008c. 'Very-High-Energy gamma rays from a Distant Quasar: How Transparent Is the Universe?' *Science*, **320**, 1752–.

Albert, J. et al., 2008. 'Vhe γ-ray observation of the crab nebula and its pulsar with the magic telescope.' *ApJ*, **674**, 2, 1037.

Albert, J. et al., 2009. 'MAGIC observations of PG 1553+113 during a multi-wavelength campaign in July 2006.' *A&A*, **493**, 467–469.

Aleksić, J. et al., 2010a. 'MAGIC observation of the GRB 080430 afterglow.' *A&A*, **517**, A5+.

Aleksić, J. et al., 2010b. 'Search for an extended VHE γ-ray emission from Mrk 421 and Mrk 501 with the MAGIC Telescope.' *A&A*, **524**, A77+.

Aleksić, J. et al., 2010c. 'Simultaneous multi-frequency observation of the unknown redshift blazar PG 1553+113 in March-April 2008.' *A&A*, **515**, A76+.

Aleksić, J. et al., 2011. 'PG 1553+113: five years of observations with MAGIC.' *submitted to ApJ*.

Aliu, E. et al., 2008. 'Observation of Pulsed γ-Rays Above 25 GeV from the Crab Pulsar with MAGIC.' *Science*, **322**, 1221.

Aliu, E. et al., 2009. 'Improving the performance of the single-dish Cherenkov telescope MAGIC through the use of signal timing.' *Astroparticle Physics*, **30**, 293–305.

Anderhub, H. et al., 2009a. 'Discovery of very High Energy γ-Rays from the Blazar S5 0716+714.' *ApJ Letters*, **704**, L129–L133.

Anderhub, H. et al., 2009b. 'Simultaneous Multiwavelength Observation of Mkn 501 in a Low State in 2006.' *ApJ*, **705**, 1624–1631.

Atkins, R. et al., 2003. 'Observation of TeV Gamma Rays from the Crab Nebula with Milagro Using a New Background Rejection Technique.' *ApJ*, **595**, 803–811.

Atwood, W.B. et al., 2009. 'The Large Area Telescope on the Fermi Gamma-Ray Space Telescope Mission.' *ApJ*, **697**, 1071–1102.

Bauleo, P.M. and Martino, J.R., 2009. 'The dawn of the particle astronomy era in ultra-high-energy cosmic rays.' *Nature*, **458**, 7240, 847–851.

Bernstein, R.A., 2007. 'The Optical Extragalactic Background Light: Revisions and Further Comments.' *ApJ*, **666**, 663–673.

Béthermin, M., Dole, H., Beelen, A. and Aussel, H., 2010. 'Spitzer deep and wide legacy mid- and far-infrared number counts and lower limits of cosmic infrared background.' *A&A*, **512**, A78+.

Blandford, R.D. and Znajek, R.L., 1977. 'Electromagnetic extraction of energy from Kerr black holes.' *MNRAS*, **179**, 433–456.

Boettcher, M., 2010. 'Models for the Spectral Energy Distributions and Variability of Blazars.' *ArXiv e-prints*.

Borla Tridon, D. et al., 2009. 'Performance of the Camera of the MAGIC II Telescope.' *ArXiv e-prints*.

Brandt, W.N. and Hasinger, G., 2005. 'Deep Extragalactic X-Ray Surveys.' *ARA&A*, **43**, 827–859.

Britzger, D. et al., 2009. 'Studies of the Influence of Moonlight on Observations with the MAGIC Telescope.' *ArXiv e-prints*.

Cambrésy, L., Reach, W.T., Beichman, C.A. and Jarrett, T.H., 2001. 'The Cosmic Infrared Background at 1.25 and 2.2 Microns Using DIRBE and 2MASS: A Contribution Not Due to Galaxies?' *ApJ*, **555**, 563–571.

Celotti, A. and Ghisellini, G., 2008. 'The power of blazar jets.' *MNRAS*, **385**, 283–300.

Chang, J. et al., 2008. 'An excess of cosmic ray electrons at energies of 300–800 gev.' *Nature*, **456**, 7220, 362–365.

Chary, R. and Pope, A., 2010. 'New Observational Constraints and Modeling of the Infrared Background: Dust Obscured Star-Formation at z>1 and Dust in the Outer Solar System.' *submitted to ApJ.*

Chaves, R.C.G., 2009. 'Extending the H.E.S.S. Galactic Plane Survey.' *ArXiv e-prints.*

Colin, P. et al., 2009. 'Performance of the MAGIC telescopes in stereoscopic mode.' *ArXiv e-prints.*

Cortina, J., Goebel, F., Schweizer, T. and for the MAGIC Collaboration, 2009. 'Technical Performance of the MAGIC Telescopes.' *ArXiv e-prints.*

Costamante, L. and Ghisellini, G., 2002. 'TeV candidate BL Lac objects.' *A&A*, **384**, 56–71.

CTA Consortium, T., 2010. 'Design Concepts for the Cherenkov Telescope Array.' *ArXiv e-prints.*

Cusumano, G. et al., 2010. 'The Palermo Swift-BAT hard X-ray catalogue III. Results after 54 months of sky survey.' *accepted for publication in A&A.*

Danforth, C.W. et al., 2010. 'Hubble/cos observations of the lyα forest toward the bl lac object 1es 1553+113.' *ApJ*, **720**, 1, 976.

Dermer, C.D., 2007. 'On Gamma Ray Burst and Blazar AGN Origins of the Ultra-High Energy Cosmic Rays in Light of First Results from Auger.' *ArXiv e-prints.*

Desert, F., Boulanger, F. and Puget, J.L., 1990. 'Interstellar dust models for extinction and emission.' *A&A*, **237**, 215–236.

Dole, H. et al., 2006. 'The cosmic infrared background resolved by Spitzer. Contributions of mid-infrared galaxies to the far-infrared background.' *A&A*, **451**, 417–429.

Domínguez, A. et al., 2011. 'Extragalactic background light inferred from AEGIS galaxy-SED-type fractions.' *MNRAS*, **410**, 2556–2578.

Donato, D., Ghisellini, G., Tagliaferri, G. and Fossati, G., 2001. 'Hard X-ray properties of blazars.' *A&A*, **375**, 739–751.

Dondi, L. and Ghisellini, G., 1995. 'Gamma-ray-loud blazars and beaming.' *MNRAS*, **273**, 583–595.

Doro, M., 2009. *Novel Reflective Elements and Indirect Dark Matter Searches for MAGIC-II and Future IACTs.* Ph.D. thesis, Padova University, Padova.

Eadie, W., Drijard, D., James, F. and Roos, M., S.B., 1988. *Statistical Methods in Experimental Physics* (North-Holland Publishing Company, Amsterdam, New-York, Oxford).

Errando Trias, M., 2009. *Discovery of very high energy gamma-ray emission from 3C 279 and 3C 66 A/B with the MAGIC telescope.* Ph.D. thesis, IFAE, Barcelona.

F., G. et al., 2007. 'Upgrade of the MAGIC Telescope with a Multiplexed Fiber-Optic 2 GSamples/s FADC Data Acquisition system.' *ArXiv e-prints.*

Falomo, R. and Treves, A., 1990. 'PG 1553 + 11 - A bright optically selected BL Lacertae object.' *PASP*, **102**, 1120–1125.

Fazio, G.G. et al., 2004. 'Number Counts at 3 μm $< \lambda <$ 10 μm from the Spitzer Space Telescope.' *ApJS*, **154**, 39–43.

Finke, J.D. and Razzaque, S., 2009. 'Constraints on the Extragalactic Background Light from very High Energy Gamma-Ray Observations of Blazars.' *ApJ*, **698**, 1761–1766.

Finke, J.D., Razzaque, S. and Dermer, C.D., 2010. 'Modeling the Extragalactic Background Light from Stars and Dust.' *ApJ*, **712**, 238–249.

Fomin, V.P. et al., 1994. 'New methods of atmospheric Cherenkov imaging for gamma-ray astronomy. I. The false source method.' *Astroparticle Physics*, **2**, 137–150.

Fossati, G. et al., 1998. 'A unifying view of the spectral energy distributions of blazars.' *MNRAS*, **299**, 433–448.

Fossati, G. et al., 2008. 'Multiwavelength Observations of Markarian 421 in 2001 March: An Unprecedented View on the X-Ray/TeV Correlated Variability.' *ApJ*, **677**, 906–925.

Franceschini, A., Rodighiero, G. and Vaccari, M., 2008. 'Extragalactic optical-infrared background radiation, its time evolution and the cosmic photon-photon opacity.' *A&A*, **487**, 837–852.

Frank, J., King, A. and Raine, D.J., 1992. *Accretion Power in Astrophysics* (Cambridge University Press, Cambridge).

Gaug, M., 2006. *Calibration of the MAGIC telescope and observation of gamma-ray bursts.* Ph.D. thesis, IFAE, Barcelona.

Georganopoulos, M., Finke, J.D. and Reyes, L.C., 2010. 'A Method for Setting Upper Limits to the Extragalactic Background Light with Fermi-LAT and TeV Observations of Blazars.' *ApJ Letters*, **714**, L157–L161.

Georganopoulos, M. and Kazanas, D., 2003. 'Decelerating Flows in TeV Blazars: A Resolution to the BL Lacertae-FR I Unification Problem.' *ApJ Letters*, **594**, L27–L30.

Ghisellini, G., Maraschi, L. and Tavecchio, F., 2009. 'The Fermi blazars' divide.' *MNRAS*, **396**, L105–L109.

Ghisellini, G., Tavecchio, F. and Chiaberge, M., 2005. 'Structured jets in TeV BL Lac objects and radiogalaxies. Implications for the observed properties.' *A&A*, **432**, 401–410.

Ghisellini, G., Tavecchio, F., Foschini, L. and Ghirlanda, G., 2010a. 'The transition between BL Lac objects and Flat Spectrum Radio Quasars.' *submitted to MNRAS*.

Ghisellini, G. et al., 1998. 'A theoretical unifying scheme for gamma-ray bright blazars.' *MNRAS*, **301**, 451–468.

Ghisellini, G. et al., 2010b. 'High-redshift Fermi blazars.' *MNRAS*, pages 1729–+.

Gilmore, R.C. et al., 2009. 'GeV gamma-ray attenuation and the high-redshift UV background.' *MNRAS*, **399**, 1694–1708.

Ginzburg, V.L. and Syrovatskii, S.I., 1964. *The Origin of Cosmic Rays* (Pergamon Press, London, New York, Etc.).

Graff, P.B., Georganopoulos, M., Perlman, E.S. and Kazanas, D., 2008. 'A Multizone Model for Simulating the High-Energy Variability of TeV Blazars.' *ApJ*, **689**, 68–78.

Green, R.F., Schmidt, M. and Liebert, J., 1986. 'The Palomar-Green catalog of ultraviolet-excess stellar objects.' *ApJS*, **61**, 305–352.

Greisen, K., 1966. 'End to the cosmic-ray spectrum?' *Phys. Rev. Lett.*, **16**, 17, 748–750.

Hauser, M.G. and Dwek, E., 2001. 'The Cosmic Infrared Background: Measurements and Implications.' *ARA&A*, **39**, 249–307.

Heitler, W., 1960. *The Quantum Theory of Radiation* (Oxford Press, Oxford).

HESS Collaboration et al., 2010. 'PKS 2005-489 at VHE: four years of monitoring with HESS and simultaneous multi-wavelength observations.' *A&A*, **511**, A52.

Hillas, A.M., 1984. 'The Origin of Ultra-High-Energy Cosmic Rays.' *ARA&A*, **22**, 425–444.

Hillas, A.M., 1985. 'Cerenkov light images of EAS produced by primary gamma.' In F. C. Jones, editor, 'International Cosmic Ray Conference,' volume 3 of *International Cosmic Ray Conference*, pages 445–448.

Hinton, J.A. and Hofmann, W., 2009. 'Teraelectronvolt Astronomy.' *ARA&A*, **47**, 523–565.

Holder, J., 2007. 'VERITAS: Status and Performance.' In M. M. Massai, N. Omodei, & G. Spandre, editor, 'Science with the New Generation of High Energy Gamma-Ray Experiments,' pages 69–+.

Hörandel, J.R., 2008. 'Cosmic-ray composition and its relation to shock acceleration by supernova remnants.' *Advances in Space Research*, **41**, 442–463.

Hörandel, J.R., 2010. 'Cosmic rays at the highest energies.' *Progress in Particle and Nuclear Physics*, **64**, 2, 351 – 359. ISSN 0146-6410. Neutrinos in Cosmology, in Astro, Particle and Nuclear Physics, International Workshop on Nuclear Physics, 31st course.

Juvela, M. et al., 2009. 'Determination of the cosmic far-infrared background level with the ISOPHOT instrument.' *A&A*, **500**, 763–768.

Kashlinsky, A., 2005. 'Cosmic infrared background and early galaxy evolution.' *Physics Reports*, **409**, 361–438.

Katarzyński, K. et al., 2006. 'Hard TeV spectra of blazars and the constraints to the infrared intergalactic background.' *MNRAS*, **368**, L52–L56.

Kellermann, K.I. et al., 1989. 'VLA observations of objects in the Palomar Bright Quasar Survey.' *AJ*, **98**, 1195–1207.

Kifune, T., 1999. 'Invariance Violation Extends the Cosmic-Ray Horizon?' *ApJ Letters*, **518**, L21–L24.

Kneiske, T.M. and Dole, H., 2010. 'A lower-limit flux for the extragalactic background light.' *A&A*, **515**, A19+.

Krawczynski, H. et al., 2004. 'Multiwavelength Observations of Strong Flares from the TeV Blazar 1ES 1959+650.' *ApJ*, **601**, 151–164.

Lacki, B.C. et al., 2010. 'On The GeV & TeV Detections of the Starburst Galaxies M82 & NGC 253.' *submitted to ApJ*.

Lagache, G., Haffner, L.M., Reynolds, R.J. and Tufte, S.L., 2000. 'Evidence for dust emission in the Warm Ionised Medium sing WHAM data.' *A&A*, **354**, 247–252.

Lagache, G., Puget, J. and Dole, H., 2005. 'Dusty Infrared Galaxies: Sources of the Cosmic Infrared Background.' *ARA&A*, **43**, 727–768.

Levenson, L.R. and Wright, E.L., 2008. 'Probing the 3.6 μm CIRB with Spitzer in Three DIRBE Dark Spots.' *ApJ*, **683**, 585–596.

Li, T. and Ma, Y., 1983. 'Analysis methods for results in gamma-ray astronomy.' *ApJ*, **272**, 317–324.

Lombardi, S., 2010. *Development of analysis tools for the MAGIC Telescopes and observation of the Segue 1 Satellite Galaxy with the MAGIC-I Telescope*. Ph.D. thesis, Padova University, Padova.

Longair, M.S., 1992. *High Energy Astrophysics* (Cambridge University Press, Cambridge).

Lopez, M. et al., 2009. 'Detection of the crab pulsar with MAGIC.' *ArXiv e-prints*.

Lopez Moya, M., 2007. *Observaciones de la Nebulosa y Pulsar del Cangrejo*. Ph.D. thesis, UCM, Madrid.

MacDonald, D. and Thorne, K.S., 1982. 'Black-hole electrodynamics - an absolute-space/universal-time formulation.' *MNRAS*, **198**, 345–382.

Madau, P. and Pozzetti, L., 2000. 'Deep galaxy counts, extragalactic background light and the stellar baryon budget.' *MNRAS*, **312**, L9–L15.

Malkov, M.A. and O'C Drury, L., 2001. 'Nonlinear theory of diffusive acceleration of particles by shock waves.' *Reports on Progress in Physics*, **64**, 429–481.

Mankuzhiyil, N., Persic, M. and Tavecchio, F., 2010. 'High-frequency-peaked BL Lacertae Objects as Spectral Candles to Measure the Extragalactic Background Light in the Fermi and Air Cherenkov Telescopes Era.' *ApJ Letters*, **715**, L16–L20.

Mannheim, K., 1993. 'The proton blazar.' *A&A*, **269**, 67–76.

Mannheim, K. and Biermann, P.L., 1992. 'Gamma-ray flaring of 3C 279 - A proton-initiated cascade in the jet?' *A&A*, **253**, L21–L24.

Maraschi, L. and Tavecchio, F., 2003. 'The Jet-Disk Connection and Blazar Unification.' *ApJ*, **593**, 667–675.

Matsumoto, T. et al., 2005. 'Infrared Telescope in Space Observations of the Near-Infrared Extragalactic Background Light.' *ApJ*, **626**, 31–43.

Mattila, K., 2006. 'The 1-μm discontinuity in the extragalactic background light spectrum: an artefact of foreground subtraction.' *MNRAS*, **372**, 1253–1258.

Mattox, J.R. et al., 1996. 'The Likelihood Analysis of EGRET Data.' *ApJ*, **461**, 396–+.

Mazin, D. and Goebel, F., 2007. 'Break in the Very High Energy Spectrum of PG 1553+113: New Upper Limit on Its Redshift?' *ApJ Letters*, **655**, L13–L16.

Mazin, D. and Raue, M., 2007. 'New limits on the density of the extragalactic background light in the optical to the far infrared from the spectra of all known TeV blazars.' *A&A*, **471**, 439–452.

Miller, H.R. and Green, R.F., 1983. 'Optical/UV Observations of the BL Lac Object, PG 1553+11.' In 'Bulletin of the American Astronomical Society,' volume 15 of *Bulletin of the American Astronomical Society*, pages 957–+.

Mirzoyan, R., Garczarczyk, M., Hose, J. and Paneque, D., 2007. 'A method to measure the mirror reflectivity of a prime focus telescope.' *Astropart. Phys.*, **27**, 509–511.

Mucke, A. et al., 1999. 'Photohadronic processes in astrophysical environments.' *PASA*, **16**, 160–6.

Nakamura, K. and Particle Data Group, 2010. 'Review of Particle Physics.' *Journal of Physics G Nuclear Physics*, **37**, 7, 075021–+. doi:10.1088/0954-3899/37/7A/075021.

Narayan, R. and Quataert, E., 2005. 'Black Hole Accretion.' *Science*, **307**, 77–80.

Nieppola, E., Tornikoski, M. and Valtaoja, E., 2006. 'Spectral energy distributions of a large sample of BL Lacertae objects.' *A&A*, **445**, 441–450.

Nikishov, A.I., 1962. *Sov. Phys. JETP*, **14**, 393.

Nilsson, K. et al., 2008. 'Detection of the host galaxy of S5 0716+714.' *A&A*, **487**, L29–L32.

Nobili, L., 2002. *Processi Radiativi ed Equazione del Trasporto nell'Astrofisica delle Alte Energie* (Cleup Editrice, Padova).

Padmanabhan, T., 2000. *Theoretical Astrophysics - Volume 1, Astrophysical Processes* (Cambridge University Press, Cambridge).

Pagliaroli, G., Vissani, F., Costantini, M.L. and Ianni, A., 2009. 'Improved analysis of SN1987A antineutrino events.' *Astroparticle Physics*, **31**, 163–176.

Perkins, D.H., 2009. *Particle Astrophysics* (Oxford Univ. Press, Oxford), 2 edition.

Pierre AUGER Collaboration et al., 2010. 'Measurement of the energy spectrum of cosmic rays above 10^{18} eV using the Pierre Auger Observatory.' *Physics Letters B*, **685**, 239–246.

Piner, B.G., Pant, N. and Edwards, P.G., 2010. 'The Jets of TeV Blazars at Higher Resolution: 43 GHz and Polarimetric VLBA Observations from 2005-2009.' *ArXiv e-prints*.

Prandini, E., 2010. 'Blazars distance indications from vhe γ-rays observations.' *Nuovo Cimento B*, **125**, 591–600.

Prandini, E. et al., 2009. 'A new upper limit on the redshift of PG 1553+113 from observations with the MAGIC Telescope.' *ArXiv e-prints*.

Prandini, E. et al., 2010. 'Constraining blazar distances with combined Fermi and TeV data: an empirical approach.' *MNRAS*, **405**, L76–L80.

Prandini, E. et al., 2011a. 'Blazars distance indications from Fermi and TeV data.' In L. Cifarelli, editor, 'accepted for publication in Il Nuovo Cimento C,' .

Prandini, E. et al., 2011b. 'TeV blazars and their distance.' *Proceeding CRF2010*.

Primack, J.R., Bullock, J.S. and Somerville, R.S., 2005. 'Observational Gamma-ray Cosmology.' In F. A. Aharonian, H. J. Völk, & D. Horns, editor, 'High Energy Gamma-Ray Astronomy,' volume 745 of *American Institute of Physics Conference Series*, pages 23–33.

Punch, M. et al., 1992. 'Detection of TeV photons from the active galaxy Markarian 421.' *Nature*, **358**, 477–+.

Rachen, J.P. and Mészáros, P., 1998. 'Photohadronic neutrinos from transients in astrophysical sources.' *Phys. Rev. D*, **58**, 12, 123005.

Raue, M. and Mazin, D., 2008. 'Optical Depth for VHE γ-RAYS from Distant Sources from a Generic EBL Density.' *International Journal of Modern Physics D*, **17**, 1515–1520.

Reimer, A. et al., 2008. 'A Hard X-Ray View of Two Distant VHE Blazars: 1ES 1101−232 and 1ES 1553+113.' *ApJ*, **682**, 775–783.

Rieger, F.M., Bosch-Ramon, V. and Duffy, P., 2007. 'Fermi acceleration in astrophysical jets.' *Ap&SS*, **309**, 119–125.

Sbarufatti, B., Treves, A. and Falomo, R., 2005a. 'Imaging Redshifts of BL Lacertae Objects.' *ApJ*, **635**, 173–179.

Sbarufatti, B. et al., 2005b. 'ESO Very Large Telescope Optical Spectroscopy of BL Lacertae Objects. I. New Redshifts.' *AJ*, **129**, 559–566.

Sbarufatti, B. et al., 2006. 'ESO Very Large Telescope Optical Spectroscopy of BL Lacertae Objects. II. New Redshifts, Featureless Objects, and Classification Assessments.' *AJ*, **132**, 1–19.

Scarpa, R. and Falomo, R., 1995. 'Spectral energy distribution of Palomar-Green BL Lacertae objects.' *A&A*, **303**, 656–+.

Scarpa, R. et al., 2000. 'The Hubble Space Telescope Survey of BL Lacertae Objects. I. Surface Brightness Profiles, Magnitudes, and Radii of Host Galaxies.' *ApJ*, **532**, 740–815.

Schlickeiser, R., 2002. *Cosmic Ray Astrophysics* (Springer-Verlag, Berlin, Heidelberg, New York).

Somerville, R.S. et al., 2008. 'A semi-analytic model for the co-evolution of galaxies, black holes and active galactic nuclei.' *MNRAS*, **391**, 481–506.

Stecker, F.W., de Jager, O.C. and Salamon, M.H., 1992. 'TeV gamma rays from 3C 279 - A possible probe of origin and intergalactic infrared radiation fields.' *ApJ Letters*, **390**, L49–L52.

Stecker, F.W., Malkan, M.A. and Scully, S.T., 2006. 'Intergalactic Photon Spectra from the Far-IR to the UV Lyman Limit for 0<z<6 and the Optical Depth of the Universe to High-Energy Gamma Rays.' *ApJ*, **648**, 774–783.

Stecker, F.W. and Scully, S.T., 2010. 'Derivation of a Relation for the Steepening of Tev-Selected Blazar γ-ray Spectra with Energy and Redshift.' *ApJ Letters*, **709**, L124–L126.

Tagliaferri, G. et al., 2008. 'Simultaneous Multiwavelength Observations of the Blazar 1ES 1959+650 at a Low TeV Flux.' *ApJ*, **679**, 1029–1039.

Takalo, L.O. et al., 2007. 'Optical Monitoring of Candidate TeV Blazars.' In L. C. Ho & J.-W. Wang, editor, 'The Central Engine of Active Galactic Nuclei,' volume 373 of *Astronomical Society of the Pacific Conference Series*, pages 249–+.

Takeda, M. et al., 1998. 'Extension of the cosmic-ray energy spectrum beyond the predicted greisen-zatsepin-kuz'min cutoff.' *Phys. Rev. Lett.*, **81**, 6, 1163–1166.

Tavecchio, F., Maraschi, L. and Ghisellini, G., 1998. 'Constraints on the Physical Parameters of TeV Blazars.' *ApJ*, **509**, 608–619.

Tavecchio, F. et al., 2010. 'TeV BL Lac objects at the dawn of the Fermi era.' *MNRAS*, **401**, 1570–1586.

Tescaro, D., 2010. *TeV γ-ray observations of nearby Active Galactic Nuclei with the MAGIC telescope: exploring the high energy region of the multiwavelength picture.* Ph.D. thesis, IFAE, Barcelona.

The H. E. S. S. Collaboration, 2007. 'H.E.S.S. ICRC 2007 contributions.' *ArXiv e-prints*.

The Pierre AUGER Collaboration et al., 2008. 'Correlation of the highest-energy cosmic rays with the positions of nearby active galactic nuclei.' *Astroparticle Physics*, **29**, 188–204.

The Pierre AUGER Collaboration et al., 2010. 'Update on the correlation of the highest energy cosmic rays with nearby extragalactic matter.' *Astroparticle Physics*, **34**, 314–326.

Tikhonov, A.N. and Arsenin, V.A., 1977. *Solution of Ill-posed Problems* (Winston & Sons, Washington).

Treves, A., Falomo, R. and Uslenghi, M., 2007. 'On the distance of PG 1553+11. A lineless BL Lacertae object active in the TeV band.' *A&A*, **473**, L17–L19.

Urry, C.M. and Padovani, P., 1995. 'Unified Schemes for Radio-Loud Active Galactic Nuclei.' *PASP*, **107**, 803–+.

Venters, T.M., 2010. 'Contribution to the Extragalactic Gamma-Ray Background from the Cascades of very High Energy Gamma Rays from Blazars.' *ApJ*, **710**, 1530–1540.

Wehrle, A.E. et al., 2001. 'Kinematics of the Parsec-Scale Relativistic Jet in Quasar 3C 279: 1991-1997.' *ApJS*, **133**, 297–320.

Yang, J. and Wang, J., 2010. 'Constraining extragalactic background light from TeV blazars.' *A&A*, **522**, A12+.

Zatsepin, G.T. and Kuz'min, V.A., 1966. 'Upper Limit of the Spectrum of Cosmic Rays.' *Soviet Journal of Experimental and Theoretical Physics Letters*, **4**, 78–+.

Useful units

The basic units used in this thesis are listed and briefly explained in this Section.

Crab (Nebula) Unit is an integral flux unit. It is the fraction of Crab Nebula flux above a certain energy threshold which corresponds to the measured or reported flux. In this work, we have adopted as the reference Crab Nebula flux the integral flux estimated from the power law fitting the differential energy spectrum, published in Albert et al. (2008).

erg unit of energy, used in astronomy. One erg is 10^{-7} J.

eV from electronvolt. It is a unit of energy often used in particle and astroparticle physics; it is equal to approximately 1.602×10^{19} J. By definition, 1 keV is 10^3 eV, 1 MeV is 10^6 eV, 1 GeV is 10^9 eV, 1 TeV is 10^{12} eV, and 1PeV is 10^{15} eV.

light year is a unit of length. Corresponds to $9{,}461\times10^{15}$ m.

Jy stands for Jansky and is an integral flux unit, often used in optical and radio astronomy. It is equivalent to 10^{26} W $\mathrm{m}^{-2}\mathrm{s}^{-1}$.

MJD stands for Modified Julian Date. Is a time unit corresponding to the number of days elapsed since midnight of November 17, 1858.

parsec is a length unit, corresponding to 30.857×10^{15} m.

phel stands for number of photo-electrons and is a unit which characterizes the images collected by a IACT. It represents the sum of the calibrated charge of a triggered event collected by each PMT of the telescope camera, in other words the `size` of a detected image.

redshift (z) is the ratio decreased by a unit between the radiation wavelength emitted by an object in Doppler motion with respect to an observer, λ_{em}, and that observed, λ_{ob}: $1 + z = \frac{\lambda_{ob}}{\lambda_{em}}$.

In astronomy it is used as a distance or time unit, and is related to the gravitational redshift experienced by the radiation traveling cosmological sitances, due to the expansion of the Universe. Therefore, it is strongly dependent on the cosmological model assumed.

In addition, we have used the following energetic regimes:

High Energy (HE) conventionally, in this work we define the HE regime as that included in the energy range from 0.1 GeV to 100 GeV.

Very High Energy (VHE) ot TeV energies conventionally set to the range between 100 GeV to tens of TeV.

Acronyms used in this thesis

AGASA Akeno Giant Air Shower Array

AGILE Astro–rivelatore Gamma a Immagini LEggero

AGN Active Galactic Nucleus

AMC Active Mirror Control

CCNN Close Compact Next Neighbors

CGRO Compton Gamma–Ray Observatory

CMB Cosmic Microwave Background

COBE COsmic Background Explorer

CR Cosmic Ray

CTA Cherenkov Telescope Array

EAS Extended Air Showers

EBL Extragalactic Background Light

EGRET Energetic Gamma Ray Experiment Telescope

FADC Fast Analog to Digital Converter

FoV Field of View

FSRQ Flat Spectrum Radio Quasar

GB Gamma–ray Backgorund

GBM GLAST Burst Monitor

GRB Gamma–Ray Burst

GZK Greisen–Zatsepin–Kuz'min

HBL High–frequency peaked BL Lac

H.E.S.S. High Energy Stereoscopic System

HAWC High Altitude Water Cherenkov Experiment

HE High Energy

HST Hubble Space Telescope

IACTs Imaging Atmospheric Cherenkov Telescopes

IBL Intermediate–frequency peaked BL-lac

IC Inverse Compton

IGM InterGalactic Medium

IP Impact Paramener

ISM InterStellar Medium

LAT Large Area Telescope

LBL Low–frequency peaked BL-lac

MAGIC Major Atmospheric Gamma Imaging Cherenkov

MARS Magic Analysis and Reconstruction Software

MC MonteCarlo

MJD Modified Julian Date

NSB Night Sky Background

PAMELA Payload for Antimatter Matter Exploration and Light-nuclei Astrophysics

PMT Photo-MultiPlier Tube

PSF Point Spread Function

PWD Pulsar Wind Nebula

QE Quantum Efficiency

RA Right Ascension

RG Radio Galaxy

RF Random Forest

SED Spectral Energy Distribution

SNR SuperNova Remnant

SSC Syncrotron Self Compton

UHE Ultra High Energy

UHECR Ultra High Energy Cosmic Ray

VERITAS Very Energetic Radiation Imaging Telescope Array System

VCSELs Vertical Cavity Surface Emitting Laser Drivers

VHE Very High Energy ($> 100\,\mathrm{GeV}$)

VLT Very Large Telescope

I wish I was as fortunate, as fortunate as me.

Wishlist – Pearl Jam

Acknowledgments

This work of Thesis is the result of more than three years of scientific collaboration with many people, who I would like to thank.

First, an obliged thanks goes to my mentor, Prof Mosé Mariotti, for his trust in me, his unwavering optimism, and for all the opportunities that he has given to me... Thank you!

It has been a great honor and pleasure for me working with Fabrizio Tavecchio, whose name has already entered in the history of blazars astrophysics. In particular, I would like to thank him for his patience in teaching me how to write a scientific article, and for all the advices and numerous skype chats and SED plots, even during holidays...

Many thanks to the MAGIC colleagues, with whom I shared the wonderful and exciting adventure of making research in the field of VHE γ–ray astrophysics. In particular, I am grateful to my PG 1553+113 friends Giacomo Bonnoli, Daniela Dorner, and Nijil Mankuzhiyil, to Pepa Becerra, for sharing with me PKS 1424+240 and for her friendship, to Alberto Dominguez and Daniel Mazin, for their help in understanding the EBL, and all the other people with whom I worked with: Laura Maraschi and her precious suggestions, Elina Lindfors, Pratick Majumdar, Manel Errando, and many many others...

My data taking shifts would not have been so pleasant without Valeria Scapin and Elvira Leonardo, in the first all–women shift of the history, and Karsten Berger, Gianluca Giavitto, and Pere Munar, in the long cloudy nights between science and loughs.

I am obliged to Carlo Bombonati, Fillippo D' Ammando, Francesco Dazzi, Alberto Dominguez, Saverio Lombardi, Abelardo Moralejo, Simona Paiano, Andrea Rossi, Cornelia Schultz, Steve Shore, and Antonio Stamerra, for their very useful comments on this manuscript. In addition, I would like to thank Sandro Ventura for his help in the examination of medical physics.

A special acknowledgment to the forever members of the MAGIC Padova Group: Roberta, Valeria, Cornelia, Simona, Saverio, Villi, Michele, Fabio, Marcos, Francesco, Alessandro, Diego, Markus, Ciro, Abelardo, Nadia, Daniele, Luigi, Antonio, Donatella and of course Mosé.

A particular thanks to Villi, with whom I shared not only the blackboard for many years, but also thoughts, feelings, fears and many songs and special moments, and to Saverio, a true friend, who kindly helped me many times!

In parallel to this work of thesis, it has been a real pleasure to invent and realize, together with Antonio, Rossella, Renzo Paolo, and Villi, the wonderful experience named MAGIC-D. A special thanks, of course, goes to the guys who have turned this project into reality: Vera, Marta, Carlo Maria, Matteo, Matteo, Riccardo, Roberto and Alberto, for the 2009 stage, and Anna, Mara, Amine, Giulio, Domenico, Stefano, Paolo, Matteo e Giulio, for the 2010 stage.

Many thanks to Luigi Tibaldo, my Ph.D. mate and friend, who shared with me

joys and pains of representation, and many discussions about everything.
My life during these years would not have been a life without the love and support of Andrea, my family, and my friends. Here, I would like to thank them all.
In particular Andrea, for the never boring 14 years connecting us, and for that day, between the Andes, when I really understood the wonderful person you are. I am ready for the Alps now!
A kiss to my sister Marianna... whatever life she will choose, I will always be with her and her contagious smile. Thanks mamy, since if I am here, dreaming, doubting, and fighting, it is also thanks to you. Thanks to Luciano, for his resolute idealism. A great hug to my grandmothers, Bruna and Vittorina, and to all my aunts, uncles and numerous cousins. A special thought goes to Sandra and Gianfranco, my second family between the Morenic hills.
How can I thank you, my friends, who colour my life with words, jokes, discussions and special moments?
Angela and Giustina, thanks to be as you are... the best friends someone can imagine! Tino, thank you for your presence, the nice time spent together between concerts, wine and loughs, and the hard time spent together, among doubts and uncertainties. Michy, thanks for your joy and simplicity... and to be there waiting for us every day, I'd like it to last forever! Thanks to all the Mantova friends: Izio for sharing the PJ passion, Chiara and Cri, for the rare and precious evenings–women, Mauro for his tiny greatness, Lusaz and the Anomia, Vanya and the tasty cheese, (organ playing) Mazzo, Ivan and Jim. Manu and Fabry, I wish you the life you dreamed so long about!
Thanks to the Padova friends: Enrico, for teaching me that we can be (very) different and still esteem us..., my brother Phobos, Davide, I am looking forward to the next carnival! Verroy, a name a security, Degiu, the first friend that follows my suggestions, Seba, my recipes friend (and future business partner?), Luca, Beppe, Ale B., Ale C., Leti, Claudia, Lucia, Simone, Nick, Nicoletta, Catte, Claudio, Valeria, the guys of the Didi's bar, the old dance friends and the new theater companions, Natalino Balasso & company for their Fog theater, that have heated long autumn evenings..., the band "Piccola Bottega Baltazar", for the exceptional musical background. Last but not least, I would like to thank Sandra, who changed in the last years my concept of space, and my new "maestri": Roberto and Andrea.